Novel Approaches to PET Imaging Neurodegeneration

by

Sean Tanzey

A dissertation submitted in partial fulfillment
Of the requirements for the degree of
Doctor of Philosophy
(Medicinal Chemistry)
in the University of Michigan
2021

Doctoral Committee:

Associate Professor, Peter J.H. Scott, Chair
Professor Timothy A. Cernak
Professor Robert A. Koeppe
Professor Andy White

Sean Tanzey

tanzeys@med.umich.edu

ORCID id: 0000-0002-7423-6142

DEDICATION

This work is dedicated to my father, Terry Tanzey, my true mentor in life. You will be missed.

ACKNOWLEDGEMENTS

This work could not have been made possible without the help of so many that I have crossed paths with. I would first like to thank my mentor, Professor Peter J.H. Scott for accepting me into his lab where I have met the finest group of scientists. His relaxed approach made things very easy-going during times that could have otherwise been very stressful during the PhD process. Thank you for being a friend. My most fond memory will be driving all the way across Michigan to see Slayer!!! My first organic chemistry mentor, Dr. Andy Mossine showed me the ropes and taught me so much than I could have ever asked for. Thank you for your friendship as well. Dr. Allen F. Brooks, who I like to refer to as the walking-talking encyclopedia, has given me such tremendous insight into all these projects. Thank you for the endless conversations, friendship, and all the beers we shared together. I developed a very close relationship with Dr. Xia Shao, my scientist mother, the most kind and funny person I have worked with in this process. Without her, all my work with carbon-11 would have been even more of a struggle. All the biochemistry performed in this work was taught to me by the eccentric Timothy Desmond, who provided the best smiles and jokes in the lab for me. Dr. Stefan Verhoog, a fellow metal head, has given me more votes of self-confidence in chemistry than anyone and has helped me to edit this work. I would also like to thank Robert Koeppe for his mentorship and allowing me the opportunity to travel abroad and learn from the experts in PET imaging analysis. I have appreciated my time in this Taj Mahal of PET centers, where I have worked alongside some of the most fun individuals in this field including the Gallium-68 crew Missy Rodnick, Jeremiah Alicea, Laura Bruton, and

Mara Clark, the animal imaging crew, Jenelle Stauff, Janna Arteaga, and Phil Sherman, the postdocs that have ventured into our lab, Stephen Thompson, Tanpreet Kaur, So Jeong Lee, Jay Wright, Ryan Pakula, and Sean Preshlock, my graduate student sisters Megan Stewart, Allie Sowa/Dumond, and Lindsey Drake and finally the undergraduates, Isaac Jackson, Tony Mufarreh, Jonathan Pham, Wade Winton, and the student I got to mentor, Jake Sypniewski. I hope to continue to work with these amazing individuals in my future career as a PhD radiochemist. Every single one of them has provided comic relief, interesting conversations, and memories that will be cherished.

Getting through these past 4 years was challenging, but I had the support of many loved ones. My strong, independent mother has taught me the virtue of working diligently and how to weather any storm. I will always look up to you.

TABLE OF CONTENTS

LIST OF FIGURES

LIST OF TABLES

LIST OF SCHEMES

ABSTRACT

Early detection of neurodegenerative diseases (NDs) has remained challenging for clinicians. To improve diagnostic confidence across the ND spectrum, there is considerable research devoted to the discovery of potential biomarkers of disease onset and progression. NDs share the common feature of progressive loss of structure and function of neurons resulting from different protein aggregates responsible for the various diseases. Alzheimer's Disease (AD), the most prevalent ND, is characterized by amyloid plaques (composed of amyloid ß (Aß) protein) and neurofibrillary tangles (composed of tau protein) within the hippocampal and cortex regions of the brain. Parkinson's Disease (PD), the second most common ND, is caused by dopaminergic neuronal loss within the basal ganglia, which controls voluntary movement, as a result from α-synuclein (α-syn) aggregation within the same region. Biologically relevant transition metals such as iron, copper, and zinc are reportedly accumulating and causing the aggregation of known neurotoxic protein aggregates at sites afflicted by neurodegenerative diseases. Detecting such metal ions may provide a means of early detection of these otherwise hard to diagnose diseases using positron emission tomography (PET) imaging agents. Radiopharmaceuticals available today for imaging of the central nervous system (CNS) are limited to those imaging the mid- to late-stages of CNS disease progression. This imaging modality provides information at the molecular level of living organisms that clinicians can use to confirm a diagnosis or assess the effectiveness of a treatment. Small molecules, peptides, and large proteins can be radiolabeled with a wide range of positron emitting isotopes with various half-lives such as carbon-11 (C-11, ^{11}C, $t_{1/2}$ = 20 min)

and fluorine-18 (F-18, ^{18}F, $t_{1/2}$ = 109.7 min). The overall objective of the work described in this thesis is to design and analyze novel PET tracers ([^{11}C]deferiprone (Chapter 2) and [^{18}F]FL2-b (Chapter 3)) that bind physiological transition metals (Cu, Zn, and Fe) which are hypothesized to accumulate abnormally in the brain early in NDs. Known metal chelators will be radiolabeled and used in preclinical animal studies to determine brain uptake, binding kinetics, metabolism, biodistribution, and be evaluated in both diseased brains and healthy controls. Additional work described includes development of a novel radiotracer, [^{11}C]AZ683, for neuroinflammation imaging (Chapter 4), where it is thought that inflammation is a result of toxic metal accumulation. Lastly, although several PET tracers are approved by the Food and Drug Administration, some of them are challenging to synthesize for routine production. Efforts to improve the synthesis of such a tracer ([^{18}F]FDOPA) using copper-mediated radiofluorination in accordance with current good manufacturing processes (cGMP) are also discussed (Chapter 5).

CHAPTER 1

Application of Positron Emission Tomography (PET) as a Molecular Imaging Tool to Investigate the Metal Hypothesis of Neurodegeneration

1.1. Introduction

Positron Emission Tomography (PET) is a noninvasive imaging technique that uses radioactive compounds (termed radiotracer since the concentration of the compound is injected at tracer concentrations) to image specific biomarkers of disease.[1] This provides information at the molecular level of living organisms that clinicians can use to confirm a diagnosis or assess the effectiveness of a treatment. Small molecules, peptides, and large proteins can be radiolabeled with a wide range of positron emitting isotopes with various half-lives such as carbon-11 (C-11, ^{11}C, $t_{1/2}$ = 20 min), fluorine-18 (F-18, ^{18}F, $t_{1/2}$ = 109.7 min), gallium-68 (Ga-68, ^{68}Ga, $t_{1/2}$ = 68 min), copper-64 (Cu-64, ^{64}Cu, $t_{1/2}$ = 12.8 hr), nitrogen-13 (N-13, ^{13}N, $t_{1/2}$ = 10 min), oxygen-15 (O-15, ^{15}O, $t_{1/2}$ = 2 min)and others.[2] The list of PET isotopes in clinical use is still expanding as new isotopes continue to be translated for PET imaging (and theragnostic) purposes (e.g. zirconium-89, scandium-44).[2,3] Whilst PET has its usefulness in the assessment and treatment of patients, it can also be applied to drug discovery by determining drug occupancy, biodistribution, pharmacokinetic (PK) properties of pharmaceutical assets in development (i.e. binding affinity = K_d, target density = B_{max}).[4]

The life of a PET radiotracer begins at the on-site production of the PET radioisotope. These isotopes are generated by bombarding a nonradioactive element (i.e. ^{14}N or ^{18}O) with a high energy proton beam originating from a cyclotron (**Figure 1.1**).[5] During bombardment, a neutron (or alpha particle if ^{11}C is being created) is ejected from the nucleus of the atom, successfully creating the unstable and short-lived radionuclide. The PET radionuclide is then transferred to the radiochemistry laboratory where it is incorporated into a bioactive molecule to generate the radiotracer. Following purification, formulation and quality control testing, the radiotracer is then injected into a patient (or animal) intravenously. The radiotracer accumulates at its target site (e.g. tumor) and the PET radionuclide undergoes positive beta decay, releasing a neutrino as well as a beta particle (+e, β^+, positron, antielectron) that can travel through tissue until its kinetic energy is low enough to interact with its antiparticle, the electron (**Figure 1.2**). When matter and antimatter collide, an annihilation event occurs where the energy released is in the form of two 511 kEV gamma photons traveling in opposite directions at 180°. A PET scanner is equipped with scintillators which produce a signal after gamma detection. This signal is interpreted by software to determine the point of origin of the annihilation event which is used to construct a 2D or 3D image (**Figure 1.2**). Systems with a higher time resolution of three nanoseconds use a time of flight method to monitor the precise difference in time of the photon detection in order to calculate the line of response, thus leading to a more accurate determination of the point of origin.[6]

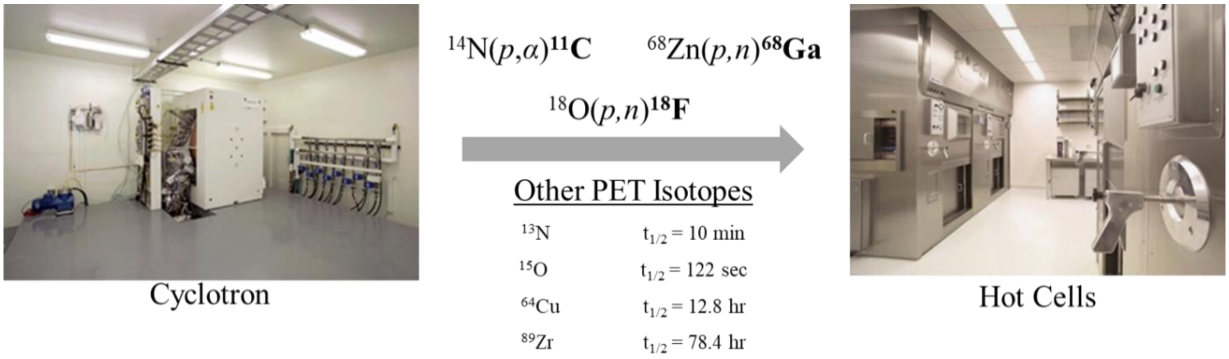

Fig. 1. 1: Overview of PET radioisotope production where a cyclotron produces a proton beam, and irradiates a particular atom that undergoes a nuclear reaction to product an unstable isotope with a short half-life and delivered to a hot cell for safety

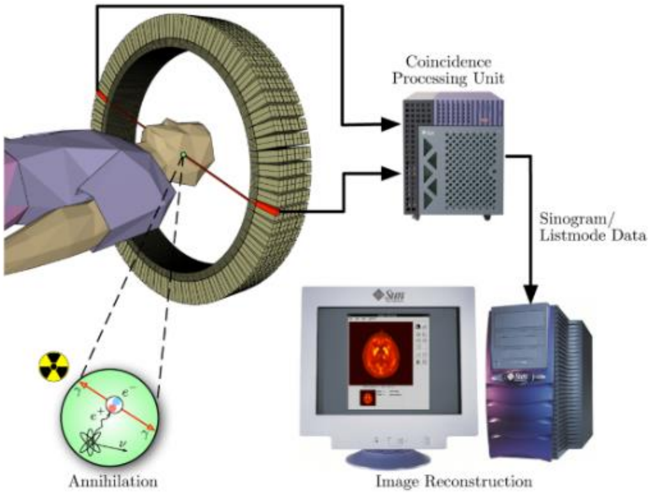

Fig. 1. 2: Schematic of acquisition of a PET scan and reconstruction of the data to create a PET image

The process of radiolabeling a molecule takes place inside a lead-shielded, automated synthesis module to limit exposure of radioactivity to the chemist (**Figure 1.2**).[7] To optimize this process, conditions can be tested manually outside of the synthesis module to ensure high radiochemical yields and purification can be achieved prior to automation and scale-up. Due to the short-lived radionuclides used, the most desirable reaction process to produce a radiotracer is simply the radiolabeling step without any further reactions (e.g. deprotection). However, drug like molecules often contain multiple chemical moieties that can interfere with the radiolabeling conditions. Protecting groups can be used to prevent undesirable side reactions from taking place, but conditions for rapid and straightforward deprotection after radiolabeling are essential.[8] Though the radiolabeling step is preferred to be the last step in the process (late-stage radiolabeling), novel compounds sometimes require manipulation to make the radiolabeling site reactive, in which case multiple chemical reactions follow the radiolabeling step. Each step is *manually* performed to optimize the conditions of the reaction. These conditions are assessed by radiochemical yield (RCY)[9] with the use of a radio-thin layer chromatography (radio-TLC) and/or high-performance liquid chromatography (HPLC) equipped with a radioactivity detector.[10] Radio-TLC can determine how much of the radioisotope was incorporated into the molecule (referred to as radiochemical conversion (RCC) or RCY), and identity can be determined by co-injection of the radiotracer on HPLC with its nonradioactive reference standard.[9] One important characteristic of a radiotracer is the molar activity (MA, A_M), which is the measured radioactivity per mole of compound measured.[9] The quantification of molar activity represents how much mass in the dose is radiolabeled versus how much is not. The cold mass (i.e. carbon-12 isotopologue of the tracer) can inhibit specific binding of the radiotracer and thus lead to a decreased signal during a PET image. Once each chemical reaction step is optimized, purification is needed to separate the radiotracer from other reaction components. This can be achieved with solid-phase extraction (SPE) cartridges or a semi-preparative HPLC. The latter is usually reverse phase, and numerous different solid-phase materials are available and are chosen depending on the physiochemical properties of the radiotracer being purified. Purification relies on polarity, pH, and hydrophobic interactions.[11] The eluent required for purification can sometimes rely on organic solvents such as acetonitrile, and the product will need to be reformulated into an injectable buffer like 10% ethanol, 0.9% saline, or phosphate-buffered saline (PBS).[12,13] Ideally the pH of the formulated radiotracer should match physiological conditions of the blood, being pH 7.4, but in practice can range from pH 4.5-8 depending on the stability of the compound.[14]

This production of PET tracers can be tedious and, if complicated production affects reliability of clinical delivery, this can limit use of a radiotracer in the clinic. To combat this, efforts to improve the synthesis of clinical PET tracers are constantly being undertaken by our lab and others[15,16] so that straightforward and reliable routine production is possible. For example, our lab introduced copper-mediated radiofluorination (CMRF) to improve the late stage radiofluorination of bioactive molecules. Chapter 5 of this thesis reports the application of CMRF to the synthesis of [^{18}F]6-fluoro-DOPA, an historical radiotracer that has long been challenging to synthesize for routine clinical use.[17,18]

Once a radiotracer has been translated into the clinic, physicians can determine if an imaging target is a suitable biomarker of disease by monitoring the accumulation or disappearance of the radiotracer throughout, for example, the course of a disease. Reflecting this, novel imaging biomarkers are eagerly sought after and development of novel PET tracers and is an active area of research development. For example, PET imaging has revolutionized dementia research. Brain PET with imaging agents targeting misfolded amyloid-β/tau proteins, cerebral glucose hypometabolism and cholinergic markers in the central nervous system (CNS) has provided a wealth of information on the mechanisms underpinning dementias including Alzheimer's disease and related disorders (ADRD), allowed clinical trial enrichment and enabled monitoring patient response to experimental therapies.[19] Despite these advances, effective treatments for ADRD remain elusive. The recent implication of neuroinflammatory pathways and disruption of metal homeostasis in ADRD offer potential solutions but require equally sophisticated imaging biomarkers. The remainder of this thesis describes our efforts to develop new radiotracers for ADRD targeting neuroinflammatory targets (Colony Stimulating Factor 1 Receptor (CSF1R), Chapter 4), metal-protein aggregates (Chapter 3) and toxic iron (Chapter 2). Chapter 6 concludes and provides future directions for each project. To put this work into the context of functional neuroimaging, the remainder of this introduction surveys the current state-of-the-art in brain PET imaging.

1.2. What Makes a Good CNS PET Target?

There are two important factors to consider when determining if a novel target is suitable for viable CNS PET imaging: its maximum concentration, represented as B_{max}, and its biodistribution. Ideally, these factors should change considerably in a diseased state so that differences can be visualized for clinicians to make proper assessments when interpreting a PET scan. For quantitative analysis and obtaining meaningful data, the B_{max} should be greater than 1 nM as the binding affinity of successful radiotracers usually have sub-nanomolar to single nanomolar affinity.[20] During the development of a successful PET tracer, its binding potential (BP = B_{max}/K_d)[21] is used to quantitate its usefulness in imaging a target. When a radiotracer is injected, the concentration can be in the picomolar range, and would thus only occupy about 0.05% of its available target. If the affinity of a radiotracer to its target exceeds the concentration of its target, then the signal obtained would hardly represent the bound target in the allotted time of a PET scan, which is about 1 – 2 hours. Therefore, in quantitative terms, if a target is to be viable for PET imaging, the B_{max} should be greater than the binding affinity of the radiotracer being used to assess it and, at least, have a threefold difference, or more, in the diseased state compared to a normal control.[22] A target's density can either increase or decrease in one or more regions during the progression of a disease of interest. This would allow for a larger or smaller BP for the radiotracer during the disease and, thus, a large difference in signal during the PET scan.[23] An ideal target can either be diffusely and ubiquitously distributed across the human brain or located in one (or more) brain region that is sizeable, as the resolution of a PET image is limited to at least 1 mm.[24–26] As long as the expression or density of the target varies in specific regions during disease, this would make it useful for assessing diseased patients by quantifying changes in the imaging biomarker during disease progression.

Unfortunately, the data corresponding to target density in normal or diseased human brains is often lacking for novel targets. When literature values are available, the *in vitro* assessment of target density from various studies are usually expressed in units of fmol/g of brain tissue or fmol/mg of protein. If it is assumed that the brain contains 100 mg of protein per g of wet tissue, which is generally the case,[27] then 1 fmol/g of brain tissue simply equates to 1 nM and 1 fmol/mg protein to 0.1 nM. Targets that have been assessed in PET scans of normal human brains have ranged from 0.5 nM to 150 nM.[28,29] When the data for a novel target is hard to obtain, quantitative autoradiography can be performed to estimate the value of the target's B_{max}. The factors for a good PET tracer that can be used in this data collection are discussed in the section explaining what makes a good CNS PET tracer (Section 1.4). It should be noted that target density estimates in animals and disease models may vary from the true B_{max} value for the target in human disease, as animal data does not necessarily always translate well to human studies.[27] This is likely due to differential density of targets that vary from species to species, or disease models not truly representing the entire molecular array of a human disease. Nonetheless, *in vitro* saturation binding studies on human brain tissue can be used with a suitable PET radiotracer to estimate the B_{max} and expert reviews are available that discuss the problems with translating target density estimated by autoradiography to PET scans.[30] Briefly, targets are more exposed during *in vitro* measurements and Blood-Brain Barrier (BBB) penetration is not a limiting factor in obtaining *in vitro* data. For a more detailed discussion on what makes a good molecular target for PET imaging, please refer to other reviews.[20,31]

1.3. Current Neurodegeneration Imaging Approaches and their Limitations

To date, only small numbers of clinical biomarkers specific to neurodegeneration have been targeted by PET radiotracers. During neurodegenerative disease (ND) progression, it is known that specific peptides aggregate into plaques and tangles in the brain regions associated with deterioration that are specific to the disease. The cause of the formation of these plaques and their subsequent consequences are currently under heated debate.[32] Nonetheless, such protein aggregates have provided a valuable target for PET radiotracers to enable the differentiation of ND that have clinical overlap.[33–35] Noninvasive imaging of protein aggregates with PET mimics the stages defined years ago by Braak *et al.* that determined the brain regions that accumulate protein aggregates during AD through immunohistochemical (IHC) staining.[36] Building on this initial work, other potential imaging biomarkers for ND have been the focus of several clinical PET radiotracer development programs including, but not limited to, proteins and enzymes expressed specifically in the synapses affected during a specific disease as well as inflammation biomarkers that are thought to occur before and lead to protein aggregates.[37,38] As this information has been thoroughly and extensively reviewed elsewhere, the main points will be discussed briefly on the current approaches to ND PET imaging and their limitations.

1.3.1. *Alzheimer's Disease*

Protein aggregates primarily associated with AD are composed of amyloid ß (Aß) and hyperphosphorylated tau (pTau).[39] Aß is the main component of senile plaques and pTau is the main component of neurofibrillary tangles (NFTs). Braak staging indicates that senile plaques begin in the transentorhinal cortex (Stage I/II) and spreads to the limbic system (Stage III/IV) that includes the hippocampus, amygdala, temporal cortex, and basal frontal cortex, and then finally widely distributed amongst the neocortex (Stage V/VI).[40] The spread of NFTs follows that of senile plaques, albeit starting just after senile plaques start to spread.[41] In other words, the spread of NFTs lags just behind that of senile plaques during progression of the disease. Aß is a cleaved product of the protein Amyloid Precursor Protein (APP). APP can be cleaved at the amino terminus by either α-secretase resulting in a non-amyloidogenic end-product, or ß-secretase, which results in the amyloidogenic end-product, Aß, which can be 36-43 amino acids (aa) long.[42] These peptides can misfold and aggregate together to form soluble oligomeric complexes, and eventually insoluble plaques that are the target of current PET tracers.[43] The formation of NFTs is not as well understood as senile plaques but is believed to occur due to hyperphosphorylation of tau protein.[44] The kinase associated with hyperphosphorylation of tau is thought to be glycogen synthase kinase 3ß (GSK3ß).[45] In the amyloid hypothesis, it is believed that the formation of senile plaques and subsequent NFTs eventually cause apoptosis and thus, neuronal cell death, which primarily effects the glutaminergic and cholinergic neurons.[39]

There are several PET tracers that have been developed to image Aß plaques, including [^{11}C]Pittsburg Compound B ([^{11}C]PiB),[46,47] [^{18}F]FDDNP,[48] [^{18}F]florbetaben,[49,50] [^{18}F]florbetapir (AV-45),[51,52] flutemetamol,[53] and [^{18}F]NAV4694.[54,55] All of these have been used to image amyloid plaque burden (**Figure 1.3**), and this information has been used for diagnosis of ADRD, clinical trial enrichment and monitoring AD patient response to therapy.[19] A drawback of the current amyloid radiotracers is they suffer from nonspecific binding. For example, the most widely used tracer, [^{11}C]PiB, suffers from high nonspecific binding in the white matter which can lead to trouble differentiating normal patients and those with mild cognitive impairment (MCI).[56] Although [^{18}F]NAV4694 has been developed to help differentiate MCI and AD, it suffers what all Aß tracers do, being unable to image the more toxic, soluble Aß oligomers that are thought to be responsible for disease progression, and is thus limited to mid-late stage imaging.[57–59] [^{18}F]Florbetaben and [^{18}F]florbetapir (AV-45) have an advantage over [^{11}C]PiB in that they are labeled with fluorine-18 (an isotope with a longer half-life and therefore, longer PET scans can be performed),.[60] [^{18}F]FDDNP forms metabolites extensively that are BBB permeable, and it may also bind to tau NFTs which is not ideal when plaques and NFTs colocalize.[61] To address the latter issue, there was need for a selective tau radiotracer and several have been developed (**Figure 1.4**) that can image NFTs, revealing staging as predicted by Braak's IHC staining.[62] However, some of these tracers (AV-1451, THK5351) have known off-target binding to MAO-B, a biomarker of inflammation, making it difficult to know how much of the signal is related solely to NFTs,[63,64] while others (PBB3) form brain penetrating metabolites that complicate image quantification. Development of 2nd generation tau radiotracers (e.g. MK-6240, PI-2620) is focused upon eliminating this off-target binding.[65]

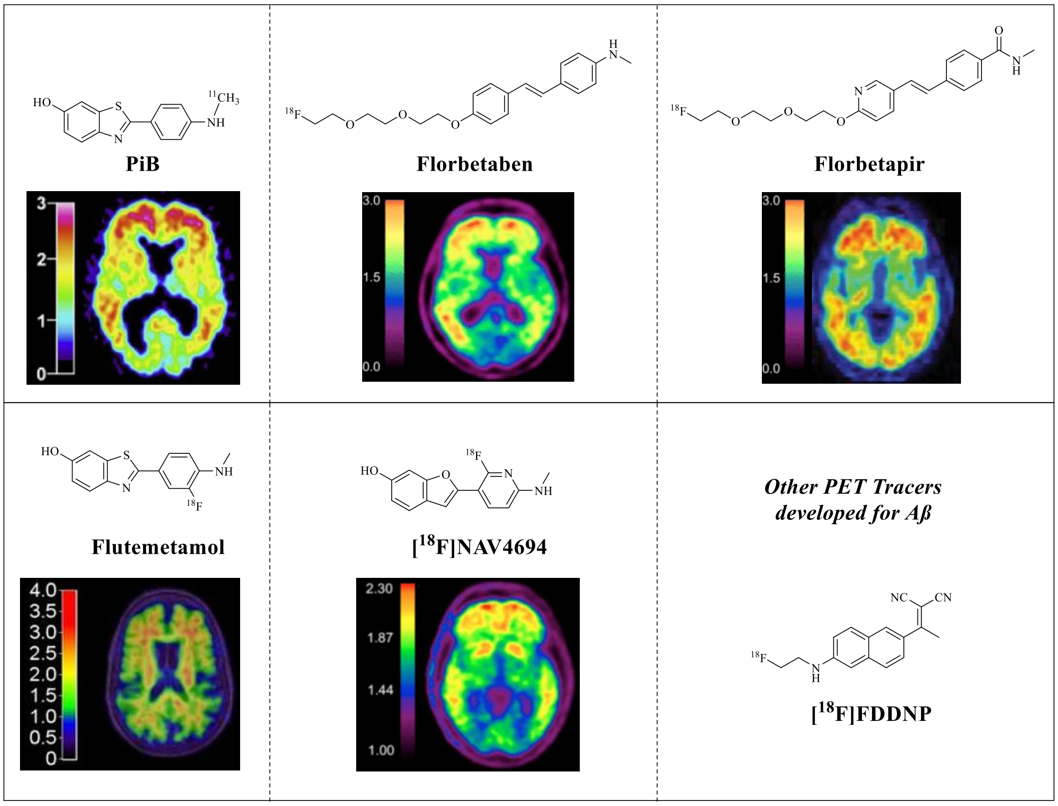

Fig. 1. 3: PET Tracers developed for Aß protein to image plaques with representative images to illustrate regional distribution. SUVR standardized uptake value ratio. Adapted from ref. 47,50,52,53,55 with permission from Elsevier, OBM Geriatrics, Journal of Nuclear Medicine, *and* Wolters Kluwer Health, Inc.

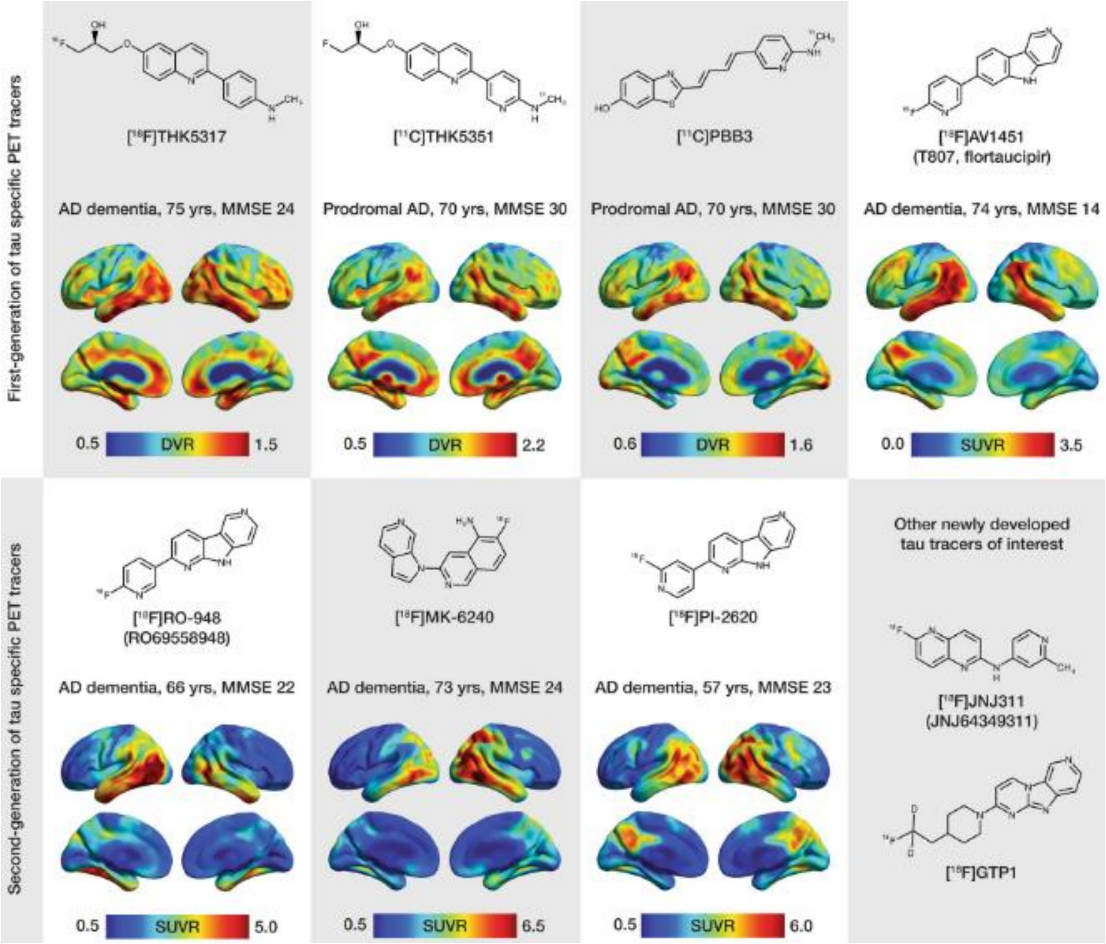

Fig. 1. 4: PET Tracers developed for Tau protein to image NFTs with representative images to illustrate regional distribution. DVR distribution volume ratio, SUVR standardized uptake value ratio. Adapted from ref. 62 with permission from Molecular Psychology

1.3.2. *Parkinson's Disease*

The major protein aggregates found in Parkinson's Disease (PD), termed Lewy bodies, are primarily composed of the peptide, α-synuclein (α-syn).[66] Braak *et al.* has also performed IHC staging of PD brains, similar to AD, where the aggregates begin in a distinct region and spread to other regions affecting specific neurons.[67] How α-syn spreads is still under investigation. First, α-syn is found in the olfactory bulb and lower raphe nuclei (Stage I/II), begins to spread into the structures of the basal ganglia, being the substantia, nigra, amygdala, and striatum (Stage III), then finally to the temporal cortex (Stage IV/V). Like the amyloid hypothesis of AD, it is believed that α-syn aggregates can also cause neuronal cell loss, primarily effecting the dopaminergic neurons.[68]

The physiological role of α -syn is vast as it plays many roles in modulating synapse proteins and the stabilizing the structure of the synapse altogether.[66] Improper functioning of α-syn would than lead to dysregulation of neurotransmitter release. As dopaminergic neurons are primarily found to regulate motor control, disease causing α-syn aggregates help to explain the exacerbation of motor symptoms found in PD patients.[69]

Unlike AD, radiotracers for PD have not been validated for its protein aggregate, α-syn, and presynaptic proteins of the dopaminergic system have been targeted instead. Some presynaptic proteins specific to dopaminergic neurons that have been targeted include the dopamine transporter (DAT),[70] targeted by [^{123}I]ß-CIT,[71] and aromatic l-amino acid decarboxylase (AADC),[72] responsible for dopamine metabolism, which is targeted by [^{18}F]FDOPA.[73] Due to the arduous task of synthesizing [^{18}F]FDOPA, its widespread use in research has been limited, and the poor spatial resolution of Single Photon Emission Computed Tomography (SPECT) agents like [^{123}I]ß-CIT confound making meaningful interpretations of early-stage imaging for PD. More general presynaptic proteins have been the target of PET tracers like VMAT2,[74] serotonin transporters,[75,76] glutaminergic mGluR5,[24] and Adenosine type 2a.[77] Imaging of these proteins makes it possible to visualize function of these synapses. Decreased expression of these proteins can be interpreted as decreased synaptic connections, and thus, decreased synaptic density. In conclusion, PET imaging of PD remains a challenge as an early stage biomarker specific to the disease remains to be easily targeted.

1.3.3. *Neuroinflammation*

Although it has been suggested that neuroinflammation during neurodegeneration is a result of protein aggregation and dying neuronal cells (where immune cells clean up the contents expelled by dying cells),[78] the neuroinflammation hypothesis opposes this view stating that chronic neuroinflammation induces oxidative stress that causes protein aggregation and neuronal cell death.[79] Whether it occurs before or after protein aggregation, several PET tracers have been developed that aim to target specific proteins associated with inflammation as it is clear that they are biomarkers of neurodegeneration

Neuroinflammation is mediated by brain specific immune cells including microglia, dendritic cells, macrophages, and myeloid cells.[80] Resting immune cells in the brain during a normal state can become activated by a pathogen, leading to increased expression of specific proteins.[81] These protein biomarkers of neuroinflammation include translocator protein 18 kDa (TSPO),[82] cyclooxygenase (COX),[83] monoamine oxidase (MAO),[84] GSK3ß,[85] and even newer targets like triggering receptor expressed on myeloid cells 2 (TREM2),[86] receptor for advanced glycation end-products (RAGE),[87] colony stimulating factor 1 receptor (CSF1R),[88] and purinergic receptors (P2X and P2Y).[89] The target, TSPO, is the most widely targeted protein of neuroinflammation that has resulted in the development of several clinical PET tracers because of evidence showing that TSPO expression in glial cells is increased during inflammation.[90–92] Unfortunately, TSPO expression is not restricted to microglial cells and 10% of the population contains a mutant TSPO caused by a single nucleotide polymorphism (SNP) that prevents binding of most PET tracers.[93] The variants COX-1/2 remain a challenge to image as COX-1 has high basal expression and PET tracers for COX-2 are not sensitive enough to detect the small changes associated with neuroinflammation.[94] MAO PET tracers reveal promising data, showing that MAO-B is overexpressed during MCI and AD.[95] PET imaging of newer targets like P2X,[96] P2Y,[97] and RAGE[98] have been successful, and tests to understand their role in early neurodegeneration are still under way. Development of PET tracers for imaging of CSF1R will be discussed in Chapter 4. Though imaging neuroinflammation may prove to be valuable in early detection of neurodegeneration, it is not specific to it. Neuroinflammation can be caused by several factors (e.g. head trauma) and the search for ND biomarkers to be imaged by PET continues. Of the emerging biomarkers, biological transition metals such as iron (Fe), copper (Cu), and zinc (Zn) are suspected to play an early role in NDs.[99]

1.4. Metal Ions as a Target for PET

When a small molecule PET tracer is injected, it will distribute into every tissue compartment that is accessible by passive diffusion (if it is not a substrate for a transporter) where it can then bind its target. Depending on the scanner used, a full body image[100] can be reconstructed to provide insight into where and how much of the tracer is binding.[101,102] Physiological transition metals pose a unique target in that they are ubiquitously distributed in organisms and utilized in various ways, performing a wide range of functions such as oxygen transport, electron transfer for oxidation and reduction reactions, enzyme catalysis of enzymatic substrates, and are even structural components.[103] Given that positron-emitting chelators can only bind a small percentage of these metals (~1% of total Fe, X% for Cu, and X% for Zn) when injected at tracer amounts and obtaining kinetic data in a short time frame (e.g. 1-2 hours after injection), we anticipate using PET to understand the nature of the accessible/chelateable labile metal pool. However, the presence of protein-bound metals helps to understand the mechanisms of diseases and predict where increases/decreases in the metal labile pools might take place within the body. Thus, a full understanding of the entire biochemical control of transition metals in the body will help to understand where metal chelating PET tracers will bind in a normal organism and how it will change its distribution in various disease states. PET imaging of physiological transition metals could provide a unique way to interrogate the mechanism of metal-related diseases that will help us probe where oxidative stress is occurring, comparable to how [^{18}F]FDG (the gold-standard of PET imaging) can provide information on areas of hyper- and hypo-metabolism in diseased states.

1.4.1. *Iron as a Target for PET*

1.4.1.1. *Iron Homeostasis*

1.4.1.1.1. *Proteins Involved in Processing Iron*

Since PET tracers are injected intravenously, we will begin our discussion of the various iron components of the blood where the first interactions with the PET tracer will take place. First and foremost, iron exists in two oxidation states at physiological conditions – ferrous (Fe^{2+}) and ferric (Fe^{3+}) iron. The lower oxidation state of Fe^{2+} makes it more soluble than Fe^{3+} in aqueous conditions where it can reach a maximum concentration of 10^{-9} -10^{-7} M (Fe^{3+} can only reach concentrations from 10^{-19} - 10^{-17} M).[104] However, the presence of protein metal transporters, storage proteins, amino acids, nucleic acids, organic chelates (citrate, acetate, glycochelates, glutathione, nitrilotriacetate) and organic salts (PO_4^{3-}) allow biological systems to contain increased concentrations of iron far beyond these limits. In the blood, iron is transported in the plasma by proteins like transferrin and ferritin as Fe^{3+},[105] but is found mostly in the red blood cells contained in hemoglobin as Fe^{2+}, responsible for oxygen transport.[106] These globin proteins utilize porphyrin prosthetic groups (**Figure 1.5**) to bind iron within their oxygen binding sites. The tetradentate coordinating character of porphyrin surrounds the equatorial binding sites of iron (**Figure 1.5**), allowing only one oxygen to bind at one axial site of Fe^{2+}. Due to the affinity of porphyrin rings with iron and its high denticity, a bidentate chelator with a small bite angle would not bind to this form of iron as it would not be able to distort the porphyrin ring to allow dissociation of one of the pyrrole groups required for chelation. A bidentate chelator that can bind both axial sites at the iron center would still need to displace the axial amino acid ligand associated with the globin protein.

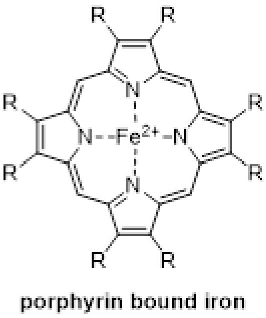

Fig. 1. 5: Equatorial binding of iron by the nitrogen containing porphyrin ring

Transferrin protein binds Fe^{3+} with four amino acid residues shown in **Figure 1.6** where it remains in a closed confirmation with carbonate, inaccessible to the outer solution until it is in an acidified environment such as an endosome.[107] Transferrin has two iron binding sites. Diferric transferrin only represents 25-30% (20 – 30 µM)[108–110] of the total plasma transferrin, as it is not completely saturated with iron at normal conditions.

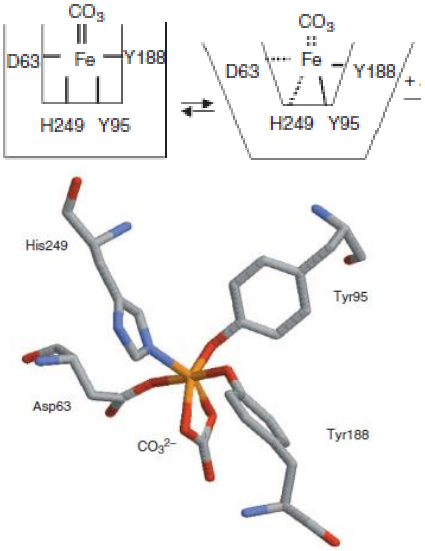

Fig. 1. 6: Transferrin iron binding site residues and schematic depicting the sampling of open and closed confirmations. Adapted from ref. 107 with permission from Elsevier

Ferritin (**Figure 1.7**) in the plasma is mostly composed of L-chain ferritin, responsible for Fe^{3+} storage. Ferritin bound iron is stored in the ferritin core as a crystalline mineral form

($[FeO(OH)]_8[FeO(H_2PO_4)]$), comparable to ferrihydrite.[111] The structure of this mineralized iron has yet to be determined, but is known to be accessible by small compounds despite the small width of the channels (1.5 nm) created by the tertiary structure of ferritin.[112] Even though iron chelators could potentially enter the ferritin core where up to 4500 iron atoms can be stored, a high amount of organic reducing agents (e.g. ascorbic acid) would be required to make the iron accessible for chelation.[113] Ferric iron is considered as a nanocrystal because it is so dense, which makes it detectable by magnetic resonance (MR) and is the primary source of iron MR images (MRIs) utilizing T2* and R2* scans. Finally, iron that is not protein-bound (also known as nontransferrin bound iron (NTBI), “free” iron, chelatable iron, or labile iron) in the plasma is thought to be mostly bound by albumin and low molecular weight ligands such as citrate in oligomeric complexes.[109,114,115] The concentration of this component in normal conditions is low enough that it is not detectable by current methods (bleomycin and other fluorescence-based assays).[114] Chelatable iron only reaches detectable concentrations in the plasma when iron homeostasis becomes disrupted during disease and transferrin is 100% saturated with iron.[114]

To allow uptake of extracellular iron, cells express both transporters and receptors on their membranes such as transferrin receptor (TfR) for uptake of diferric transferrin and divalent metal transporter 1 (DMT1) for uptake of NTBI.[116] Depending on the organ compartment, other iron transporting proteins (i.e. lactoferrin) would have their own receptors like lactoferrin receptor in secretory glands (milk, tears, saliva) and melanotransferrin receptor in microglial cells of the brain.[107] Although TfR and the other related receptors do not bind iron directly, their expression levels are directly related to the homeostasis of the intracellular iron concentration. High expression of TfR leads to higher concentrations of intracellular iron, where as a decrease in TfR expression leads to less iron being trafficked into the cell. After transferrin binds TfR, an endosome is formed where it is then acidified to release Fe^{3+} into the endosome to be reduced to Fe^{2+}. DMT1, present on the endosomal membrane, transports Fe^{2+} into the cytosol to be available for use. Just like the plasma, cytosolic iron can be found to be protein-bound or freely associated with cytosolic biological chelators (e.g. citrate and glutathione).[117] When Fe^{2+} thus enters the cytosol, it will become a part of the labile iron pool (LIP), composed of hydrated forms of Fe^{2+}/Fe^{3+} being complexed with water and various physiological buffer salts such as phosphate (PO_4^{3-}), acetate (CH_3COO^-), and carbonate (CO_3^{2-}).[118] Although the complete nature of LIP is still not understood, it has been suggested that single amino acids, nucleic acids, and other biological chelators mentioned previously are found here to help solubilize the iron.[104] The LIP provides a source of iron that can either be stored into ferritin, incorporated into non-heme iron enzymes, or shuttled to the mitochondria for use in generation of heme or iron-sulfur clusters (ISCs), a cofactor used in proteins involved in electron transfer.

Ferritin, as discussed above, functions as intracellular Fe^{3+} storage. Ferritin is composed of 24 subunits, referred to as Heavy (H) and Light (L) chain ferritin, that can have varying ratios of H:L chains depending on the tissue ferritin is being expressed in.[112,119] The H chain subunit has inherent ferroxidase activity located at the four amino acid residue site, Glu-27, Glu-62, His-65, and Gln-141, where iron oxidation of Fe^{2+} found in the LIP occurs. The resulting Fe^{3+} is funneled through the three-fold channel (**Figure 1.7**) where a negative electric potential gradient created by a series of carboxylate amino acids directs Fe^{3+} towards the ferritin core to be used at a nucleation site where the mineralization of iron will take place.[112]

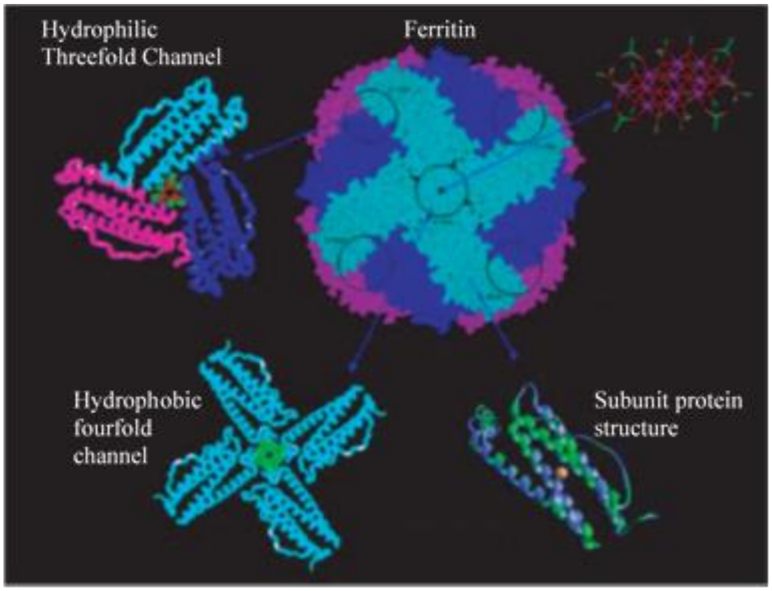

Fig. 1. 7: Structure of Ferritin and the breakdown of its individual components. Adapted from ref. 111 with permission from University of Washington

Cells express metal chaperones that help transport metals within the cell and load them into metalloproteins.[103] For iron to move out of the LIP and be utilized by the cell, Poly(rC)-binding proteins act as iron ion chaperones, delivering them to enzymes and the mitochondrial iron importer, mitoferrin.[120] The driving force for the movement of free iron out of the LIP to its protein-bound destinations is an affinity gradient, where stronger affinities for iron increases from chelators, to chaperones, to apoenzymes and apoproteins.[121] Thus, if an iron chelating PET tracer diffused into the cell, the LIP would be its primary target. For a chelator to strip iron from metallated protein, it would need picomolar affinity for iron or large concentrations and a lot of time for nanomolar affinity chelators, two factors that cannot be reached during a PET study.

Within the mitochondria contains cellular machinery responsible for the biosynthesis of heme and ISCs. This includes ferrochelatase,[122] a metal insertase that inserts iron into protoporhyrin IX to form heme, and frataxin,[123] an iron chaperone used in the production of ISCs. It should be noted that ISCs can be chaperoned themselves through the cytosol by two proteins, monothiol glutaredoxins (Grxs)[124] and BolA-like proteins.[125] ISCs can exist as either Fe_2S_2 rhomb (tetrahedral, **Figure 1.8** left) or F_4S_4 cubane (distorted octahedral, **Figure 1.8** right) and bound into the protein by terminal cystines.[126] Fe_4S_4 Heme and ISCs form the basis of most protein-bound iron which are inert to outside chelators.

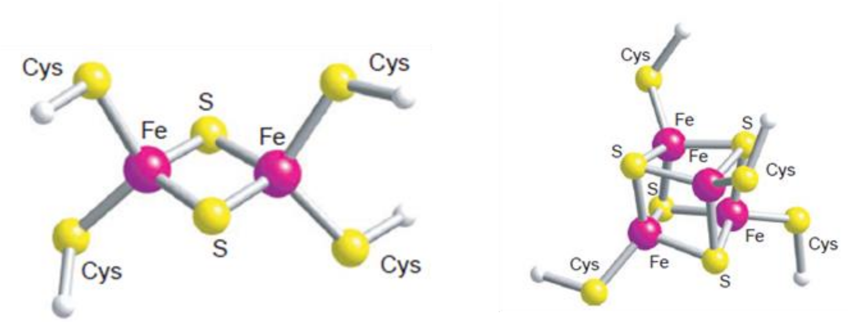

Fig. 1. 8: Tetrahedral ISC (left) and distorted octahedral ISC (right) conformations. Adapted from ref. 119 with permission from Elsevier

ISCs are contained within Iron Regulatory Proteins (IRP, previously known as Iron Response Element (IRE)-binding proteins) which function by maintaining mRNA translation of iron storage and uptake proteins (**Figure 1.9**) .[104] This function is mediated by the binding of apo-IRPs (without its ISC) to the IRE located in the noncoding region (UTRs) of these mRNAs. IREs can be found in the 5'-UTR, associated with initiation of translation, or the 3'-UTR, associated with mRNA stability and degradation. When iron is abundant in the cell, ISC production is increased at which point it can become incorporated into IRP-1 to form the holo-IRP-1 (with its ISC), resulting in a conformational change and subsequent dissociation from the mRNA. To visualize the role of IRE/IRP regulation of iron, the mRNA of H- and L-chain ferritin contain IREs in the 5'-UTR region, and when intracellular iron concentration is high, ferritin expression will increase to store the incoming iron. Likewise, the mRNA of TfR contains an IRE in its 3'-UTR, and thus, when iron concentration is high, the mRNA of TfR will be degraded, causing less iron to be incorporated into the cell. IRP-1 is ubiquitously expressed, while IRP-2 is found mainly in the brain and intestine.

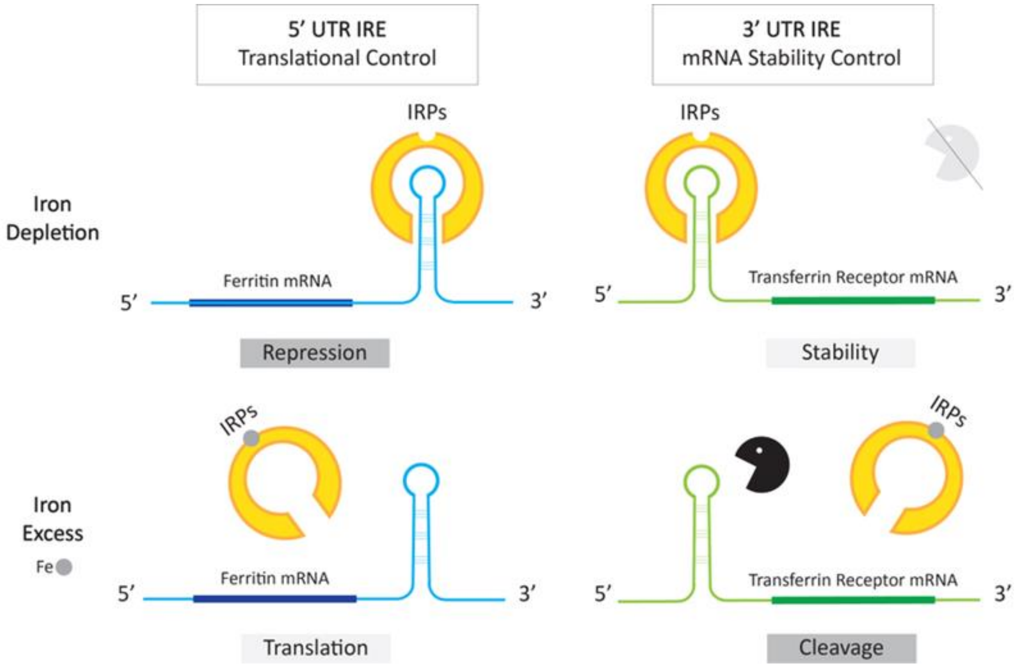

Fig. 1. 9: IRE motif on mRNA at 3‘ end prevents mRNA degradation by binding to IRP (top right) and IRE motif on mRNA at 5’ end prevents translation by binding to IRP (top left). Excess iron leads to dissociation of IRP from IRE motif (bottom). Adapted from ref. [127] with permission from Creative Commons Attribution

Nonheme enzymes (and those not utilizing ISCs) found in humans use amino acid residues to coordinate iron formed in the LIP. Proteomic analysis of these enzymes reveals that there are recurring structural motifs that have been defined by the course of evolution. For iron, these include tetrahedral $Fe(Cys)_4$ and $Fe(His)_3$ units, as well as the facial motif that is 2-His-1-carboxylate triad used in oxygenases.[126] The latter motif is accessible to specific substrates that become oxidized by iron and dioxygen. The active site of enzymes is very strict on accepting a variety of substrates, so iron chelator access to these sites would be tightly controlled. If there are any nonheme enzymes that are promiscuous and allow metal chelators to bind iron within their active sites, it would be negligible and unrepresentative of an iron chelating PET tracer image being that all of these enzymes together represent 0.002% of the total iron in the body.[108,110]

1.4.1.1.2. *Locations and Concentrations of Iron*

The average amount of iron found within the adult human male/female is approximately 3-5 g.[108,110,128] It is widely distributed throughout the body because of the many roles iron participates in. The concentration of iron in tissue compartments will differ based on the tissue's roles and varying cell types within these compartments. To note, measuring iron remains a difficult task with no method being the standard for its quantification. Total iron can be measured by various *ex vivo* and *in vitro* methods, but will not distinguish the natural distribution of iron in its various oxidation states and its coordination environment whether it be protein-bound or labile in differing cellular compartments (mitochondria, cytoplasm, nucleus, etc.). The intracellular LIP and NTBI of the plasma is the most difficult to quantitate because it requires methodology that does not perturb the cellular environment (sample destruction) which is normally used to prepare tissue samples for the *ex vivo* methods. Traditionally, histochemical methods were used to determine relative differences in iron, beginning with Perls' Prussian Blue stain for Fe^{3+} in 1867,[129] followed by modifications for improved staining or detection of Fe^{2+} (Turnbull's method).[130] Development in spectroscopic and spectrometric technologies have since been able to allow the simultaneous determination of both Fe^{2+} and Fe^{3+} present in samples and their direct quantification with detection limits below 1 ppt (ICP-MS and FAAS).[103] When spatial resolution is taken into account in order to determine where in the cell these ions are found, the detection limit is less efficient in the ppb range when used in tandem with techniques such as laser ablation (LA).[103] To assess the LIP *in vivo*, fluorescent probes (small molecules and proteins) have been used for iron quantification which give beautiful molecular images of living cells with information of the cellular distribution of chelatable iron.[131,132] Finally, MR has been used to measure iron in multiple organs of living organisms by taking advantage of its inherent paramagnetic property, but its quantification does not correlate to the chelatable iron.[133] However, MR metal sensors can be used to interrogate the chelatable iron, but it is limited by their poor sensitivity and the high concentrations of probe required. Thus, the use of iron chelating PET probes, which have markedly higher sensitivity, could then be yet another tool to provide information on metal homeostasis of a living organism at the molecular level, which is currently not an area of active research (until now). For a more detailed discussion of the various methods used for studying metals and their concentrations in biological systems, please refer to the reviews that have already covered this topic.[103,128,134]

Beginning in the blood we find the oxygen carrying RBCs that make up ~69% of the iron content contained in hemoglobin and myoglobin.[108,110] About 0.1% (~3 mg) of the total iron content is transported in the blood (and interstitial fluid) by transferrin (pFe = 23.6),[105,107] reaching concentrations from 30-50 µM.[135] The other protein-Fe^{3+} serum transporter, ferritin, contains 30% of the total iron content when considering intracellular storage as well,[108,112] but only reaches 23-700 nM in the blood.[136] As stated earlier, NTBI (citrate monomers and oligomeric iron complexes and albumin iron) is undetectable during normal conditions, but from the detection limits of the methods used for its quantification (fluorescence quenching,[137–139] and nitrilotriacetic acid (NTA) capture with measurement by isotope dilution mass spectrometry (IDMS)[140]), we can infer that <0.1 µM is present at any given time. Here we have the concentration of iron within the blood in all its various forms, which is then transported through endothelial cells to the different organs of the body where it can be utilized further for detoxification in the liver, oxidative metabolism in the brain and heart, as well as regeneration of RBCs in the spleen and bone marrow.

When an iron chelating PET tracer is injected it first flows to the heart to be pumped to the rest of the body. According to the first pass effect, it will be metabolized and interact with iron deposits in the liver. The liver, being the site of xenobiotic metabolism, will contain high amounts of heme iron stored in Cytochrome P450's of hepatocytes, where oxidation and secondary metabolism of drugs takes place. During the first two hours of a PET scan, it is assumed that a steady-state equilibrium is reached, and therefore any metabolism of the tracer is negligible, given the metabolic half-life of the tracer is suitable for this assumption.[141,142] Also, interactions of iron chelators with heme bound iron will not take place as discussed previously. The total nonheme iron content of the liver has been reported to be 5-20 µmol/g dry weight by chemical assays of biopsy samples[143] and 8-16 µmol/g dry weight reported by T2* weighted MRI scans.[144] Bone marrow performs erythropoiesis (production of RBCs) in the adult human body which requires a lot of heme iron obtained from the blood recycling function of the spleen to produce hemoglobin and myoglobin. Diffusion of metal chelating PET probes into the bone marrow is unlikely to occur and the iron content in this region is usually only graded by histochemical staining (Perls' Blue). White blood cell (WBC) formation and RBC storage mostly takes place in the spleen where iron content (mostly nonchelatable heme iron for these cell types) seems to be the greatest at <200 µmol/g dry weight as measured by MRI.[145] The next organ with the most iron content following the spleen and liver, is the heart where oxidative metabolism is occurring through the use of ISCs and heme containing cytochrome c complexes in the electron transport chain that drives energy production for the pumping of the cardiac walls. The iron content of the beating heart reaches 4-8 µmol/g dry weight as measured by T2* weighted MRI scans.[146] Finally, the brain, although containing less overall iron than the organs just discussed, contains specific regions where the concentration of nonheme iron is far more dense than the liver and heart.[147] The brain regions with the greatest iron content include the globus pallidus (GP), substantia nigra (SN), interpeduncular nucleus (IPN), thalamus (TH), dentate gyrus (DG), and red nucleus (RN), reaching levels from 150-210 µg/g protein (**Figure 1.10**).[148] These brain regions are associated with body movement and are the most affected in neurological movement disorders such as Parkinson's Disease. Brain regions associated with memory and affected greatly in dementia related diseases (e.g.

Alzheimer's Disease) include the cerebral cortex (CC), hippocampus (HIPP), and frontal cortex (FC) which contain iron in concentrations a little less than 50 μg/g protein (**Figure 1.10**).[148] With the total iron content of each organ laid out, a picture of where iron chelating PET tracers will accumulate has been developed.

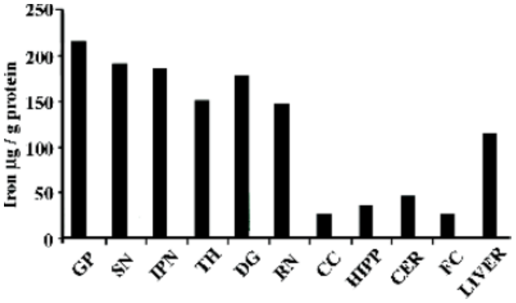

Fig. 1. 10: Iron concentration in μg/g protein in various brain regions compared to liver. Globus Pallidus (GP); Substantia Nigra (SN); Interpeduncular Nucleus (IPN); Thalamus (TH); Dentate Gyrus (DG); Red Nucleus (RN); Cerebral Cortex (CC), Hippocampus (HIPP), Cerebellum (CER), Frontal Cortex (FC). Adapted with permission from ref. 147 with permission from Elsevier

Moving from the blood, to the interstitial fluid of tissue compartments, and finally uptake into cells, iron will reach the crossroads of its metabolic cycle in the cytoplasm where it can be distributed to ferritin for storage, incorporated into nonheme enzymes by iron chaperones located in the cytoplasm, or loaded into the mitochondria for production of heme and ISCs proteins. Of the 3-5 g of iron in the body, 400 mg of it is used intracellularly. The iron concentration per cell and its distribution will vary depending on its demands given the different cell types found in each organ. Of the intracellular iron, more than 95% is protein-bound.[117] The use of radioactive iron (^{55}Fe) delivered to cardiomyocytes coupled with native gel electrophoresis allowed the determination of the nature of iron distribution within these cells. The distribution of iron changes depending on the source of radioactive iron (^{55}Fe-transferrin or ^{55}Fe-citrate). The ratio between iron found in the LIP and iron incorporated into various metalloproteins would change (indicated in the pie charts), highlighting that NTBI uptake is a preferred pathway for the source of iron in the LIP. Ferritin-stored iron represents 63-65% of iron found in each cell with the remaining iron being labile in the cytoplasm or active in metalloproteins.[149] The concentration of the LIP found in hepatocytes was determined to be 5.4 µM by using the fluorescent probe CP94.[150] In resting erythroid and myeloid cells (precursor cells to RBCs found in the bone marrow), the LIP concentration was estimated in the range of 0.2-1.5 µM by using the fluorescent probe calcein.[151] In neurons, intracellular iron concentrations have been reported to range from 0.5 to 1.0 mM,[152] which is mostly stored in ferritin (33%-90%, **Figure 1.11**).[108,110] The concentration of the LIP in neuronal cells using fluorescent probes has not been reported, but the fluorescent probe, RPE, has been used to visualize the LIP in neuronal SH-S5Y5 cells with a LOD down to 0.1 µM.[153]

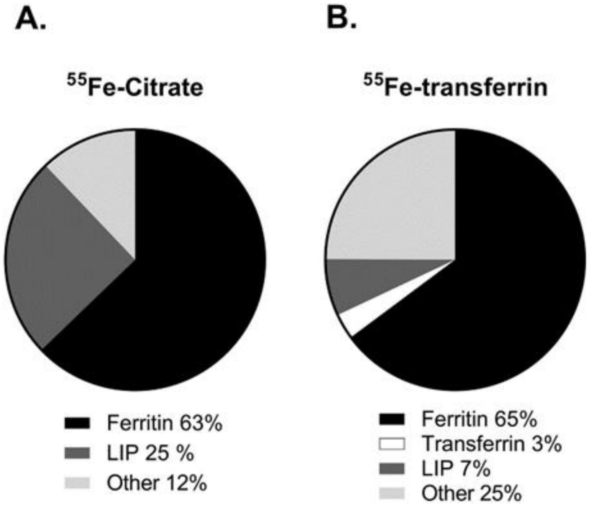

Fig. 1. 11: Intracellular iron distribution when using either radioactive (^{55}Fe) label iron as a source (left) or protein-bound iron as a source (right). Adapted with permission from ref. 149 with permission from Elsevier

Next, a discussion on the perturbations of the mechanistic control over the intracellular concentration of chelatable iron will help to better understand how diseases will affect the tracer uptake within these compartments

1.4.1.2. *Iron Dyshomeostasis*

The many proteins involved in iron transport, storage, and usage not only help to circumvent the limitations of iron solubility, but provide a means for its tight regulation due to its potent redox activity that results in the formation of reactive oxygen species (ROS). Aqueous iron

(Fe^{2+}/Fe^{3+}) of the LIP can participate in Fenton type oxidation[154] of hydrogen peroxide (H_2O_2) produced in the cell:

$$Fe^{2+} + H_2O_2 \longrightarrow Fe^{3+} + \cdot OH + OH^-$$

$$Fe^{3+} + H_2O_2 \longrightarrow Fe^{2+} + \cdot OOH + H^+$$

The free radicals (·OH, ·OOH) formed from these reactions can go on to react with biomolecules such as nucleic acids found in DNA/RNA and amino acids found in proteins. Radicals formed on these biomolecules can lead to point mutations in DNA during replication[155] and misfolding of proteins leading to aggregate formation.[156] The LIP also leads to oxidation of other biomolecules such as neurotransmitters (i.e. oxidation of dopamine to 6-hydroxydopamine (6-OHDA) and the dopamine quinone (6-OHDA-Q)).[157] The concentration of the LIP is maintained during homeostasis where production of ROS is limited and the radicals can be mitigated by cellular antioxidants (ascorbic acid, vitamin E, etc.). However, if any proteins responsible for iron regulation became dysfunctional, iron dyshomeostasis can occur where a small increase in the concentration of the LIP can lead to overproduction of ROS that cannot be suppressed by biological antioxidants, leading to oxidative stress within the cell. This is the basis of iron related diseases and its mechanism has been used to theorize its potential role in neurodegenerative diseases. We will look at the evidence that has accumulated to establish the iron hypothesis or neurodegeneration, specifically at AD, PD, and amyotrophic lateral sclerosis (ALS), where it is thought that earlier diagnosis (with the help of PET scanning) of these incurable diseases can lead to favorable outcomes in future clinical trials.

1.4.1.2.1. *Iron's Role in Alzheimer's Disease*

Alzheimer's Disease (AD), being the most common dementia-related disease, is characterized by a progressive loss of neurons and buildup of protein plaques containing amyloid-ß (Aß) in the cerebral cortex.[39] The cerebral cortex is responsible for memory and learning. The brain regions associated with the heaviest burden of neurodegeneration and Aß plaques is found in the entorhinal cortex and hippocampus of the temporal lobe as well as the prefrontal cortex of the frontal lobe. As stated earlier, the normal brain will maintain iron concentrations less than 50 µg/g dry weight tissue in these regions.[148] The first reports of elevated iron in these regions of Alzheimer's disease post-mortem tissue came to us in 1992 by Connor *et al.*[158] using histochemical staining and spectrophotometric analysis for the determination of nonheme iron. For spectrophotometric analysis, the method first described by Foy *et al.*[153] was used which required boiling tissue homogenate in trichloroacetic acid and treating with reducing agents (sodium ascorbate). This results in any ferric iron extracted being converted to Fe^{2+} and released from the ferritin protein. The histochemical stain for iron employed was Perl's method, which stains only for reactive Fe^{3+}. Thus, the iron measured was representative of the total iron in these samples rather than specifically measuring the toxic redox active LIP. Another aspect of these studies that should be noted is that the brain samples used were fixed in formalin, which has since been shown to allow leakage of trace metals,[159] and therefore an underestimation of the total iron would have been measured. It was concluded by immunohistochemistry of ferritin and transferrin as well as histochemical staining of Fe^{3+}, that iron levels are increased substantially around Aß plaques.[158] However, the total level of iron when compared to age-matched, normal tissue is relatively unchanged. Later, Mössbauer Spectroscopy, which has the ability to differentiate the valence states of iron (Fe^{2+} and Fe^{3+}) in a tissue sample, was used in 2011 to assess iron hippocampal levels of freshly prepared AD and normal post-mortem tissue not stored in formalin.[160] This technique places the normal hippocampal iron concentration at 45 µg/g wet tissue, similar to the levels described by other methods.[147,148] A significant increase in iron of the AD tissue was measured to be 66 µg/g wet tissue (a 1.5 fold increase). This study also demonstrated that H- and L-chain ferritin was substantially increased, being 3-fold higher in AD than compared to control tissue. Finally, MRI can measure large concentrations of paramagnetic iron (ferritin being the source) which has been pivotal in correlating iron increases in AD.[133] It was shown in 2013 that the hippocampus has increased iron deposition of AD patients.[161] However, meta-analysis of iron MRI data have shown that increases of iron deposition in AD brains is not significantly different from age-matched control patients, indicating brain iron increase is a phenomenon of the aging process.[162] Thus, the need to measure the more toxic ROS producing iron found in the LIP of AD patients is outlined by current methods either not being applicable to a living organism or not being sensitive enough to measure the less concentrated LIP.

The mechanism for the accumulation of iron in AD specific brain regions is not well understood. Attempts to explain the dysregulation of iron control in these cell types has pointed to the involvement of the iron transporter, TfR, the amyloid precursor protein (APP), and its post-translationally cleaved product, Aß. As mentioned earlier, a large concentration of TfR was found by IHC to be localized around Aß plaques.[158] An increase in iron uptake mediated by TfR could help explain why iron is elevated in AD, but it is not currently understood why overexpression would occur in specific brain regions. Later studies in 2004 indicated that trace metals in buffers and culture media were the culprit for *in vitro* Aß aggregation,[163] perhaps explaining that around 1mM of iron could be found in amyloid plaques. APP, a transmembrane protein, has been shown to be able to bind metals[164] and its mRNA contains an IRE in the 5'-UTR.[165] The upregulated translation of APP and accumulation of its cleaved product Aß is perhaps the product of iron accumulation, where these proteins are acting to help in iron storage when ferritin becomes saturated. Unfortunately, iron binding with APP still maintains redox active properties,[166] leading to toxic accumulation of both protein aggregates and ROS. Perhaps, iron accumulation prior to APP's upregulated translation is not necessary as it has been shown that the dysregulation in the binding of IRPs to IRE was found to occur in AD brains.[167] This would result in aberrant APP and TfR translation, leading to accumulation of iron and metal-protein aggregates. The formation of toxic metal-protein aggregates, if indeed causative of neurotoxicity, has been imaged by our group, using the Cu^{2+}-Aß binding radiotracer [^{18}F]FL2-b, discussed in Chapter 3, where we see a significant increase in binding on Alzheimer's diseased tissue over control.[168]

1.4.1.2.2. *Iron's Role in Parkinson's Disease*

Parkinson's Disease (PD), the second most common neurodegenerative disease, is characterized by a loss of dopaminergic neurons within the substantia nigra pars compacta (SNc) and striatum as well as buildup of protein plaques known as Lewy Bodies composed of α-synuclein (α-syn) starting from the brain stem and olfactory bulb, then spreading to the SNc, amygdala, hypothalamus, prefrontal cortex, and hippocampus.[169] Dopaminergic neurons release the neurotransmitter dopamine and is responsible for motor control, which is why shaking, rigidity, and slowness of movement are the clinical manifestations of the disease. Severe progression of the disease can be accompanied by dementia as α-syn accumulates in the brain regions associated with memory and learning in the later stages of the disease.[170]

Post-mortem iron analysis of PD samples was first performed in 1968 using X-ray fluorescent spectroscopy of formalin fixed tissue.[171] This method (and the limitations associated with formalin fixed tissue previously discussed in section 1.4.1.2.1) measured relative qualitative differences in total iron content of PD and control tissue. It was determined that an increase in iron was measurable in PD tissue relative to normal brain tissue. The LOD for this method is 10 µg/g dried tissue. Subsequent findings in the late 1980's by Youdim used spectrophotometric methods (using ferrozine® to measure Fe^{2+}) to confirm increases in total iron content in the SN PD post-mortem tissue homogenate (~85 µg/g wet tissue) compared to control (~48 µg/g wet tissue).[172,173] Although an Fe^{2+} chelator was used, tissues were homogenized with hydrochloric acid (HCl) and pepsin, which would destroy the ferritin shell and leach Fe^{3+} that would eventually become reduced to Fe^{2+}. Thus, the Fe^{2+} concentration mentioned in these studies is not indicative of the concentration of the LIP, which is greatly overestimated in these studies. Later in 1995, total iron content was measured by a colorimetric assay in which total iron was found to be elevated in the GP (~7 mg/g protein) and FC (~3 mg/g protein) of PD post-mortem samples over elderly controls.[174] Due to the limitations of these methods, precise characterization of iron content was needed and development of spectroscopic methods suitable to biological samples were used in later experiments. Mössbauer spectroscopy is such a method and was used in 1996 by Galazka-Friedman *et al*.[175] where the SN iron content was measured in control and PD tissue samples. No change in total iron content was observed in both sample types (~160 µg/g wet tissue). These values, although inconsistent with previous findings, were determined by a more reliable method and thus the values of total iron are more similar to those reported by other methods. As seen in experiments performed by X-ray absorption fine structure (EXAFS) in 1999, structures of the basal ganglia in PD samples were used revealing a significant increase in total iron compared to control in both the lateral GP (295 µg/g vs. 207 µg/g wet tissue) and SN (281 µg/g vs. 140 µg/g wet tissue), with a mild increase of iron in the FC (51 µg/g vs. 42 µg/g wet weight).[176] Later, Galazka-Friedman *et al.*[177] in 2010, showed that an increase in the LIP of PD samples could be measured by AA, reaching a concentration of 90 ng/g in the SN. Meta-analysis of both postmortem and *in vivo* MRI measurement was published in 2016 confirming that brain iron levels were increased in both the SN and RN of PD patients.[178]

The evidence for the mechanism of iron accumulation in PD is not conclusive, just as in AD. It was first suggested that PD could be a glutathione metabolism disorder. Experiments in 1986 by Perry and Yong demonstrated that the total glutathione content in the SN of PD was significantly decreased.[179] As discussed earlier, glutathione is a biological chelator of iron in the LIP. If less glutathione is present, iron could be coordinated to a lesser extent resulting in redox active iron accumulating in the LIP and subsequently uncontrolled ROS production. Dopamine, being the neurotransmitter produced in the neurons of the SN, contains a catechol moiety that can chelate Fe^{3+}. Dopamine and Fe^{3+} form a redox active species that can result in the oxidation of dopamine to form neuromelanin polymers.[157] The resulting neuromelanin can serve as an alternative source for Fe^{3+} storage.[180] Given that there is decreased concentration of L-chain ferritin and increased H-chain ferritin in the SN of PD patients,[181] the decreased ability to store iron in this brain region coupled with the increased ability to convert Fe^{2+} to Fe^{3+} through the inherent ferroxidase activity of H-ferritin and decreased chelators in the LIP, the formation of neuromelanin may serve to protect the neuron from oxidative stress.[182] An influx of iron cannot be explained by overexpression of TfR as it was shown by autoradiography that the receptor density and distribution of TfR remains unchanged in PD.[183] IHC of lactotransferrin receptors revealed heavy staining for the receptor in regions associated with α-synuclein build up,[176] but since the expression of lactotransferrin receptor is limited to macrophages, this most likely reveals that macrophages are accumulating around dying neurons and taking up excess iron expelled from them. Finally, in 2008 it was shown that DMT1 accumulates in the SN of PD and was needed for the progression of the disease in PD animal models.[184] The increased DMT1 expression on the cellular surface of dopaminergic neurons would implement the increased uptake of NTBI as the mechanistic pathway for the increase in concentration of the LIP. Thus, dysfunction in either iron storage or increased

NTBI transport into the cell are viable mechanisms of increased oxidative stress in dopaminergic neurons. Oxidative stress would then result in α-syn misfolding and aggregation. In fact, it has been shown that iron is highly concentrated in Lewy bodies (α-syn aggregates) and that α-syn is able to bind free iron.[185] The resulting Fe-α-syn complex is also redox active, which would lead to further oxidative damage to the cell and inducing neuronal death.

1.4.1.2.3. *Iron's Role in Amyotrophic Lateral Sclerosis*

Amyotrophic Lateral Sclerosis (ALS) is a neuromuscular degenerative disease that effects the lower motor neurons in the spinal cord and upper motor neurons in the motor cortex of the brain.[186] It is characterized by the presence of intraneuronal inclusions termed Bunina bodies found in the surviving lower motor neurons, composed of cystatin C and transferrin.[187,188] Skein-like protein aggregates are also found in the neurons of the motor cortex and spinal cord, which has recently been identified as being composed of phosphorylated-Tar DNA binding protein-43 (pTDP-43).[189] The mechanism of ALS disease progression is not well understood as only 2% of cases are genetically linked, with the remaining being sporadic.[190]

Elevated iron concentrations in post-mortem ALS tissue was first reported in 1993 by using neutron activation analysis on the grey matter of the frontal and occipital regions of the brain.[191] Increases in iron were also confirmed in fresh ALS lumbar spinal cord tissue by using the same technique a year later.[192] By 1995, laser microprobe mass spectroscopy confirmed increases of iron in the spinal cord by 1.5-2 times greater in the nucleus and cytoplasm of ALS neurons over control.[193] ICP-MS was used in 2003 on formalin-fixed brain tissue to observe a significant increase of iron in ALS frontal lobe (303 µg/g dry weight), temporal lobe (357 µg/g dry weight), and cerebellum (342 µg/g dry weight).[194] The most significant brain region to be affected in ALS is the motor cortex of the frontal lobe which normally has iron concentrations at 251 μg/g dry weight tissue.

These post-mortem studies showing elevated iron levels is accompanied by clinical findings of increases in iron as well. T2 relaxation MRI studies were used first in 1995[195] and later in 2012[196] and 2013[197] to assess ALS patients that show low intensity areas in regions with brain atrophy. The later MRI studies showed the iron increase could be associated with microglia accumulation in the motor cortex and that the hypointensities in this region is solely a biomarker for ALS. Increased serum ferritin levels were found in ALS patients in 2008.[198] A study was then performed showing that this increase in serum ferritin has a deleterious impact on the survival of ALS patients, as higher iron storage correlated to the severity of the disease.[199]

The mechanism of iron buildup in ALS is still unclear and remains an uninvestigated area. Animal models with ALS-type mutations have showed increases in expression of TfR, indicating an increase in iron uptake of neurons.[200] DMT1 has also been found to have increased expression in these animal models.[201] Superoxide dismutase (SOD) is an enzyme that has been shown to release iron from ferritin, which may result in increased ROS production.[202] Indeed, SOD1 mutations are the most common in genetic related ALS. Whether oxidative stress or iron accumulation occurs first in the disease progression, increases in iron levels is still an early biomarker of ALS and can predict neurodegeneration.

1.4.2. *Copper as a Target for PET*

1.4.2.1. *Copper Homeostasis*

1.4.2.1.1. *Proteins Involved in Processing Copper*

In biological systems, copper is found mostly in two oxidation states, being cupric (Cu^{2+}, $3d^9$) and cuprous (Cu^+, $3d^{10}$) ions. Just like iron, it can exist in either a protein-bound pool or free labile pool in both the intracellular and extracellular environment. Cu^{2+}, being the most abundant form in physiological conditions, is mostly protein-bound, while the reduced form, Cu^{+}, is found free in solution and existing briefly in the electron transfer cycles in cuproenzymes. In the blood, protein-bound copper is transported by ceruloplasmin, as well as albumin and transcuprein.[203] To a lesser extent, but still a real fraction exists other proteins that make up the extracellular protein-bound copper, including: lysyl oxidase, amine oxidase, SOD, metallothionein, blood clotting factors V and VIII, and ferroxidase II.[204]

Unlike iron, prosthetic groups for binding copper do not exist, and instead proteins bind copper directly through their amino acid side chains and backbone amide groups. The copper centers of proteins can be classified into five types: type I-III, Cu_A, and Cu_Z (**Figure 1.12**).[205] These copper centers are typically embedded in pockets between the loops of ß-barrel folds and are completely shielded from the solvent to prevent unnecessary redox reactions with solvent and organic molecules. From **Figure 1.12**, it is seen that the main amino acid residues for copper binding are histidine, forming a trigonal plane at the equatorial sites. For type 1 centers, however, the copper binding ligands differ in that it has the $Cys(His)_2$ motif. These equatorial amino acids are accompanied by an axial ligand, being methionine or oxygen (either from water, hydroxide anion, oxygen, or an amino acid) to form a tetracoordinated copper center that can accommodate a variety of geometries: tetrahedral, trigonal, trigonal pyramidal, trigonal bipyramidal, square pyramidal, and octahedral. Type III and Cu_A centers are dinuclear (contain two copper atoms) clusters bridged by one oxygen (in type III) or two sulfurs (in type Cu_A). The significant difference between these two dinuclear copper centers is the ability to have a fixed valence state (Cu(I)/Cu(II) in Type III) where the shared valence electron is localized to one copper atom or a mixed valence state (Cu(1.5)—Cu(1.5) where the shared electron is delocalized between both coppers. The Cu_Z

center contains a four-copper cluster and has only been found in Nitrous-oxide reductase of prokaryotes. Several cuproproteins may have multiple copper centers with multiple types being present in the same protein. Interestingly, Cu^{2+} ion is coordinated tightly by these sites, but when it is reduced during electron transfer reactions, the geometry remains unchanged. No displacement of ligands is needed during redox cycles and is instead accompanied by an elongation of the ligand bonds during the formation of Cu^{+}. The mechanism of electron transfer in cupredoxins (copper proteins that perform electron transfer) is thought to occur mainly through an outer-sphere mechanism where the transfer of an electron from the oxidation center to the reduction center occurs without the formation of a covalent bond.[206] Inner-sphere electron transfer mechanisms, although rare, is mediated by an intermediate ligand between the oxidation and reduction centers.

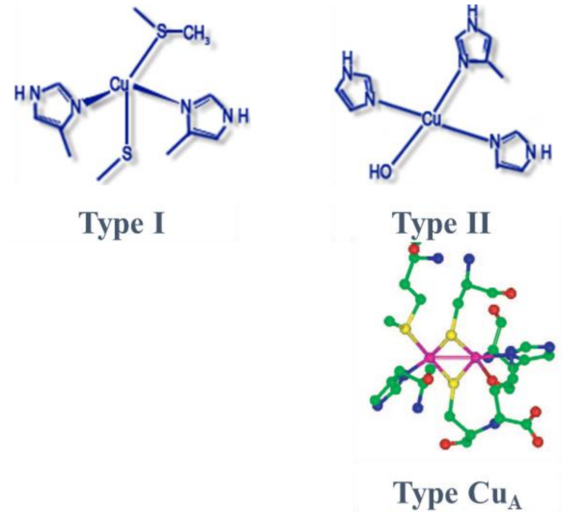

Type I

Type II

Type III

Type Cu_A

Fig. 1. 12: Common motifs used in proteins for copper binding centers. Adapted from ref. 205 with permission from Elsevier.

Although it is the largest source of plasma copper (95%), ceruloplasmin’s main function is ferroxidase activity (the oxidation of Fe^{2+} to Fe^{3+}), and not just transporting copper.[207] Due to copper only becoming incorporated into ceruloplasmin intracellularly, albumin and transcuprein are thought to be the main transporters for exchangeable copper in the plasma, preventing an accumulation of free copper in the plasma that is redox active. Ceruloplasmin can bind six copper ions deep within its tertiary structure in several types of centers: one type 1, two type 3, and one type 2.[208] These centers, being responsible for iron oxidation, can react with other biological reducing agents such as ascorbic acid. Due to its ferroxidase activity, ceruloplasmin can be seen as an inhibitor of DNA damage by reducing the production of ROS (mediated by Fe^{2+}). The most abundant protein in the plasma, albumin, can transport various metal ions. A Cu^{2+} binding site has been identified in the N-terminus where four nitrogens from the N-terminal amino nitrogen, two backbone nitrogens and one histidine nitrogen, coordinate copper in a distorted square planar arrangement with an affinity of 10^{-17} M.[209] Multiple copper atoms can bind albumin beyond this site more loosely, and it is thought that free histidine present in the plasma can coordinate to these coppers to form an albumin-Cu-His complex with a dissociation constant of 10^{-22} M.[210] The other most common large protein associated with copper (10-15%) is transcuprein,[204] a macroglobulin (also known as alpha-2-macroglobumin, α_2M). Transcuprein has even higher affinity for Cu^{2+} than albumin (transcuprein is less concentrated than albumin in the plasma and could still outcompete binding for Cu^{2+} in plasma samples),[211] and is thus thought to be the main transporter of exchangeable copper absorbed into the plasma. The copper coordination site in transcuprein has yet to be determined. Other large, copper-containing proteins include ferroxidase II, amino oxidase, and extracellular SOD. Ferroxidase II accounts for 5% plasma ferroxidase activity (the rest being performed by ceruloplasmin) and has been shown that the copper associated with this protein cannot be removed by chelation with diethyldithiocarbamate.[212] Only a large concentration of a high affinity copper chelator (0.1 M EDTA) at pH 4-5 was able to partly remove the copper bound to Ferroxidase II. This is essentially the case for all the protein-bound copper in the plasma talked about thus far. However, Ferroxidase II only accounts for 0.07% of plasma copper and all other protein-bound copper (extracellular SOD, lysyl oxidase, amine oxidase, blood clotting factors V and VIII, and histidine-rich glycoprotein) represents an even smaller fraction. The last fraction of plasma copper is free or associated with low-molecular weight ligands that is accessible by chelation by displacement of one of the ligands. These low-molecular weight ligands include amino acids such as histidine and cysteine as well as histamine and glyclhistidyllysine (GHL) which can form mono or homo/hetero-bisligand copper complexes (e.g. Histamine$_2$-Cu^{2+} and cystinate-histidinate Cu(II) complex).[203] The GHL and histamine Cu(II) complexes bind tightly to copper with formation constants of 10^{38} and 10^{21} respectively. The stability constants of amino acids with Cu^{2+}, however, are relatively weaker with histamine having the most stable formation of 17.5 for bisligand Cu(II) complexes (CuL_2).[213] These amino acid copper complexes would be competitive with exogenous chelators for Cu^{2+}, and thus represent a fraction of free copper that could potentially be imaged by Cu^{2+} chelating PET radiotracers.

For copper to be transported from the blood to various tissue compartments and into cells requires Copper Transporter 1 (CTR1, **Figure 1.13**).[214] Movement of copper into cells is an energy-independent process as the abundance of cations (K$^+$, Na$^+$, Ca^{2+}) in the extracellular environment provides an electric gradient that allows diffusion of Cu^{2+}/Cu$^+$ across the plasma membrane mediated by CTR1. Ceruloplasmin is thought to be the main source of copper to peripheral tissue (i.e. heart and brain) and first requires the reduction of Cu^{2+} to Cu$^+$.[215] However, other copper plasma components can deliver copper to cells as well, such as the case for hepatocytes where dietary copper is first taken up and transported by albumin, transcuprein, GHL, and amino acids to the liver where it can then be incorporated into ceruloplasmin in the Trans Golgi Network (**Figure 1.13**) .[204] Once in the cell, copper can exist in a free labile pool (such as the case for iron) where it exists with small molecule chelators (e.g. glutathione).[216] This source of intracellular copper would be in equilibrium with any exogenously provided chelators, and thus would be responsible for any signal detected by copper chelating PET tracers.

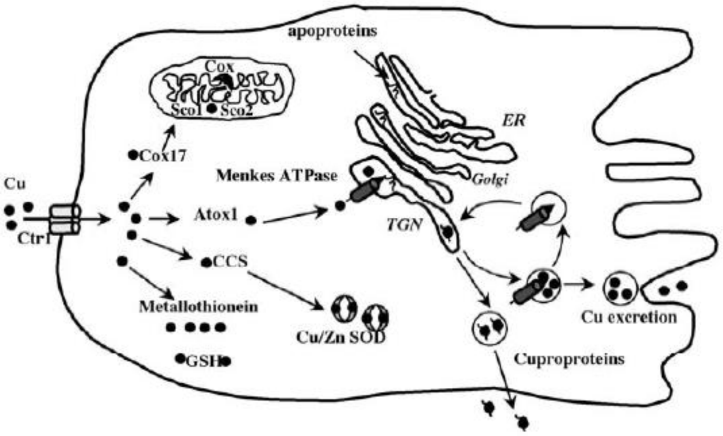

Fig. 1. 13: Intracelular copper homeostasis. Copper is transported into the cell as Cu^+ by CTR1 where it becomes oxidized in the cytoplasm in the labile copper pool (LCP). It can be shuttled to various cellular organelles by copper chaperones (COX17, ATOX1, and CCS) to be incorporated into various metalloproteins. Copper is excreted by the cell in vesicles formed from the Trans Golgi Network (TGN). Adapted from ref. 216 with permission from Springer Nature

Like iron, the affinities of various protein drive the movement of intracellular copper from the labile copper pool (LCP) to chaperones, to cuproenzymes and organelle copper transporters, and finally copper containing proteins.[121] Three copper chaperones have been identified and deliver copper to different targets. From the LCP, copper can become incorporated into copper chaperone for superoxide dismutase (CCS),[217] which, as its namesake suggests, shuttles copper to SOD1 found in the plasma. The copper chaperone, Atox1,[218] shuttles copper to Menkes ATPase (ATP7A), the copper transported involved in delivering copper to the Trans Golgi Network. Finally, Cytochrome c oxidase 17 (Cox17)[219] delivers copper into the mitochondria to be incorporated into cytochrome c oxidase (**Figure 1.13**). The copper binding motif associated with all these chaperones and transporters is the MXCXXC found in the amine terminus that binds Cu^+.[216] The TGN allows incorporation of Cu^{2+} into newly synthesized and folded proteins from the endoplasmic reticulum, where they can be shuttled to various parts of the cell in vesicles. ATP7B is found on the membrane of these vesicles that can then efflux any excess copper out of the cell.

The CNS provides an even more complicated story for copper homeostasis as free copper has been shown to participate in neuronal signaling[220–222] and brain specific proteins can mediate copper intake/efflux.[223] Unlike all other tissue compartments, the brain is protected by the strict regulation of the BBB. Ctr1 is not expressed on BBB endothelium, and it has been suggested that ATP7A is responsible for transport of Cu^+ into the CSF.[224] In the CSF, copper is transported by all the plasma components known to transport copper with the exception of ceruloplasmin which accounts for <1% CSF copper. In addition to the other CSF copper transporting proteins, Prion protein and APP are also known to have copper binding motifs and can participate in copper intake/efflux.[223] Pools of free copper contained in synaptic vesicles within axon terminals have been shown to be released at micromolar levels into the synaptic cleft after neuronal depolarization, which can then have proconvulsant activity on GABAergic neurons.[221,222] The presences of prion protein and APP at the cellular membrane suggests that copper reuptake can be mediated by these proteins and preventing toxic-redox activity of Cu^{2+} in the neuronal extracellular space. Thus, dysregulation of these copper-binding proteins can have serious implications in neurodegenerative diseases.

1.4.2.1.2. *Locations and Concentrations Copper*

There is around 90-120 mg of copper in the adult human body distributed throughout all organs in various concentrations (**Figure 1.14**).[204,225,226] The same methods that have been used to quantitate iron have also been used for the quantification of total copper *ex vivo* and *in vitro*. The limits of these methods have already been discussed in the section related to iron quantification. The main difference for copper detection *ex vivo* is the histochemical staining employed which exists a myriad of indicators including hemotoxylin,[227] rubeanic acid (dithiooxamide),[228] rhodanine and diphenylcarbazide,[229] dethylthioocarbamate,[229] dithizone,[230] orcein,[231,232] bathocuproine disulfonate,[233] and the nonspecific Timm's staining.[234] Fluorescent probes have also been used to detect chelatable copper *in vivo*.[128] Copper, unlike iron, is not detectable by endogenous MRI methods, and only one copper-specific MRI contrast agent utilizing a PIDA moiety for Cu^{2+} chelation has been reported.[235]

The largest amount of copper is found in the musculoskeletal system, comprising three quarters of the entire copper body store as it is needed due to the high energy demands of movement and cell production.[236] The main function of copper in this area of the body is to oxidize the superoxide anion formed during cellular energy production and preventing toxic radical formation. The liver and brain contain similar amounts of copper, being around 10% each (**Figure 1.14**). The rest of the copper content resides in the serum (5%), where it is suspected that only 2.5% of the plasma copper is chelatable (being < 0.5 µM), which would be the smallest amount contributing to the signal of copper chelating PET probes. The CSF closely mimics the plasma in terms of chelatable copper (ceruloplasmin being essentially absent in the CSF) in that the total copper content of CSF reaches 0.5-2.5 µM.[237,238]

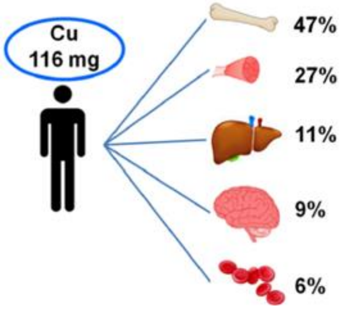

Fig. 1. 14: Biodistribution of copper. Adapted from ref. 204 with permission from PubMed Central.

The brain distribution of copper varies in each region and is highly abundant in the gray matter. The locus coeruleus is a region of the brain stem with the most abundant copper at 1.3 mM.[239,240] The next brain region with high levels of copper is the substantia nigra at 11.4 µg/g wet tissue weight (0.4 mM).[224,239] ICP-MS has been used to determine copper levels in the putamen

(4.5 µg/g wet tissue), body of caudate (5.1 µg/g wet tissue), cerebellum (4.8 µg/g wet tissue) and the anterior cingulate cortex (4.0 µg/g wet tissue).[224] Atomic absorption spectroscopy has been used to measure copper in the nerve terminals and synaptic clefts of hippocampal neurons and found that copper can reach almost 1 mM intracellularly and be released into the synaptic cleft upon depolarization to reach up to 30 µM in the extracellular space.[241] Copper levels up to 200 µM in the synaptic cleft have also been measured.[242] The use of these spectroscopic and spectrometric methods, again, do not differentiate between the different copper pools, and thus this provides a measurement of total copper in the regions just discussed.

Within the cell, it was first thought that only one copper ion exists, this result being extrapolated from biochemical methods on yeast cells.[243] It was later determined that yeast cells actually contain large pools of labile free copper that can exchange from the cytoplasm to the mitochondria, but it is not well understood how.[244] In neurons, large vesicles of free copper exist at the terminal, but it is not known what this exact concentration is. Fluorescent probes for copper have not been used to detect free, chelatable copper in neuronal cells, representing another avenue of metal biology work that remains to be completed.

1.4.2.2. *Copper Dyshomeostasis*

Like iron, copper is also redox active and can interchange between the cuprous and cupric oxidation states.[245] Under normal conditions, copper is tightly regulated by being mostly bound to protein away from the protein's surface to prevent exposure to the solution where Fenton-like chemistry using Cu^+ can occur to produce ROS:

$$Cu^+ + H_2O_2 \longrightarrow Cu^{2+} + \cdot OH + OH^-$$

Hydroxyl radicals formed from copper chemistry can go on to react with other macromolecules as described previously. One toxic mechanism of ROS' is lipid peroxidation, which has dire consequences on low density lipoprotein receptor-related protein 1 (LRP1) function, a receptor which plays a role in Aß clearance from the brain.[225]

The redox active role of copper is utilized by several cuproenzymes, which functions as a reductant for iron oxidation, a key step in iron metabolism as well as superoxide processing to form H_2O_2. If the cuproenzymes responsible for these functions were to become dysregulated, it would subsequently lead to accumulation of toxic Fe^{2+} and/or H_2O_2, resulting in increased ROS production mediated by iron Fenton chemistry.[226] The toxic role of copper has been well established for multiple neurodegenerative diseases (Wilson's Disease, Menkes Disease) and is also hypothesized to contribute to AD, PD, and ALS.[225]

1.4.2.2.1. *Copper's Role in Alzheimer's Disease*

The extent of clinical research of copper in AD has not been studied to the same magnitude as iron. For example, published histochemical studies of metal in AD tissue has been limited to iron and zinc. Endogenous MRI methods are limited to the detection of two metals, iron and calcium, and has not been used to study copper. *In vitro* methods looking at the total concentrations of copper have been studied in normal human brain tissue with the same methods used for iron, but this has not been extended to the study of copper in AD tissue. Clinical evidence for the toxic role of copper in AD is revealed through atomic absorption spectrophotometry, where the total copper content was measured in the CSF and plasma/serum of AD patients.[246,247] A meta analyses of studies looking at copper levels in these fluids showed no difference between copper levels in the CSF of AD and elderly healthy controls, and instead, showed a larger ratio of copper in the plasma of AD patients.[248] Free copper was not directly measured in these samples. Instead, the ceruloplasmin copper of the plasma and CSF could be measured using immunohistochemistry, and the extent of non-ceruloplasmin copper ("free" copper) could be calculated by subtraction of ceruloplasmin copper from the total copper content. This demonstrated that free copper was highly elevated in AD plasma and, also had up to a 25% increase in the CSF. As the contents of this "free" copper is mostly made up of albumin and transcuprein/α2M, the exact concentration of chelatable copper accessible to a copper chelating PET probe is not known. Nonetheless, this evidence demonstrates that even a small increase in free copper due to the dysregulation of copper metabolism is enough to elicit AD.

The biochemical mechanisms that result in increased free copper of AD patients has not been the focus of studies thus far. However, genetic profiling in AD patients of certain transporters regulating copper metabolism, like ATP7B, are underway.[250–252] Although the mechanism of free copper accumulation in AD is unknown, the direct consequence of its accumulation has been studied and plays a toxic role in AD. Copper exerts its toxic role through the AD related proteins, APP[253–256] and its posttranslational cleaved product, Aß.[257–259] Copper has been detected in large concentrations within Aß plaques.[260] It has been shown that Aß can directly bind copper and exert toxic redox activity by forming H_2O_2 upon reduction of Cu^{2+}, and then subsequent oxidation of Cu^+ with the H_2O_2 just produced to form hydroxyl radicals.[258]

$$Cu^{2+}\text{-Aß} + O_2 + 2H_2O + e^- \longrightarrow Cu^{+}\text{-Aß} + 2H_2O_2$$

$$Cu^{+}\text{-Aß} + H_2O_2 \longrightarrow Cu^{2+}\text{-Aß} + \cdot OH + OH^-$$

The presence of copper can cause aggregation of Aß *in vitro*, and treatment with a copper chelator can resolubilize and disassemble the formed protein aggregates.[261] From this information, it has been theorized that the formation of Aß aggregates in the synaptic cleft during AD could then be the result of unregulated free copper being released in the synapse after cholinergic neuronal depolarization, where Aß might initially act to sequester redox active copper, but then is aggregated upon the presence of synaptic Zn^{2+} (**Figure 1.15**). APP contains a copper binding domain (CBD) near the amine terminus.[262] The CBD of APP is exposed to the solvent (like the Aß binding motif) and can also participate in redox reactions. Binding of copper to APP induces dimerization and subsequent cleavage of APP into non-Aß fragments.[253] This soluble APP can act as a copper chaperone in the extracellular fluid. The connection between copper and APP dyshomeostasis is still unclear.

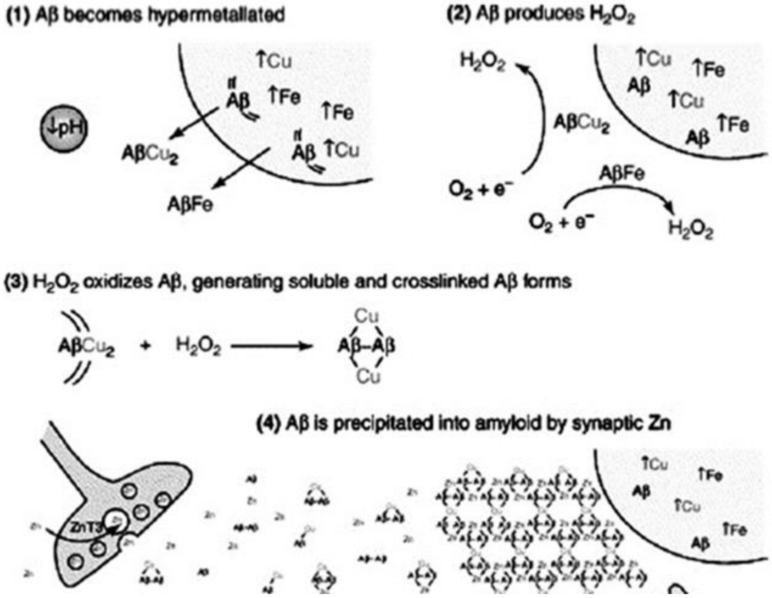

Fig. 1. 15: Copper ions bind to o soluble Aß and released from the cell (1) where the copper-Aß complex can participate in a redox reaction with water and oxygen to produce ROS (2) leading to crossing copper-Aß complexes (3). Further aggregation is induced by synaptic zinc (4). Adapted from ref. 249 with permission from American Chemical Society.

1.4.2.2.2. *Copper's Role in Parkinson's Disease*

Although the amount of evidence for copper toxicity in PD is less than that for AD, the findings are very significant and establish that copper has a toxic role to play in PD. Human post-mortem analysis in 1989 using techniques such as AAS indicate that total copper content is largely decreased in the substantia nigra and other structures of the basal ganglia from at least 25 µg/g dry weight to 17 µg/g dry weight., the region of the brain most severely affected in PD.[173] Overall however, the total copper content is relatively unchanged in the early stages of PD. This reduction in intracellular total copper can lead to reduced SOD1 activity, and thus prevent superoxide accumulation during the energy demands of neuronal activation.[263] Along with reduced SOD1 activity, reduced ferroxidase activity as a result of less copper would also lead to an accumulation of redox active iron, promoting even further oxidative stress. On the other hand, free copper was largely increased in the contents of the CSF where a level of 3.2 µg/l is indicative of idiopathic PD. As indicated above, an increase in free copper would be detrimental to neuronal survival, as this would result in an increase of ROS production and oxidative stress. Indeed, in 2008, it was reported that free Cu^{2+} could induce degeneration of dopaminergic neurons (the main neuronal type in the substantia nigra). The copper-dependent production of ROS can be mediated by several molecules, including the catechol-containing neurotransmitters (e.g. dopamine). Oxidized dopamine upon Cu^{2+} catalysis can generate DNA damage and promote dopaminergic neuronal loss.[264,265]

Just as in AD, copper has been found to be largely associated with the protein aggregates of PD and even induces their formation. A-syn, being the major component of Lewy bodies and found in the presynaptic terminal of neurons, has been determined to be capable of binding copper ions, forming a redox active pair that can go on to produce hydroxyl radicals.[266]

To account for the decrease in copper in the affected regions of PD, immunohistochemistry has been done to analyze copper proteins of post-mortem PD tissue. It was revealed that the copper transporters, CTR1 and ATP7A were decreased in these regions.[240] This could indicate that copper would have trouble being trafficked into the cell and being incorporated into cuproenzymes. Being stuck in the extracellular environment of dopaminergic synapses, large concentrations of free copper would then bind dopamine and α-syn in this space, become redox active, and thus cause cellular damage to the cell membrane and eventually, DNA damage of the surrounding neurons.[267]

1.4.2.2.3. *Copper's Role in Amyotrophic Lateral Sclerosis*

The onset of ALS can be sporadic (98% of cases) or associated with genetics (2% of cases) and is termed familial ALS (fALS).[190] The most common fALS genetic mutation is acquired in SOD1 which can result in either toxic gain-of-function or loss-of-function. SOD1, being a copper and zinc containing enzyme, was thus the first connection of ALS to copper dyshomeostasis. Investigations into SOD1 related fALS has been performed to also help understand mechanisms of sporadic ALS. Thus, much of the research related to copper and sporadic ALS has focused on the functioning of SOD1.

Clinical measurements of copper content in ALS patients has been contradicting. In 2003, ICP-MS was used to measure various trace metals in formalin-fixed ALS brain tissue of multiple brain regions.[194] This method, measuring total copper concentrations, revealed no discernable difference in copper concentrations of the gray matter between control and ALS patients. This is a remarkable difference than AD and PD, in that total concentration of copper can help differentiate other neurodegenerative diseases, highlighting different mechanisms of neurodegeneration that are more susceptible in different brain regions. Although no change in total copper was detected by ICP-MS, serum copper was measured in 2006 from different ALS patients and found that they had undetectable levels of serum copper and low serum ceruloplasmin.[268] However, a recent article as of 2018, examining copper and lipid content of the plasma of ALS patients highlights that heterogeneity exists in the blood copper concentrations with some patients having higher serum copper, or no change at all.[269] This may be likely due to different food eating habits, differences in lab test methods, and the multifactorial molecular profiles of sporadic ALS. This mirrors fALS in that SOD1 can either have a gain or loss in function, and just as shown here, sporadic ALS can either have high or low copper levels in the plasma. One of the most creative studies to date looking at CSF copper content used ICP-MS to examine isotopic differences between Cu-63 and Cu-65, two stable isotopes of copper.[270] Surprisingly, ALS patients had a significantly higher amount of Cu-65 within the CSF. These results may be explained by the preference of protein aggregates having better affinity for the heavier isotopic metal. As SOD1 aggregates are known to be metal depleted, this may result in high metalation of soluble SOD1 in the CSF over the intracellular SOD1 aggregates.

The mechanism of SOD1's toxic role in ALS can either be explained by a pro-oxidant gain of function or as a loss-of-function in its ability to reduce superoxide anions and sequester radicals.[271] In the gain-of-function mutations, SOD1 becomes misfolded and copper is no longer able to bind copper in its proper binding site, and instead binds Cu^{2+} in a solvent exposed site where it can react with water molecules to produce hydroxyl radicals. Loss-of-functions mutations in SOD1 are similar in that the protein becomes misfolded and cannot bind copper appropriately, but instead just becomes inactive. As a result, copper that can no longer end up incorporated into SOD1 will remain free when the chaperones become oversaturated. This also would result in oxidative stress due to increased free copper in solution and a build-up of superoxide ions that are not being reduced. In cases where SOD1 mutations is not the cause of ALS phenotypes, other proteins involved in copper homeostasis have been studied in preclinical models. In fact, an accumulation of inactive cuproenzymes could be restored by overexpression of CTR1.[272] This suggests that improper transport of copper into the cell is likely a cause of intracellular copper deficiency in ALS mouse models. Overexpression of CCS has also been shown to result in a decrease of SOD1 metallation.[273] This is probably due to copper being exchanged between multiple CCS in the cytosol, making it harder to find SOD1. Thus, in cases where there is no decrease of copper, the copper content is most likely bound to chaperones and lower molecular weight ligands, unable to reach their cellular endpoints.

One of the strongest lines of evidence of coppers involvement in ALS is the fact that copper chelators can alleviate symptoms in ALS animal models. This would suggest that the toxic role of copper is most likely mediated through redox activity, as is the case in other neurodegenerative diseases, whether it is free or protein bound. A recent study in 2017 demonstrated that overexpression metallothionein could protect against SOD1 mutant ALS mice.[274] Thus, when copper no longer becomes bound to SOD1 and becomes free and redox active, metallothionein can act as a buffer by binding and inactivating redox active copper.

1.4.3. *Zinc as a Target for PET*

1.4.3.1. *Zinc Homeostasis*

1.4.3.1.1. *Proteins Involved in Processing Zinc*

Unlike iron and copper, zinc (Zn^{2+}) is not redox active and maintains its divalent state in physiological conditions due the stability of its electron configuration having a full d-shell: $[Ar]3s^23p^63d^{10}$. Although it has been termed a “boring” element[275] because of this, it is a cofactor in all six classes of enzymes: oxidoreductases, transferases, hydrolases, lyases, isomerases, and ligases. Since it is not redox active, zinc’s main roles in biology serves as either a Lewis acid in catalysis of substrates or a stabilizer for the structure of proteins. However, in the brain it is the second most common metal, with iron being the first, where it can function on neurotransmission as it is stored as free metal in presynaptic vesicles.[276] Due to its divalent character, structural motifs for binding Zn^{2+} are similar to those binding Cu^{2+}. Thus, the proteins found in maintaining copper homeostasis also overlap with Zn^{2+} homeostasis.[126]

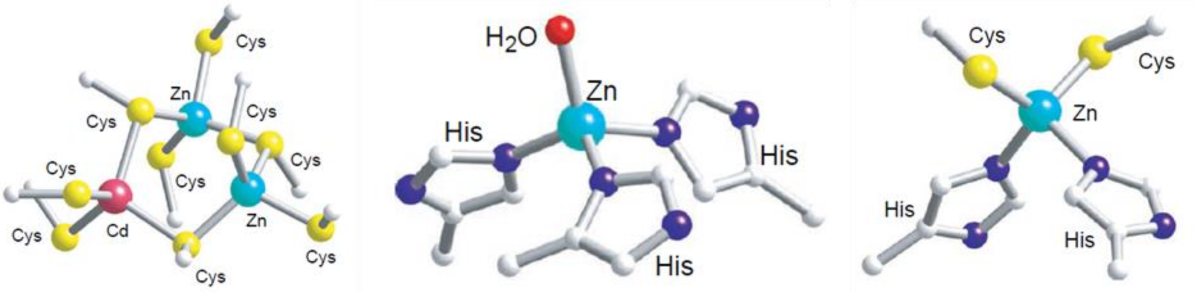

Fig. 1. 16: Common zinc binding centers of metalloproteins. Adapted from ref. 119 with permission from Elsevier

Within proteins, Zn^{2+} can either be tetra- or penta-coordinated. Zn^{2+} prefers a tetrahedral geometry being tetra-coordinated by at least one acidic ligand and the others being neutral, but can also adopt an octahedral geometry when it is to become penta-coordinated, usually by solvent molecules such as water and hydroxide ions (**Figure 1.16**). The most common ligands utilized by proteins for binding Zn^{2+} are cysteine and histidine. The Zn^{2+} binding sites can either be comprised of all cysteine ligands ($Zn_2Cd(Cys)_9$), such as the site in metallothionein (MT), or all histidine ($Zn(His)_3(H_2O)$), such as the case for carbonic anhydrase, or an equal mixture of both ($Zn(His)_x(Cys)_2$), which is found in the zinc finger structural motif of transcription factors. Of course, exceptions to these most common binding sites are also seen, especially in the case of multi-zinc binding domains.

In the blood, zinc takes advantage of copper and iron blood transporting proteins such as transferrin and α_2M, but estimates ranging from 30-98% of plasma zinc is found to be bound to the most abundant protein in plasma, being albumin.[277–279] The remaining plasma zinc is bound to α_2M. There is a small portion that is bound to low-molecular weight ligands which could be made up of glutathione, or amino acid complexes. It has been shown that Zn^{2+} can directly bind to DNA, with guanine having the highest affinity.[280] Thus, any nucleic acids found in the plasma could also be a part of this low-molecular weight Zn^{2+} pool.[281]

The binding affinity of albumin to Zn^{2+} is moderate, being 10^{-7} M.[279] Even though this zinc is protein bound, it is regarded as exchangeable because of this moderate affinity. Up to 92% of albumin bound zinc can be probed by fluorescent probes at 25 µM.[282] Structural data for the zinc binding site in albumin is not available, but it has been probed by using Zn K-edge x-ray absorption fine structure (EXAFS) spectroscopy.[279] The side chains thought to be responsible for coordination of Zn^{2+} in albumin are His^{67}, Asn^{99}, His^{247}, and Asp^{249} (**Figure 1.17**). A backbone carbonyl group and a water molecule form the fifth and sixth ligand with an overall distorted octahedral geometry.

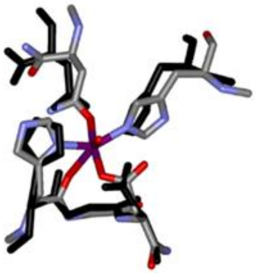

Fig. 1. 17: Model for Zn^{2+} coordination center in albumin. Adapted from ref. 279 with permission from American Society of Biochemistry and Molecular Biology

The understanding of the mechanism for uptake of Zn^{2+} into cells from the blood is not concrete. Since free Zn^{2+} is cytotoxic, it is not clear if the ion dissociates from albumin first in order to be transported into the cell or if a direct interaction between a Zn^{2+} carrier and transporter takes place. One thing is for certain, a large gradient exists where extracellular zinc can reach millimolar concentrations while being at picomolar concentrations in the cell.[283] However, there is currently no evidence for a Zn^{2+} pump in mammalian cells. Several transporters have been suggested. The most accepted pathway for Zn^{2+} to be shuttled into the cytoplasm of cells is through the Zrt-/Irt-like protein (ZIP) zinc transporter.[284,285] It is thought that Zn^{2+} uptake through ZIP occurs via a symporter mechanism with HCO_3^- as the counter ion. The SLC30 genes, which encode for zinc transporters (ZnTs) are expressed on membranes of either the cellular surface or vesicles and organelles within the cell.[278,283] ZnT-1 is ubiquitously expressed on plasma membranes and could play a role in Zn^{2+} transport into the cell. It has been suggested, however, that ZnT-1 affects Zn^{2+} influx by regulating L-type calcium channels (LTCC), which can directly import Zn^{2+} into the cell. Of the ten ZnTs, ZnT-3 is expressed exclusively in the brain which is responsible for insertion of Zn^{2+} into synaptic vesicles to be excreted into the synaptic cleft. Other ZnTs expressed in the brain and have been found to have altered expression in AD are ZnT-4,-5, and -6.

Once inside the cell, MT will bind to Zn^{2+} (K_d ~ 0.1 pM) in order to buffer the cytoplasm and shuttle Zn^{2+} to its cellular destinations.[281,286] This is the only chaperone for Zn^{2+} that has been discovered. The machinery for Zn^{2+} homeostasis is thus, not as complex, or not as well understood as the machinery for copper and iron homeostasis. This is odd given that Zn^{2+} is a cofactor for ten percent of human proteins. Therefore, its primary cellular destination will be to the Golgi apparatus and ER where protein folding will take place and Zn^{2+} can stabilize the tertiary structures during this folding process. The importance of Zn^{2+} as a structural element is indicated by the fact that proteins bind Zn^{2+} with single nanomolar to sub picomolar affinity, making it difficult for any Zn^{2+} chelator to leach this metal ion from its protein ligands.

1.4.3.1.2. *Locations and Concentrations Zinc*

The adult human body contains on average about 2-3 g of Zn^{2+}.[278] The measurement of Zn^{2+} in human tissue is not as arduous as measuring iron and copper, for only one oxidation state exists for zinc (being Zn^{2+}) at physiological conditions. Therefore, tissue preparation for *ex vivo* or *in vitro* methods do not have to worry about changing the nature of Zn^{2+} as the measurement will represent the total amount of Zn^{2+} in the sample. However, Zn^{2+} can be a common contaminant from multiple sources including air, water for sample preparation, and other reagents that are known to contain traces amount of Zn^{2+}. These contaminations can easily be remediated by the use of proper blanking samples that will account for any Zn^{2+} contamination. Just as atomic absorption was used to measure iron and copper, so too has it been used to measure zinc. In addition to AA, particle-induced x-ray emission (PIXE) and neutron absorption analysis (NAA) has also been used to measure Zn^{2+}, but is not easy to implement in every lab as it requires the use of an ion beam for either neutron or proton irradiation for NAA or PIXE respectively. For visualizing zinc distribution in tissue, histochemical methods have been utilized. Unlike iron and copper, there exists a Zn^{2+} specific histochemical stain that visualizes only free, chelatable Zn^{2+} as the stain utilizes the chelator diphenylthiocarbazone (dithizone) for a colorimetric reaction resulting in a shift from a green to red color upon reaction with Zn^{2+}. This stain was first applied to various animal tissues by Mager *et al.*in 1953,[287] and subsequently applied to human brain tissue in 1955 by Maske.[288]

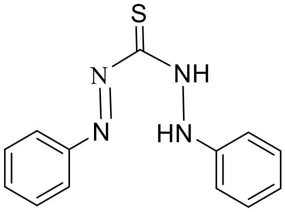

Dithizone

Fig. 1. 18: Structure of dithizone

For *in vivo* methods, fluorescent Zn^{2+} chelating probes and Zn^{2+} chelating MRI contrast agents have been used successfully.[128] In fact, the development of metal chelating probes has been largely focused on Zn^{2+} because of its inability to undergo redox activity upon chelation and thus providing a stable probe interaction. The key to these *in vivo* methods is that they interact with free and exchangeable Zn^{2+} ions which make them an asset for understanding the dyshomeostasis of this metal during disease. Although this metal is utilized ubiquitously in varying ways throughout the entire body, these probes and the work of others have demonstrated that chelatable Zn^{2+} is primarily found in the CNS for use in neurons, possibly either for stabilization of key neurotransmitter stores or synaptic transmission.[276,289]

Zn^{2+} is essentially insoluble in neutral water, but because physiological fluids have buffering salts and metal chelating organic compounds and proteins, free Zn^{2+} concentrations can become very high, and even into millimolar concentrations when taking into account protein bound Zn^{2+}. In the blood, there exists two pools of Zn^{2+}, being the protein bound Zn^{2+} and exchangeable/labile Zn^{2+} that is mostly found bound to albumin. Albumin-Zn^{2+} should not be considered protein bound Zn^{2+} because of its moderate affinity and its ability to be probed by fluorescent chelators. Thus, albumin-Zn^{2+} is considered exchangeable as it can easily exchange Zn^{2+} to other carriers or chelators. Although about 35 mg of the total 2-3 g of Zn^{2+} is found in the blood (0.1% of total body Zn^{2+}) 85% of that is found in the various blood cells (erythrocytes, leukocytes, platelets, etc.) being permanently bound to protein (**Figure 1.19**).[278] The remaining Zn^{2+} in the plasma is either protein-bound, micro-ligand-bound, or free ionic Zn^{2+}. In the serum about 80% is loosely bound to albumin and 20% is tightly bound to α_2M. The concentration of Zn^{2+} bound to low molecular weight ligands (cysteine, histidine, and GSH) is estimated to be about 10-20 µg/L (0.15-0.3 µM for a maximum total of 100 µg Zn^{2+}). The amount of free ionic Zn^{2+} is even far less, being around 0.2-1.0 nM (**Figure 1.20**).

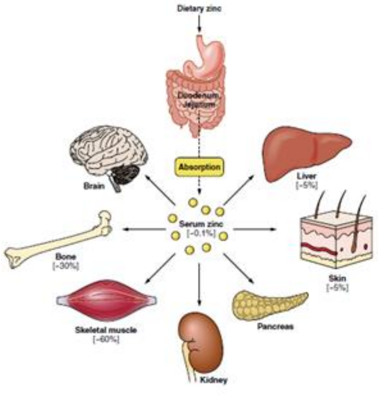

Fig. 1. 19: Biodistribution of zinc. Adapted from ref. 278 with permission from The American Physiological Society

The blood can transport all Zn^{2+} pools and chelators to different tissue compartments. The musculoskeletal system comprises the most Zn^{2+} being 30% in the bone and 60% in the muscle.

Most of the Zn^{2+} found in these tissue compartments is mostly permanently protein bound. The remaining 10% is found in the skin and liver where 5% is stored in the skin and the other 5% being stored and being implemented in its final proteinaceous form in the liver to be distributed to the rest of the body.

Passing from the blood through the BBB to the brain, the concentration of Zn^{2+} in the CSF mirrors that of the plasma, being 10-20 µg/L. The brain represents a unique organ for Zn^{2+} in that some neurons, designated Zn^{2+} containing neurons (as the neurons responsible for a wide range of neurotransmitters such as glutamate and acetylcholine can contain vesicular Zn^{2+}) contain large pools of Zn^{2+} in presynaptic vesicles that can be released into the synapse. So, even though the brain contains 10 µg Zn^{2+}/g wet brain tissue weight, specific brain regions can contain dense regions of Zn^{2+} due to neurons having these Zn^{2+} synaptic vesicles which accounts for 5-15% of the total Zn^{2+} in the brain. The gray matter, where most of the nerve endings (synaptic clefts) reside, contain 0.15-0.2 mM Zn^{2+} altogether. This is a lot more than the gray matter only having only 33-35 ppm (~ 0.5 µM) in total. Using the *ex vivo* methods previously described, brain regions have been measured for their total Zn^{2+} content, with the hippocampus containing the most at 300 µg/g wet tissue. The cerebellum has been measured and ranges from 45-70 µg/L. The brain regions containing the most sync have been determined by histochemistry, thus visualizing that most of the Zn^{2+} can be attributed to the synaptic vesicular Zn^{2+} and is found in the hippocampus and cerebrocortex.

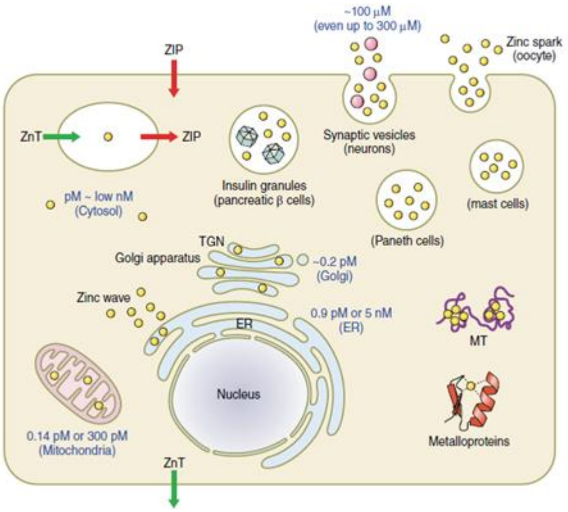

Fig. 1. 20: Intracellular zinc distribution and its various concentrations in different organelles. Adapted from ref. 278 with permssion from The American Physiological Society

Inside the cell, three pools of Zn^{2+} are found, being either protein bound, labile, or the vesicular Zn^{2+}. The vesicular Zn^{2+} pool is found only in neurons and possibly pancreatic insulin secreting cells where Zn^{2+} is stored in the hundreds of micromolar range. The nature of this Zn^{2+} is undetermined whether it is bound to exchangeable ligands or remains as free ions. Within the cytosol of most cells, Zn^{2+} is in the picomolar range and can be either free or protein bound. Mitochondria can have 0.14-300 pM Zn^{2+} at any given time and the TGN and ER can contain 0.9 pM – 5 nM where Zn^{2+} can become permanently bound to protein or stored in synaptic vesicles (**Figure 1.20**).

1.4.3.2. *Zinc Dyshomeostasis*

Zinc's toxic role is not quite the same as iron and copper for it cannot produce ROS directly by any redox reaction. However, Zn^{2+} can indirectly cause the production of ROS and induce oxidative stress within neurons by interacting with proteins in the mitochondria responsible for antioxidant defense.[290] One of the hallmarks of Zn^{2+} in neurodegeneration studies is its ability to induce aggregation of peptides associated with NDs such as Aß[291] and TDP43.[292] Due to zinc's roles in cellular biology as either a structural or functional component of proteins, its dyshomeostasis can severely affect cellular processes. Since it is a structural component in transcription factors, anything causing Zn^{2+} to be unable to bind to zinc finger motifs would then cause dysregulation in DNA synthesis, and possibly a reduction in the expression of critical proteins necessary for the cell life cycle.[293] Being a functional component of metalloenzymes, zinc depletion would result in reduced enzymatic function that is critical for CNS function, resulting in mental lethargy and neurodegeneration.[294] Finally, free Zn^{2+} has been found to be neurotoxic at increased levels by inhibiting proteins of the ETC and tricarboxylic acid cycle (TCA).[295] The mechanism by which Zn^{2+} becomes dysregulated in cells is straightforward, being that a varying expression of zinc transporters and MT would cause either a decrease or increase in cytosolic labile Zn^{2+}. Both increases and decreases of Zn^{2+} have been found in neurodegenerative studies which can both lead to neuronal cell death. The differential dysregulation of Zn^{2+} for various ND diseases (AD, PD, and ALS) will be discussed here.

1.4.3.2.1. *Zinc's Role in Alzheimer's Disease*

The role which Zn^{2+} plays in AD is as straightforward as the mechanisms regulating its homeostasis. One interesting note, however, is that total levels of Zn^{2+} have been found to be decreased in NDs, including AD.[294] How a decrease in total Zn^{2+} might propagate neurodegeneration is uncertain. As has been discussed previously, Zn^{2+} has been shown to induce the aggregation of Aß. With a decreased concentration of Zn^{2+} in certain brain regions, this could result in increased solubilization of Aß oligomers, which are thought to be more toxic than Aß plaques (**Figure 1.21**).[58]

Studies that look to the expression of ZnTs contradicts the data that showed a decreased Zn^{2+} concentration. ZnT-1, responsible for transporting Zn^{2+} out of the cell has been found to have increased expression in human AD brains.[296] This would indicate that increased Zn^{2+}

concentrations would be present in the neuronal extracellular space, and thus exacerbate Aß plaque formation. Moreover, ZnT-6, responsible for transporting cytosolic Zn^{2+} into the TGN is also increased.[296,297] Increased Zn^{2+} in the TGN in AD brains would indicate that Zn^{2+} could possibly be binding the metal-binding domain of APP in this cellular organelle, which would lead to Aß as the cleavage product during APP processing. There have been studies contradicting ZnT-1 expression, indicating that there is actually a decreased amount of ZnT-1 in the hippocampus.[298] This would help to explain why there is increased cytosolic Zn^{2+} in this region.[299] ZnT-3, responsible for loading cytosolic Zn^{2+} into synaptic vesicles has been shown to be significantly reduced in the brains of AD patients.[300] Altered expression levels of ZnT-3 could be the result of inadequate release of synaptic Zn^{2+} into the synaptic cleft. The structural machinery or signaling cascade responsible for shuttling the vesicular Zn^{2+} towards the cellular membrane could be corrupted and lead to increased cytoplasmic Zn^{2+}. With synaptic Zn^{2+} remaining in the cell due to this, this would lead to a decrease in ZnT-3 expression where loading of Zn^{2+} is no longer needed. Finally, another Zn^{2+} transporter, ZIP1, is associated with AD in that there is evidence that it is significantly increased during disease progression.[301] ZIP1 is responsible for delivering Zn^{2+} from the extracellular milieu into the cytoplasm.[302]

To counter increased cytosolic Zn^{2+}, MT expression is increased to buffer toxic amounts of Zn^{2+}, which can bind up to nine Zn^{2+} atoms.[286,303] Of the four types of MT, MT-3 is exclusively expressed in the brain. In AD brains, it has been found that MT-3 expression is reduced.[304] Loss of its protective effects would lead to an exacerbation of pathogenic processes already discussed in the AD brain. The increased cytosolic Zn^{2+} would induce neuron toxicity by inhibiting energy production and promoting ROS production.

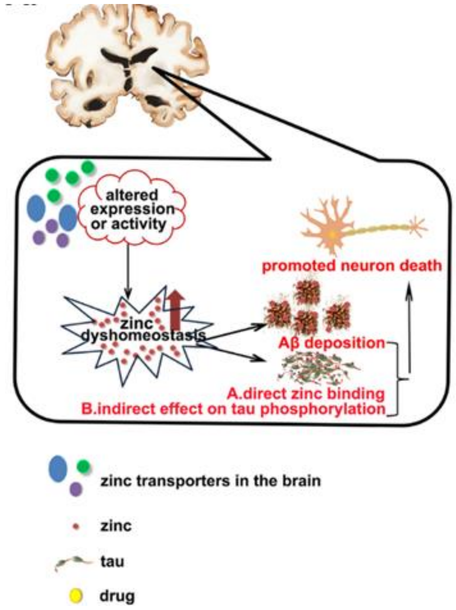

Fig. 1. 21: Zinc dyshomeostasis leads to Aß deposition and neuronal cell death. Adapted from ref. 295 with permssion from Springer Nature

1.4.3.2.2. *Zinc's Role in Parkinson's Disease*

Studies examining Zn^{2+} in PD remain few and far between as it is considered mostly an iron related disease. Thus, post-mortem, clinical, and pre-clinical evaluations have focused on measuring iron and using various iron detection methods. As we have seen, Zn^{2+}, can play a role in neurodegeneration. However, the mechanisms regarding Zn^{2+} homeostasis have not been probed in PD patients or models and represents a nonactive area of research.

Nonetheless, studies utilizing ICP to measure iron levels in PD brains in 1989[305] and 1992[306] by Dexter *et al.* also examined copper and zinc levels with interesting findings that they differ in PD brains when compared to healthy aged-matched controls. With Zn^{2+} levels being a little less than 1µmol/g dry weight in the substantia nigra, they observed a 54% increase in Zn^{2+} concentration in this brain region, being around 1500 nmol/g dry weight. One surprising finding is that CSF Zn^{2+} concentrations are lower in PD patients in several studies. One study in 2011 reported an increase in CSF Zn^{2+},[307] however metanalysis of most clinical CSF measurements of Zn^{2+} indicates that there is an overall decrease in Zn^{2+}.[308]

The mechanisms regarding these fluctuations in Zn^{2+} have not been proposed. Seeing as there is a net increase in SN Zn^{2+} found in the cytoplasm and a decrease in extracellular Zn^{2+}, this would indicate that, like in AD, the expression of ZnT-1 is under expressed in the SN, resulting in an accumulation of Zn^{2+} within neurons located in this region, making it unavailable for cycling in the CSF. Unfortunately, experiments looking at zinc transporters have not been performed on PD brains or even PD animal models. As we have seen, an increase in cytosolic Zn^{2+} would lead to increased intracellular oxidative stress. Biomarkers of oxidative stress such as hydrogen peroxide and lipid peroxidation are widely found in PD, suggesting that neuronal cell death in this region is largely metal-mediated.

1.4.3.2.3. *Zinc's Role in Amyotrophic Lateral Sclerosis*

ALS has many pathological processes that occur during disease, which are oxidative stress, glutamate excitotoxicity, neuroinflammation, neurofilament dysregulation, mitochondrial damage, protein aggregation, and apoptosis.[309] Zinc plays a role in all these pathological processes and an increase in free cytosolic Zn^{2+} would only exacerbate these problems. The study of formalin-fixed ALS tissue in 2003[194] (discussed in both the iron and copper sections) also measure Zn^{2+} concentrations in the grey and white matter using ICPMS. Just like the Zn^{2+} measured in PD brains, ALS brains have a 50% increase of Zn^{2+} in the gray and white matter when compared to control being 104 µg/g dry weight and 68 µg/g dry weight, respectively. The nature of this increased Zn^{2+} is most likely in the form of cytosolic free Zn^{2+} due to the alterations of Zn^{2+} protein function and expression.

SOD1, being the most common mutagenic protein associated with ALS, is a Zn^{2+}/Cu^{2+} containing enzyme. Most SOD1 mutations in ALS patients are within the Zn^{2+} binding site, causing an inability to bind the metal ion.[310] When Zn^{2+} is no longer bound to SOD1, its primary role of sequestering ROS reverses and actually causes the formation of them. Thus, SOD1 mutations in either fALS or sporadic ALS contribute to oxidative stress two fold, by increase ROS production and increasing free Zn^{2+} as it is no longer bound to SOD1, which can go on to induce oxidative stress by inhibiting mitochondrial proteins involved in the ETC. The inability to protect the cell from increasing cytosolic Zn^{2+} is further exacerbated by decreased expression of MT and ZnT-3 and ZnT-6 found in the spinal cord of human ALS patients.[311,312] Even SOD1 mutant ALS mouse models have this decreased expression.[313] As MT is thought to buffer the cell from free Zn^{2+}, the loss of this protective role would only increase oxidative damage to the cell during ALS.

Finally, it has been shown that Zn^{2+} induces the aggregation of TDP43 (**Figure 1.22**),[292] the primary protein aggregate thought to cause toxicity and leading to cell death in ALS.[314] It is then not surprising that the PET tracer designed to bind Cu^{2+}/Zn^{2+}-protein aggregates has a two-fold binding potential in ALS motor cortex post-mortem tissue when compared to age-matched control.[315] This could be further evidence that increased free Zn^{2+} and Zn^{2+}-protein aggregates occur in the motor cortex of ALS patients (see chapter 3).

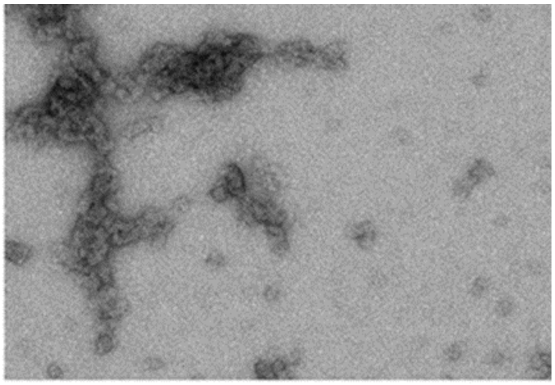

Fig. 1. 22: Amyloid-like aggregates of TDP-43 protein induced by zinc. Adapted from ref. 292 with permission from Springer Nature

1.5. What Makes a Good CNS PET Tracer?

Several essential factors will help predict if a small molecule will become a successful PET radiotracer for CNS PET imaging. The exception to these rules includes macromolecular structures such as natural products, peptides, and antibodies. First, the pharmacokinetic (PK) properties of a molecule will determine if it is BBB permeable, second its pharmacological attributes are revealed through binding affinity and specificity studies, third chemical structure will determine if it is suitable for late-stage radioisotope labeling, and finally, toxicity studies will ensure that the molecule can be safely administered in a clinical setting immediately after its production. *The most important factor here is being BBB permeable and should be validated as quickly as possible by preliminary animal studies before any optimization of the compound's synthesis, formulation, or determination of other pharmacological attributes (ADMET, K_d, etc.) are undertaken*.

Often, during small molecule PET tracer development, leads are chosen from drug discovery programs where a compound has known affinity for its target and is often optimized according to Lipinski's rule of 5 to exhibit good pharmacological effects.[316] Although this makes it a good drug candidate, one distinguishing feature of a CNS PET tracer is that it should readily wash out from the brain in a short time frame so that kinetic data can be measured during a patient's PET scan in one to two hours.[30,31] Therefore, a molecule with a short biological half-life is desired. This makes a case that chemical matter in drug discovery programs that are often neglected because of short half-life (as the main goal is to exhibit a therapeutic effect over a long time frame before another dose is administered again) would make excellent candidates for radiotracer discovery.[317] For a small molecule to be BBB permeable, Lipinski's rule of 5 is generally followed, but can also be modified to be a "rule of 3",[318] as chemical matter that has successfully crossed the BBB have these attributes:

- MWt < 300 Da
- $\mathrm{clogD}_{7.4} > 1$ and < 3
- HBDs < 3

- TPSA < 80Ǻ^2

A small molecule with these physiochemical properties is likely to cross the BBB, but several other factors may complicate the story. Radiotracers are injected intravenously where serum protein known as albumin, tends to bind small molecules nonspecifically.[31] If a PET tracer binds albumin excessively, it will be hard for the molecule to dissociate from the blood and diffuse into the brain quickly during the course of a PET scan. The BBB also has efflux proteins such as p-glycoprotein (Pgp) which are responsible for removing xenobiotics from the brain.[319] Sometimes, it is found during PET tracer development that a molecule can be a substrate for Pgp and seem to have little no brain uptake. Substrates for Pgp is promoted by high lipophilicty, the occurrence of a formal positive charge at physiological pH (pH 7.4) and containing multiple aromatic groups.[320] Another chemical moiety that often prevents small molecules from passing the BBB is a carboxylic acid.[321] Esters can be metabolized to esters and thus prevent BBB permeability. This brings us to another factor that complicates BBB permeability, being that a small molecule can be extensively metabolized in the blood and liver before enough radiotracer enters the brain.[30] A polar metabolite that is not BBB permeable is desirable and much care should be taken to understand which enzyme metabolizes the radiotracer so that an inhibitor may be administered beforehand if one is available. Once all these factors are overcome, the peak standard uptake value (SUV) of a radiotracer in the total brain should typically be at least 2 or greater to be a successful candidate.

Once inside the brain, metabolic enzymes can also be present that may lead to trapped metabolites, and further complicate the analysis of the acquired image.[322] The radiotracer should have high potency (single digit nM to sub-nM) and high selectivity for its target. Low non-specific binding of a PET tracer will allow a good signal to noise ratio when interpreting the reconstructed image. Protein targets sometimes have more than one binding site. Ideally, it should be determined that the PET tracer occupies only one site to simplify the kinetic analysis where only type of complex is formed between the radiotracer and target ($R^* + P \rightarrow R^*P$).

During radiosynthesis of the PET tracer, ^{11}C-methylation and nucleophilic [^{18}F]fluoride are often used.[323] Heteroatoms (e.g. O, N or S) are chemical moieties often labeled by carbon-11. A molecule that contains more than one heteroatom should take care to ensure methylation of the desired atom is achieved which can be promoted using protecting groups. Alkyl fluorides are used in PET tracers but can sometimes be eliminated during metabolism to promote the occurrence of bone binding [^{18}F]F^-.[324,325] Thus, scaffolds with aromatic fluorides are emerging prevalently in the PET tracer chemical space. It is difficult to achieve fluorination of electron rich aromatic groups however,[326] and the success of late-stage fluorination of this chemical moiety is discussed in Chapter 5 in the synthesis of [^{18}F]FDOPA.[327,328] Finally, dosimetry studies are performed (normally in rodents) after a cGMP compliant synthesis method has been developed to ensure that the radiotracer is safe for injection to patients.

1.6. Metal Chelators as PET Tracers

Metal chelators can be classified based on how many donor atoms interact with the metal center. The term dentate, meaning toothlike, refers to the donor atoms being like teeth that bite down on the metal. Bidentate, tridentate, tetradentate, and hexadentate chelators are commonly encountered in the clinical space. The higher the denticity, the more affinity a chelator will have for a metal.[329] Transition metals normally form tetrahedral or octahedral geometries, which requires four or six points, respectively (in other words four or six donating atoms from ligands).[330] Thus, a hexadentate ligand is able to form a 1:1 complex with a metal. The affinity constant is concentration dependent, and thus far less hexadentate chelators are required to fully complex a metal than a tridentate or bidentate ligand which would require the formation of a 2:1 or 3:1

complex for full coordination of the metal. Unfortunately, hexadentate chelators are large and contain at least 6 donor atoms, being higher than the hydrogen bond donors required for a good CNS small molecule. Thus, hexadentate ligands will have very low success in crossing the BBB barrier.

1.6.1. *Iron Chelators as PET Tracers*

With biological iron (Fe^{2+}/Fe^{3+}) having a role in neurodegeneration, being able to detect the dyshomeostasis of this ion in patients via PET imaging would be beneficial to the healthcare community. Chelators for Fe^{2+} also have affinity for other biological divalent metals such as Cu^{2+} and Zn^{2+}, and thus, having a PET tracer that targets solely Fe^{2+} might be impossible.[329] Though, there are chelators that have high affinity for Fe^{2+} and fluorescent sensors for Fe^{2+} have been developed,[331,332] these small molecules have their limitations and their ability to chelate Zn^{2+} would make it difficult to discern information from a PET image of a living organism. The discussion of iron chelators will, thus, be restricted to Fe^{3+} specific chelators.

1.6.1.1. *Iron Chelating Chemical Scaffolds*

Fe^{3+} is the only essential trivalent metal found in biological systems (Al^{3+} and Ga^{3+} occur in trace amounts that is negligible) and will be a great metal source for specific binding of iron chelating PET tracers. Due to this high charge density (3+), the most stable bonds with ligands are achieved though weakly polarizable atoms, such as oxygen. The scaffolds containing high Fe^{3+} binding affinity and specificity include catechols, hydroxamates, hydroxypyridinones, and hydroxycarboxylates (the most basic example being citric acid).[329] It should be noted that aminocarboxylates have high affinity for Fe^{3+} but are not specific as they chelate divalent metals due to the polarizable nitrogen atoms that they contain.

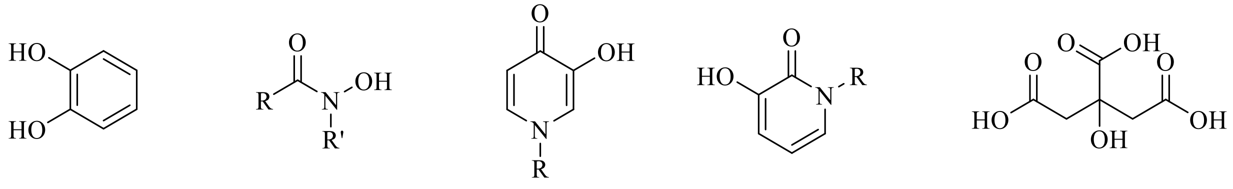

Catechol **Hydroxamate** **Hyrdoxypyridinones** **Hydroxycarboxylates**

Fig. 1. 23: Scaffolds of common iron chelators

Pros and cons are associated with each of these scaffolds. Catechols, although having high affinity for Fe^{3+} are pH sensitive due to their high affinity for protons. At physiological pH, they contain a net charge due to deprotonation of the -OH groups and are therefore, unlikely to permeate membranes by simple diffusion.[333] Hydroxamates and hydroxypyridinones can form neutral complexes with Fe^{3+} which will help with being able to permeate membranes by non-facilitated diffusion.[333] Unfortunately for hydroxamates, a bidentate ligand containing this scaffold is unable to solubilize Fe^{3+} at physiological pH due to its low affinity, and thus only hexadentate hydroxamates would be suitable. The cons of hexadentate chelators for CNS PET imaging were discussed up above. Hydroxycarboxylates are tridentate chelators having the ability to form polymer complexes with iron.[334,335] This strong affinity for iron may contribute to readily stripping iron from macromolecular structures and thus might not represent only free chelatable iron in a biological system. Thus, hydroxypyridinones stand out amongst the scaffolds as being the most suitable for PET tracer development because of its high affinity, selectivity, and ability to cross membranes by passive diffusion.

1.6.1.2. *Clinical Iron Chelators*

As most PET tracer development begins with using molecules that have already been optimized for human use, it would be best to look at iron chelators that have already gained FDA approval. The three most commonly used FDA approved iron chelators in the clinic are deferoxamine, deferasirox, and deferiprone.[336]

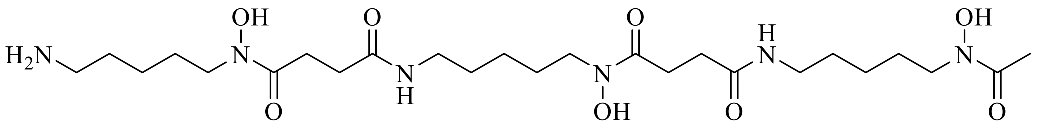

Desferrioxamine-B

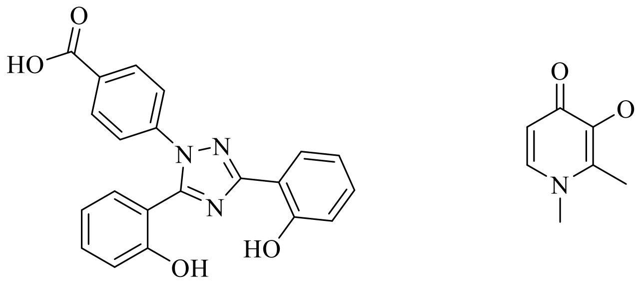

Deferasirox **Deferiprone**

Fig. 1. 24: FDA approved iron chelators

The high denticity of desferrioxamine-B and its high molecular weight make it poorly orally available.[337] This inability to permeate membranes in the GI indicate just how challenging it would be to cross the BBB. It is known that desferrioxamine-B does not cross the BBB and is also not effective at removing iron during iron overload. Deferasirox, although not a typical catechol, contains phenolic groups with similar pKa's and would contain a net negative charge due to the benzylic acid moiety. These are a known scaffold that do not cross the BBB and would thus not make a good CNS PET tracer candidate. Deferiprone, on the other hand, containing the hydroxypyridinone scaffold, is a good candidate, and has been shown to get into the brain of rodents when administered orally.[338] The development of [^{11}C]deferiprone as a possible PET tracer is described in Chapter 2.

1.6.1.3. *Investigational Iron Chelators*

Due to potential challenges selecting FDA-approved iron chelators as PET tracer candidates, some work has gone in to optimizing iron chelating scaffolds to be biologically active having long biological/metabolic half-lives, good oral availability, and adequate lipophilicity to diffuse across physiological membranes. One of the concerns with optimizing these scaffolds to be an adequate drug is that it might make it less advantageous as a PET tracer. For example, to improve a drug candidate for treating iron toxicity, it needs to be able to remove iron from Tf in the blood. Chelators with high denticity such as tetra- and hexadentate chelators were developed to as they can quickly form a 1:1 complex unlike bidentate ligands. Thus, iron chelating scaffolds were linked together to make hexadentate ligands and can be mixed and matched.[339] Selected examples include:

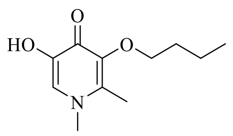

BU-O-3,4-HOPO

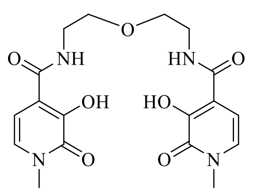

5LIO-3,2-HOPO

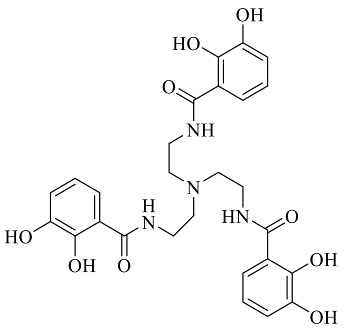

TRENCAM

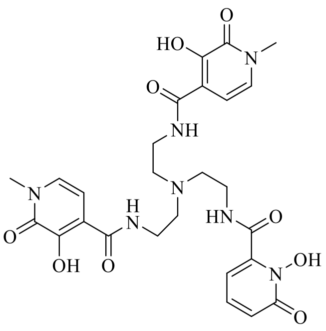

TREN-1,2,3-HOPO

Fig. 1. 25: Examples of iron chelators in literature

Unfortunately, the drawback of these iron chelators is their large molecular weight, making it a risk to use in CNS PET tracer development. Although these molecules have not been tested for BBB permeability, assumptions can be made that those containing catechols will contain a net negative charge at physiological pH and not diffuse to the brain. It would be interesting, however, to test the hexadentate hydroxypyridinones containing chelators. To further optimize the hydroxypyridinone chelators, modifications have been made to the alkyl substituents.[340] A possible target for lipophilic hydroxypyridinones is the metalloenzyme 5-lipoxygenase.[341] Modifications of deferiprone at the R_1 alkyl chain shows that increased lipophilicty incases affinity for this target, and thus increased percent inhibition. This inhibition can be further decreased by increasing the length of the alkyl chain at the R_2 position where it is thought that steric hindrance blocks binding to the active site. A chelator of this class would have high Fe^{3+} affinity, **selectivity**, and be able to permeate physiologicial membranes. An interesting class of fluorescent sensors for Fe^{3+} have been developed and shown to cross cellular membranes, but their use for crossing the BBB has yet to be challenged. A review on these molecular imaging chelator probes has been reviewed by Chang *et al.*[128]

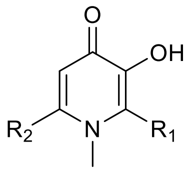

R_1	**R_2**	**MW**	***$D_{7.4}$***	**logP**	**ClogP (R_2)**	**R_2 length (Å)**	**molecular width (Å)**	**% inhibition**	**biological activity**
H	H	125	0.25 ± 0.04	−0.60	0.2	1.1	4.32	59.4	0.16
CH_3	H	139	0.17 ± 0.01	−0.77	0.88	2.15	5.55	39.4	−0.19
CH_2CH_3	H	153	0.62 ± 0.01	−0.21	1.53	3.48	6.79	48.5	−0.03
$CH_2CH_2CH_3$	CH_3	181	2.50 ± 0.10	0.4	2.05	4.7	9.25	30	−0.37
$CH_2CH_2CH_2CH_3$	CH_3	195	8.05 ± 1.70	0.9	2.58	5.97	10.5	29.6	−0.38
CH_2OCH_3	CH_3	183	0.39 ± 0.07	−0.41	−0.42	4.44	8.95	14.8	−0.76
$CH_2NHCOCH_3$	CH_3	210	0.15 ± 0.01	−0.82	−1.31	5.83	10.36	18.5	−0.64
$CH_2NHCOCH_2CH_3$	CH_3	224	0.19 ± 0.02	−0.72	−0.78	7.12	11.67	13.5	−0.81
$CH_2NHCOCH(CH_3)_2$	CH_3	238	0.45 ± 0.01	−0.35	−0.47	7.1	11.68	21	−0.58
$CH_2NHCO(CH_2)_2NHCOCH_3$	CH_3	281	0.02 ± 0.004	−1.70	−1.67	10.88	15.43	3.8	−1.40
$CH_2NHCO(CH_2)_2CONHCH_2CH_2CH_3$	CH_3	309	0.20 ± 0.005	−0.70	−0.61	13.5	18.08	2.1	−1.67

Table 1. 1: Physicochemical Properties and 5-Lipoxygenase Inhibitory Activity of 2-Substituted 3-Hydroxypyridin-4-ones

1.6.2. *Copper/Zinc Chelators as PET Tracers*

Since copper is found mostly in the divalent state within biological systems, chelators that target the divalent metals Cu^{2+} and Zn^{2+} will be discussed togther. It should be noted that most divalent metal chelators have a strong affinity for Cu^{2+} *in vitro*, but in physiological conditions where both metals are present in the biological matrix, it is difficult to say that the binding of these chelators is limited to one specific metal, and should be considered that a signaled derived form a PET tracer with these chelating scaffolds originate from both Cu^{2+} and Zn^{2+}. For example, the chelating scaffold N,N,N',N'-tetrakis(2-pyridil-methyl)ethylendiamine (TPEN) has a strong binding affinity for Cu^{2+}, but is used as an exclusive Zn^{2+} chelator in fluorescent probes.[342] The hard and soft acids and bases principle (HSAB) helps explain why donor atoms on a ligand can provide selecitivity or prefence for specifc metal ions. As stated before, atoms that are considered hard bases, like anionic oxygen, prefer the hard trivalent metal Fe^{3+}.[329] Conversely, soft basic atoms, like sulfur, prefer soft metals such as Cu^{+} over divalent metals like Ca^{2+}. Neutral oxygen and nitrogen donor atoms prefer borderline hard/soft metal ions like Zn^{2+} and Cu^{2+}.

1.6.2.1. *Divalent Metal Chelating Chemical Scaffolds*

There is a wide variety of chemical scaffolds with divalent metal binding affinity including acyclic and macrocyclic amino chelators, hydroxyquinolines, dithiocarbamates, diamine chelators, pyrithiones, and thiosemicarbazones. Aminocarboxylate chelators such as EDTA also have the ability to chelate divalent metals, but binds a wide variety of metals with nonspecificity.[343] Other divalent metal chelators are known such as the inorganic thiomolybdate chelators[344] (which is unamicable for PET isotope labeling) and cuprizone chelators[345] that can inhibit copper-dependent mitochondrial enzymes.

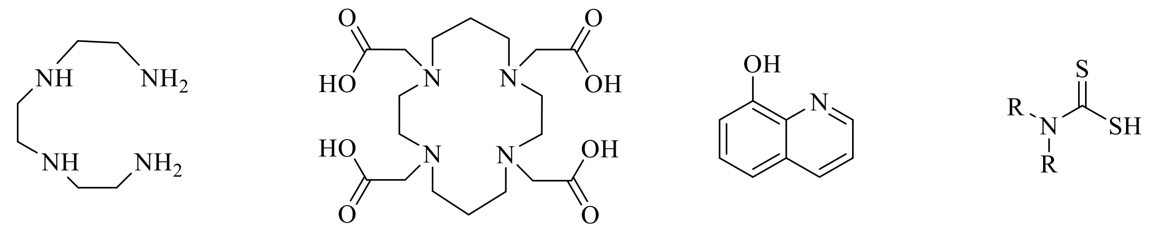

acyclic amino chelator (Trientine) **macrocyclic amino chelator (TETA)** **8-hydroxyquinoline** **dithiolcarbamate**

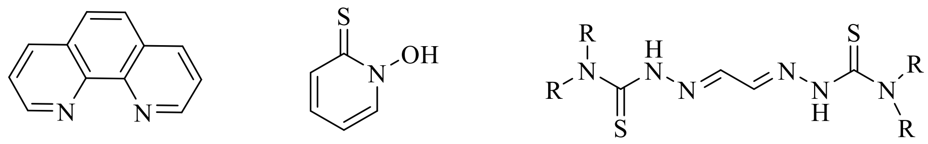

diamine **pyrithione** **thiosemicarbazone**

Fig. 1. 26: Scaffolds of common divalent metal chelators

Chelators containing acyclic amino chelating scaffolds have high affinity for Cu^{2+} but have been observed to compete for copper bound to albumin within the serum with high efficiency.[346] Using this scaffold in a PET tracer, then, would result in an overestimation of accumulating free copper in diseases as albumin copper is not toxic without uncontrolled redox activity. An interesting acyclic amino chelating scaffold with high affinity for Cu^{2+} is TPEN. However, the formation of this complex depends on the stoichiometry, the condition of the complex formation, and the presence of competing ligands.[347,348] With these factors, TPEN is actually very selective for Zn^{2+} in biological systems and is thus, used as specific Zn^{2+} chelators.[349] Macrocyclic amino chelators, such as 1,4,7,10-tetraazacyclododecane-1,4,7,10-tetracetic acid (DOTA) bind Cu^{2+} with even higher affinity and its size prevents itself from forming complexes with protein bound copper. These structures are permeable to cellular membranes. The carboxylic acid moieties, however, might make it challenging to cross the BBB. Linking this chelating scaffold with a peptide that targets an importer to cross the BBB (i.e. linking DOTA to Tf to target TfR) would ensure higher brain uptake.[350]

Hydroxyquinolines have increased lipophilicity over the other scaffolds due to the fused aromatic rings. The more simple hydroxyquinolines do not cross the BBB readily,[351] but with increased lipophilicity by addition of substituents to the aromatic groups helps to overcome this limitation as some hydroxyquinolines have been observed to cross the BBB which will be discussed in the clinical copper/zinc chelators section. Specificity for metal ions with this scaffold can be changed by converting the hydroxy substituent to a primary amine, resulting in an aminoquinoline that preferentially binds Zn^{2+}.[352,353] Diamines, being another aromatic bidentate chelator, includes two nitrogen donor atoms that is also capable of diffusing through the cell membrane. The geometry preferred upon bis-complexation of diamines with Cu^{2+} results in a reduction of the metal ion to a tightly bound Cu^{+} complex.[342] Although this would not be suitable for Cu^{2+}-selective fluorescence imaging, this would be adequate to measure the total free copper in a patient during the acquisition of a PET image. These aromatic groups provide an opportunity for fluorine-18 labeling, which would result in increased lipophilicity and thus enhanced BBB permeability.

The remaining sulfur containing chelators provide a site for carbon-11 methylation at the secondary or tertiary nitrogen atoms. The dithiocarbamate chelator, N,N-diethyl-dithiocarbamate (DDC) has been confirmed to be able to strip metal from metalloenzymes such as copper from Cu,Zn-SOD.[354–356] Derivatization of this scaffold for PET tracer development would thus provide overestimation of free copper ions in biological systems as well. Furthermore, thiosemicarbazones are known to be toxic to hepatocytes.[357,358] This scaffold also binds Cu^{2+} tightly and would lead to slow washout of a PET tracer containing this scaffold as the copper complex formed is not as facile when compared to the hydroxyquinolines and diamine chelating scaffolds.

1.6.2.2. *Clinical Copper/Zinc Chelators*

Divalent metal chelators have been used clinically since it was discovered that copper overload was linked to Wilson's Disease (WD) in 1948.[359,360] The first copper chelator to be used, British anti-Lewisite (BAL),[361] contained a dithiol moiety for donor atoms. Given the vast side effects associated with its use (thiol groups lead to toxicity[362] and is one of the limitations described for the similar chelating scaffolds discussed previously), various other copper chelators gained popularity for WD treatment such as D-penicillamine[363] and trientine.[364] Given the structures of these available treatments, its not readily apparent where PET isotope labeling can be done without modification. This would lead to different pharmacological properties and would need to undergo a long process of validation before human use of a PET analoge could be used in humans.

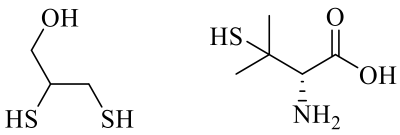

BAL **D-penicillamine**

Fig. 1. 27: FDA approved coper chelators

An antifungal agent was first used in 1964, known as clioquinol,[365] belonging to the class of hydroxyquinolines. It has since been retired from FDA approval, but is still used in clinical trials where it is suspected that copper plays a role in disease. For example, it has been shown to breakup copper-Aß aggregates in animal models by redistributing copper from the extracellular space to intracellular compartments to regain homeostasis.[366] It's derivative, PBT2, has also been used in clinical trials for AD.[367] PET radiolabeling of PBT2 has been achieved by Vasdev *et al.*[368] and will be discussed in Chapter 3. Radiolabeling hydroquinoline scaffolds revealed that increased lipophilicity is needed to cross the BBB.

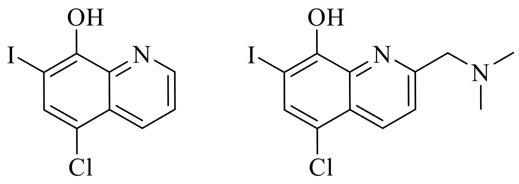

clioquinol **PBT2**

Fig. 1. 28: Cu/Zn chelators used in clinical trials for AD

1.6.2.3. *Investigational Copper/Zinc Chelators*

Although it has been used clinically, development of elesclomol[369] for FDA approval is still being undertaken by Glaxo-Smith-Kline (GSK) in the treatment of cancer. Elesclomol has very high affinity for copper. It is membrane permeable and contains N-methyl groups suitable for caron-11 methylation. Although selectively methylation of nitrogen over sulfur is a synthetic challenge, protecting groups may help to work around this limitation. One might foresee a problem with trapping of this compound into compartments containing copper, as a second chelator is used to help sequester copper from this compound during treatment.

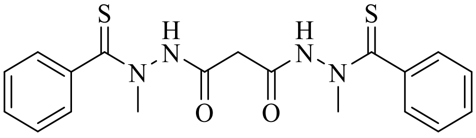

elesclomol

Fig. 1. 29: Structure of Elesclomol

In an attempt to produce divalent metal chelators specific for binding metal-Aß complex aggregates, work was undertaken by Lim *et al.*[370,371] that combined the Aß binding stilbene scaffold with the N,N-diamine chelating scaffold to produce the compound L2-b and its derivatives. The compound showed high selectivity for Cu^{2+} over Zn^{2+}-Aß complexes. It is membrane permeable and was demonstrated to break up Aß aggregates. With an opportunity to label L2-b via carbon-11 and fluorine-18 radiochemistry, work by our group demonstrated that

L2-b can cross the BBB with high brain uptake and was further evaluated in autoradiography studies. The details of these experiments are discussed in Chapter 3.

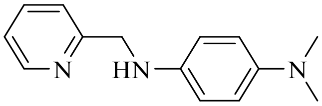

L2-b

Fig. 1. 30: Structure of L2-b

In addition to these compounds, several Zn^{2+} and Cu^{+}/Cu^{2+} specific fluorescent probes have been developed and reviewed elsewhere.[128]

1.7. Measuring Metal Dyshomeostasis with MRI

Iron can be measured by endogenous MRI signal relaxation and has been applied to the clinic to estimate iron levels in a variety of patients including young adults, elderly, stroke patients, and ND patients, whilst copper and zinc measurement by MRI requires the use of a contrast agent and has been limited to preclinical testing. To begin, iron imaging with MRI has proven an asset to connect iron dyshomeostasis to brain aging and development of neurocognitive symptoms.[372] Paramagnetic iron is detected by MRI through the relaxation of neighboring water molecules. A large concentration of iron is needed to induce resonance of this, and thus, all forms of iron can contribute to this signal.[373,374] The majority of an iron MRI signal is thought to be induced by ferritin iron which accounts for > 90% of total iron in the brain. Several methods have been used to estimate iron levels.[375] Due to its paramagnetic nature, iron can have a relatively long transverse relaxation rate (R2) and a short relaxation time constant, T2 (=1/R2).[376] Due to the reliance of water to produce a signal, a region with low water content can diminish the validity of an R2 scan to be a suitable index of iron content.[375] To overcome this issue, R2' (=1/T2') MRI scans have been used which has greater sensitivity, allowing the measurement of iron content by looking at the variation in phase of the signal.[377] This index is more associated with the presence of iron and allows differentiation from diamagnetic calcium, a source of signal in just an R2 scan. By summing the relaxation due to spin-spin interaction (R2) and local susceptibility (R2'), an R2* (=1/T2*) image can be constructed.[162,378] Artificial intensity values can be measured, however, in this method and is sensitive to background field inhomogeneity that is unrelated to iron concentrations. Inherent problems with measuring phase shift and relating this to iron concentration is that detectable shifts is limited by -180 and 180°.[379] Large concentrations of iron that cause a phase shift greater than 180° will "wrap" to the opposite scale extreme and bias against the detection of iron, suggesting the presence of diamagnetic minerals. Myelin can also contribute to the susceptibility of the measurement and confound the results.[372] Field-dependent R2 increase (FDRI) methodology was developed where two images are taken at different field strengths and are believed to be unaffected by myelin.[380,381]

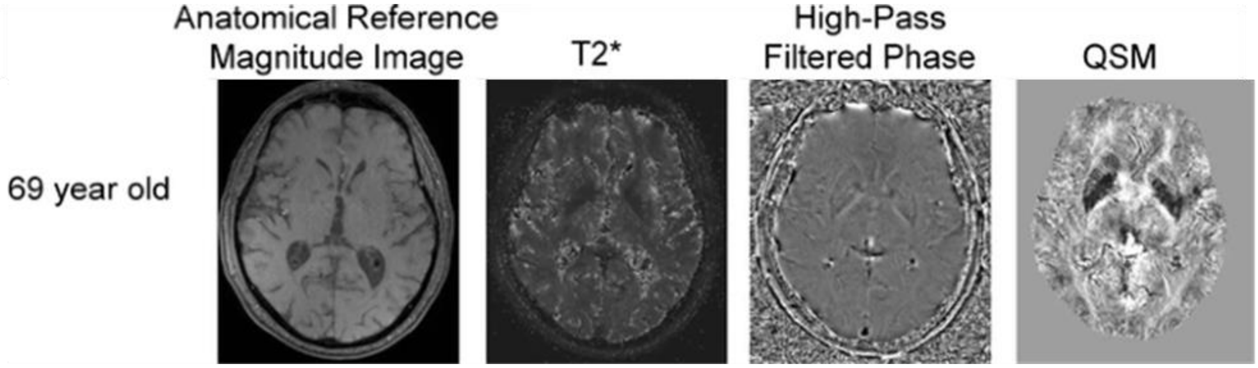

Fig. 1. 31: Example MR images for healthy young, middle-aged, and older adults; a similar mid-brain slice was chosen for each person to showcase the basal ganglia structures that have large concentrations of iron (an arrow points to the globus pallidus, a region with the greatest iron content in the brain across all ages). On T2*-weighted images, iron appears hypointense (dark intensity values). The high-pass filtered phase and quantitative susceptibility mapping (QSM) images were inverted so that iron also corresponds to hypointensity. Adapted from ref. 372 with permission from Springer Nature.

It is clear, so far, that MRI then is unable to quantify absolute concentration of iron, but only approximate differences in the relative iron content.[372] This becomes further problematic when comparing between studies that use the same method of estimation, where regional iron content varies between the studies. There has yet to be a standardized method established for estimating brain iron with MRI and none of them can readily distinguish between heme and nonheme iron. Thus, a method with suitable sensitivity where the signal is directly dependent on the free iron concentration and quantify iron at the nanomolar range *in vivo* is heavily desired. PET offers a suitable alternative then to validate metal dyshomeostasis in CNS diseases.

1.8. Summary

PET is a powerful tool for the clinical setting by aiding in the diagnosis of various diseases. It has shown tremendous success in the diagnosis of cancers and monitoring various therapy agents. PET agents developed for diagnostic purposes in this space have even been used for treatment themselves by incorporating alpha emitting radioisotopes attached to tumor targeting proteins and antibodies. Unfortunately, this success has not extended to the space of NDs. Though PET has aided in identifying ND that have overlapping clinical symptoms, the biomarkers available for ND remain limited to mid-late stage imaging. Protein aggregation and neuroinflammation are the primary targets of PET for ND imaging. It is hypothesized that these biomarkers are a result of metal dyshomeostasis based on evidence of changes in its concentration that has been measured by various methods. MRI has provided a noninvasive way to image the accumulation of iron in patients but has a wide range of limitations. One of these limitations includes that MRI measures all iron and does not differentiate toxic labile iron which is present at very low concentrations. Due to the increased sensitivity of PET, metal chelating PET tracers hold promise in differentiating these diseases at earlier stages than is currently possible. The transition metals Fe, Cu, and Zn are present in the brain at concentrations that are detectable by PET. The increase or decrease in concentrations of these metals during disease progression can then be validated by metal chelating PET tracers *in vivo*, a current field of active research demonstrated by this dissertation. Metal chelators with the most potential for CNS PET imaging are small molecule bidentate chelators that form neutral complexes at physiological pH. Metals are either protein bound or found in labile pools. Protein bound metals are mostly inaccessible to small molecule bidentate chelators, and thus the only target for a PET tracer with this scaffold would be the labile metal pools. Metal chelators specific for Fe^{3+} and Cu^{2+}/Zn^{2+} would be able to differentiate NDs as these metals accumulate in different brain regions during disease progression.

1.9. REFERENCES

1 S. M. Ametamey, M. Honer and P. A. Schubiger, *Chem. Rev.*, 2008, **108**, 1501–1516.

2 M. Conti and L. Eriksson, *EJNMMI Phys.*, , DOI:10.1186/s40658-016-0144-5.

3 R. M. Lambrecht, *Soc. Nucl. Med.*, 1971, 753–766.

4 M. A. Mintun, M. E. Raichle, M. R. Kilbourn, G. F. Wooten and M. J. Welch, *Ann. Neurol.*, 1984, **15**, 217–227.

5 P. Schmor, in *Reviews Of Accelerator Science And Technology*, 2011, pp. 103–116.

6 P. P. Tai, Y. F., *J. Neurol. Neurosurg. Psychiatry*, 2004, **75**, 669–676.

7 V. Pichler, N. Berroteŕan-Infante, C. Philippe, C. Vraka, E. M. Klebermass, T. Balber, S. Pfaff, L. Nics, M. Mitterhauser and W. Wadsak, *J. Nucl. Med.*, 2018, **59**, 1350–1354.

8 M. B. Smith, *Org. Synth.*, 2010, 587–622.

9 H. H. Coenen, A. D. Gee, M. Adam, G. Antoni, C. S. Cutler, Y. Fujibayashi, J. M. Jeong, R. H. Mach, T. L. Mindt, V. W. Pike and A. D. Windhorst, *Nucl. Med. Biol.*, 2017, **55**, v–xi.

10 S. Thompson, M. R. Kilbourn and P. J. H. Scott, *ACS Cent. Sci.*, 2016, **2**, 497–505.

11 *Pract. HPLC Method Dev.*, 1997, 174–232.

12 K. H. Diehl, R. Hull, D. Morton, R. Pfister, Y. Rabemampianina, D. Smith, J. M. Vidal and C. Van De Vorstenbosch, *J. Appl. Toxicol.*, 2001, **21**, 15–23.

13 K. Serdons, A. Verbruggen and G. Bormans, *J. Nucl. Med.*, 2008, **49**, 2071.

14 P. J. H. Scott, *Radiochemical Syntheses: Radiopharmaceuticals for Positron Emission Tomography, Vol. 1*, 2012.

15 Y. Li, D. K. Hamlin, M. K. Chyan, R. Wong, E. F. Dorman, R. C. Emery, D. R. Woodle, R. L. Manger, M. Nartea, A. L. Kenoyer, J. J. Orozco, D. J. Green, O. W. Press, R. Storb, B. M. Sandmaier and D. Scott Wilbur, *PLoS One*, 2018, **13**, 1–17.

16 T. L. Collier, D. L. Yokell, E. Livni, P. A. Rice, S. Celen, K. Serdons, R. Neelamegam, G. Bormans, D. Harris, A. Walji, E. D. Hostetler, I. Bennacef and N. Vasdev, *J. Label. Compd. Radiopharm.*, 2017, **60**, 263–269.

17 A. V. Mossine, S. S. Tanzey, A. F. Brooks, K. J. Makaravage, N. Ichiishi, J. M. Miller, B. D. Henderson, M. B. Skaddan, M. S. Sanford and P. J. H. Scott, *Org. Biomol. Chem.*, 2019, **17**, 8701–8705.

18 A. V. Mossine, S. S. Tanzey, A. F. Brooks, K. J. Makaravage, N. Ichiishi, J. M. Miller, B. D. Henderson, T. Erhard, C. Bruetting, M. B. Skaddan, M. S. Sanford and P. J. H. Scott, *Nat. Protoc.*, , DOI:10.1038/s41596-020-0305-9.

19 A. C. Dupont, B. Largeau, D. Guilloteau, M. J. Santiago Ribeiro and N. Arlicot, *Contrast Media Mol. Imaging*, , DOI:10.1155/2018/7043578.

20 L. Zhang and A. Villalobos, *EJNMMI Radiopharm. Chem.*, 2017, **1**, 1–12.

21 R. B. Innis, V. J. Cunningham, J. Delforge, M. Fujita, A. Gjedde, R. N. Gunn, J. Holden, S. Houle, S. C. Huang, M. Ichise, H. Iida, H. Ito, Y. Kimura, R. A. Koeppe, G. M. Knudsen, J. Knuuti, A. A. Lammertsma, M. Laruelle, J. Logan, R. P. Maguire, M. A. Mintun, E. D. Morris, R. Parsey, J. C. Price, M. Slifstein, V. Sossi, T. Suhara, J. R. Votaw, D. F. Wong and R. E. Carson, *J. Cereb. Blood Flow Metab.*, 2007, **27**, 1533–1539.

22 S. Patel and R. Gibson, *Nucl. Med. Biol.*, 2008, **35**, 805–815.

23 W.-D. Heiss and K. Herholz, *J. Nucl. Med.*, 2006, **47**, 302–12.

24 D. Li, H. Shan, P. Conti and Z. Li, *Am. J. Nucl. Med. Mol. Imaging*, 2012, **2**, 29–32.

25 M. Miyamoto, T. Miyamoto, J. Saitou and T. Sato, *Sleep Med.*, 2020, **68**, 50–56.

26 W. W. Moses, *Nucl. Instruments Methods Phys. Res. Sect. A Accel. Spectrometers, Detect. Assoc. Equip.*, 2011, **648**, S236–S240.

27 M. Banay-Schwartz, A. Kenessey, T. DeGuzman, A. Lajtha and M. Palkovits, *Age (Omaha).*, 1992, **15**, 51–54.

28 A. Marutle, U. Warpman, N. Bogdanovic and A. Nordberg, *Brain Res.*, 1998, **801**, 143–149.

29 W. Sihver, P. G. Gillberg and A. Nordberg, *Neuroscience*, 1998, **85**, 1121–1133.

30 V. W. Pike, *Trends Pharmacol. Sci.*, 2009, **30**, 431–440.

31 V. W. Pike, *Curr. Med. Chem.*, 2016, **23**, 1818–69.

32 S. Przedborski, M. Vila and V. Jackson-Lewis, *J. Clin. Invest.*, 2003, **111**, 3–10.

33 A. Del Sole, S. Malaspina and A. Magenta Biasina, *Funct. Neurol.*, 2016, **31**, 205–215.

34 D. Aarsland, E. Londos and C. Ballard, *Int. Psychogeriatrics*, 2009, **21**, 216.

35 R. S. Desikan, H. J. Cabral, C. P. Hess, W. P. Dillon, C. M. Glastonbury, M. W. Weiner, N. J. Schmansky, D. N. Greve, D. H. Salat, R. L. Buckner and B. Fischl, *Brain*, 2009, **132**, 2048–2057.

36 B. J. Hanseeuw, R. A. Betensky, E. C. Mormino, A. P. Schultz, J. Sepulcre, J. A. Becker, H. I. L. Jacobs, R. F. Buckley, M. R. LaPoint, P. Vannini, N. J. Donovan, J. P. Chhatwal, G. A. Marshall, K. V. Papp, R. E. Amariglio, D. M. Rentz, R. A. Sperling and K. A. Johnson, *Alzheimer's Dement.*, 2018, **14**, 1281–1292.

37 J. P. Holland, S. H. Liang, B. H. Rotstein, T. L. Collier, N. A. Stephenson, I. Greguric and

N. Vasdev, *J. Label. Compd. Radiopharm.*, 2014, **57**, 323–331.

38 V. Narayanaswami, K. Dahl, V. Bernard-Gauthier, L. Josephson, P. Cumming and N. Vasdev, *Mol. Imaging*, 2018, **17**, 1–25.

39 D. J. Selkoe and J. Hardy, *EMBO Mol. Med.*, 2016, **8**, 595–608.

40 H. Braak and E. Braak, *Acta Neuropathol.*, 1991, **82**, 239–259.

41 I. Alafuzoff, T. Arzberger, S. Al-Sarraj, I. Bodi, N. Bogdanovic, H. Braak, O. Bugiani, K. Del-Tredici, I. Ferrer, E. Gelpi, G. Giaccone, M. B. Graeber, P. Ince, W. Kamphorst, A. King, P. Korkolopoulou, G. G. Kovács, S. Larionov, D. Meyronet, C. Monoranu, P. Parchi, E. Patsouris, W. Roggendorf, D. Seilhean, F. Tagliavini, C. Stadelmann, N. Streichenberger, D. R. Thal, S. B. Wharton and H. Kretzschmar, *Brain Pathol.*, 2008, **18**, 484–496.

42 Y. Zhang, R. Thompson, H. Zhang and H. Xu, *Brain*, 2011, 1–13.

43 P. A. Adlard, B. A. Tran, D. I. Finkelstein, P. M. Desmond, L. A. Johnston, A. I. Bush and G. F. Egan, *Front. Neurosci.*, 2014, **8**, 1–23.

44 M. Goedert, *Trends Neurosci.*, 1993, 16, 460–465.

45 N. Ohkubo, Y. D. Lee, A. Morishima, T. Terashima, S. Kikkawa, M. Tohyama, M. Sakanaka, J. Tanaka, N. Maeda, M. P. Vitek and N. Mitsuda, *FASEB J.*, 2003, **17**, 295–297.

46 W. E. Klunk, H. Engler, A. Nordberg, Y. Wang, G. Blomqvist, D. P. Holt, M. Bergström, I. Savitcheva, G.-F. Huang, S. Estrada, B. Ausén, M. L. Debnath, J. Barletta, J. C. Price, J. Sandell, B. J. Lopresti, A. Wall, P. Koivisto, G. Antoni, C. A. Mathis and B. Långström, *Ann. Neurol.*, 2004, **55**, 306–319.

47 N. George, E. Gean, A. Nandi, J. R. Brašić and D. F. Wong, *Radiotracers Used to Image the Brains of Patients with Alzheimer's Disease*, Elsevier, 2014.

48 J. Shin, V. Kepe, J. R. Barrio and G. W. Small, *J. Alzheimer's Dis.*, 2011, **26**, 135–145.

49 O. Sabri, J. Seibyl, C. Rowe and H. Barthel, *Clin. Transl. Imaging*, 2015, **3**, 13–26.

50 A. M. Clarfield, H. Bergman and E. Larson, *Ann. Long-Term Care*, 1999, **7**, 168.

51 V. Camus, P. Payoux, L. Barré, B. Desgranges, T. Voisin, C. Tauber, R. La Joie, M. Tafani, C. Hommet, G. Chételat, K. Mondon, V. de La Sayette, J. P. Cottier, E. Beaufils, M. J. Ribeiro, V. Gissot, E. Vierron, J. Vercouillie, B. Vellas, F. Eustache and D. Guilloteau, *Eur. J. Nucl. Med. Mol. Imaging*, 2012, **39**, 621–631.

52 P. M. Doraiswamy, R. A. Sperling, R. E. Coleman, K. A. Johnson, E. M. Reiman, M. D. Davis, M. Grundman, M. N. Sabbagh, C. H. Sadowsky, A. S. Fleisher, A. Carpenter, C. M. Clark, A. D. Joshi, M. A. Mintun, D. M. Skovronsky and M. J. Pontecorvo, *Neurology*, 2012, **79**, 1636 LP – 1644.

53 L. E. Collij, E. Konijnenberg, J. Reimand, M. ten Kate, A. den Braber, I. L. Alves, M. Zwan, M. Yaqub, D. M. E. van Assema, A. M. Wink, A. A. Lammertsma, P. Scheltens, P. J. Visser, F. Barkhof and B. N. M. van Berckel, *J. Nucl. Med.*, 2019, **60**, 541–547.

54 Z. Cselényi, M. E. Jönhagen, A. Forsberg, C. Halldin, P. Julin, M. Schou, P. Johnström, K.

Varnäs, S. Svensson and L. Farde, *J. Nucl. Med.*, 2012, **53**, 415–424.

55 C. C. Rowe, G. Jones, V. Dore, S. Pejoska, L. Margison, R. S. Mulligan, J. Gordon Chan, K. Young and V. L. Villemagne, *J. Nucl. Med.*, 2016, **57**, 1233–1237.

56 M. T. Fodero-Tavoletti, C. C. Rowe, C. A. McLean, L. Leone, Q. X. Li, C. L. Masters, R. Cappai and V. L. Villemagne, *J. Nucl. Med.*, 2009, **50**, 198–204.

57 C. A. McLean, R. A. Cherny, F. W. Fraser, S. J. Fuller, M. J. Smith, K. Beyreuther, A. I. Bush and C. L. Masters, *Ann. Neurol.*, 1999, **46**, 860–866.

58 M. E. Larson and S. E. Lesné, *J. Neurochem.*, 2012, **120**, 125–139.

59 D. Sehlin, X. T. Fang, L. Cato, G. Antoni, L. Lannfelt and S. Syvänen, *Nat. Commun.*, 2016, **7**, 1–11.

60 M. T. Fodero-Tavoletti, D. Brockschnieder, V. L. Villemagne, L. Martin, A. R. Connor, A. Thiele, M. Berndt, C. A. McLean, S. Krause, C. C. Rowe, C. L. Masters, L. Dinkelborg, T. Dyrks and R. Cappai, *Nucl. Med. Biol.*, 2012, **39**, 1042–1048.

61 G. Luurtsema, R. C. Schuit, K. Takkenkamp, M. Lubberink, N. H. Hendrikse, A. D. Windhorst, C. F. M. Molthoff, N. Tolboom, B. N. M. van Berckel and A. A. Lammertsma, *Nucl. Med. Biol.*, 2008, **35**, 869–874.

62 A. Leuzy, K. Chiotis, L. Lemoine, P. G. Gillberg, O. Almkvist, E. Rodriguez-Vieitez and A. Nordberg, *Mol. Psychiatry*, 2019, 1112–1134.

63 L. Lemoine, A. Leuzy, K. Chiotis, E. Rodriguez-Vieitez and A. Nordberg, *Alzheimer's Dement. Diagnosis, Assess. Dis. Monit.*, 2018, **10**, 232–236.

64 L. R. Drake, J. M. Pham, T. J. Desmond, A. V. Mossine, S. J. Lee, M. R. Kilbourn, R. A. Koeppe, A. F. Brooks and P. J. H. Scott, *ACS Chem. Neurosci.*, 2019, **10**, 3839–3846.

65 C. Aguero, M. Dhaynaut, M. D. Normandin, A. C. Amaral, N. J. Guehl, R. Neelamegam, M. Marquie, K. A. Johnson, G. El Fakhri, M. P. Frosch and T. Gomez-Isla, *Acta Neuropathol. Commun.*, 2019, **7**, 37.

66 A. Bellucci, M. Zaltieri, L. Navarria, J. Grigoletto, C. Missale and P. Spano, *Brain Res.*, 2012, **1476**, 183–202.

67 H. Braak, K. Del Tredici, H. Bratzke, J. Hamm-Clement, D. Sandmann-Keil and U. Rüb, *J. Neurol.*, 2002, **249**, 1–1.

68 Z. A. Sorrentino, M. S. Goodwin, C. J. Riffe, J. S. Dhillon, Y. Xia, K. Gorion, N. Vijayaraghavan, K. N. Mcfarland, L. I. Golbe, A. T. Yachnis and B. I. Giasson, 2019, **2**, 1–22.

69 S. Sveinbjornsdottir, *J. Neurochem.*, 2016, 318–324.

70 D. J. Brooks, *Ageing Res. Rev.*, 2016, **30**, 114–121.

71 T. Brücke, S. Asenbaum, W. Pirker, S. Djamshidian, S. Wenger, C. Wöber, C. Müller and I. Podreka, 1997, pp. 9–24.

72 M. Hadjiconstantinou and N. H. Neff, *CNS Neurosci. Ther.*, 2008, **14**, 340–351.

73 M. Pretze, C. Wängler and B. Wängler, *Biomed Res. Int.*, 2014, **2014**, 1–12.

74 P. K. Alexander, Y. Lie, G. Jones, C. Sivaratnam, S. Bozinvski, R. S. Mulligan, K. Young, V. L. Villemagne and C. C. Rowe, *J. Nucl. Med.*, 2017, **58**, 1815–1820.

75 W. C. Drevets, E. Frank, J. C. Price, D. J. Kupfer, D. Holt, P. J. Greer, Y. Huang, C. Gautier and C. Mathis, *Biol. Psychiatry*, 1999, **46**, 1375–1387.

76 D. Martinez, M. Slifstein, R. Gil, D. Hwang, Y. Huang, A. Perez, W. G. Frankle, M. Laruelle, J. Krystal and A. Abi-dargham, *Biol. Psychiatry*, 2010, **65**, 175–180.

77 A. Vuorimaa, E. Rissanen and L. Airas, *Contrast Media Mol. Imaging*, , DOI:10.1155/2017/6975841.

78 A. Currais, W. Fischer, P. Maher and D. Schubert, *FASEB J.*, 2017, **31**, 5–10.

79 L. Guzman-Martinez, R. B. Maccioni, V. Andrade, L. P. Navarrete, M. G. Pastor and N. Ramos-Escobar, *Front. Pharmacol.*, 2019, **10**, 1–17.

80 A. Waisman, R. S. Liblau and B. Becher, *Lancet Neurol.*, 2015, **14**, 945–955.

81 M. A. Meraz-Ríos, D. Toral-Rios, D. Franco-Bocanegra, J. Villeda-Hernández and V. Campos-Peña, *Front. Integr. Neurosci.*, 2013, **7**, 1–15.

82 E. L. Werry, F. M. Bright, O. Piguet, L. M. Ittner, G. M. Halliday, J. R. Hodges, M. C. Kiernan, C. T. Loy, J. J. Kril and M. Kassiou, *Int. J. Mol. Sci.*, 2019, **20**, 1–21.

83 S. H. Choi, S. Aid and F. Bosetti, *Trends Pharmacol. Sci.*, 2009, **30**, 174–181.

84 J. Saura, J. M. Luque, A. M. Cesura, G. Huber, M. Da Prada, V. Chan-Palay, J. Loffler and J. . Richards, 1994, **62**, 15–30.

85 D. W. Maixner and H.-R. Weng, *J. Pharm. Pharmacol.*, 2013, **1**, 001.

86 L. M. Bekris, M. Khrestian, E. Dyne, Y. Shao, J. A. Pillai, S. M. Rao, S. M. Bemiller, B. Lamb, H. H. Fernandez and J. B. Leverenz, *J. Neuroimmunol.*, 2018, **319**, 19–27.

87 F. Fang, L.-F. Lue, S. Yan, H. Xu, J. S. Luddy, D. Chen, D. G. Walker, D. M. Stern, S. Yan, A. M. Schmidt, J. X. Chen and S. S. Yan, *FASEB J.*, 2010, **24**, 1043–1055.

88 M. R. P. Elmore, A. R. Najafi, M. A. Koike, N. N. Dagher, E. E. Spangenberg, R. A. Rice, M. Kitazawa, B. Matusow, H. Nguyen, B. L. West and K. N. Green, *Neuron*, 2014, **82**, 380–397.

89 E. Beamer, F. Gölöncsér, G. Horváth, K. Beko, L. Otrokocsi, B. Koványi and B. Sperlágh, *Neuropharmacology*, 2016, **104**, 94–104.

90 K. D. McCarthy and T. K. Harden, *J. Pharmacol. Exp. Ther.*, 1981, **216**, 183–191.

91 Y. Itzhak, L. Baker and M. D. Norenberg, *Glia*, 1993, **9**, 211–218.

92 L. A. Karchewski, S. Bloechlinger and C. J. Woolf, *Eur. J. Neurosci.*, 2004, **20**, 671–683.

93 D. R. Owen, A. J. Yeo, R. N. Gunn, K. Song, G. Wadsworth, A. Lewis, C. Rhodes, D. J. Pulford, I. Bennacef, C. A. Parker, P. L. Stjean, L. R. Cardon, V. E. Mooser, P. M. Matthews, E. A. Rabiner and J. P. Rubio, *J. Cereb. Blood Flow Metab.*, 2012, **32**, 1–5.

94 B. Ji, K. Kumata, H. Onoe, H. Kaneko, M. R. Zhang, C. Seki, M. Ono, M. Shukuri, M. Tokunaga, T. Minamihisamatsu, T. Suhara and M. Higuchi, *Brain Res.*, 2013, **1533**, 152–162.

95 S. F. Carter, M. Schöll, O. Almkvist, A. Wall, H. Engler, B. Långström and A. Nordberg, *J. Nucl. Med.*, 2012, **53**, 37–46.

96 B. Janssen, D. J. Vugts, S. M. Wilkinson, D. Ory, S. Chalon, J. J. M. Hoozemans, R. C. Schuit, W. Beaino, E. J. M. Kooijman, J. Van Den Hoek, M. Chishty, A. Doméné, A. Van Der Perren, A. Villa, A. Maggi, G. T. Molenaar, U. Funke, R. V. Shevchenko, V. Baekelandt, G. Bormans, A. A. Lammertsma, M. Kassiou and A. D. Windhorst, *Sci. Rep.*, 2018, **8**, 1–10.

97 B. Janssen, D. J. Vugts and G. T. Molenaar, *EJNMMI Radiopharm. Chem.*

98 B. P. Cary, A. F. Brooks, M. V. Fawaz, L. R. Drake, T. J. Desmond, P. Sherman, C. A. Quesada and P. J. H. Scott, *ACS Chem. Neurosci.*, 2016, **7**, 391–398.

99 A. I. Bush and R. E. Tanzi, *Neurotherapeutics*, 2008, **5**, 421–432.

100 H. W. Kwon, A. K. Becker, J. M. Goo and G. J. Cheon, *Nucl. Med. Mol. Imaging (2010).*, 2017, **51**, 22–31.

101 B. Foster, U. Bagci, A. Mansoor, Z. Xu and D. J. Mollura, *Comput. Biol. Med.*, 2014, **50**, 76–96.

102 H. J. Harms, S. de Haan, P. Knaapen, C. P. Allaart, M. T. Rijnierse, R. C. Schuit, A. D. Windhorst, A. A. Lammertsma, M. C. Huisman and M. Lubberink, in *Mathematics and Physics of Emerging Biomedical Imaging*, National Academy of Sciences, Washington, D.C., 1996, p. 260.

103 E. J. New, *Dalt. Trans.*, 2013, **42**, 3210–3219.

104 R. Crichton, in *Inorganic Biochemistry of Iron Metabolism: From Molecular Mechanisms to Clinical Consequences*, ed. R. Crichton, John Wiley & Sons, Ltd, Chichester, UK, 2nd edn., 2009, vol. 1, pp. 223–269.

105 R. Crichton, in *Inorganic Biochemistry of Iron Metabolism: From Molecular Mechanisms to Clinical Consequences*, 2001, vol. 1, pp. 133–169.

106 L. Pauling and C. D. Coryell, *Proc. Natl. Acad. Sci.*, 1936, **22**, 210–216.

107 E. A. Dertz and K. N. Raymond, *Compr. Coord. Chem. II*, 2004, **8**, 141–168.

108 Iron Transport and Cellular Uptake, https://sickle.bwh.harvard.edu/iron_transport.html.

109 P. Brissot, M. Ropert, C. Le Lan and O. Loréal, *Biochim. Biophys. Acta - Gen. Subj.*, 2012, **1820**, 403–410.

110 N. V. Bhagavan and C.-E. Ha, *Essentials Med. Biochem.*, 2015, 511–529.

111 R. Casiday and R. Frey, Iron Use and Storage in the Body: Ferritin and Molecular Representations, http://www.chemistry.wustl.edu/~edudev/LabTutorials/Ferritin/Ferritin.html.

112 R. Crichton, in *Inorganic Biochemistry of Iron Metabolism: From Molecular Mechanisms to Clinical Consequences*, John Wiley & Sons Ltd., 2nd edn., 2001, vol. 1.

113 J. P. Laulhère, F. Barcelò and M. Fontecave, *BioMetals*, 1996, **9**, 303–309.

114 R. C. Hider, 2002, **32**, 50–54.

115 R. W. Evans, R. Rafique, A. Zarea, C. Rapisarda, R. Cammack, P. J. Evans, J. B. Porter and R. C. Hider, *J. Biol. Inorg. Chem.*, 2008, **13**, 57–74.

116 M. Hadzhieva, E. Kirches and C. Mawrin, *Neuropathol. Appl. Neurobiol.*, 2014, **40**, 240–257.

117 Z. I. Cabantchik, *Front. Pharmacol.*, 2014, **5 MAR**, 1–11.

118 O. Kakhlon and Z. I. Cabantchik, *Free Radic. Biol. Med.*, 2002, **33**, 1037–1046.

119 A. K. Powell, in *Comprehensive Coordination Chemistry II*, eds. J. L Que and W. B. Tolman, Elsevier Ltd, 2nd edn., 2002, pp. 169–194.

120 I. Yanatori, D. Richardson, S. Toyokuni and F. Kishi, *Biochim. Biophys. Acta - Gen. Subj.*, 2020, **1864**, 129685.

121 L. Banci, I. Bertini, S. Ciofi-Baffoni, T. Kozyreva, K. Zovo and P. Palumaa, *Nature*, 2010, **465**, 645–648.

122 G. C. Ferreira, R. Franco, S. G. Lloyd, I. Moura, J. J. G. Moura and B. H. Huynh, *J. Bioenerg. Biomembr.*, 1995, **27**, 221–229.

123 I. H. Castro, M. F. Pignataro, K. E. Sewell, L. D. Espeche, M. G. Herrera, M. E. Noguera, L. Dain, A. D. Nadra, M. Aran, C. Smal, M. Gallo and J. Santos, eds. J. R. Harris and J. Marles-Wright, Springer International Publishing, Cham, 2019, pp. 393–438.

124 E. Herrero and M. A. De La Torre-Ruiz, *Cell. Mol. Life Sci.*, 2007, **64**, 1518–1530.

125 A. G. Frey, D. J. Palenchar, J. D. Wildemann and C. C. Philpott, *J. Biol. Chem.*, 2016, **291**, 22344–22356.

126 J. Que and W. B. Tolman, *Compr. Coord. Chem. II*, 2004, **8**, 1–15.

127 S. Pereira, University of Liverpool, 2015.

128 E. L. Que, D. W. Domaille and C. J. Chang, *Chem. Rev.*, 2008, **108**, 1517–1549.

129 M. Perls, *Virchows Arch. Pathol. Anat. Physiol. Klin. Med.*, 1867, **39**, 42.

130 H. Spatz, *Zeitschrift für die gesamte Neurol. und Psychiatr.*, 1922, **77**, 261–390.

131 Y. Ma, V. Abbate and R. C. Hider, *Metallomics*, 2015, **7**, 212–222.

132 S. K. Sahoo and G. Crisponi, *Molecules*, , DOI:10.3390/molecules24183267.

133 P. Dusek, M. Dezortova and J. Wuerfel, *Imaging of Iron*, Elsevier Inc., 1st edn., 2013, vol. 110.

134 J. Galazka-Friedman, E. R. Bauminger, K. Szlachta and A. Friedman, *J. Phys. Condens. Matter*, , DOI:10.1088/0953-8984/24/24/244106.

135 H. Sun, H. Li and P. J. Sadler, *Chem. Rev.*, 1999, **99**, 2817–2842.

136 K. K. Shattnawi, M. Alomari, N. Al-Sheyab and A. Bani Salameh, *Sci. Rep.*, 2018, **8**, 2–7.

137 W. Breuer, A. Ronson, I. N. Slotki, A. Abramov, C. Hershko and Z. I. Cabantchik, *Blood*, 2000, **95**, 2975–2982.

138 W. Breuer, M. J. J. Ermers, P. Pootrakul, A. Abramov, C. Hershko and Z. I. Cabantchik, *Blood*, 2001, **97**, 792–798.

139 M. W. Garbowski, Y. Ma, S. Fucharoen, S. Srichairatanakool, R. Hider and J. B. Porter, *Transl. Res.*, 2016, **177**, 19-30.e5.

140 D. Yang, X. Q. Ng and T. Walczyk, *J. Anal. At. Spectrom.*, 2019, **34**, 1988–1997.

141 E. D. Morris, C. J. Endres, K. C. Schmidt, B. T. Christian, R. F. Muzic and R. E. Fisher, *Emiss. Tomogr. Fundam. PET SPECT*, 2004, 499–540.

142 M. Villien, H. Y. Wey, J. B. Mandeville, C. Catana, J. R. Polimeni, C. Y. Sander, N. R. Zürcher, D. B. Chonde, J. S. Fowler, B. R. Rosen and J. M. Hooker, *Neuroimage*, 2014, **100**, 192–199.

143 Y. Deugnier, S. Margules, P. Brissot, J. C. Bisconte, M. Bourel and B. Ferrand, *J. Clin. Pathol.*, 1982, **35**, 45–51.

144 D. Hernando, Y. S. Levin, C. B. Sirlin and S. B. Reeder, *J. Magn. Reson. Imaging*, 2014, **40**, 1003–1021.

145 E. Hitti, P. A. Eliat, E. Abgueguen, M. Ropert, P. Leroyer, P. Brissot, Y. Gandon, H. Saint-Jalmes and O. Loréal, *J. Magn. Reson. Imaging*, 2010, **32**, 639–646.

146 J. P. Carpenter, T. He, P. Kirk, M. Roughton, L. J. Anderson, S. V. De Noronha, M. N. Sheppard, J. B. Porter, J. M. Walker, J. C. Wood, R. Galanello, G. Forni, G. Catani, G. Matta, S. Fucharoen, A. Fleming, M. J. House, G. Black, D. N. Firmin, T. G. St. Pierre and D. J. Pennell, *Circulation*, 2011, **123**, 1519–1528.

147 R. R. Crichton, D. T. Dexter and R. J. Ward, *Coord. Chem. Rev.*, 2008, **252**, 1189–1199.

148 M. E. GÖTZ, K. DOUBLE, M. GERLACH, M. B. H. YOUDIM and P. RIEDERERE, *Ann. N. Y. Acad. Sci.*, 2004, **1012**, 193–208.

149 M. Krijt, A. Jirkovska, T. Kabickova, V. Melenovsky, J. Petrak and D. Vyoral, *Biochim. Biophys. Acta - Gen. Subj.*, 2018, **1862**, 2895–2901.

150 Y. Ma, H. De Groot, Z. Liu, R. C. Hider and F. Petrat, *Biochem. J.*, 2006, **395**, 49–55.

151 S. Epsztejn, O. Kakhlon, H. Glickstein, W. Breuer and Z. I. Cabantchik, *Anal. Biochem.*, 1997, **248**, 31–40.

152 A. Fiedler, T. Reinert, M. Morawski, G. Brückner, T. Arendt and T. Butz, *Nucl. Instruments Methods Phys. Res. Sect. B Beam Interact. with Mater. Atoms*, 2007, **260**, 153–158.

153 Z. Aydin, *Dr. Diss.*, , DOI:10.1016/0003-2697(67)90113-3.

154 H. J. H. Fenton, *J. Chem. Soc., Trans.*, 1894, **65**, 899–910.

155 E. C. Friedberg, G. C. Walker and W. Siede, *DNA repair and mutagenesis*, ASM Press, Washington, D.C. :, 1995.

156 N. Gregersen and P. Bross, in *Methods in Molecular Biology*, 2010, vol. 648, pp. 3–23.

157 D. J. Hare and K. L. Double, *Brain*, 2016, **139**, 1026–1035.

158 J. R. Connor, S. L. Menzies, S. M. St. Martin and E. J. Mufson, *J. Neurosci. Res.*, 1992, **31**, 75–83.

159 E. R. Bauminger, M. Barcikowska, A. Friedman, J. Galazka-Friedman, D. Hechel and I. Nowik, *Hyperfine Interact.*, 1994, **91**, 853–857.

160 J. Gałązka-Friedman, E. R. Bauminger, K. Szlachta, D. Koziorowski, R. Tomasiuk, A. Jaklewicz, Z. K. Wszołek, D. Dickson, K. Kaplińska and A. Friedman, *Acta Phys. Pol. A*, 2011, **119**, 81–83.

161 Z. Luo, X. Zhuang, D. Kumar, X. Wu, C. Yue, C. Han and J. Lv, *PLoS One*, 2013, **8**, 3–9.

162 A. Daugherty and N. Raz, *Neuroimage*, 2013, **70**, 113–121.

163 X. Huang, C. S. Atwood, R. D. Moir, M. A. Hartshorn, R. E. Tanzi and A. I. Bush, *J. Biol. Inorg. Chem.*, 2004, **9**, 954–960.

164 S. O. Dahms, I. Könnig, D. Roeser, K. H. Gührs, M. C. Mayer, D. Kaden, G. Multhaup and M. E. Than, *J. Mol. Biol.*, 2012, **416**, 438–452.

165 J. T. Rogers, A. I. Bush, H. H. Cho, D. H. Smith, A. M. Thomson, A. L. Friedrlich, D. K. Lahiri, P. J. Leedman, X. Huang and C. M. Cahill, *Biochem. Soc. Trans.*, 2008, **36**, 1282–1287.

166 J. A. Duce, A. Tsatsanis, M. A. Cater, S. A. James, E. Robb, K. Wikhe, S. L. Leong, K. Perez, T. Johanssen, M. A. Greenough, H.-H. Cho, D. Galatis, R. D. Moir, C. L. Masters, C. McLean, R. E. Tanzi, R. Cappai, K. J. Barnham, G. D. Ciccotosto, J. T. Rogers and A. I. Bush, *Cell*, 2010, **142**, 857–867.

167 D. J. Piñero, J. Hu and J. R. Connor, *Cell. Mol. Biol. (Noisy-le-grand).*, 2000, **46**, 761–776.

168 B. P. Cary, A. F. Brooks, M. V Fawaz, X. Shao, T. J. Desmond, G. M. Carpenter, P. Sherman, C. A. Quesada, R. L. Albin and P. J. H. Scott, *ACS Med. Chem. Lett.*, 2015, **6**, 112–116.

169 H. Braak, K. Del Tredici, U. Rüb, R. A. . de Vos, E. N. . Jansen Steur and E. Braak, *Neurobiol. Aging*, 2003, **24**, 197–211.

170 J. Meireles and J. Massano, *Front. Neurol.*, 2012, **MAY**, 1–15.

171 K. M. Earle, *J. Neuropathol. Exp. Neurol.*, 1968, **27**, 1–14.

172 E. Sofic, P. Riederer, H. Heinsen, H. Beckmann, G. P. Reynolds, G. Hebenstreit and M. B. H. Youdim, *J. Neural Transm.*, 1988, **74**, 199–205.

173 P. Riederer, E. Sofic, W. -D Rausch, B. Schmidt, G. P. Reynolds, K. Jellinger and M. B. H. Youdim, *J. Neurochem.*, 1989, **52**, 515–520.

174 D. A. Loeffler, J. R. Connor, P. L. Juneau, B. S. Snyder, L. Kanaley, A. J. DeMaggio, H. Nguyen, C. M. Brickman and P. A. LeWitt, *J. Neurochem.*, 1995, **65**, 710–716.

175 J. Gałązka-Friedman, E. R. Bauminger, A. Friedman, M. Barcikowska, D. Hechel and I. Nowik, *Mov. Disord.*, 1996, **11**, 8–16.

176 P. D. Griffiths, B. R. Dobson, G. R. Jones and D. T. Clarke, *Brain*, 1999, **122**, 667–673.

177 A. Wypijewska, J. Galazka-Friedman, E. R. Bauminger, Z. K. Wszolek, K. J. Schweitzer, D. W. Dickson, A. Jaklewicz, D. Elbaum and A. Friedman, *Park. Relat. Disord.*, 2010, **16**, 329–333.

178 J. Y. Wang, Q. Q. Zhuang, L. B. Zhu, H. Zhu, T. Li, R. Li, S. F. Chen, C. P. Huang, X. Zhang and J. H. Zhu, *Sci. Rep.*, 2016, **6**, 1–13.

179 T. L. Perry and V. W. Yong, *Neurosci. Lett.*, 1986, **67**, 269–274.

180 P. F. Good, C. W. Olanow and D. P. Perl, *Brain Res.*, 1992, **593**, 343–346.

181 L. Zecca, M. Gallorini, V. Schünemann, A. X. Trautwein, M. Gerlach, P. Riederer, P. Vezzoni and D. Tampellini, *J. Neurochem.*, 2001, **76**, 1766–1773.

182 D. Ben-Shachar, P. Riederer and M. B. H. Youdim, *J. Neurochem.*, 1991, **57**, 1609–1614.

183 P. D. Griffiths and A. R. Crossman, *Neurosci. Lett.*, 1996, **211**, 53–56.

184 J. Salazar, N. Mena, S. Hunot, A. Prigent, D. Alvarez-Fischer, M. Arredondo, C. Duyckaerts, V. Sazdovitch, L. Zhao, L. M. Garrick, M. T. Nuñez, M. D. Garrick, R. Raisman-Vozari and E. C. Hirsch, *Proc. Natl. Acad. Sci. U. S. A.*, 2008, **105**, 18578–18583.

185 B. Wolozin and N. Golts, *Neurosci. a Rev. J. bringing Neurobiol. Neurol. psychiatry*, 2002, **8**, 22–32.

186 S. Vucic, J. D. Rothstein and M. C. Kiernan, *Trends Neurosci.*, 2014, **37**, 433–442.

187 K. Okamoto, Y. Mizuno and Y. Fujita, *Neuropathology*, 2008, **28**, 109–115.

188 Y. Mizuno, M. Amari, M. Takatama, H. Aizawa, B. Mihara and K. Okamoto, *Acta Neuropathol.*, 2006, **112**, 597–603.

189 M. Neumann, D. M. Sampathu, L. K. Kwong, A. C. Truax, M. C. Micsenyi, T. T. Chou, J. Bruce, T. Schuck, M. Grossman, C. M. Clark, L. F. McCluskey, B. L. Miller, E. Masliah, I. R. Mackenzie, H. Feldman, W. Feiden, H. A. Kretzschmar, J. Q. Trojanowski and V. M.-Y. Lee, *Science (80-.).*, 2006, **314**, 130–133.

190 D. R. Rosen, T. Siddique, D. Patterson, D. A. Figlewicz, P. Sapp, A. Hentati, D. Donaldson,

J. Goto, J. P. O’Regan, H.-X. Deng, Z. Rahmani, A. Krizus, D. McKenna-Yasek, A. Cayabyab, S. M. Gaston, R. Berger, R. E. Tanzi, J. J. Halperin, B. Herzfeldt, R. Van den Bergh, W.-Y. Hung, T. Bird, G. Deng, D. W. Mulder, C. Smyth, N. G. Laing, E. Soriano, M. A. Pericak–Vance, J. Haines, G. A. Rouleau, J. S. Gusella, H. R. Horvitz and R. H. Brown, *Nature*, 1993, **362**, 59–62.

191 M. Yasui, K. Ota and R. M. Garruto, *Neurotoxicology*, 1993, **14**, 445–450.

192 P. G. Ince, P. J. Shaw, J. M. Candy, D. Mantle, L. Tandon, W. D. Ehmann and W. R. Markesbery, *Neurosci. Lett.*, 1994, **182**, 87–90.

193 E. J. Kasarskis, L. Tandon, M. A. Lovell and W. D. Ehmann, *J. Neurol. Sci.*, 1995, **130**, 203–208.

194 K. Gellein, R. M. Garruto, T. Syversen, T. E. Sjøbakk and T. P. Flaten, *Biol. Trace Elem. Res.*, 2003, **96**, 39–60.

195 Y. Imon, S. Yamaguchi, Y. Yamamura, S. Tsuji, T. Kajima, K. Ito and S. Nakamura, *J. Neurol. Sci.*, 1995, **134**, 27–32.

196 J. Y. Kwan, S. Y. Jeong, P. van Gelderen, H. X. Deng, M. M. Quezado, L. E. Danielian, J. A. Butman, L. Chen, E. Bayat, J. Russell, T. Siddique, J. H. Duyn, T. A. Rouault and M. K. Floeter, *PLoS One*, , DOI:10.1371/journal.pone.0035241.

197 A. Ignjatović, Z. Stević, S. Lavrnić, M. Daković and G. Bačić, *J. Magn. Reson. Imaging*, 2013, **38**, 1472–1479.

198 E. F. Goodall, M. S. Haque and K. E. Morrison, *J. Neurol.*, 2008, **255**, 1652–1656.

199 Y. Nadjar, P. Gordon, P. Corcia, G. Bensimon, L. Pieroni, V. Meininger and F. Salachas, *PLoS One*, 2012, **7**, 2–7.

200 Q. Wang, X. Zhang, S. Chen, X. Zhang, S. Zhang, M. Youdium and W. Le, *Neurodegener. Dis.*, 2011, **8**, 310–321.

201 M. Hadzhieva, E. Kirches, A. Wilisch-Neumann, D. Pachow, M. Wallesch, P. Schoenfeld, I. Paege, S. Vielhaber, S. Petri, G. Keilhoff and C. Mawrin, *Neuroscience*, 2013, **230**, 94–101.

202 B. J. Turner and K. Talbot, *Prog. Neurobiol.*, 2008, **85**, 94–134.

203 M. C. Linder, ed. M. C. Linder, Springer US, Boston, MA, 1991, pp. 73–134.

204 M. C. Linder and M. Hazegh-Azam, *Am. J. Clin. Nutr.*, 1996, **63**, 797S-811S.

205 Y. Lu, *Compr. Coord. Chem. II*, 2004, **8**, 91–122.

206 C. W. Kellett, W. B. Swords, M. D. Turlington, G. J. Meyer and C. P. Berlinguette, *Nat. Commun.*, , DOI:10.1038/s41467-018-07263-1.

207 C. G. HOLMBERG and C. B. LAURELL, *Acta Chem. Scand.*, 1947, **1**, 944–950.

208 I. Bento, C. Peixoto, V. N. Zaitsev and P. F. Lindley, *Acta Crystallogr. Sect. D Biol. Crystallogr.*, 2007, **63**, 240–248.

209 S. J. Lau and B. Sarkar, *Biochem. J.*, 1981, **199**, 649–656.

210 B. Sarkar, .

211 M. C. Linder and C. A. Goode, *FASEB J.*, 1988, **2**, Abstract 6538.

212 D. Prince, G. Morgan and S. H. Jones, **137**, 129–137.

213 P. M. May, P. W. Linder and D. R. Williams, *J. Chem. Soc.*, 1977, **2**, 588–595.

214 J. Lee, M. M. O. Peña, Y. Nose and D. J. Thiele, *J. Biol. Chem.*, 2002, **277**, 4380–4387.

215 L. Banci, I. Bertini, K. S. McGreevy and A. Rosato, *Nat. Prod. Rep.*, 2010, **27**, 695–710.

216 M. L. Schlief and J. D. Gitlin, *Mol. Neurobiol.*, 2006, **33**, 81–90.

217 A. C. Rosenzweig, *Acc. Chem. Res.*, 2001, **34**, 119–128.

218 S. J. Lin and V. C. Culotta, *Proc. Natl. Acad. Sci. U. S. A.*, 1995, **92**, 3784–3788.

219 D. Moira Glerum, A. Shtanko and A. Tzagoloff, *J. Biol. Chem.*, 1996, **271**, 14504–14509.

220 D. E. Hartter and A. Barnea, *Synapse*, 1988, **2**, 412–415.

221 J. Kardos, I. Kovács, F. Hajós, M. Kálmán and M. Simonyi, *Neurosci. Lett.*, 1989, **103**, 139–144.

222 M. Sato, K. Ohtomo, T. Daimon, T. Sugiyama and K. Iijima, *J. Histochem. Cytochem.*, 1994, **42**, 1585–1591.

223 J. Stöckel, J. Safar, A. C. Wallace, F. E. Cohen and S. B. Prusiner, *Biochemistry*, 1998, **37**, 7185–7193.

224 K. M. Davies, D. J. Hare, V. Cottam, N. Chen, L. Hilgers, G. Halliday, J. F. B. Mercer and K. L. Double, *Metallomics*, 2013, **5**, 43–51.

225 R. Giampietro, F. Spinelli, M. Contino and N. A. Colabufo, *Mol. Pharm.*, 2018, **15**, 808–820.

226 M. Manto, *Toxics*, 2014, **2**, 327–345.

227 C. L. GREEN, *Am. J. Pathol.*, **31**, 545–53.

228 L. L. UZMAN, *Lab. Invest.*, 1956, **5**, 299–305.

229 J. S. HOWELL, *J. Pathol. Bacteriol.*, 1959, **77**, 473–484.

230 W. F. MCNARY, *J. Histochem. Cytochem.*, 1960, **8**, 124–130.

231 P. Sipponen, *Scand. J. Gastroenterol.*, 1976, **11**, 545–552.

232 T. Shikata, T. Uzawa, N. Yoshiwara, T. Akatsuka and S. Yamazaki, *Jpn. J. Exp. Med.*, 1974, **44**, 25–36.

233 G. Frederick Smith and D. H. Wilkins, *Anal. Chem.*, 1953, **25**, 510–511.

234 F. TIMM, *Z. Zellforch. Microsk. Anat. Histochem.*, 1961, **2**, 332–341.

235 E. L. Que and C. J. Chang, *J. Am. Chem. Soc.*, 2006, **128**, 15942–15943.

236 R. Squitti and R. Polimanti, *Am. J. Neurodegener. Dis.*, 2013, **2**, 46–56.

237 D. R. Brown, K. Qin, J. W. Herms, A. Madlung, J. Manson, R. Strome, P. E. Fraser, T. Kruck, A. Von Bohlen, W. Schulz-Schaeffer, A. Giese, D. Westaway and H. Kretzschmar, *Nature*, 1997, **390**, 684–687.

238 V. Nischwitz, A. Berthele and B. Michalke, *Anal. Chim. Acta*, 2008, **627**, 258–269.

239 L. Zecca, A. Stroppolo, A. Gatti, D. Tampellini, M. Toscani, M. Gallorini, G. Giaveri, P. Arosio, P. Santambrogio, R. G. Fariello, E. Karatekin, M. H. Kleinman, N. Turro, O. Hornykiewicz and F. A. Zucca, *Proc. Natl. Acad. Sci.*, 2004, **101**, 9843–9848.

240 K. M. Davies, S. Bohic, A. Carmona, R. Ortega, V. Cottam, D. J. Hare, J. P. M. Finberg, S. Reyes, G. M. Halliday, J. F. B. Mercer and K. L. Double, *Neurobiol. Aging*, 2014, **35**, 858–866.

241 A. I. Bush, *Curr. Opin. Chem. Biol.*, 2000, **4**, 184–191.

242 A. Hopt, S. Korte, H. Fink, U. Panne, R. Niessner, R. Jahn, H. Kretzschmar and J. Herms, *J. Neurosci. Methods*, 2003, **128**, 159–172.

243 T. D. Rae, P. J. Schmidt, R. A. Pufahl, V. C. Culotta and T. V. O'Halloran, *Science (80-.).*, 1999, **284**, 805–808.

244 P. A. Cobine, L. D. Ojeda, K. M. Rigby and D. R. Winge, *J. Biol. Chem.*, 2004, **279**, 14447–14455.

245 I. Spasojević, M. Mojović, Z. Stević, S. D. Spasić, D. R. Jones, A. Morina and M. B. Spasić, *Redox Rep.*, 2010, **15**, 29–35.

246 R. Squitti, M. Ventriglia, G. Barbati, E. Cassetta, F. Ferreri, G. Dal Forno, S. Ramires, F. Zappasodi and P. M. Rossini, *J. Neural Transm.*, 2007, **114**, 1589–1594.

247 R. Squitti, F. Bressi, P. Pasqualetti, C. Bonomini, R. Ghidoni, G. Binetti, E. Cassetta, F. Moffa, M. Ventriglia, F. Vernieri and P. M. Rossini, *Neurology*, 2009, **72**, 50–55.

248 S. Bucossi, M. Ventriglia, V. Panetta, C. Salustri, P. Pasqualetti, S. Mariani, M. Siotto, P. M. Rossini and R. Squitti, *J. Alzheimer's Dis.*, 2011, **24**, 175–185.

249 E. Gaggelli, H. Kozlowski, D. Valensin and G. Valensin, *Chem. Rev.*, 2006, **106**, 1995–2044.

250 R. Squitti, R. Polimanti, S. Bucossi, M. Ventriglia, S. Mariani, D. Manfellotto, F. Vernieri, E. Cassetta, F. Ursini and P. M. Rossini, *Rejuvenation Res.*, 2013, **16**, 3–10.

251 S. Bucossi, S. Mariani, M. Ventriglia, R. Polimanti, M. Gennarelli, C. Bonvicini, P. Pasqualetti, F. Scrascia, S. Migliore, F. Vernieri, P. M. Rossini and R. Squitti, *Int. J. Alzheimers. Dis.*, , DOI:10.4061/2011/973692.

252 S. Bucossi, R. Polimanti, S. Mariani, M. Ventriglia, C. Bonvicini, S. Migliore, D. Manfellotto, C. Salustri, F. Vernieri, P. M. Rossini and R. Squitti, *J. Alzheimer's Dis.*, 2012, **29**, 913–919.

253 G. Multhaup, T. Ruppert, A. Schlicksupp, L. Hesse, E. Bill, R. Pipkorn, C. L. Masters and K. Beyreuther, *Biochemistry*, 1998, **37**, 7224–7230.

254 A. R. White, G. Multhaup, F. Maher, S. Bellingham, J. Camakaris, H. Zheng, A. I. Bush, K. Beyreuther, C. L. Masters and R. Cappai, *J. Neurosci.*, 1999, **19**, 9170–9179.

255 A. R. White, G. Multhaup, D. Galatis, W. J. McKinstry, M. W. Parker, R. D. Pipkorn, K. Beyreuther, C. L. Masters and R. Cappai, *J. Neurosci.*, 2002, **22**, 365–376.

256 T. Borchardt, J. Camakaris, R. Cappai, C. L. Masters, K. Beyreuther and G. Multhaup, *Biochem. J.*, 1999, **344**, 461–467.

257 G. F. Z. Da Silva, W. M. Tay and L. J. Ming, *J. Biol. Chem.*, 2005, **280**, 16601–16609.

258 C. Opazo, X. Huang, R. A. Cherny, R. D. Moir, A. E. Roher, A. R. White, R. Cappai, C. L. Masters, R. E. Tanzi, N. C. Inestrosa and A. I. Bush, *J. Biol. Chem.*, 2002, **277**, 40302–40308.

259 D. Beauchemin and R. Kisilevsky, *Anal. Chem.*, 1998, **70**, 1026–1029.

260 C. S. Atwood, R. D. Moir, X. Huang, R. C. Scarpa, N. M. E. Bacarra, D. M. Romano, M. A. Hartshorn, R. E. Tanzi and A. I. Bush, *J. Biol. Chem.*, 1998, **273**, 12817–12826.

261 X. Huang, C. S. Atwood, M. A. Hartshorn, G. Multhaup, L. E. Goldstein, R. C. Scarpa, M. P. Cuajungco, D. N. Gray, J. Lim, R. D. Moir, R. E. Tanzi and A. I. Bush, *Biochemistry*, 1999, **38**, 7609–7616.

262 K. J. Barnham, W. J. McKinstry, G. Multhaup, D. Galatis, C. J. Morton, C. C. Curtain, N. A. Williamson, A. R. White, M. G. Hinds, R. S. Norton, K. Beyreuther, C. L. Masters, M. W. Parker and R. Cappai, *J. Biol. Chem.*, 2003, **278**, 17401–17407.

263 M. C. Boll, M. Alcaraz-Zubeldia, S. Montes and C. Rios, *Neurochem. Res.*, 2008, **33**, 1717–1723.

264 W. R. Yu, H. Jiang, J. Wang and J. X. Xie, *Neurosci. Bull.*, 2008, **24**, 73–78.

265 W. A. Spencer, J. Jeyabalan, S. Kichambre and R. C. Gupta, *Free Radic. Biol. Med.*, 2011, **50**, 139–147.

266 R. M. Rasia, C. W. Bertoncini, D. Marsh, W. Hoyer, D. Cherny, M. Zweckstetter, C. Griesinger, T. M. Jovin and C. O. Fernández, *Proc. Natl. Acad. Sci. U. S. A.*, 2005, **102**, 4294–4299.

267 A. Villar-Piqué, G. Rossetti, S. Ventura, P. Carloni, C. O. Fernández and T. F. Outeiro, *Commun. Integr. Biol.*, 2017, **10**, 1–4.

268 C. C. Weihl and G. Lopate, *Muscle and Nerve*, 2006, **34**, 789–793.

269 A. N. A. B. Barros, M. E. T. Dourado, L. D. F. C. Pedrosa and L. Leite-Lais, *J. Nutr. Metab.*, , DOI:10.1155/2018/5678698.

270 L. Sauzéat, E. Bernard, A. Perret-Liaudet, I. Quadrio, A. Vighetto, P. Krolak-Salmon, E. Broussolle, P. Leblanc and V. Balter, *iScience*, 2018, **6**, 264–271.

271 F. Kitamura, N. Fujimaki, W. Okita, H. Hiramatsu and H. Takeuchi, *Biochemistry*, 2011, **50**, 4242–4250.

272 J. B. Hilton, K. Kysenius, A. R. White and P. J. Crouch, *Exp. Neurol.*, 2018, **307**, 118–128.

273 M. Son, K. Puttaparthi, H. Kawamata, B. Rajendran, P. J. Boyer, G. Manfredi and J. L. Elliott, *Proc. Natl. Acad. Sci. U. S. A.*, 2007, **104**, 6072–6077.

274 S. Ono, *Curr. Pharm. Des.*, 2018, **23**, 5001–5009.

275 H. Vahrenkamp, *Chemie unserer Zeit*, 1988, **22**, 73–84.

276 C. J. Frederickson, *Int. Rev. Neurobiol.*, 1989, **31**, 145–238.

277 J. K. Chesters and M. Will, *Br. J. Nutr.*, 1981, **46**, 111–118.

278 T. Kambe, T. Tsuji, A. Hashimoto and N. Itsumura, *Physiol. Rev.*, 2015, **95**, 749–784.

279 C. A. Blindauer, I. Harvey, K. E. Bunyan, A. J. Stewart, D. Sleep, D. J. Harrison, S. Berezenko and P. J. Sadler, *J. Biol. Chem.*, 2009, **284**, 23116–23124.

280 S. Aoki and E. Kimura, *Chem. Rev.*, 2004, **104**, 769–787.

281 A. Krężel and W. Maret, *J. Biol. Inorg. Chem.*, 2006, **11**, 1049–1062.

282 P. Zalewski, A. Truong-Tran, S. Lincoln, D. Ward, A. Shankar, P. Coyle, L. Jayaram, A. Copley, D. Grosser, C. Murgia, C. Lang and R. Ruffin, *Biotechniques*, 2006, **40**, 509–520.

283 I. Sekler, S. L. Sensi, M. Hershfinkel and W. F. Silverman, *Mol. Med.*, 2007, **13**, 337–343.

284 T. Kambe, A. Hashimoto and S. Fujimoto, *Cell. Mol. Life Sci.*, 2014, **71**, 3281–3295.

285 T. Fukada and T. Kambe, *Metallomics*, 2011, **3**, 662–674.

286 P. González-Duarte, in *Comprehensive Coordination Chemistry II*, Elsevier, 2003, pp. 213–228.

287 M. MAGER, W. F. MCNARY and F. LIONETTI, *J. Histochem. Cytochem.*, 1953, **1**, 493–504.

288 H. Maske, *Klin. Wochenschr.*, 1955, **33**, 1058–1058.

289 A. S. Prasad and A. S. Prasad, *Biochem. Zinc*, 1993, 149–164.

290 S. L. Sensi, D. Ton-That, P. G. Sullivan, E. A. Jonas, K. R. Gee, L. K. Kaczmarek and J. H. Weiss, *Proc. Natl. Acad. Sci. U. S. A.*, 2003, **100**, 6157–6162.

291 A. I. Bush, W. H. Pettingell, G. Multhaup, M. D. Paradis, J. P. Vonsattel, J. F. Gusella, K. Beyreuther, C. L. Masters and R. E. Tanzi, *Science (80-.).*, 1994, **265**, 1464–1467.

292 C. Garnier, F. Devred, D. Byrne, R. Puppo, A. Y. Roman, S. Malesinski, A. V. Golovin, R. Lebrun, N. N. Ninkina and P. O. Tsvetkov, *Sci. Rep.*, 2017, **7**, 1–10.

293 M. Cassandri, A. Smirnov, F. Novelli, C. Pitolli, M. Agostini, M. Malewicz, G. Melino and G. Raschellà, *Cell Death Discov.*, , DOI:10.1038/cddiscovery.2017.71.

294 B. Szewczyk, *Front. Aging Neurosci.*, 2013, **5**, 1–12.

295 Y. Xu, G. Xiao, L. Liu and M. Lang, *Mol. Brain*, 2019, **12**, 1–12.

296 G. Lyubartseva, J. L. Smith, W. R. Markesbery and M. A. Lovell, *Brain Pathol.*, 2010, **20**, 343–350.

297 J. L. Smith, S. Xiong, W. R. Markesbery and M. A. Lovell, *Neuroscience*, 2006, **140**, 879–888.

298 M. A. Lovell, J. L. Smith, S. Xiong and W. R. Markesbery, *Neurotox. Res.*, 2005, **7**, 265–271.

299 C. Sindreu, À. Bayés, X. Altafaj and J. Pérez-Clausell, *Mol. Brain*, 2014, **7**, 1–7.

300 N. Beyer, D. T. R. Coulson, S. Heggarty, R. Ravid, G. B. Irvine, J. Hellemans and J. A. Johnston, *Mol. Neurodegener.*, 2009, **4**, 1–10.

301 N. Beyer, D. T. R. Coulson, S. Heggarty, R. Ravid, J. Hellemans, G. B. Irvine and J. A. Johnston, *J. Alzheimer's Dis.*, 2012, **29**, 863–873.

302 L. Belloni-Olivi, C. Marshall, B. Laal, G. K. Andrews and J. Bressler, *J. Neurosci. Res.*, 2009, **87**, 3221–3230.

303 J. Carrasco, P. Adlard, C. Cotman, A. Quintana, M. Penkowa, F. Xu, W. E. Van Nostrand and J. Hidalgo, *Neuroscience*, 2006, **143**, 911–922.

304 W. H. Yu, W. J. Lukiw, C. Bergeron, H. B. Niznik and P. E. Fraser, *Brain Res.*, 2001, **894**, 37–45.

305 D. T. Dexter, F. R. Wells, A. J. Lee, F. Agid, Y. Agid, P. Jenner and C. D. Marsden, *J. Neurochem.*, 1989, **52**, 1830–1836.

306 D. T. Dexter, P. Jenner, A. H. V. Schapira and C. D. Marsden, *Ann. Neurol.*, 1992, **32**, S94–S100.

307 I. Hozumi, T. Hasegawa, A. Honda, K. Ozawa, Y. Hayashi, K. Hashimoto, M. Yamada, A. Koumura, T. Sakurai, A. Kimura, Y. Tanaka, M. Satoh and T. Inuzuka, *J. Neurol. Sci.*, 2011, **303**, 95–99.

308 K. Du, M. Y. Liu, X. Zhong and M. J. Wei, *Sci. Rep.*, 2017, **7**, 1–8.

309 A. P. Smith and N. M. Lee, *Amyotroph. Lateral Scler.*, 2007, **8**, 131–143.

310 S. D. Boyd, M. S. Ullrich, J. S. Calvo, F. Behnia, G. Meloni and D. D. Winkler, *Molecules*, 2020, **25**, 1–14.

311 H. G. T. Blaauwgeers, M. Anwar Chand, F. M. Van Den Berg, J. M. B. Vianney De Jong and D. Troost, *J. Neurol. Sci.*, 1996, **142**, 39–44.

312 J. M. Morahan, B. Yu, R. J. Trent and R. Pamphlett, *Amyotroph. lateral Scler. other Mot. neuron Disord. Off. Publ. World Fed. Neurol. Res. Gr. Mot. Neuron Dis.*, 2005, **6**, 115–117.

313 S. Nagano, M. Satoh, H. Sumi, H. Fujimura, C. Tohyama, T. Yanagihara and S. Sakoda, *Eur. J. Neurosci.*, 2001, **13**, 1363–1370.

314 M. Neumann, D. M. Sampathu, L. K. Kwong, A. C. Truax, M. C. Micsenyi, T. T. Chou, J. Bruce, T. Schuck, M. Grossman, C. M. Clark, L. F. McCluskey, B. L. Miller, E. Masliah, I. R. Mackenzie, H. Feldman, W. Feiden, H. A. Kretzschmar, J. Q. Trojanowski and V. M.-Y. Lee, *Science (80-.).*, 2006, **314**, 130–133.

315 Y. Nagai, N. Miyakawa, H. Takuwa, Y. Hori, K. Oyama, B. Ji, M. Takahashi, S. T. Slocum and Y. Xiong, *J. Cereb. Blood Flow Metab.*, 2019, **39**, 524–608.

316 C. A. Lipinski, F. Lombardo, B. W. Dominy and P. J. Feeney, *Adv. Drug Deliv. Rev.*, 2001, **64**, 4–17.

317 E. D. Agdeppa and M. E. Spilker, *AAPS J.*, 2009, **11**, 286–299.

318 T. T. Wager, X. Hou, P. R. Verhoest and A. Villalobos, *ACS Chem. Neurosci.*, 2010, **1**, 435–449.

319 M. L. Amin, *Drug Target Insights*, 2013, **2013**, 27–34.

320 T. J. Raub, *Mol. Pharm.*, 2006, **3**, 3–25.

321 B. Pavan, A. Dalpiaz, N. Ciliberti, C. Biondi, S. Manfredini and S. Vertuani, *Molecules*, 2008, **13**, 1035–1065.

322 C. S. Ferguson and R. F. Tyndale, *Trends Pharmacol. Sci.*, 2011, **32**, 708–714.

323 X. Deng, J. Rong, L. Wang, N. Vasdev, L. Zhang, L. Josephson and S. H. Liang, *Angew. Chemie - Int. Ed.*, 2019, **58**, 2580–2605.

324 S. A. Harmon, T. Perk, C. Lin, J. Eickhoff, P. L. Choyke, W. L. Dahut, A. B. Apolo, J. L. Humm, S. M. Larson, M. J. Morris, G. Liu and R. Jeraj, *J. Clin. Oncol.*, 2017, **35**, 2829–2837.

325 Y. Pan, *ACS Med. Chem. Lett.*, 2019, **10**, 1016–1019.

326 J. S. Wright, T. Kaur, S. Preshlock, S. S. Tanzey, W. P. Winton, L. S. Sharninghausen, A. F. Brooks, M. S. Sanford and P. J. H. Scott, *Copper-Mediated Late-stage Radiofluorination: Five Years of Impact on Pre-clinical and Clinical PET Imaging*, Springer International Publishing, 2020.

327 A. V. Mossine, S. S. Tanzey, A. F. Brooks, K. J. Makaravage, N. Ichiishi, J. M. Miller, B. D. Henderson, M. B. Skaddan, M. S. Sanford and P. J. H. Scott, *Org. Biomol. Chem.*, , DOI:10.1039/c9ob01758e.

328 A. V. Mossine, S. S. Tanzey, A. F. Brooks, K. J. Makaravage, N. Ichiishi, J. M. Miller, B. D. Henderson, T. Erhard, C. Bruetting, M. B. Skaddan, M. S. Sanford and P. J. H. Scott, *Nat. Protoc.*, 2020, **15**, 1742–1759.

329 Z. D. Liu, D. Y. Liu and R. C. Hider, in *Iron Chelation Therapy. Advances in Experimental Medicine and Biology*, ed. C. Hershko, Springer US, Boston, MA, 2002, pp. 141–166.

330 M. Atanasov and D. Reinen, *Compr. Coord. Chem. II*, 2004, **1**, 669–678.

331 F. Petrat, U. Rauen and H. De Groot, *Hepatology*, 1999, **29**, 1171–1179.

332 W. Breuer, S. Epsztejn, P. Millgram and I. Z. Cabantchik, *Am. J. Physiol. - Cell Physiol.*, , DOI:10.1152/ajpcell.1995.268.6.c1354.

333 R. C. Hider and A. D. Hall, *Prog. Med. Chem.*, 1991, **28**, 41–173.

334 T. G. Spiro, G. Bates and P. Saltman, *J. Am. Chem. Soc.*, 1967, **89**, 5559–5562.

335 J. Strouse, S. W. Layten and C. E. Strouse, *J. Am. Chem. Soc.*, 1977, **99**, 562–572.

336 N. Mobarra, M. Shanaki, H. Ehteram, H. Nasiri, M. Sahmani, M. Saeidi, M. Goudarzi, H. Pourkarim and M. Azad, *Int. J. Hematol. Stem Cell Res.*, 2016, **10**, 239–247.

337 K. H. M. Kuo and M. Mrkobrada, *Hemoglobin*, 2014, **38**, 409–421.

338 A. M. Fredenburg, R. K. Sethi, D. D. Allen and R. A. Yokel, *Toxicology*, 1996, **108**, 191–199.

339 I. Turcot, A. Stintzi, J. Xu and K. N. Raymond, *JBIC J. Biol. Inorg. Chem.*, 2000, **5**, 634–641.

340 Z. D. Liu, R. Kayyali, R. C. Hider, J. B. Porter and A. E. Theobald, *J. Med. Chem.*, 2002, **45**, 631–639.

341 P. C. Waldmeier, A. M. Buchle and A. F. Steulet, *Biochem. Pharmacol.*, 1993, **45**, 2417–2424.

342 X. Ding, H. Xie and Y. J. Kang, *J. Nutr. Biochem.*, 2011, **22**, 301–310.

343 T. Zhang, J. M. Liu, X. F. Huang, B. Xia, C. Y. Su, G. F. Luo, Y. W. Xu, Y. X. Wu, Z. W. Mao and R. L. Qiu, *J. Hazard. Mater.*, 2013, **262**, 464–471.

344 L. Zhang, J. Lichtmannegger, K. H. Summer, S. Webb, I. J. Pickering and G. N. George, *Biochemistry*, 2009, **48**, 891–897.

345 A. Taraboletti, T. Walker, R. Avila, H. Huang, J. Caporoso, E. Manandhar, T. C. Leeper, D. A. Modarelli, S. Medicetty and L. P. Shriver, *Biochemistry*, 2017, **56**, 1518–1528.

346 B. Sarkar, A. Sass-Kortsak, R. Clarke, S. H. Laurie and P. Wei, *Proc. R. Soc. Med.*, 1977, **70 Suppl 3**, 13–18.

347 N. Hirayamaa, S. Iimuroa, K. Kubonob and H. Kokusenc, *Talanta*, 1996, **43**, 621–626.

348 C. A. Blindauer, M. T. Razi, S. Parsons and P. J. Sadler, *Polyhedron*, 2006, **25**, 513–520.

349 C. Armstrong, W. Leong and G. J. Lees, *Brain Res.*, 2001, **892**, 51–62.

350 K. B. Johnsen, A. Burkhart, F. Melander, P. J. Kempen, J. B. Vejlebo, P. Siupka, M. S. Nielsen, T. L. Andresen and T. Moos, *Sci. Rep.*, 2017, **7**, 1–13.

351 S. H. Liang, J. P. Holland, N. A. Stephenson, A. Kassenbrock, B. H. Rotstein, C. P. Daignault, R. Lewis, L. Collier, J. M. Hooker and N. Vasdev, *ACS Chem. Neurosci.*, 2015, **6**, 535–541.

352 K. Komatsu, K. Kikuchi, H. Kojima, Y. Urano and T. Nagano, *J. Am. Chem. Soc.*, 2005, **127**, 10197–10204.

353 S. K. Rastogi, P. Pal, D. E. Aston, T. E. Bitterwolf and A. L. Branen, *ACS Appl. Mater. Interfaces*, 2011, **3**, 1731–1739.

354 D. Cocco, L. Calabrese, A. Rigo, E. Argese and G. Rotilio, *J. Biol. Chem.*, 1981, **256**, 8983–8986.

355 H. P. Misra, *J. Biol. Chem.*, 1979, **254**, 11623–11628.

356 M. Ye and A. M. English, *Biochemistry*, 2006, **45**, 12723–12732.

357 H. Wu, X. Sun, Y. Lu, X. Fang and M. Li, *Synth. React. Inorganic, Met. Nano-Metal Chem.*, 2015, **45**, 1859–1863.

358 A. E. Stacy, D. Palanimuthu, P. V. Bernhardt, D. S. Kalinowski, P. J. Jansson and D. R. Richardson, *J. Med. Chem.*, 2016, **59**, 4965–4984.

359 B. M. Mandelbrote, M. W. Stanier, R. H. S. Thompson and M. N. Thruston, *Brain*, 1948, **71**, 212–228.

360 J. N. CUMINGS, *Brain*, 1948, **71**, 410–415.

361 J. A. Vilensky and K. Redman, *Ann. Emerg. Med.*, 2003, **41**, 378–383.

362 R. Munday, *Free Radic. Biol. Med.*, 1989, **7**, 659–673.

363 J. Peisach and W. E. Blumberg, *Mol. Pharmacol.*, 1969, **5**, 200–209.

364 R. S. Dubois, D. O. Rodgerson and K. Michael Hambidge, *J. Pediatr. Gastroenterol. Nutr.*, 1990, **10**, 77–81.

365 P. H. Unit, S. S. Hospital and P. Alto, 1963, 396–401.

366 R. A. Cherny, C. S. Atwood, M. E. Xilinas, D. N. Gray, W. D. Jones, C. A. McLean, K. J. Barnham, I. Volitakis, F. W. Fraser, Y. S. Kim, X. Huang, L. E. Goldstein, R. D. Moir, J. T. Lim, K. Beyreuther, H. Zheng, R. E. Tanzi, C. L. Masters and A. I. Bush, *Neuron*, 2001, **30**, 665–676.

367 N. G. Faux, C. W. Ritchie, A. Gunn, A. Rembach, A. Tsatsanis, J. Bedo, J. Harrison, L. Lannfelt, K. Blennow, H. Zetterberg, M. Ingelsson, C. L. Masters, R. E. Tanzi, J. L. Cummings, C. M. Herd and A. I. Bush, *J. Alzheimer's Dis.*, 2010, **20**, 509–516.

368 H. S. Krishnan, V. Bernard-Gauthier, M. S. Placzek, K. Dahl, V. Narayanaswami, E. Livni, Z. Chen, J. Yang, T. L. Collier, C. Ran, J. M. Hooker, S. H. Liang and N. Vasdev, *Mol. Pharm.*, 2018, **15**, 695–702.

369 J. R. Kirshner, S. He, V. Balasubramanyam, J. Kepros, C. Y. Yang, M. Zhang, Z. Du, J. Barsoum and J. Bertin, *Mol. Cancer Ther.*, 2008, **7**, 2319–2327.

370 J. S. Choi, J. J. Braymer, R. P. R. Nanga, A. Ramamoorthy and M. H. Lim, *Proc. Natl. Acad. Sci. U. S. A.*, 2010, **107**, 21990–21995.

371 M. W. Beck, S. B. Oh, R. A. Kerr, H. J. Lee, S. H. Kim, S. Kim, M. Jang, B. T. Ruotolo, J. Y. Lee and M. H. Lim, *Chem. Sci.*, 2015, **6**, 1879–1886.

372 A. M. Daugherty and N. Raz, *Neuropsychol. Rev.*, 2015, **25**, 272–287.

373 S. Ogawa, T. M. Lee, A. R. Kay and D. W. Tank, *Proc. Natl. Acad. Sci. U. S. A.*, 1990, **87**, 9868–9872.

374 L. Pauling and C. D. Coryell, *Proc. Natl. Acad. Sci.*, 1936, **22**, 159–163.

375 E. M. Haacke, N. Y. C. Cheng, M. J. House, Q. Liu, J. Neelavalli, R. J. Ogg, A. Khan, M. Ayaz, W. Kirsch and A. Obenaus, *Magn. Reson. Imaging*, 2005, **23**, 1–25.

376 S. Siemonsen, J. Finsterbusch, J. Matschke, A. Lorenzen, X. Q. Ding and J. Fiehler, *Am. J. Neuroradiol.*, 2008, **29**, 950–955.

377 R. J. Ordidge, J. M. Gorell, J. C. Deniau, R. A. Knight and J. A. Helpern, *Magn. Reson. Med.*, 1994, **32**, 335–341.

378 B. Yao, T. Q. Li, P. van Gelderen, K. Shmueli, J. A. de Zwart and J. H. Duyn, *Neuroimage*, 2009, **44**, 1259–1266.

379 E. M. Haacke, J. Tang, J. Neelavalli and Y. C. N. Cheng, *J. Magn. Reson. Imaging*, 2010, **32**, 663–676.

380 G. Bartzokis, J. L. Cummings, C. H. Markham, P. Z. Marmarelis, L. J. Treciokas, T. A. Tishler, S. R. Marder and J. Mintz, *Magn. Reson. Imaging*, 1999, **17**, 213–222.

381 A. Pfefferbaum, E. Adalsteinsson, T. Rohlfing and E. V. Sullivan, *Neuroimage*, 2009, **47**, 493–500.

CHAPTER 2

Development of Iron Chelating PET Radiotracers in Assessing Neurodegenerative Diseases

2.1. Introduction

Iron is hypothesized to play a role in the early stages of neurodegenerative diseases (NDs) by inducing oxidative stress via the formation of reactive oxygen species (ROS) through Fenton chemistry.[1] The exact mechanisms of iron toxicity in inducing diseases such as Alzheimer's Disease (AD), Parkinson's Disease (PD), and Amyotrophic Lateral Sclerosis (ALS) has been reviewed in Chapter 1. Though high levels of iron can be detected in distinct brain regions by magnetic resonance (MR) imaging, this signal represents the total iron content.[2] Only a small percentage of total iron in cells is considered to be toxic, which is the free, non-protein bound labile iron pool (LIP).[3,4] The concentration of iron in the LIP varies in different cell types and has been determined to be in the range of 0.1 – 5.4 µM in healthy cells.[5–8] Atomic absorption spectroscopy has been used to measure the LIP in PD tissue and found to have a concentration of 90 ng/g tissue (1.6 µM) in the substantia nigra (SN).[9] Only total iron concentrations have been reported in brain regions effected by AD[10–13] and ALS,[14–16] but show a significant increase compared to normal control tissue. The LIP is accessible by iron chelators whereas all remaining iron is protein bound and not available for chelation.[17]

MRI has been crucial to correlating AD progression to increases in iron levels, and has even been used to show that iron concentrations can predict the neurodegeneration of the putamen.[18] Since a large concentration of iron is needed to produce a significant change in the MR signal, where most of the signal is thought to occur from ferritin-stored iron, a more sensitive technique for non-invasive imaging of iron is highly sought. These large changes in concentration of iron occur at later stages of disease. It is hypothesized that diagnosis of NDs before clinical symptoms start to manifest will help in preventing or stopping the progression of neurodegeneration by enabling therapeutic intervention at this earlier time point.[19]

A study using an iron chelating fluorescent probe indicated that neuronal cells contain less than 0.1 µM of iron in the LIP as this was the limit of detection of the probe and barely any signal was visible.[7] When a ND diseased model cell type was used, iron could be visualized by the probe. Being that targets for Positron Emission Tomography (PET) tracers typically need a concentration above 1 nM to produce a signal suitable for analysis,[20] a PET probe selective for iron in the LIP would be sensitive enough to detect these small changes, filling a void of iron imaging currently not possible with MRI.

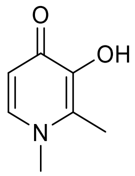

1

Fig. 2.1: Structure of Deferiprone (DFP**)**

An iron-specific chelating PET probe would need good blood-brain barrier (BBB) permeability (mediated by low molecular weight (≤300 g/mol) and a cLogP between 1 – 3), have high metabolic stability ($t_{1/2} > 3.1$h), and form a 1:1 complex with iron at low concentrations.[21] Deferiprone (DFP, **Figure 2.1**) was selected for this purpose because it is already approved for human use by the Food and Drug Administration (FDA) in the treatment of iron toxicity.[22] DFP is also currently in phase II clinical trials for delaying dementia in AD, Mild Cognitive Impairment (MCI), and PD.[23,24] We reasoned that translation of a radiolabeled version of DFP would be straightforward because toxicity studies, which are typically expensive, have already been completed for this compound and can be administered up to a maximum dose of 99 mg/kg/day.[25] Other FDA-approved iron chelators include deferoxamine-B and deferasirox, both of which have limited to no BBB permeability,[26] while DFP has been shown to be BBB permeable in rodents and to reduce iron levels in the human brain.[23,27] This suggests that a DFP-based PET radiotracer should have good BBB permeability. Since the other iron chelators deferoxamine-B and deferasirox are known not to cross the cellular membrane and chelate iron in the cells, DFP was chosen as the lead candidate around which to explore development of a potential PET tracer for quantification of CNS iron levels. In this chapter we describe our efforts to develop [^{11}C]DFP.

2.2. Results and Discussion

2.2.1. *First synthesis of [^{11}C]DFP with a nonprotected precursor*

Initial attempts to synthesize carbon-11 labeled deferiprone ([^{11}C]DFP, **3**) were performed with N-desmethyl precursor **2** by reacting with [^{11}C]CH_3OTf in dimethylformamide (DMF) at room temperature (**Scheme 2.1**). Two possible methylation sites are available on commercially available precursor **2**. The pK_a for nitrogen of 4-pyridinones is lower than other secondary amines (pKa ~ 38) at a pK_a of 15,[28] while the alcohol moiety has a pK_a similar to phenols (~10).[28] We hypothesized that the nitrogen, being more nucleophilic than alcohols (higher basicity) would preferentially be radiolabeled, and that the limiting reagent being [^{11}C]CH_3OTf would allow for only methylation of one site and not both. Also, we hypothesized that [^{11}C]DFP ([^{11}C]**3)** could be separated during purification from the alternate O-methyl product [^{11}C]**4** if any formed. In a highly polar solvent such as DMF this proved to be the case, and the N-methyl product ([^{11}C]DFP) was observed during quality control testing, confirmed by co-injection with unlabeled reference standards of **3** and **4**. However, the yield of [^{11}C]DFP was quite low (0.5% from 1 Ci [^{11}C]CH_3I), with formation of an unknown product incorporating most of the radioactivity (**Figure 2.5**). Initially, this unknown side product was thought to be [^{11}C]DFP since after collection of a pure sample, it had the same retention time as the DFP standard **6** on an analytical HPLC column (**Figure 2.2a**). However, QC analysis with a different HPLC system gave more narrow peaks and revealed the radioactive compound to be an impurity and not [^{11}C]DFP (**Figure 2.2b**).

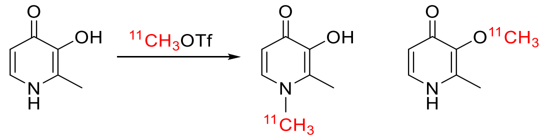

2 **3** **4**

Scheme 2. 1: Synthesis of [^{11}C]DFP and 2-methoxy-4-pyridone 4

a)

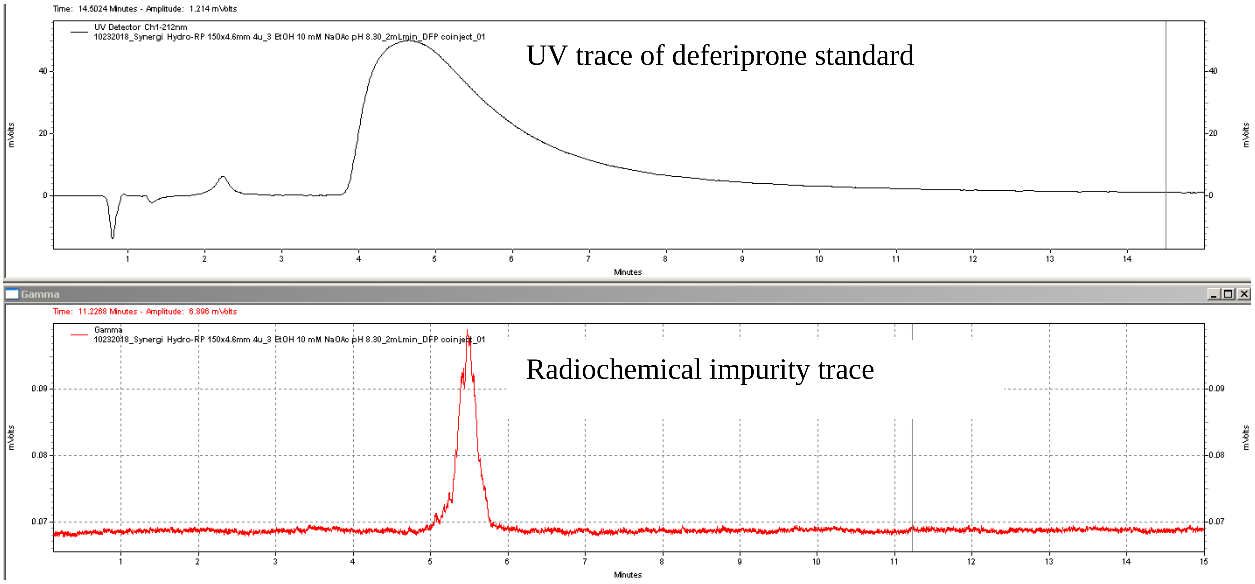

b)

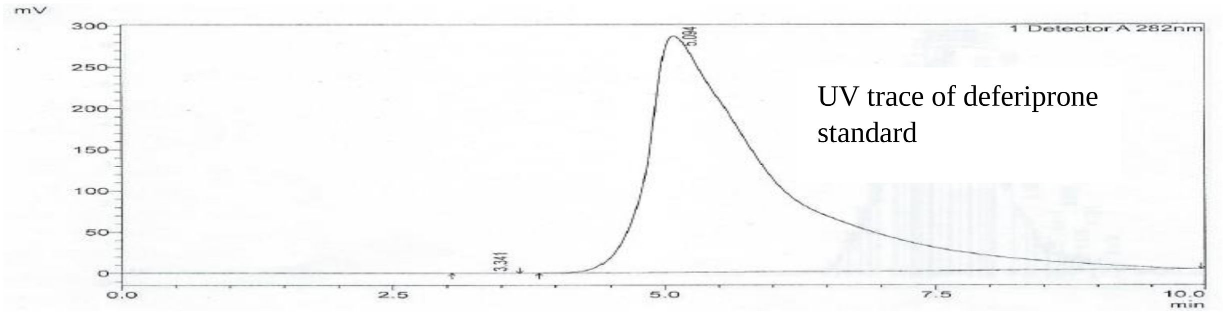

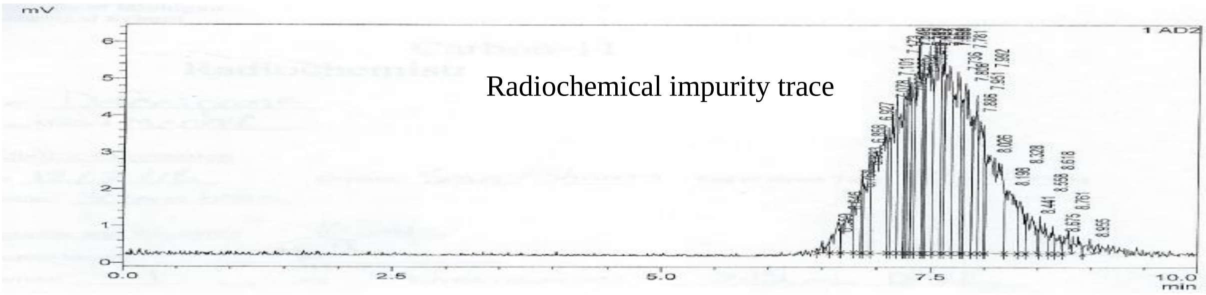

Fig. 2. 2: QC co-injection of unknown rad impurity with DFP standard on two HPLC systems

To increase the yield of [^{11}C]DFP, various reaction conditions were tested. The temperature of the reactor was decreased to 0°C to trap as much [^{11}C]CH_3OTf in the reactor as possible and then heating to 60°C for 3 minutes to overcome any thermodynamic barrier to the formation of [^{11}C]DFP. Unfortunately, this resulted in a lower radiochemical yield of [^{11}C]DFP (0.1% from 1 Ci [^{11}C]CH_3I), while concomitantly increasing yields of the unknown side product. Bicarbonate (HCO_3^-), with a pKa of 6 was added to deprotonate the ammonium ion formed after methylation (pKa ~ 4, **Scheme 2.2**), to increase the reaction rate to form **3**. Bicarbonate is not basic enough to deprotonate the alcohol, and thus hypothesized that it would reduce the preference to form **4**. This proved to be the case, and formation of the unknown side product was decreased, while the overall RCY of [^{11}C]DFP increased (1% from 1 Ci [^{11}C]CH_3I). The chromatogram of the semi-prep HPLC purification (**Figure 2.6**) revealed the product to be streaking, suggesting that [^{11}C]DFP could be prone to radiolytic decomposition.[29]

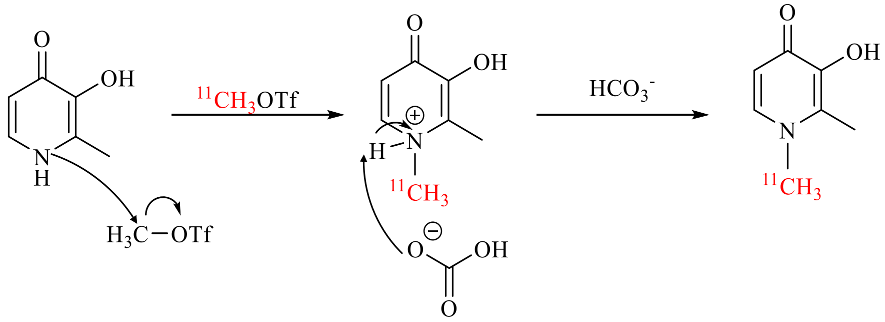

Scheme 2. 2: Mechanism of N-methylation to form [^{11}C]DFP in the presence of base

The methylating agent was switched to [^{11}C]CH_3I for kinetic control since it is less reactive than [^{11}C]CH_3OTf and would favor formation of [^{11}C]DFP due to the nitrogen being the more nucleophilic of the two potential methylation positions. Instead, this resulted in decreased yield (**Table 2.1**, **entry 1**). Precursor **2** is sparingly soluble in DMF. To test if passing the methylating source through a more concentrated solution of this inside an HPLC loop (termed Loop chemistry), volatile, flushable solvents such as ethanol or butanone were used (**Table 2.1**, **entry 3 and 5**). It was hypothesized that by decreasing the polarity of the solvent, the production of the unknown side product could be mitigated if it were not stabilized by a polar solvent. However, decreasing the polarity of the solvent revealed to be favorable for forming **4** over [^{11}C]DFP, as shown in **Table 2.1**, **entry 5** (dielectric constants are given for the solvents used in **Table 2.2**). It is known that less polar solvents stabilize the transition state in preference for O-alkylation over N-alkylation.[30]

Method	Solvent	Base	Temp	HPLC Buffer	RCY	Comments
MeI (Reactor)	DMF	HCO_3	rt	5% EtOH 10mM NaH_2PO_4 pH 2.73	1.60%	Reduced Impurity
MeOTf (Reactor)	DMF	HCO_3	rt	" " + 1mM Ascorbic Acid	4.40%	Broadening of product peak with coelution of rad impurtiy
PiB (Loop)	10µl DMSO/ 100µL EtOH	-	rt	" "	0%	Precursor does not dissolve in straight ethanol
MeOTf (Reactor)	10µl DMSO/ 100µL EtOH	HCO_3	rt	" "	0%	
PiB (Loop)	10µl DMSO/ 100µL Butanone	-	rt	" "	0%	O-methyl observed at same retention time of product on semiprep
FMZ (Reactor)	10µl DMSO/ 200µL Acetone	HCO_3	0-60°C	" "	0%	Larger impurity peak

Table 2. 1: Solvent screen and reactions in HPLC loop to increase yield of [^{11}C]DFP

Solvent	ε
DMSO	46.7
DMF	36.7
EtOH	24.5
Acetone	20.7
Butanone	18.5

Table 2. 2: Dielectric constants given for various solvents tested

2.2.2. *Solving the Issue of Radiolysis*

Radiolysis is the decomposition of a molecule by ionizing radiation, thought to be mediated by the formation of single electron species when the chemical bonds in water become cleaved by high energy radiation to form hydroxyl radicals, hydrogen radicals, and hydrated electrons.[31,32] These radicals can go on to react with the radiolabeled compound to form a radiolytic byproduct or the radiation from the unstable isotope attached to the molecule could lead directly to the breaking of bonds within the structure. When this occurs, the radiolytic product(s) can be confirmed by formation of a new peak(s) in the radio-HPLC chromatogram over time. In the case of [^{11}C]DFP, however, no radiolytic product was observed, but instead a gradual decrease of the area under the curve of the [^{11}C]DFP signal was noticed. The decrease in area under the curve was observed to be faster than the normal decay of a carbon-11 (**Table 2.3**).

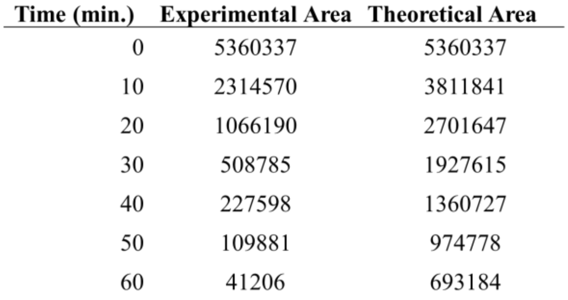

Time (min.)	Experimental Area	Theoretical Area
0	5360337	5360337
10	2314570	3811841
20	1066190	2701647
30	508785	1927615
40	227598	1360727
50	109881	974778
60	41206	693184

Table 2. 3: AUC of [^{11}C]DFP gamma peak on an analytical HPLC column compared to the theoretical decay of carbon-11 revealing radiolysis of the product to form a volatile byproduct

Several methods have been used to inhibit radiolysis of other PET radiotracers.[31] Switching from an acetonitrile (MeCN) semi-preparative HPLC buffer to an ethanolic buffer can decrease the rate of radiolysis due to the antioxidant properties of ethanol.[33] Inclusion of other antioxidants such as ascorbic acid (aka vitamin C) during purification and formulation of a radiotracer has also been shown to mitigate radiolysis. Further, sodium nitrate ($NaNO_3$) has also been used to completely inhibit the radiolysis of [^{11}C]iomazenil.[32] The theory behind the use of these agents is their ability to act as radical scavengers. Ethanol, ascorbate, and nitrate all have very fast reaction rates with radicals, usually faster than the desired radiotracer. Therefore, these additives prevent the radiolytic decomposition of PET radiotracers by quenching radicals present in the formulated dose before they can react with the radiotracer. The mechanism of radiolytic decomposition is often radiotracer specific, and so use of an additive can have different outcomes. Ascorbate has a higher reaction rate with hydroxyl radicals than nitrate ($k_{OH^*.} = 7.2 \times 10^9$ vs. 3.1×10^9) while nitrate has a higher reaction rate with hydrated electrons than ascorbate ($k_{e^*aq} = 1.0 \times 10^9$ vs. 3.5×10^8).[34,35]

Since an ethanol buffer was already being used in our purification system (2% ethanol, 10mM $NaHPO_4$) an additive with a larger radical reaction rate constant needed to be used. When ascorbic acid was used as an additive in the semi-preparative HPLC buffer, streaking of [^{11}C]DFP became even more dramatic (**Table 2.1**, **entry 2**) suggesting radiolysis was still occurring. $NaNO_3$ was added to the dose vial before collection of [^{11}C]DFP from HPLC. A sample of the formulated product was taken for stability testing which revealed results similar to those described in **Table 2.3**, indicating that radiolysis had not been inhibited. Both ascorbic acid and sodium nitrate could not fully inhibit radiolysis. However, use of highly concentrated ascorbic acid in the final dose did slow down the rate of decomposition as indicated by HPLC.

2.2.3. *Synthesis of [^{11}C]DFP with a benzyl protected precursor*

Although the addition of base to the reaction proved helpful to increase the RCY of [^{11}C]DFP, not enough product was being isolated for preclinical studies. In order to perform a nonhuman primate scan, at least 5 mCi of product is needed. However, only 500 µCi – 1 mCi was being collected that was suitable for injection. Therefore, a protected precursor was desired to eliminate the competing O-methylation reaction. Protecting the hydroxyl group of 3-hydroxy-2-methylpyridin-4(1H)-one (**1**) proved difficult to achieve due to the insolubility of **2** in numerous organic solvents. Trimethylsilyl (TMS), tert-butyldimethylsilyl, carbonate, and benzyl protecting groups were attempted to protect the alcohol, with only the benzyl protection being successful for isolation of product (**Scheme 2.3a**). A database search of benzyl-protected compound **5** illustrated that it was commercially available and thus did not have to be prepared manually before radiosynthesis. Although deprotection of benzyl groups often requires hydrogen and a palladium catalyst[36] (which is not easily adapted for use in an automated radiosynthesis module), in this case we were gratified to observe complete removal of the benzyl group upon treatment with 6N hydrochloric acid (HCl) at 120°C for 3 minutes (**Scheme 2.3b**).

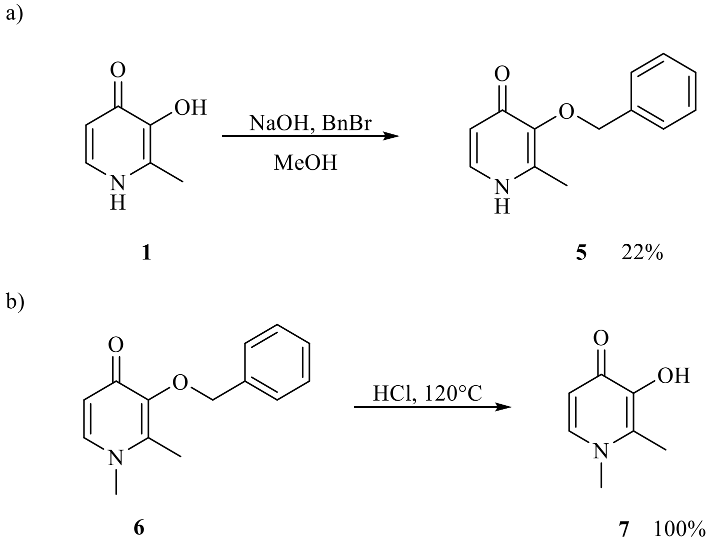

Scheme 2. 3: Synthesis of a benzyl protected precursor and subsequent deprotection

Carbon-11 labeling of benzyl-protected precursor **5** (**Scheme 2.4**) proved high yielding when the reaction mixture was sampled for HPLC analysis (17.7% RCY non-decay corrected (NDC), 33.8 mCi from 200 mCi of [^{11}C]CH_3I). Although the unlabeled reference standard could be deprotected with 6N HCl (**Scheme 2.3**), this high concentration of acid was a concern for routine use in an automated synthesis module. Several HCl concentrations (2N, 4N, 6N, and conc.) at various temperatures were tested manually with the crude reaction mixture containing **7**. However, this screen revealed that the lowest concentration that could fully remove the benzyl protecting group in a short amount of time (3 min.) suitable for use in an automated synthesis of [^{11}C]DFP was found to be 6N and so we moved forward with these conditions.

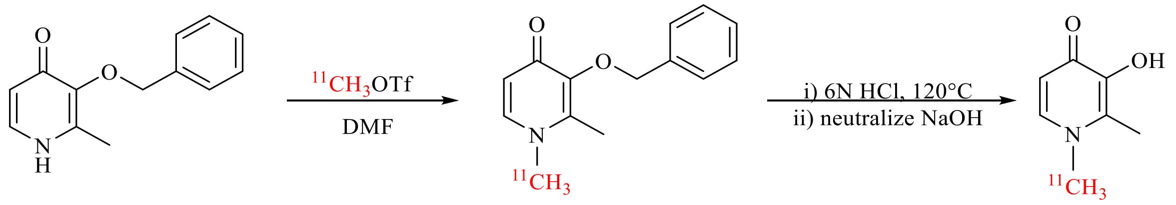

5 **8** 17.7% RCY NDC **3** 4.6% RCY NDC

Scheme 2. 4: Radiosynthesis of [^{11}C]DFP from a benzyl protected precursor

Since [^{11}C]DFP is prone to radiolysis, steps were taken to prevent radiolytic decomposition at every part of the synthesis. The protected intermediate **7** was found to be stable, and thus ascorbic acid was added to the 6N HCl used for deprotection to prevent radiolysis once [^{11}C]DFP was formed. Heating of this solution led to a black/yellow mixture as a result of oxidation of the ascorbic acid. Since ascorbate and nitrate failed to completely inhibit radiolysis, it was assumed that the mechanism of decomposition was mediated directly through the radiolabeled compound and thus, an alternative method was used. By adding deferiprone standard to the deprotection solution, a higher yield of [^{11}C]DFP was achieved (due to carrier added synthesis) and found to be stable when the product was collected directly off the semi-preparative column and formulated with 500 mg ascorbic acid. It is thought that the cold standard added during the deprotection prevents radiolysis by acting as a radical scavenger, most likely with a faster reaction rate then that previously described with ascorbic acid. The added benefit of using the cold standard is that it does not decompose or oxidize at the high temperature needed for deprotection.

2.2.4. *Semi-preparative HPLC Development*

During the course of these studies, a range of semi-preparative HPLC conditions was continuously adapted until baseline separation of product from precursor was achieved and

[^{11}C]DFP could be appropriately purified. Though the precursors used and cold standard of deferiprone had ≥3 minute difference in retention time in most systems, translating it to an automated synthesis module where the whole reaction mixture was injected onto the column was challenging and often times co-elution of precursor and product occurred, leading to a decrease in effective molar activity (MA). Though the deprotected precursor does not contain the N -methyl group, it still contains the iron chelating scaffold. This could interfere with the signal to noise ratio (SNR) by blocking specific sites of binding for [^{11}C]DFP. In order to provide high quality PET images sought by the imaging community, this contaminant precursors minimizes the effective administered mass and therefore a misrepresentative image of how a [^{11}C]DFP image is meant to look. First a Polar-Reverse Phase (RP) semi-preparative column (250 x 10 mm) with a 5µ particle size was used with a 15% MeCN 10 mM sodium acetate (NaOAc) buffer (pH 8). It was thought that streaking of the standards on this system was caused by a high pH where the standards were partially deprotonated leading to formation of a charged species (**Figure 2.3**).

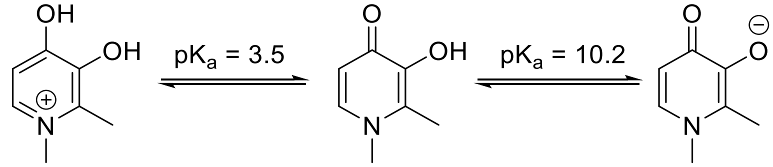

Fig. 2. 3: Tautomerization equilibrium of DFP

Reducing the pH to 3.75 by switching the buffering salt from acetate to monobasic sodium phosphate ($NaHPO_4$) and adjusting with phosphoric acid, the standard peaks immediately became sharper. Though this proved helpful for better identification on the analytical Hydro-RP column (150 x 4.6 mm, 4 µ particle size), precursor **2** still coeluted with [^{11}C]DFP from the semi-preparative column. Switching to a HILIC or NH_2 stationary phase switch the order of elution and resulted in the product eluting before the precursor. Although this led to efficient separation of the product from the precursor, 98% MeCN was utilized as the mobile phase, and was challenging to reformulate into an injectable formulation using an automated synthesis module. When using the benzyl-protected precursor **5** to synthesize [^{11}C]DFP, deprotected precursor **2** could also form during deprotection since not all of **5** gets methylated. To get efficient separation of [^{11}C]DFP from **2** and **5**, we resorted to using an analytical Hydro-RP HPLC column (250 x 4.6 mm) with a large 10 µ particle size. When using this column, efficient separation of the precursor from the standard was achieved with a 2% EtOH buffer (**Figure 2.7 and 2.8**). It was noticed that after adding deferiprone standard to the deprotection solution, a higher yield of [^{11}C]DFP was achieved. Though it is suspected this is helping by mitigating radiolysis, it could also be possible that the higher concentration of a chelating moiety is preventing loss of product by blocking metal binding sites in the stainless steel HPLC system (stainless steel loop, stainless steel column head, etc.). This prompted a change in the buffering salt from monobasic phosphate to citrate, an organic acid found in biological systems that is also a tridentate metal chelator. After switching to a 10mM sodium citrate buffer and keeping the pH at 3.75, the yield of [^{11}C]DFP markedly increased to 50% RCY NDC, confirming that a stainless steel HPLC system can cause loss in production of metal chelating scaffolds where exposed metal binding sites can potentially leach product.

With an efficient and reproducible synthesis finally achieved for [^{11}C]DFP, producing 46 mCi (4.6% Yield from 1 Ci [^{11}C]CH_3I with a molar activity (MA) of 170 Ci/mmol, preclinical studies could now be performed. The synthesis of [^{11}C]DFP as it currently stands is shown in **Scheme 2.5**. The product could be efficiently separated from all UV and radioactive impurities (98% radiochemical purity) using the Synergi Hydro-RP HPLC column with a 4.6 mm diameter and 10 µ particle size with a 2% ethanol 10 mM citrate buffer containing at least 1 mM of ascorbic acid at pH 3.75 (t_R = 13 min)

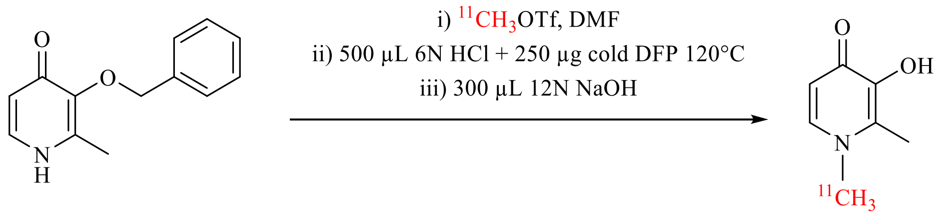

5

3 4.6% RCY NDC

Scheme 2. 5: Radiosynthesis of [^{11}C]DFP using cold standard

2.2.5. *Preclinical Imaging Analysis*

Though there is published data of DFP being able to pass the BBB of rodents at therapeutic doses,[27] we still needed to confirm that our PET tracer was BBB penetrable since there are instances of compounds entering the brain at therapeutic doses but not at PET microdoses (typically only pM amounts). This failure can sometimes be attributed to the compound being an efflux transporter (i.e. p-glycoprotein, p-gp) substrate where not enough compound is added to completely saturate the transporter so that some of the compound can stay in the brain.

During initial evaluation of [^{11}C]DFP in rat, a female Sprague-Dawley rat (430 g) was injected with **3** (0.228 mCi) i.v. via tail vein injection. The rat was scanned for 60 min post-injection of the radiotracer (see experimental section for detailed scanning procedure) and revealed that the PET tracer had little brain uptake with a standard uptake value (SUV) of 0.3 with a fast washout returning to baseline after 30 minutes post-injection (**Figure 2.4).**

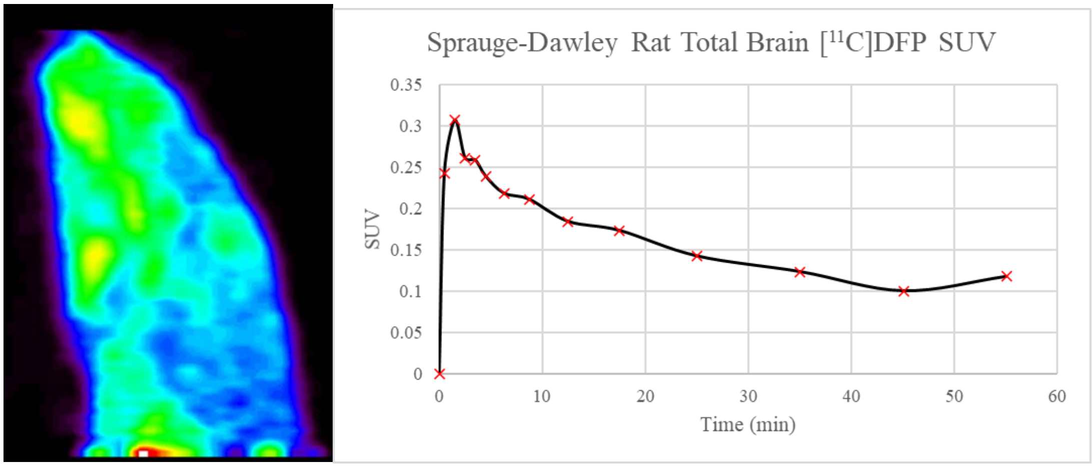

Fig. 2. 4: 1-hour PET image of Sprague-Dawley rat and the time activity curve (TAC) of [^{11}C]DFP in the brain

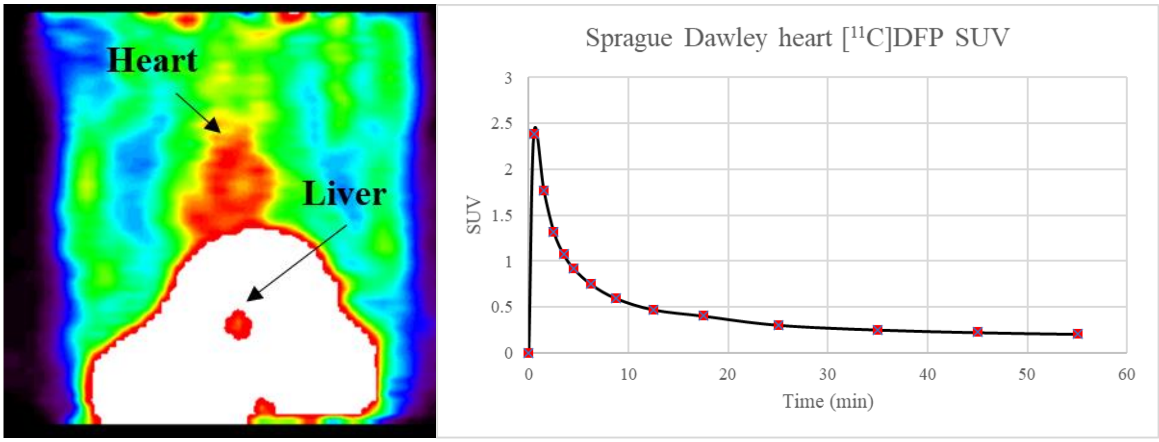

Fig. 2. 5: 1-hour PET image of Sprague-Dawley rat and the time activity curve (TAC) of [^{11}C]DFP in the heart

Measurement of iron in the heart is key to the clinical management of patients at risk of siderotic cardiomyopathy. Normally, this is achieved by MRI, but physicians have an interest in using PET to visualize the heart for iron overload. [^{11}C]DFP showed good initial uptake into the rodent heart within the first minute with a peak SUV of 2.5 (**Figure 2.5**) with fast washout. This higher uptake is expected, being that the heart is mostly composed of blood and muscle cells, which have the most amount of iron after the liver. The live is clearly visible in this image, and shows the highest uptake, where iron is stored and used extensively in cytochrome P450's for oxidative reactions.

The levels of iron in the brain have measured in aging rats where it was found that the highest level of iron occurs during the neonatal stage of the rat's life span and subsequently decreases after growth and remains at low concentrations through most of the adult life.[37] This could explain the low uptake of [^{11}C]DFP, being that its target, iron, is prevented from reaching high concentrations in the rats brain due its inherent toxicity if not regulated properly. It could also be due to the fact stated earlier that DFP could be a substrate for P-gp and not enough compound is present during the PET scan to saturate the efflux transporter for effective brain uptake. Further studies would need to be done to confirm this such as blocking p-gp with Cyclosporin A before imaging.

Since inter-species differences are sometimes apparent between rodents and non-human primates due to the higher metabolic rate in rodents and differing BBB efflux systems, imaging in rhesus macaque brain was also performed (**Figure 2.6**). Imaging studies were performed in a young, mature female rhesus monkey and radiotracer [^{11}C]DFP (3.93 mCi) was injected i.v. via a venous catheter inserted into one hind limb of the monkey and scanned for 60 min. Fortunately, unlike the rodent, [^{11}C]DFP exhibited high brain uptake in NHP reaching a peak SUV of 7.7. The total brain uptake could be attributed to a majority of the signal arising from the cortex, cerebellum, and the subcortical structures like the thalamus and striatum, with peak SUV's reach 1-3 in these regions. This correlates well with known iron concentrations in the various brain structures of humans where the most iron is found in the basal ganglia structures in the midbrain. Further, MRI has been used to assess iron levels in NHPs and also found that iron concentrations were high in the globus pallidus, thalamus, cortex, and cerebellum. Seeing that the image achieved with our tracer correlates well with the data from other groups, this suggests that [^{11}C]DFP is binding iron and the image is representative of the LIP.

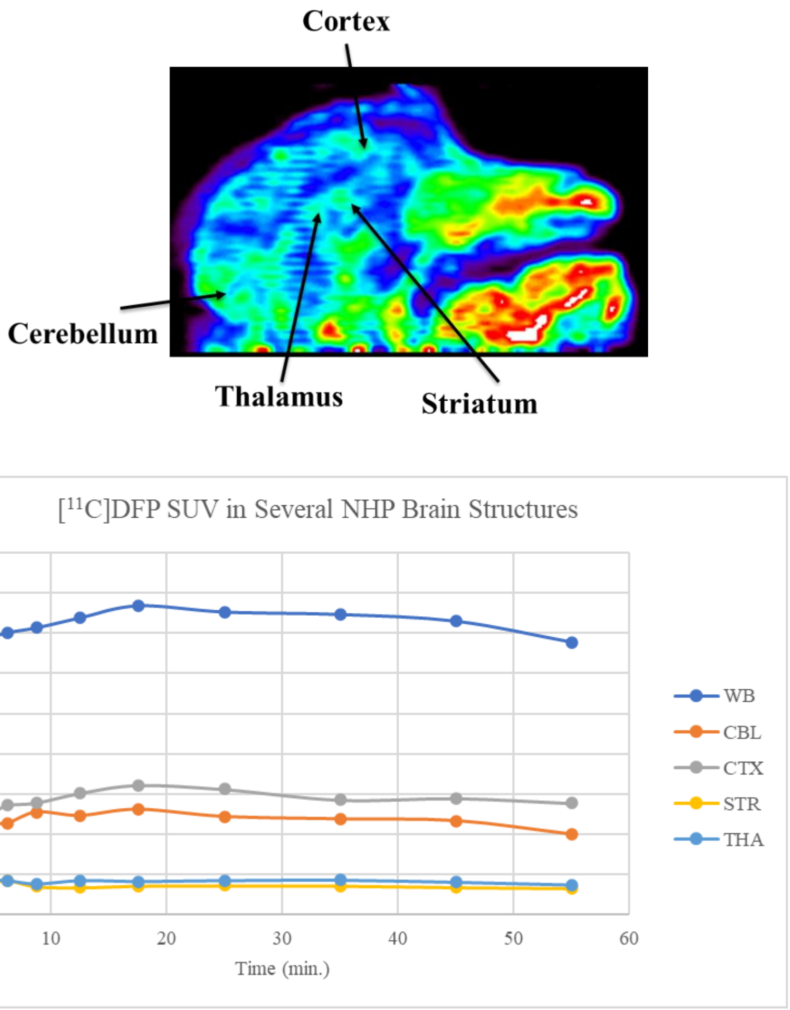

Fig. 2. 6: 1-hour PET image of Rhesus Macaque NHP and the time activity curve (TAC) of [^{11}C]DFP in the total brain, cortex (CTX), Cerebellum (CER), Thalamus (THA), and Striatum (STR).

[^{11}C]DFP also shows slow washout from the brain in NHP. When a PET tracer is observed to have a slow washout, it is thought that it is being trapped in the brain either by forming a trapped metabolite or becoming covalently bonded to its target. This is unlike the kinetics observed in the rat and could possibly be due to the difference in iron concentrations. It is possible for deferiprone to form highly stable 2:1 or 3:1 complexes with one iron atom. However, it is known that transient 1:1 complexes are favored when low concentrations of chelator are used and since the concentration of [^{11}C]DFP is injected in the nM range, this is probably the type of complex that is being formed and not irreversibly binding the iron atom. One possible reason for what seems like

[^{11}C]DFP is slowly washing out is its low molar activity. Normally, tracers with a MA > 500 Ci/mmol highlights the target specifically, saturating those sites without interference from the cold mass. However, since we use cold standard in our synthesis, the molar activity is decreased and we could be seeing nonspecific binding of [^{11}C]DFP. This can be tested by performing a self-blocking study, where DFP is given to the animal before injection of [^{11}C]DFP at 1000x the concentration of the radiochemical dose.

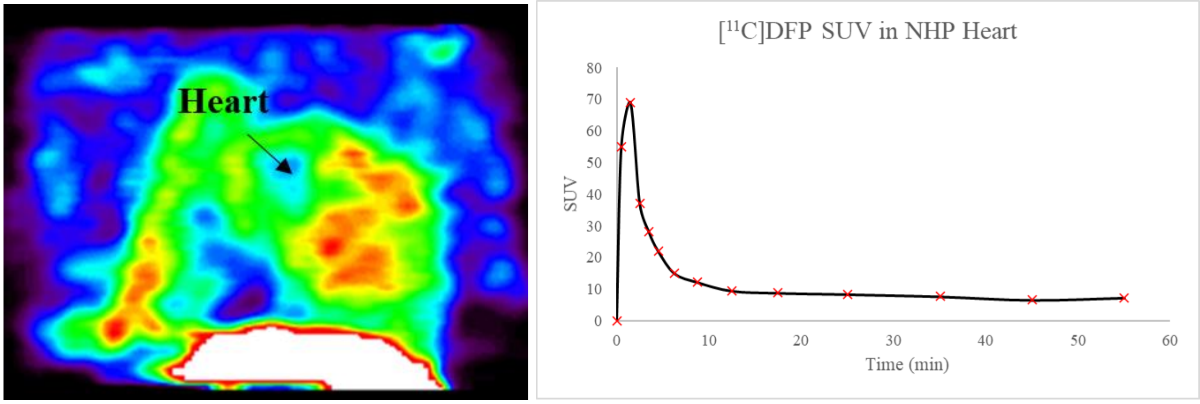

Fig. 2. 7: 1-hour PET image of Rhesus Macaque NHP and the time activity curve (TAC) of [^{11}C]DFP in heart

The remarkably high uptake of [^{11}C]DFP in the heart is observed to be mostly in the chambers of the heart where most of the blood is pooled (**Figure 2.7**). Unlike the kinetics in the rodent, it takes a little longer to reach the maximum SUV of 68 at 2 minutes and has slower washout before returning to a baseline SUV of 7 at 30 minutes.

2.3. Conclusions

The synthesis of [^{11}C]DFP proved to be more difficult and less straightforward than initially thought. Though the more nucleophilic position (being the nitrogen) was thought to be favored for methylation in the presence of the limiting reagent [^{11}C]CH_3OTf, the oxygen position proved to be favored in certain conditions. Also, unknown radiolabeled impurities were seen, and being that there were only two sites for potentially carbon-11 labeling, this was a tremendous surprise and became difficult to try to determine the identity of these side products. A benzyl-protected precursor proved favorable to synthesize the desired product given its commercial availability. Even the purification during semi preparative HPLC proved challenging because the amount of precursor left over would streak into the desired product for collection. Choosing an HPLC column with a small diameter and large particle size allowed for more efficient separation. Preclinical imaging studies proved [^{11}C]DFP can pass the BBB of both rodents and NHPs. Even though the uptake of [^{11}C]DFP was low in rodent, possibly due to low brain iron concentrations in adult rodents, the uptake in the NHP brain was extremely high with a peak SUV of ~8. This uptake would allow for quantification of the LIP available in the brain and be able to detect small changes in its homeostasis. However, the molar activity of [^{11}C]DFP still needs to be improved and determination of the specific binding should be assessed. However, this work has laid the groundwork for synthesizing the first BBB permeable iron chelating PET Tracer, and that it is worth optimizing this PET tracer for human use and testing the metal hypothesis of ND.

2.4. Materials and Methods

2.4.1. *Organic Synthesis*

General Considerations

All the chemicals were commercially available and used without purification. Automated flash chromatography was performed with Biotage Isolera Prime system. High-performance liquid chromatography was performed using a Shimadzu LC-2010A HT system. ^{1}H-NMR spectra were acquired using a Varian 500 apparatus (500 MHz) in $CDCl_3$ or CD_3OD. δ are reported in ppm relative to tetramethylsilane (δ = 0), J are given in Hz. Mass spectra were measured on an Agilent Technologies (Santa Clara CA, USA) Q-TOF HPLC-MS or Micromass (Manchester, UK) VG 70-250-S Magnetic sector mass spectrometer employing the electrospray ionization (ESI) method.

Compounds Synthesized

Preparation of 3-(benzyloxy)-2-methylpyridin-4(1H)-one (**5**):

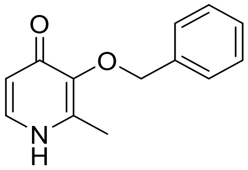

3-hydroxy-2-methylpyridin-4(1H)-one (10 mg, 0.08 mmol) was dissolved with 500 µL MeOH in a 5 mL round bottom flask attached to a water condenser. 1 M of sodium hydroxide (NaOH, 80 µL, 1 equiv.) was added to this solution. Benzyl bromide (104 µL, 10 equiv.) was added to this reaction mixture and left to stir for 2 days under reflux. The reaction mixture was extracted 3x with ethyl acetate and water, rinsed with brine, and dried over sodium sulfate. The crude product was dried over silica and loaded onto a silica column for purification by flash chromatography to provide **4** in 45% yield. A dibenzyl protected product was also observed and was separated during purification. ^{1}H NMR (499 MHz, Chloroform-*d*) δ 7.76 – 6.78 (m, 5H), 5.97 (s, 1H), 5.49 (s, 1H), 5.07 (s, 2H), 2.38 (s, 3H). [M + H], Expected 216.1019, Found 216.1029

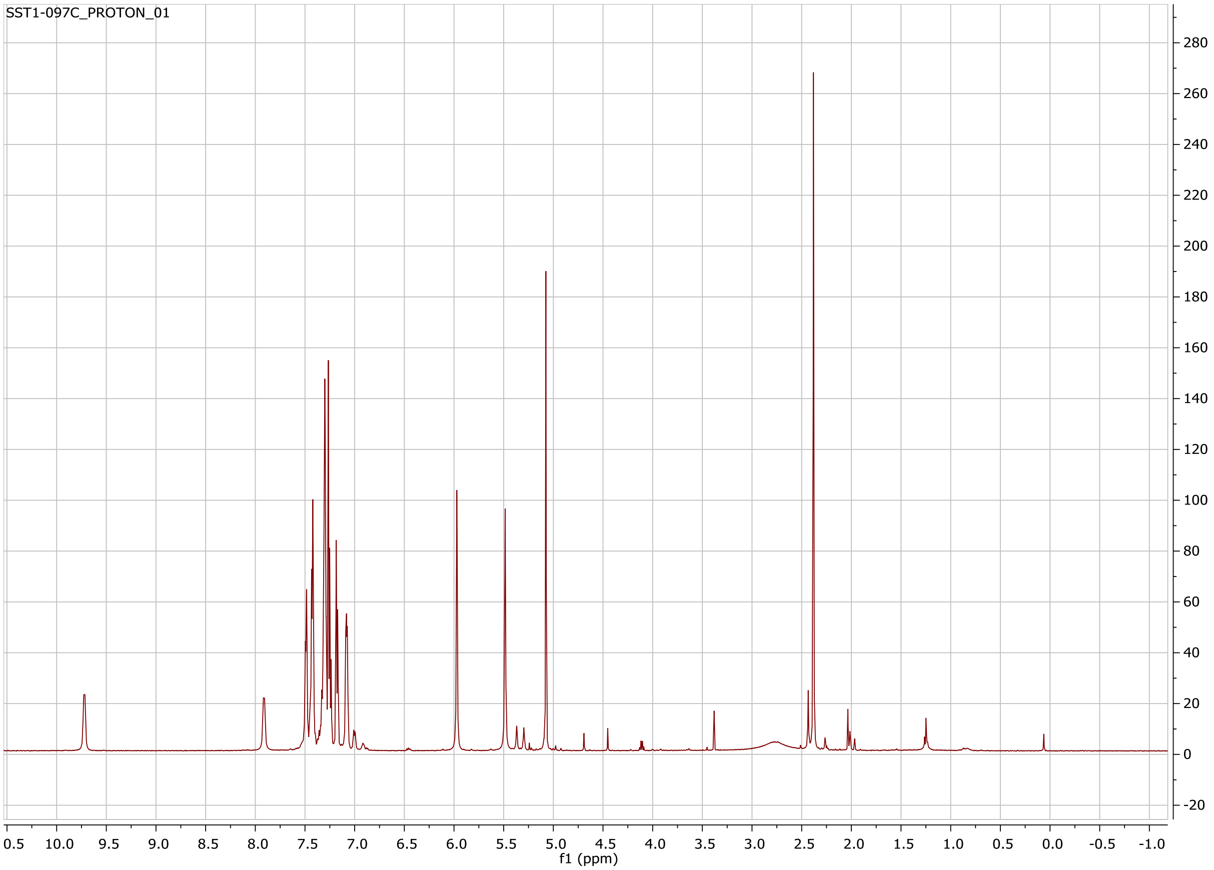

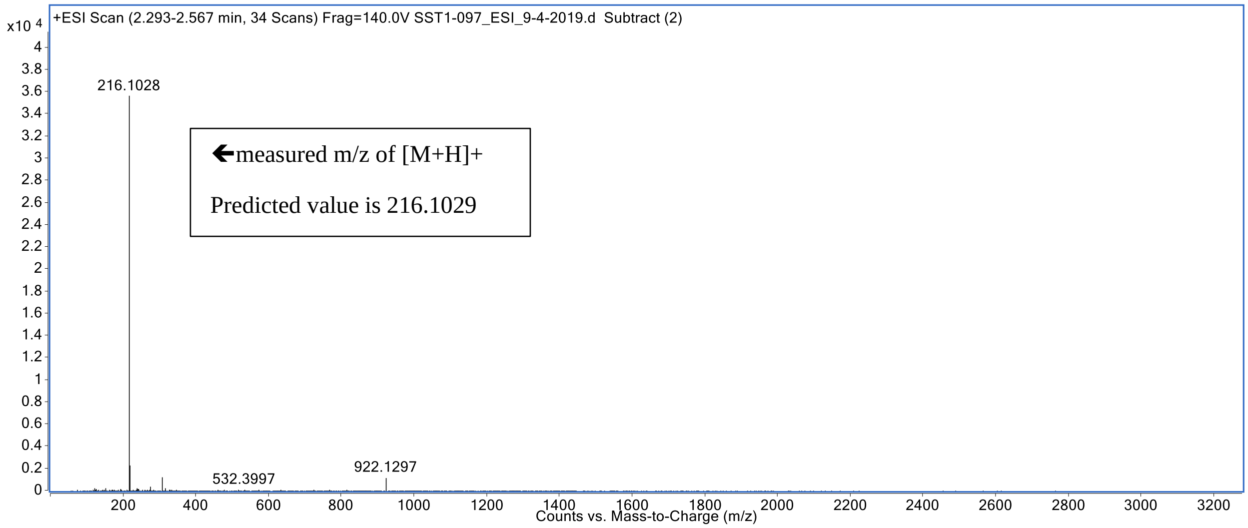

Preparation of 3-(benzyloxy)-1,2-dimethylpyridin-4(1H)-one (**6**):

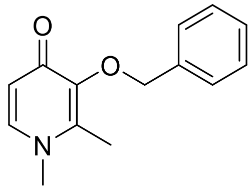

3-hydroxy-1,2-dimethylpyridin-4(1H)-one (**6**, deferiprone, 140 mg, 1 mmol) was dissolved with 140 µL MeOH in a 5 mL round bottom flask attached to a condenser. 1 M of sodium hydroxide (NaOH, 100 µL) was added to this solution. Benzyl bromide (130 µL) was added to this reaction mixture and left to stir for 2 days under reflux. The reaction mixture was extracted 3x with ethyl acetate and water, rinsed with brine, and dried over sodium sulfate. The crude product was dried over silica and loaded onto a silica column for purification by flash chromatography to provide **4** in 45% yield. ^{1}H NMR (499 MHz, Chloroform-*d*) δ 7.43 – 7.37 (m, 2H), 7.35 – 7.25 (m, 3H), 7.17 (d, *J* = 7.5 Hz, 1H), 6.37 (d, *J* = 7.5 Hz, 1H), 5.19 (s, 2H), 3.50 (s, 3H), 2.08 (s, 3H).

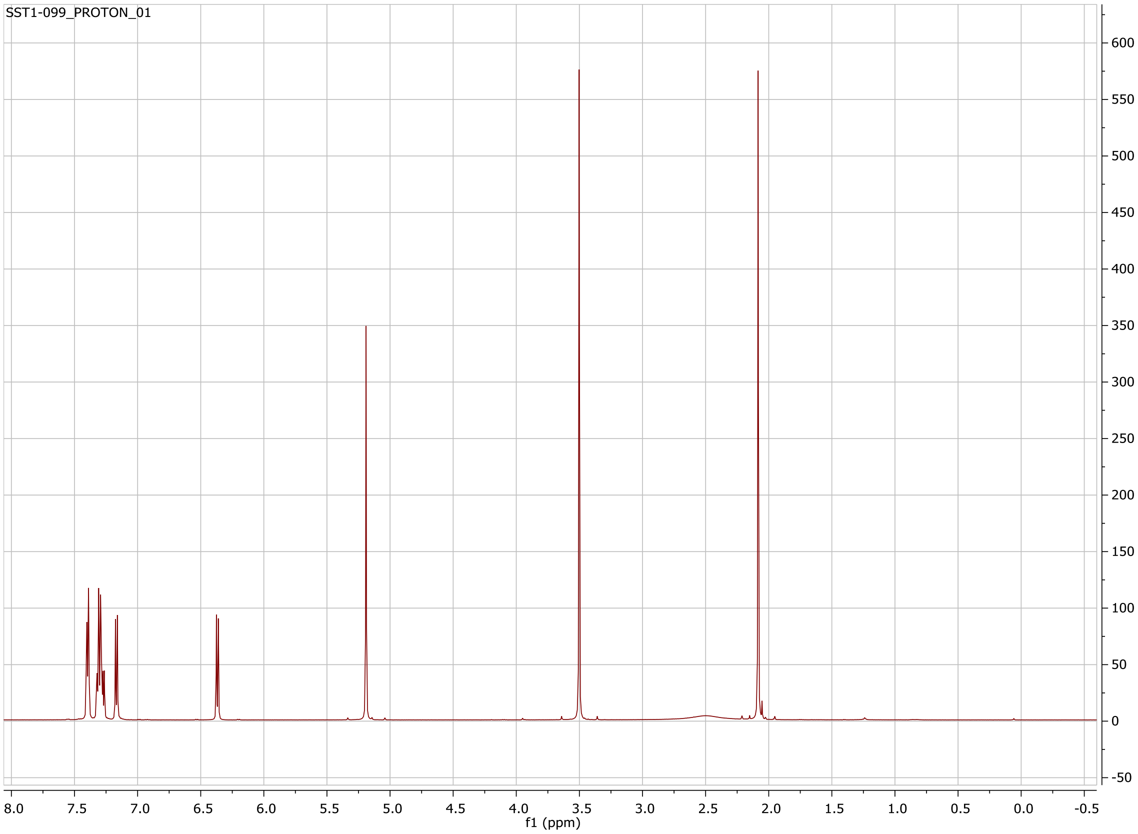

2.4.2. *Radiochemistry*

General Considerations

All the chemicals were purchased from commercially available suppliers and used without purification: Sterile Water for Injection, USP were purchased from Hospira, USP was obtained from Akorn Inc. (Lake Forest IL, USA) HPLC was performed using a Shimadzu (Kyoto, Japan). LC-2010A HT system equipped with a Bioscan B-FC-1000 radiation detector, and HPLC columns were acquired from Phenomenex (Torrance CA, USA). Other synthesis components were obtained as follows: sterile filters were acquired from MilliporeSigma (Burlington MA, USA). GE FX_{Cpro} automated synthesis module was used for all radiosynthesis experiments (**Figure 2.8**).

2.4.2.1. *Preparation of [^{11}C]MeI and [^{11}C]MeOTf*

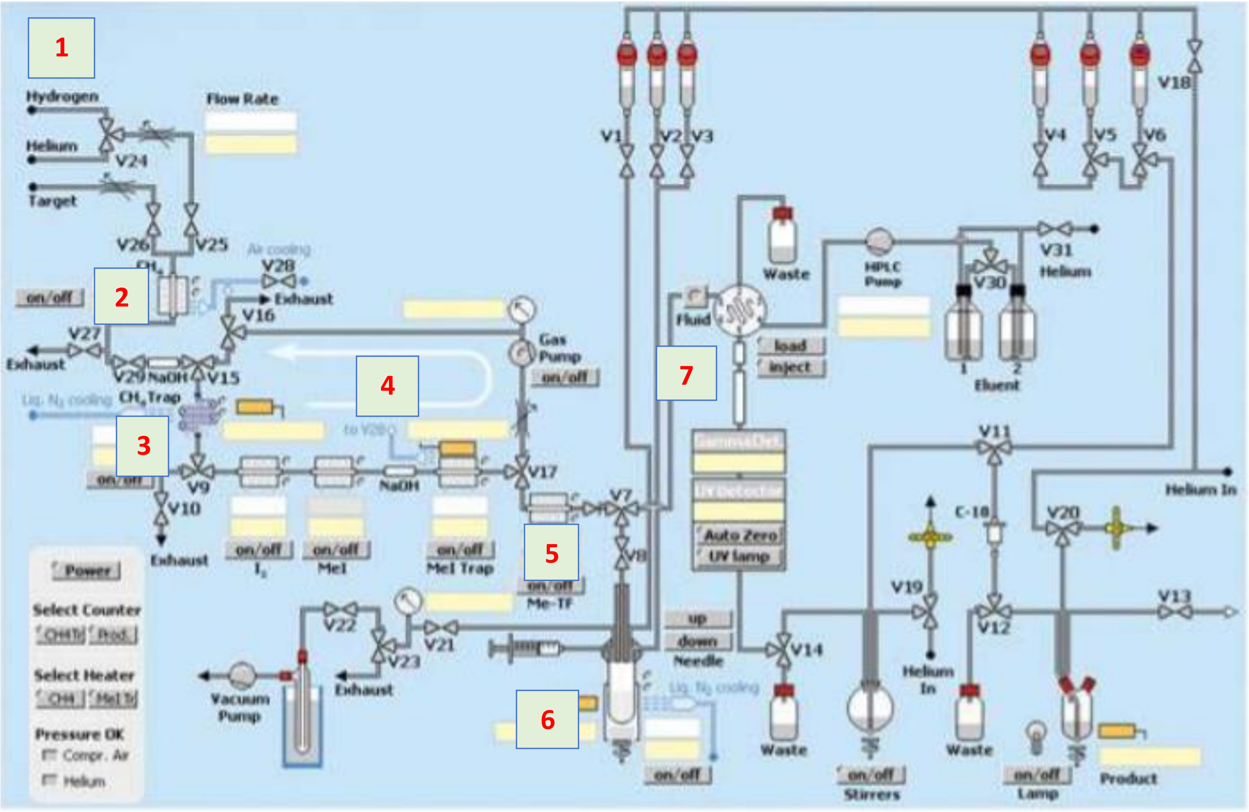

Fig. 2. 8: Schematic of automated radiosynthesis module GE Tracerlab FX_{Cpro}

$[^{11}C]CO_2$ was produced with a General Electric Healthcare (GE, Uppsala, Sweden) PETTrace cyclotron via the $^{14}N(p,\alpha)^{11}C$ reaction. High purity N_2 (g) containing 0.5% O_2 was irradiated at 40 μA for 30 min to generate $[^{11}C]CO_2$ (~ 3 Ci, 111 GBq), which was delivered to a GE TRACERLab FXC-Pro synthesis module (**Fig. 2.8, 1**) through a Teflon delivery line by nitrogen pressure directly to a column packed with 0.3 g of molecular sieve and 0.2 g of Shimalite–Nickle where it was trapped at room temperature. The column was then sealed under hydrogen gas and heated to 350°C for 20 s to reduce the $[^{11}C]CO_2$ to $[^{11}C]CH_4$ (**Fig. 2.8, 2**). The $[^{11}C]CH_4$ was passed through a column of phosphorous pentoxide desiccant and trapped on a column of carbosphere cooled to −75°C (with liquid nitrogen) (**Fig. 2.8, 3**). Gaseous $[^{11}C]CH_4$ was released by heating the carbosphere column to 80°C. Once released, the methane entered a circulation loop, which includes a gas pump, a column of iodine at 100°C, the TRACERLab standard iodine reactor tube at 720°C, two adjacent columns of Ascarite II, and a column of Porapak Q at room temperature (**Fig. 2.8, 4**). The gaseous mixture was circulated for 5 min, whereas $[^{11}C]MeI$ accumulated on the Porapak column. $[^{11}C]MeI$ (~0.9 Ci, 33.3 GBq) was then released from the Porapak column and either delivered directly to the awaiting reactor (or loop), or passed through a silver triflate column (**Fig. 2.8, 5**) , by heating the Porapak column to 190°C. The contents of the silver triflate-Graphpac column were prepared as follows: silver trifluoromethanesulfonate (5 g) was dissolved in anhydrous acetonitrile (100 mL), and the resulting solution was transferred into a round-bottomed flask containing graphite (10 g). The mixture was stirred, and then the solvent was evaporated to complete dryness *in vacuo*. The resulting $[^{11}C]CH_3OTf$ was delivered to the reactor (**Fig. 2.8, 6**) or loop (**Fig. 2.8, 7**).

2.4.2.2. *Reactor Radiosynthesis of [^{11}C]DFP according to* ***Scheme 2.1***

[^{11}C]MeOTf was sparged into the reactor at 15 mL/min through a solution of precursor **2** (1 mg) in DMF/Ethanol/Acetone (100 µL) at room temperature for 3 min or at 0°C and heated to 60°C for 3 min. Following radiolabeling, the reaction mixture was diluted with HPLC mobile phase (1 mL) and purified by semipreparative HPLC (column: Phenomenex Synergi, Polar-RP 5µ, 10 × 250 mm (or Synergi Hydro-RP 4µ 10 x 250 mm) ; mobile phase: 15% acetonitrile (or 5% Ethanol), 10 mM NaOAc (or Na_2HPO_4), pH = 8 (or 3.75); flow rate: 4 mL/min; see **Figure 2.9 and 2.10** for a representative semipreparative HPLC trace). The peak corresponding to [^{11}C]DFP was collected (t_R: 4.74 min. (or 7 min.)) in a round bottom collection flask and transferred to the product vial. After collection in a dose vial, modifications to the dose could be made by alteration of pH or reformulation from MeCN to a saline solution by trapping and eluting off a C18 waters cartridge.

Representative semi-preparative HPLC Chromatogram when using ***HPLC system 2.1***

Column: SYNERGI Polar-RP 5 µ 250 x 10 mm | Buffer: 15% MeCN 10 mM NaOAc pH 8

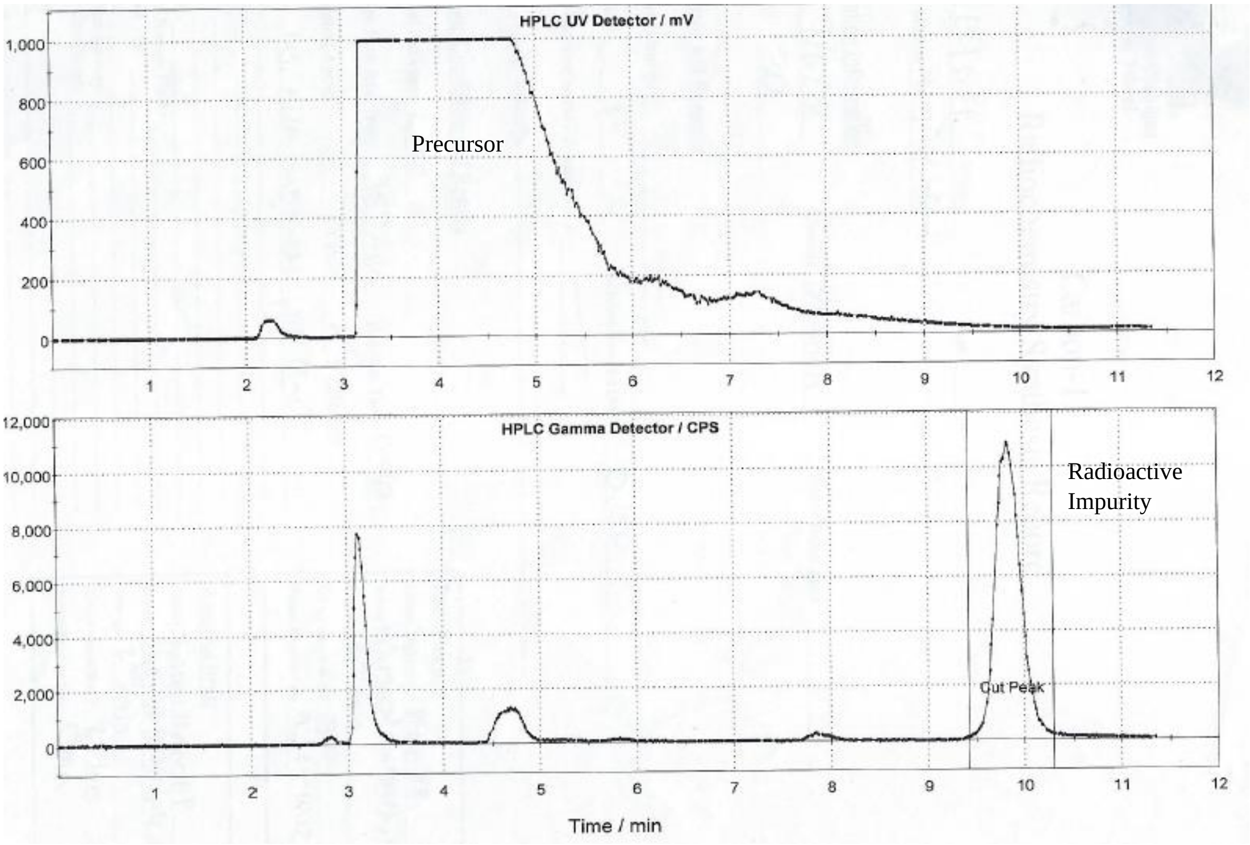

Fig. 2. 9: Semi-prep HPLC chromatogram after [^{11}C]DFP according to Scheme 2.1

*Representative semi-rep HPLC Chromatogram when using **HPLC system 2***

Column: SYNERGI Hydro-RP 4 µ 250 x 10 mm | Buffer: 5% EtOH 10 mM $NaHPO_4$ pH 2.75

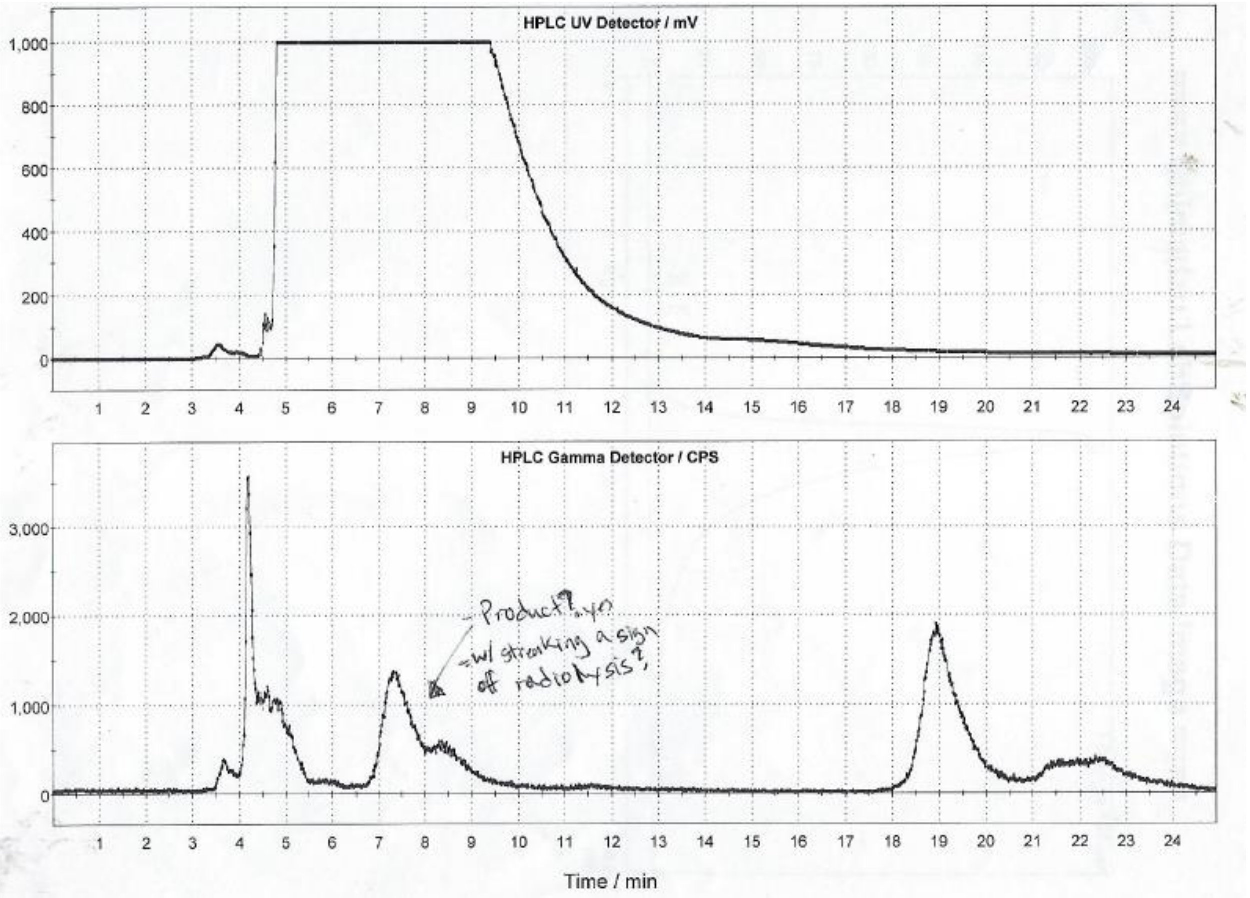

Fig. 2. 10: Semi-prep HPLC chromatogram after [^{11}C]DFP according to **Scheme 2.1**

2.4.2.3. *Loop Radiosynthesis of [^{11}C]DFP tested in* ***Table 2.1***

The Tracerlab synthesis module was configured as illustrated in **Figure 2.11** and loaded as follows: 2 mL steel HPLC loop: 3-hydroxy-2-methylpyridin-4(1H)-one (1.0 mg) in ethanol or butanone/DMSO (100 μL); Vial 4: Semi Preparative HPLC Buffer for Injection, USP (7 mL); Vial 5: Ethanol (0.5 mL); Vial 6: 0.9% NaCl for Injection, USP (9. (System 2) 5 mL. The precursor solution was loaded onto the HPLC loop (2 mL, steel) and conditioned with nitrogen gas for 20 s at 10 mL/min. The [^{11}C]methyl triflate was passed through the HPLC loop at 15 mL/min for 5 min. The reaction mixture was then purified using semipreparative HPLC system 2: 4 mL/min. The product peak was never observed, so no collection occurred.

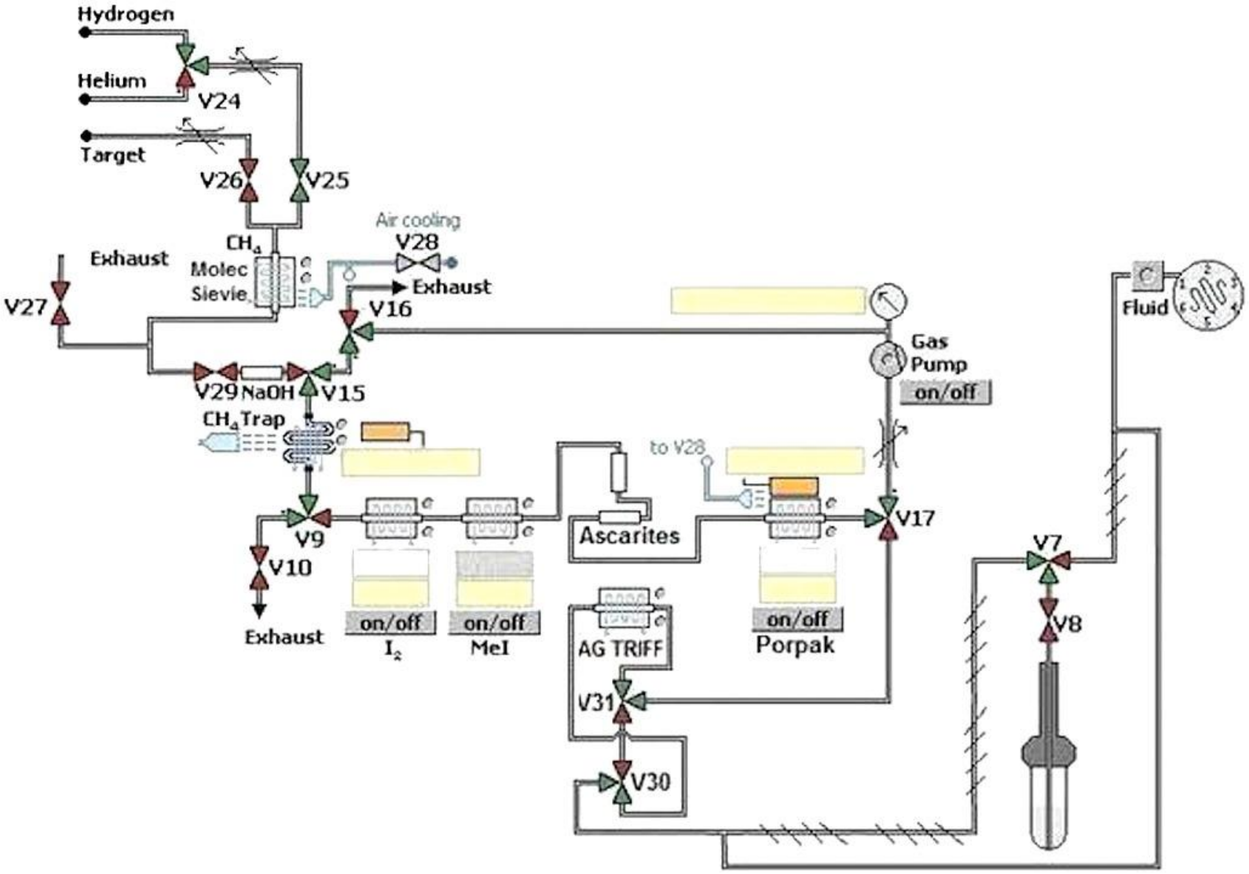

Fig. 2. 11: Schematic of FX_CPro synthesis module reconfigured for Loop Chemistry. $[^{11}C]CH_3OTf$ bypasses reactor to be passed through HPLC loop that contains precursor

2.4.2.4. *Reactor Radiosynthesis of $[^{11}C]$DFP according to **Scheme 2.5***

$[^{11}C]$MeOTf was sparged into the reactor at 15 mL/min through a solution of precursor **5** (1 mg) in DMF (100 µL) at room temperature for 3 min for 3 min. Following radiolabeling, 500 µL of 6N HCl containing 250 µg DFP from Vial 1 was added to the reaction mixture and heated at 120°C for 3 min. After cooling to 60°C, the reaction mixture was quenched with 300 µL of 12N NaOH from Vial 2 and the resulting mixture was purified by semipreparative HPLC (column: Phenomenex Synergi, Hydro-RP 10µ, 4.6 × 250 mm ; mobile phase: 2% EtOH 10 mM NaOAc (or 10 mM Sodium Citrate), 1mM Ascorbic Acid pH = 3.75; flow rate: 0.5 mL/min for 3 min. → 0.7 mL/min for 1 min. → 0.9 mL/min for 1 min. → 1.0 mL/min until product eluted ; see **Figure 2.12 and 2.13** for a representative semipreparative HPLC trace). The peak corresponding to

[^{11}C]DFP (t_R: 13.5 – 16 min.) was collected directly into the product vial containing 100 µL sterile water and 100 µL of a 500 mg/mL Ascorbic Acid solution (50 µg).

*Representative semi-rep HPLC Chromatogram when using **HPLC system 3***

Column: SYNERGI Hydro-RP 10 µ 4.6 x 250 mm | Buffer: 2% EtOH 10 mM NaOAc 1mM Ascorbic Acid pH 3.75

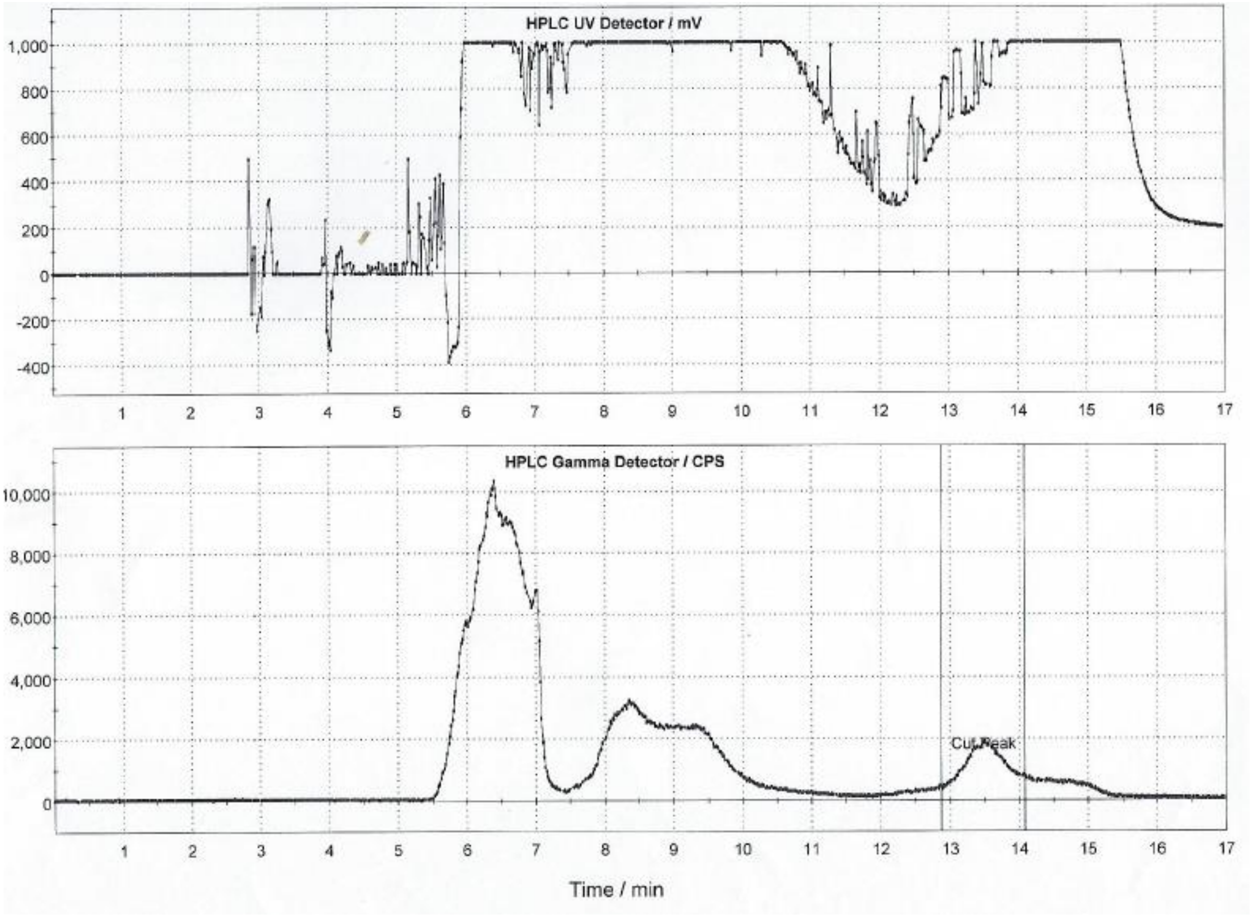

Fig. 2. 12: Semi-prep HPLC chromatogram after [^{11}C]DFP according to Scheme 2.4 using HPLC system 3

*Representative semi-rep HPLC Chromatogram when using **HPLC system 4***

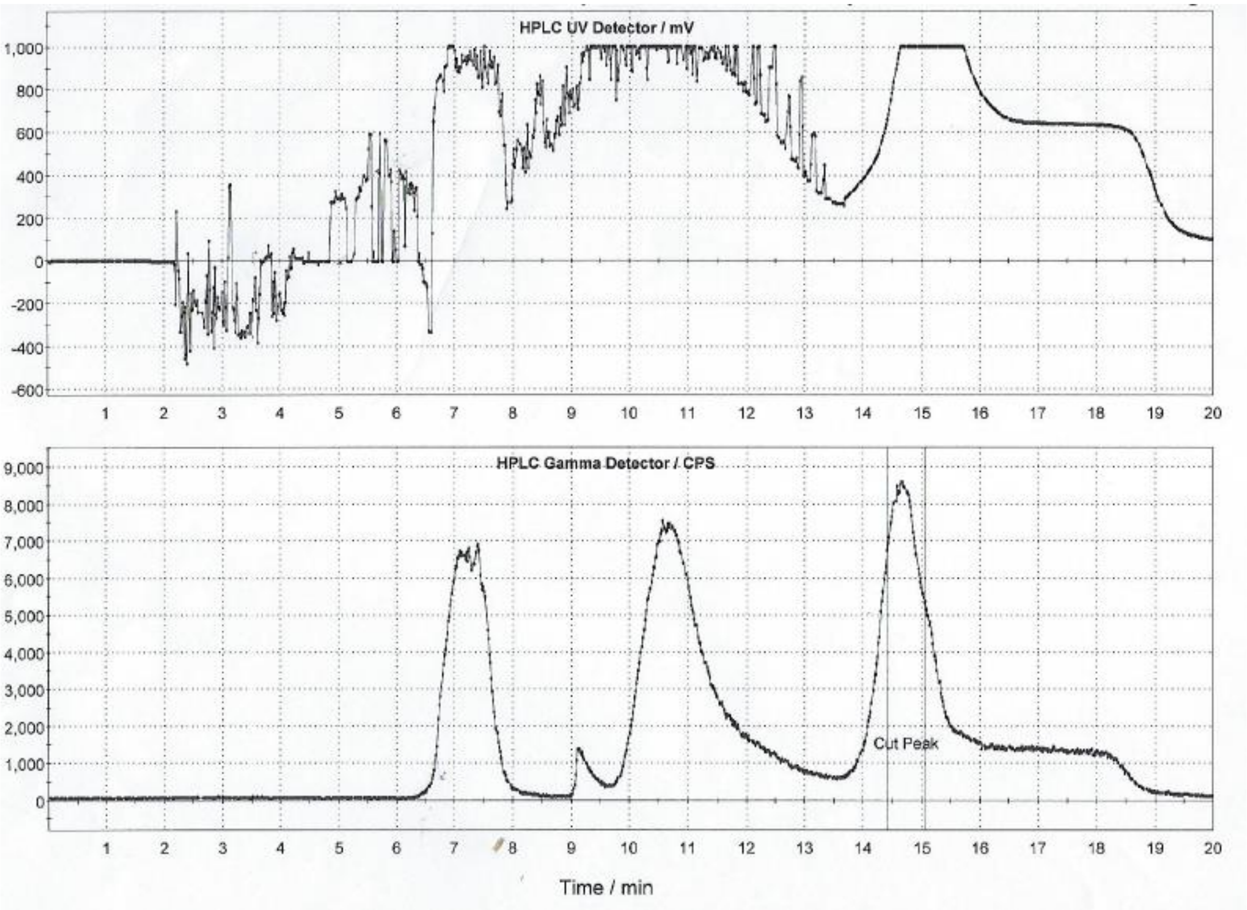

Fig. 2. 13: Semi-prep HPLC chromatogram after [^{11}C]DFP according to Scheme 2.4 using HPLC system 4.

2.4.3. *Quality Control of [^{11}C]DFP*

Doses were visually examined and required to be clear, colorless, and free of particulate matter. The pH of the doses was determined by applying a small amount of the dose to pH-indicator strips and determined by visual comparison to the scale provided. pH needs to be between 4.5 and 7.5, and the pH of each [^{11}C]DFP dose synthesized in this study was either 5.0 after radiosynthesis according to **Scheme 2.1** or pH 7.0 after using radiosynthesis according to **Scheme 2.5**.

Analytical HPLC | Analytical HPLC was performed using a Shimadzu LC-2010A HT system equipped with a Bioscan B-FC-1000 radiation detector (column: Phenomenex SYNERGI Hydro-R, 4µ, 4.6 × 150 mm; mobile phase: 2% ethanol, 10 mM sodium citrate pH: 3.75; flow rate: 2.0 mL/min). Analysis confirmed radiochemical purity 97% (t_R of [^{11}C]DFP ~3 min; see **Figure**

2.14 for a typical analytical HPLC trace) and coinjection with unlabeled reference standard **7** confirmed radiochemical identity.

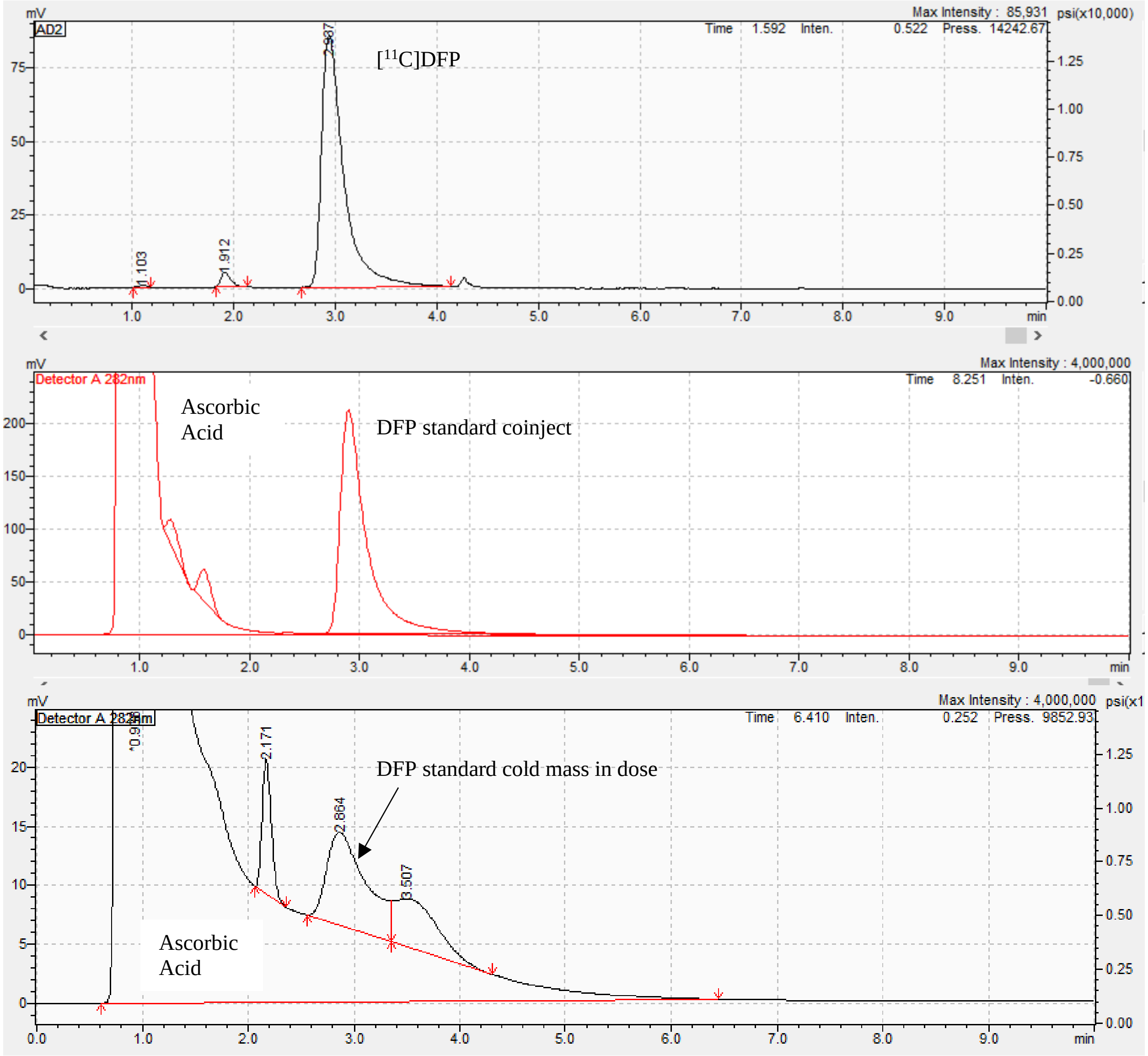

Fig. 2. 14: Analytical HPLC chromatography of [^{11}C]DFP according to Scheme 2.4 with semi-prep HPLC system 4 used for purification

Analysis confirmed O-methylation was achieved from reaction conditions in **Table 2.1 entry 5** with no N-methylation occurring by coinjection with DFP standard 6 and comparison with unlabeled reference standard confirmed radiochemical identity (see **Figure 2.15** for a coinjection HPLC trace).

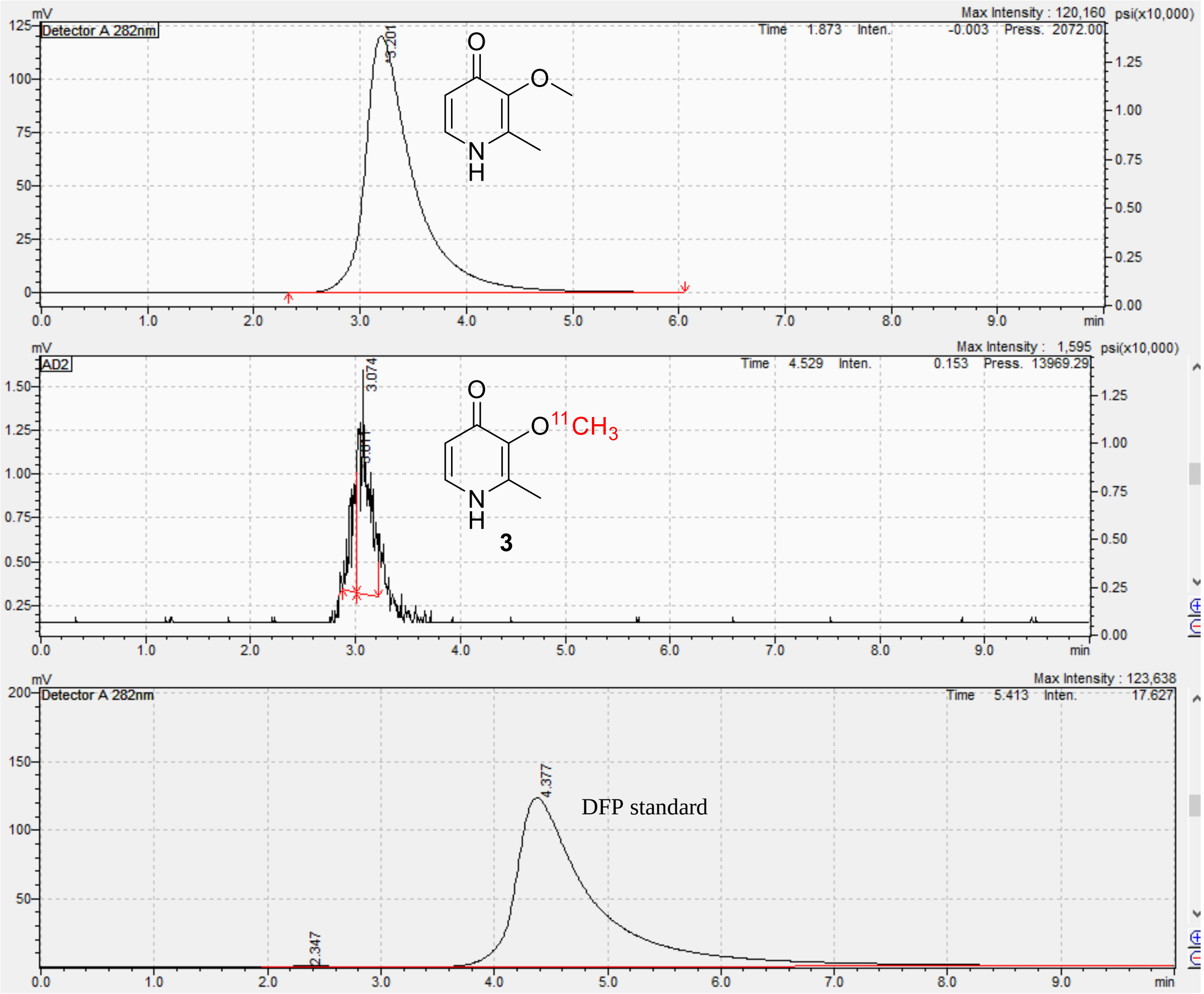

Fig. 2. 15: Analytical HPLC chromatogram confirming the identity of O-methyl product 4

2.4.4. *Preclinical PET Imaging*

General Considerations

Rodent and primate imaging studies were performed at the University of Michigan (UM) using a Concorde (CTI-Concorde, Knoxville TN, USA) MicroPET P4 scanner. The University of Michigan is accredited by the Council on Accreditation of the Association for Assessment and Accreditation of Laboratory Animal Care (AAALAC International, Frederick MD, USA) and imaging studies were conducted in accordance with the standards set by the Institutional Animal

Care and Use Committee (IACUC) at the University of Michigan (PRO00008103: Biodistribution and Pharmacokinetics of Radiolabeled Compounds; Approval date: 1/16/2018).

Animal Husbandry and Housing

Husbandry and housing for rodents and primates is provided by the University Laboratory for Animal Medicine (ULAM) at UM, and animal facilities are in compliance with the regulations defined by the US Department of Agriculture (USDA).

Monkeys: The University of Michigan PET Center has maintained 2 rhesus macaques for ~15 years and the monkeys are individually housed in adjacent steel cages (83.3 cm high × 152.4 cm wide × 78.8 cm deep) equipped with foraging boxes. They are currently housed in adjacent cages as repeated attempts to socially house them in the same cage have been unsuccessful due to aggressive incompatibility. Cages are metal and do contain gridded floors for radiation safety reasons (radioactive waste is contained to the gridded floor and is easier to clean). Temperature and humidity are carefully controlled, and the monkeys are kept on a 12 h light/12 h dark schedule. Monkeys are fed Lab Fiber Plus Monkey Diet (PMI Nutrition Intl. LLC, Shoreview MN, USA) that is supplemented with fresh fruit and vegetables daily. Water and enrichment toys (manipulanda and food-based treats) are available continuously in the home cage.

Rodents: Rats are housed in Allentown #3 micro ventilated cages (27 cm wide × 49 cm deep × 27 cm high, floor area 923 Sq cm) with animal housing densities set by ULAM and the Guide for the Care and Use of Laboratory Animals. Housing is located on ventilated racks with continuous water and air supply exchange. All animals are provided with LabDiet 5LOD as well as enrichment materials and are on a light schedule of 12 h light/12 h dark.

2.4.3.3. *Rodent Imaging Protocol*

Rodent imaging studies were done using a female Sprague–Dawley rat (weight = 237 g, n = 1). The rat was anesthetized (isoflurane), intubated, and positioned in the PET scanner. Following a transmission scan, the animal was injected (via intravenous (i.v.) tail vein injection) with [^{11}C]DFP (2 mCi) as a bolus over 1 min, and the brain and heart imaged separately for 60 min (5 × 1 min frames-2 × 2.5 min frames-2 × 5 min frames-4 × 10 min frames).

2.4.3.4. *Primate Imaging Protocol*

Primate imaging studies were done using a mature female rhesus monkey (weight = 9.4 kg, n = 1).The animal was anesthetized in the home cage with ketamine and transported to the PET imaging suite. The monkey was intubated for mechanical ventilation, and anesthesia was continued with isoflurane. Anesthesia was maintained throughout the duration of the PET scan. A venous catheter was inserted into one hind limb and the monkey was placed on the PET gantry with its head secured to prevent motion artifacts. Following a transmission scan, the animal was injected i.v. with [^{11}C]DFP (3.9 mCi) as a bolus over 1 min, and the brain imaged for 60 min (5 × 2 min frames-4 × 5 min frames-3 × 10 min frames).

PET Image Analysis

Emission data were corrected for attenuation and scatter, and reconstructed using the 3D maximum a priori (3D MAP) method. By using a summed image, regions of interest (ROI) were drawn on multiple planes, and the volumetric ROIs were then applied to the full dynamic data set to generate time-radioactivity curves.

2.5. REFERENCES

1 M. Hadzhieva, E. Kirches and C. Mawrin, *Neuropathol. Appl. Neurobiol.*, 2014, **40**, 240–257.

2 A. M. Daugherty and N. Raz, *Neuropsychol. Rev.*, 2015, **25**, 272–287.

3 P. Brissot, M. Ropert, C. Le Lan and O. Loréal, *Biochim. Biophys. Acta - Gen. Subj.*, 2012, **1820**, 403–410.

4 O. Kakhlon and Z. I. Cabantchik, *Free Radic. Biol. Med.*, 2002, **33**, 1037–1046.

5 Y. Ma, H. De Groot, Z. Liu, R. C. Hider and F. Petrat, *Biochem. J.*, 2006, **395**, 49–55.

6 S. Epsztejn, O. Kakhlon, H. Glickstein, W. Breuer and Z. I. Cabantchik, *Anal. Biochem.*, 1997, **248**, 31–40.

7 Y. Wei, Z. Aydin, Y. Zhang, Z. Liu and M. Guo, *ChemBioChem*, 2012, **13**, 1569–1573.

8 Z. Aydin, *Dr. Diss.*, , DOI:10.1016/0003-2697(67)90113-3.

9 J. Y. Wang, Q. Q. Zhuang, L. B. Zhu, H. Zhu, T. Li, R. Li, S. F. Chen, C. P. Huang, X. Zhang and J. H. Zhu, *Sci. Rep.*, 2016, **6**, 1–13.

10 J. Galazka-Friedman, E. R. Bauminger, K. Szlachta and A. Friedman, *J. Phys. Condens. Matter*, , DOI:10.1088/0953-8984/24/24/244106.

11 R. R. Crichton, D. T. Dexter and R. J. Ward, *Coord. Chem. Rev.*, 2008, **252**, 1189–1199.

12 P. Dusek, M. Dezortova and J. Wuerfel, *Imaging of Iron*, Elsevier Inc., 1st edn., 2013, vol. 110.

13 Z. Luo, X. Zhuang, D. Kumar, X. Wu, C. Yue, C. Han and J. Lv, *PLoS One*, 2013, **8**, 3–9.

14 E. J. Kasarskis, L. Tandon, M. A. Lovell and W. D. Ehmann, *J. Neurol. Sci.*, 1995, **130**, 203–208.

15 K. Gellein, R. M. Garruto, T. Syversen, T. E. Sjøbakk and T. P. Flaten, *Biol. Trace Elem. Res.*, 2003, **96**, 39–60.

16 Y. Nadjar, P. Gordon, P. Corcia, G. Bensimon, L. Pieroni, V. Meininger and F. Salachas, *PLoS One*, 2012, **7**, 2–7.

17 R. Crichton, in *Inorganic Biochemistry of Iron Metabolism: From Molecular Mechanisms to Clinical Consequences*, John Wiley & Sons Ltd., 2nd edn., 2001, vol. 1.

18 A. M. Daugherty and N. Raz, *Neuroimage*, 2016, **128**, 11–20.

19 A. I. Bush, *Curr. Opin. Chem. Biol.*, 2000, **4**, 184–191.

20 V. W. Pike, *Curr. Med. Chem.*, 2016, **23**, 1818–69.

21 T. T. Wager, X. Hou, P. R. Verhoest and A. Villalobos, *ACS Chem. Neurosci.*, 2010, **1**, 435–449.

22 I. Taro Pharmaceuticals U.S.A., Deferiprone Package Insert, https://dailymed.nlm.nih.gov/dailymed/medguide.cfm?setid=5af1643d-4c6e-4668-ae9b-1046f0ad6d8a.

23 G. Abbruzzese, G. Cossu, M. Balocco, R. Marchese, D. Murgia, M. Melis, R. Galanello, S. Barella, G. Matta, U. Ruffinengo, U. Bonuccelli and G. L. Forni, *Haematologica*, 2011, **96**, 1708–1711.

24 A. Martin-Bastida, R. J. Ward, R. Newbould, P. Piccini, D. Sharp, C. Kabba, M. C. Patel, M. Spino, J. Connelly, F. Tricta, R. R. Crichton and D. T. Dexter, *Sci. Rep.*, 2017, **7**, 1398.

25 R. Galanello, *Ther. Clin. Risk Manag.*, 2007, **3**, 795–805.

26 N. Mobarra, M. Shanaki, H. Ehteram, H. Nasiri, M. Sahmani, M. Saeidi, M. Goudarzi, H. Pourkarim and M. Azad, *Int. J. Hematol. Stem Cell Res.*, 2016, **10**, 239–247.

27 A. M. Fredenburg, R. K. Sethi, D. D. Allen and R. A. Yokel, *Toxicology*, 1996, **108**, 191–199.

28 pKa values were estimated using MarvinSketch.

29 P. J. H. Scott, B. G. Hockley, H. F. Kung, R. Manchanda, W. Zhang and M. R. Kilbourn, *Appl. Radiat. Isot.*, 2009, **67**, 88–94.

30 R. E. Hartung, M. C. Wall, S. Lebreton, M. Smrcina, E. I. P. Drive and O. Valley, 2017, **94**, 1305–1313.

31 T. Fukumura, R. Nakao, M. Yamaguchi and K. Suzuki, *Appl. Radiat. Isot.*, 2004, **61**, 1279–1287.

32 B. T. Fukumura, M. Yamaguchi and K. Suzuki, 2004, **123**, 119–123.

33 K. Serdons, A. Verbruggen and G. Bormans, *J. Nucl. Med.*, 2008, **49**, 2071.

34 M. Anbar and P. Neta, *Int. J. Appl. Radiat. Isot.*, 1967, **18**, 493–523.

35 G. V Buxton, C. L. Greenstock, W. P. Helman, A. B. Ross, G. V Buxton, C. L. Greenstock, P. Helman and A. B. Ross, , DOI:10.1063/1.555805.

36 P. G. M. Wuts and T. W. Greene, *Greene's Protective Groups in Organic Synthesis*, John Wiley & Sons, Inc., Hoboken, NJ, USA, 2006.

37 A. Jane, I. Roskams and J. R. Connor, *J. Neurochem.*, 1994, **63**, 709–716.

CHAPTER 3

Development of Copper/Zinc Chelating Scaffolds as PET Radiotracers in Assessing Neurodegenerative Diseases

3.1. Introduction

The role of copper (Cu^{2+}/Cu^{+}) and zinc (Zn^{2+}) in neurodegenerative diseases (NDs) has been extensively reviewed in Chapter 1. Briefly copper, being a redox active metal, can bind to small peptides implicated in NDs such as amyloid-ß (Aß), α-synuclein (α-syn) and Tar DNA Binding Protiein-43 (TDP-43), and react with H_2O_2 to form hydroxyl radicals. This results in oxidative stress and eventually neuronal cell death.[1] Zinc exhibits toxic effects by inducing the aggregation of these small peptides like Aß[2] and TDP-43.[3] We hypothesized that imaging the presence of the resulting metal-protein complexes or accumulation of the divalent metals (Cu^{2+}/Zn^{2+}) in certain brain regions would allow detection of neurodegeneration at an earlier time point than is currently possible using, for example, amyloid positron emission tomography (PET). For an overview of current clinical PET radiotracers for imaging neurodegeneration, please refer to Chapter 1. This is an ambitious hypothesis, yet the development of such radiotracers would allow biological studies on preclinical animal models, human diseased tissue, and early-stage ND patients to better understand the roles which metal dysregulation plays in neurodegeneration and at what time points.

The first attempt to radiolabel a metal chelating scaffold was reported by Bush *et al.*[4] in 2006. The divalent metal chelator clioquinol (CQ), which was used in Phase II clinical trials for Alzheimer's Disease (AD),[5] was radioiodinated with iodine-125 to create the single-photon emission computed tomography (SPECT) agent [^{125}I]CQ (**Figure 3.1**). Hydroxyquinoline scaffolds were the primary focus in creating metal-chelating radiotracers for the next ten years as even PET isotopologs of CABS13 and PBT-2 (another divalent metal chelator used in clinical trials of AD) were developed by Vasdev *et al.*[6–8] The SPECT agent [^{125}I]CQ and the PET agent [^{18}F]CABS13 showed moderate brain uptake. When [^{18}F]CABS13 was tested in a non-human primate (NHP) however, it had no brain uptake (**Figure 3.1**). This animal species difference in brain uptake of [^{18}F]CABS13 is thought to be due to a primate-specific efflux transporter. [^{11}C]PBT-2 showed high brain uptake into a NHP. One compound that was found in a high-throughput screen (HTS) that saved yeast ND cell models burdened with α-syn and TDP-43 toxicity was HQ415, a small molecule containing a hydroxyquinoline moiety. A methoxy-group proved advantageous to be radiolabeled with carbon-11. [^{11}C]HQ415 revealed high brain uptake in NHP PET scans performed by our lab (**Figure 3.1**),[9] concurrent with Vasdev's development of [^{11}C]PBT-2. Thus, two divalent metal chelating PET radiotracers with high brain uptake were revealed in 2018.[8,9] As carbon-11 has a short half-life (~20 min.) compared to fluorine-18 (~110 min.), a fluorine-18 analog of the hydroxyquinoline PET radiotracers is highly sought after in order to perform preclinical evaluation such as autoradiography. Attempts to synthesize fluorine-18 labelled HQ415 (**Figure 3.2**) are discussed in this chapter.

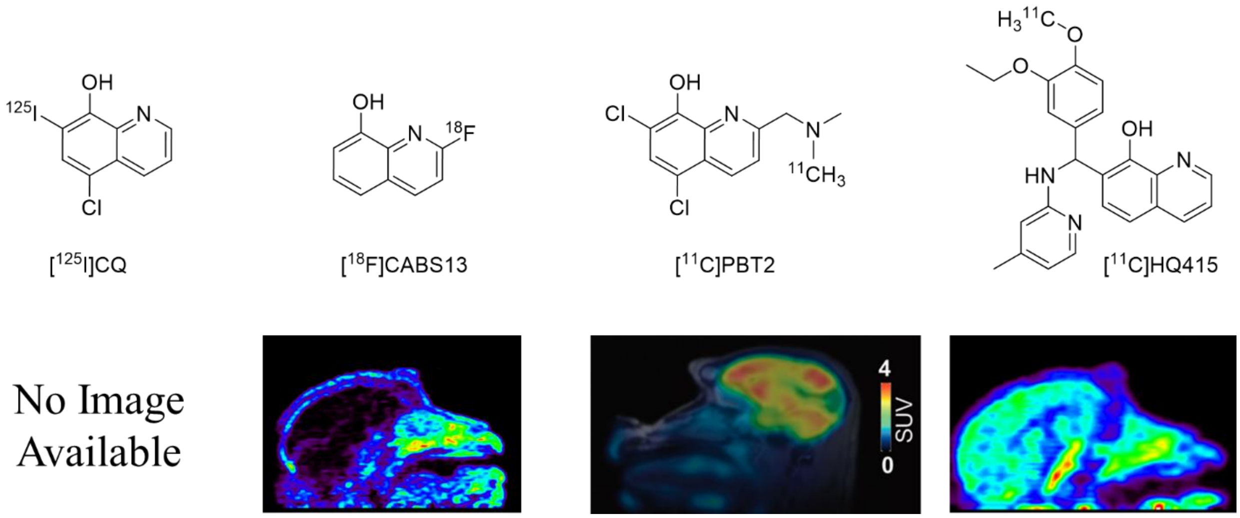

Fig. 3. 1: Structures and brain uptake images using hydroxyquinoline scaffold PET tracers in NHP with [^{125}I]CQ[4] and [^{18}F]CABS13[6-8] showing little to no brain uptake and [^{11}C]PBT2[8] as well as [^{11}C]HQ415[9] having high SUV

Finally, a novel metal-chelating scaffold based on creating a stilbene derivative (a common scaffold known to bind Aß) was reported by Mi Hee Lim *et al.*[10,11] It was shown that the N,N-bidentate chelating moiety could bind Zn^{2+} and Cu^{2+} with higher affinity for the latter metal. The compound, known as L2-b, was shown to disrupt Aß aggregation and also confirmed to interact with Cu^{2+}-Aß complexes. The dimethyl aniline on the compound afforded an opportunity for carbon-11 labeling. Fluorine-18 labelling of the aniline moiety also allowed our group to show that the compound gets into the brain (**Figure 3.3**), as well as have high specific binding in AD cortex tissue when compared to age-matched controls.[12] Autoradiographic assessment of other ND tissue such as dementia with Lewy bodies (DLBD) and Parkinson's Disease (PD) were performed with [^{11}C]L2-b (**Figure 3.2**), showing high binding potential (BP) as well. We hypothesized that L2-b was not specific to just metal-Aß complexes but could potentially bind metal-protein aggregates that can form ß-pleated sheets. One peptide aggregate that has yet to be quantified using molecular imaging techniques is TDP-43, the protein aggregate that is implicated in Amyotrophic Lateral Sclerosis (ALS). It has been shown that Zn^{2+} can bind the N-terminus of TDP-43 *in vitro* and cause its aggregation into amyloid-like aggregates.[3] Herein we describe efforts to synthesize of [^{18}F]FHQ415 and the assessment of [^{18}F]FL2-b in ALS tissue. We wanted to determine if this approach could differentiate ALS brain tissue from control region matched tissue through autoradiography studies. A radiotracer with a higher BP in ALS tissue would greatly benefit the medical field, helping physicians to monitor this debilitating disease by being able to visualize the accumulation of toxic biomarkers present only during disease.

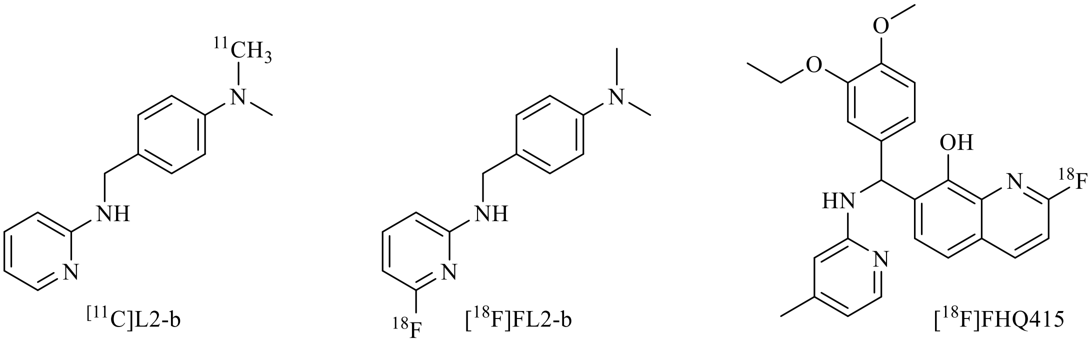
[^{11}C]L2-b [^{18}F]FL2-b [^{18}F]FHQ415

Fig. 3. 2: Alternative metal chelating PET Tracer [^{11}C]L2-b and the desired fluorine-18 derivatives of L2-b and HQ415.

To assess if [^{18}F]FL2-b could be used as a radioligand for ALS, autoradiography was performed on post-mortem ALS tissue slices (20 µm thick). Post-mortem tissue can be used for the quantitative determination of binding parameters (K_d, B_{max}) for novel radioligands through saturated binding studies. The use of intact tissue slices was chosen, as opposed to traditional tissue homogenate because of the ability to visualize anatomical regions as well as the regional distribution patterns of radiotracer binding, which can then be compared to immunohistochemical staining of the protein of interest (i.e.TDP-43 aggregates) on the same tissue. Also, in tissue homogenates, not all binding sites are equally accessible to the radioligand which could lead to an underestimation of the target density (B_{max}).

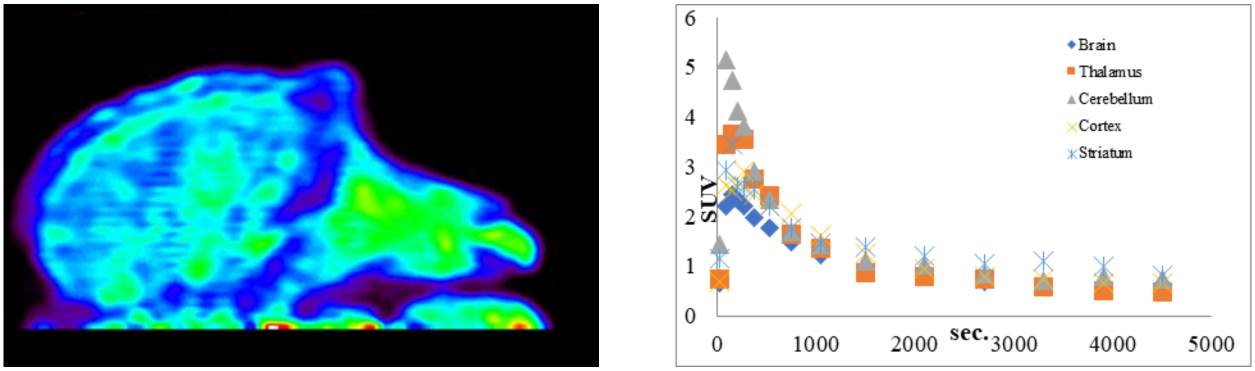

Fig. 3. 3: NHP brain uptake of [^{18}F]FL2-b

3.2. Results and Discussion

3.2.1. *[^{18}F]FHQ415*

Synthesis of [^{18}F]FHQ415, Precursor, and Standard

Based on our synthesis of the [^{11}C]HQ415 precursor and standard,[9] we envisioned performing the same Betti reaction to synthesize a fluorine-18 labeling precursor with either the pyridine or hydroxyquinoline containing a labile moiety for fluorine-18 labeling at the 2 position of the quinoline or 6-position of the 2-amino pyridine, which has the least electron density for nucleophilic fluoride to attach (**Scheme 3.1**).

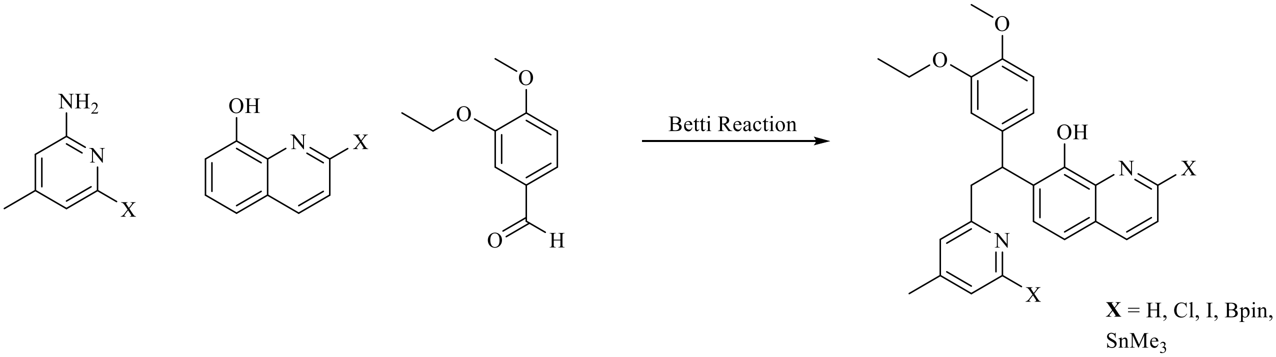

Scheme 3. 1: First step in potential synthesis of [^{18}F]FHQ415 precursor

Looking into commercially available hydroxyquinolines and 2-amino-pyridines, chlorine substituents were readily available. As the synthesis of an ^{18}F-hydroxyquinoline had already been reported with the synthesis of CABS13,[6,7] we decided to investigate the analogous labeling strategy for HQ415. The reported synthesis takes advantage of a benzyloxymethyl acetal (BOM) protecting group on the 8-hydroxy functionality. Anticipating that a BOM group would cause steric collision and reduce the yield for protected-HQ415, a methoxymethyl (MOM) was used to mitigate this risk (**Scheme 3.2**). The fluoro MOM-protected HQ415 (**6**) was synthesized in a microwave reactor with anhydrous tetrabutylammonium fluoride (TBAF) in modest yields. Product identity was confirmed by NMR and mass spectrometry. Deprotection of the MOM group with HCl provided **7** in 25 % yield as measured by HPLC.

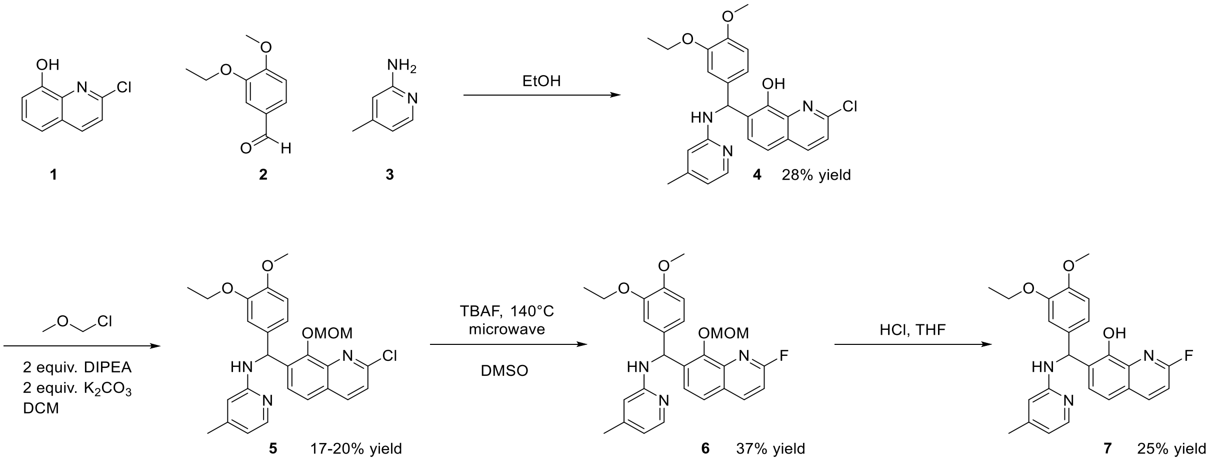

Scheme 3. 2: First attempt to synthesize [^{18}F]FHQ415 precursor and standard

Isolation and storage of standard **7** revealed that it was unstable. Thus, during the initial attempt to radiolabel precursor **5** (**Scheme 3.3**) with fluorine-18, standard was prepared immediately before the radiosynthesis and extracted from the reaction mixture without purification. Crude product **7** was then coinjected with the radiochemical reaction mixture to determine if **9** had been synthesized. Initial radiofluorination with tetraethylammonium (TEA) fluoride at 140°C of **5** gave 2% radiochemical yield (RCY) of MOM-protected [^{18}F]FHQ415 (**[^{18}F]6**) and was confirmed by co-injection with **6** on an analytical High-Performance Liquid Chromatography (HPLC) column. Surprisingly, the unprotected aniline did not hinder the fluorination reaction. Once this product was confirmed, different conditions for deprotection of

[^{18}F]6 were investigated to afford [^{18}F]FHQ415 (**Table 3.1**). Premature deprotection of the MOM group took place during the radiofluorination step indicated by a gamma peak with a retention time (r.t.) matching the FHQ415 (**7**) standard. Analytical HPLC analysis of the deprotection reactions B, C, and D revealed a gamma peak matching the r.t. of 7, confirming the production of **[^{18}F]7** with yields reported in **Table 3.1**. As HCl is a milder acid than trifluoracetic acid (TFA), we omitted running HPLC analysis of the conditions after confirming HCl worked at low concentrations and room temperature (rt).

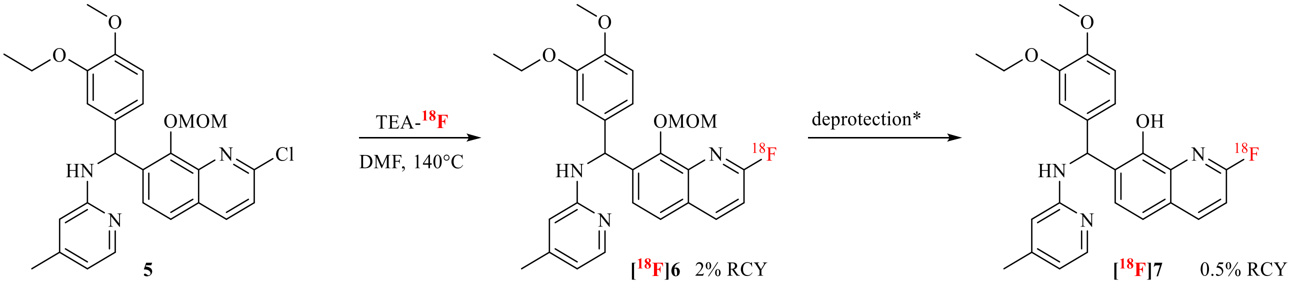

Scheme 3. 3: Radiosynthesis of [^{18}F]FHQ415. *See Table 3.1 for deprotection yields.

Deprotection Conditions	RCC	Confirmed Product 9 by HPLC
conc. HCl at 100°C	>99%	no
conc. HCl at rt	>99%	yes
4 M HCl in dioxane at 100°C	>99%	yes
4M HCl in dioxate at rt	89.35%	yes
TFA at 100°C	65.30%	NA
TFA at rt	74.90%	NA

Table 3. 1: Deprotection reactions of MOM-[^{18}F]FHQ415 (8) to form 9

Knowing that the precursor was suitable for radiolabeling, the synthesis of standard needed to be optimized. To increase the yield of the fluorination step for production of **6**, several fluorination conditions were tested. Use of anhydrous TBAF using thermal heat instead of a microwave at 140° was attempted. Use of dipinacol TBAF ((Pin)$_2$TBAF), cesium fluoride (CsF), or tetramethylammonium fluoride (TMAF) as a fluorinating reagent at rt or 100°C did not provide the desired product (**Scheme 3.4**). Noticing that the free hydrogen bond of the aniline could be inhibiting the fluorination by formation of an H-F bond, it was protected with a tert-butyloxycarbonyl (BOC) group and tested again with TMAF at 80°C (**Scheme 3.5**). These conditions afforded conversion of the chloro-HQ415 (**10**) to the fluoro-HQ415 (**11**), However, complete conversion was not observed by NMR, and **10** and **11** could not be separated from each other by flash chromatography.

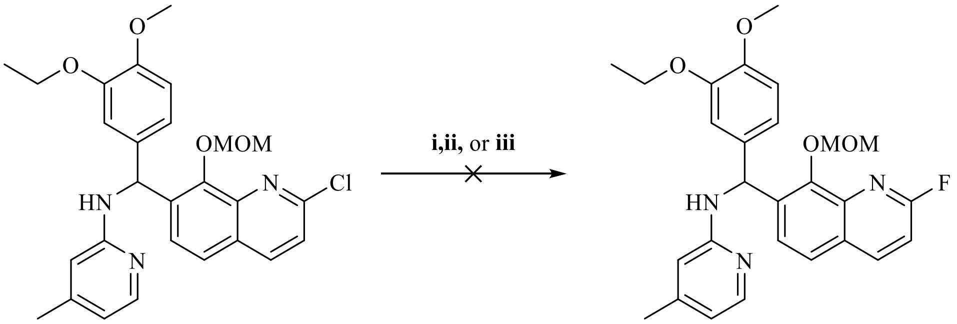

Scheme 3. 4: Various fluorinating reagents tested i) (Pin)$_2$TBAF, ii) TMAF, and iii) CsF. All reagents were tested using DMF as solvent at either rt, 80°C, or 100°C.

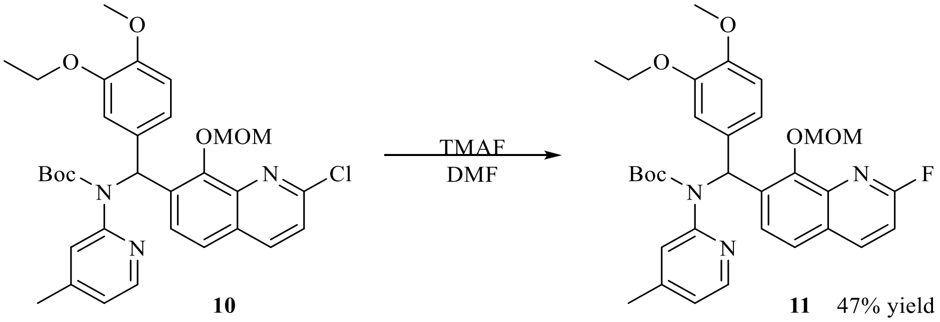

10

11 47% yield

Scheme 3. 5: Successful fluorination of fully protected [^{18}F]FHQ415 precursor

To prevent having to run two separate protecting reactions on scale up of the chloro-HQ415 precursor **10**, diBoc-protected chloro-HQ415 (**12**) was synthesized in 66% yield using Boc$_2$O and catalytic 4-(dimethylamino)pyridine (DMAP). Fluorination of **12** using TMAF afforded diboc-protected fluoro-HQ415 (**13**) standard in 43% yield (**Scheme 3.6**).

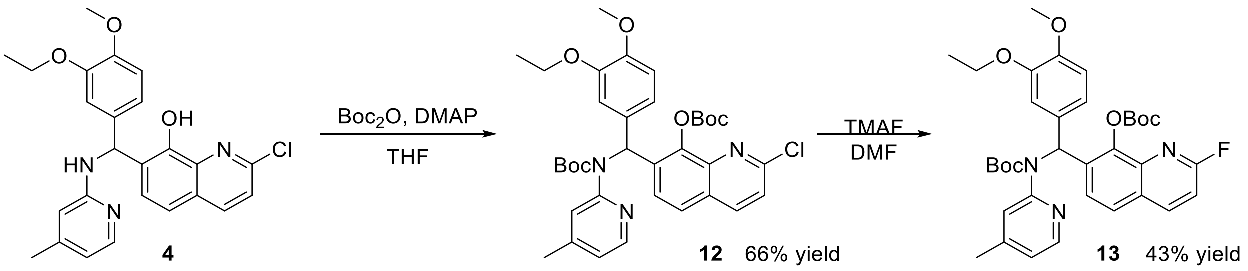

Scheme 3. 6: Synthesis of [18F]FHQ415 precursor **12** and protected fluoro-HQ415 standard **13**

Future work will optimize yield of [18F]HQ415 **9** to produce amounts suitable for use in preclinical evaluation (*in vitro* autoradiography and *in vivo* PET imaging).

3.2.2. *[18F]FL2-b*

Synthesis of [18F]FL2-b and Autoradiograhy of ALS tissue

[18F]FL2-b was synthesized in 3.2% radiochemical yield (RCY: 58 mCi from 1.8 Ci $^{18}F^-$) according to our recently reported procedure.[13] By comparing specific binding of [18F]FL2-b in diseased brains with that of age-matched controls (**Table 3.2**), we investigated whether [18F]FL2-b binds to the TDP-43 aggregates over-expressed in ALS tissue that are not present in healthy brains. The K_d of [18F]FL2-b in motor cortex tissue was calculated to be 9.8 ± 1.4 nM, almost identical to that found in the autoradiography studies performed on frontal cortex tissue (K_d = 9.4 nM) reported previously.[12] The B_{max} calculated in both ALS and age-matched control tissue was found to be 12.9 ± 0.2 nM and 7.7 ± 1.3 nM respectively (see section 3.3 Material and Methods). Thus, the specific binding of [18F]FL2-b can be attributed to a target that has twice the density in ALS tissue when compared to control. However, the target responsible for the specific binding in ALS still needed to be elucidated. Since L2-b was designed to bind metal-protein aggregates (e.g. Cu^{2+}-Aß)and have no affinity when the metal was absent, it was suspected that [18F]FL2-b could be binding metal-TDP-43 aggregates, as it has been shown that Zn^{2+} can induce amyloid like aggregation of TDP-43, the protein responsible for aggregates found in ALS.[3]

Tissue Identifier	Pathological Diagnosis	Brain Region	Age at Death	Sex
1670	ALS	CTX	57	F
729	CON	CTX	59	M
1739	ALS	CTX	51	M
1539	CON	CTX	53	F
1705	ALS	CTX	77	F
1432	CON	CTX	83	F

Table 3. 2: Tissue identifiers

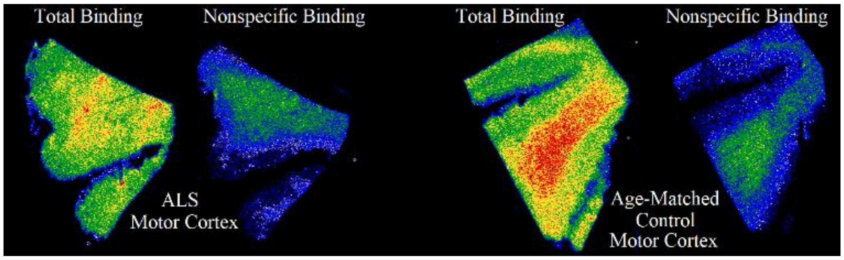

Fig. 3. 4: [^{18}F]FL2-b autoradiography in ALS motor cortex tissue sections

Specific Binding Analysis of [^{18}F]FL2-b: How does it bind?

To test if the binding of [^{18}F]FL2-b was attributable to metal chelation, autoradiography was performed in the presence of 50 µM EDTA (1000x the [^{18}F]FL2-b concentration), a general metal chelator used to block any metal binding sites. The total binding of [^{18}F]FL2-b was significantly reduced in the presence of EDTA, comparable to that of nonspecific binding in ALS tissue (**Figure 3.5b**) or even more so in the age matched control tissue (**Figure 3.5a**), strongly suggesting that the specific binding of [^{18}F]FL2-b is indeed mediated through metal-chelation.

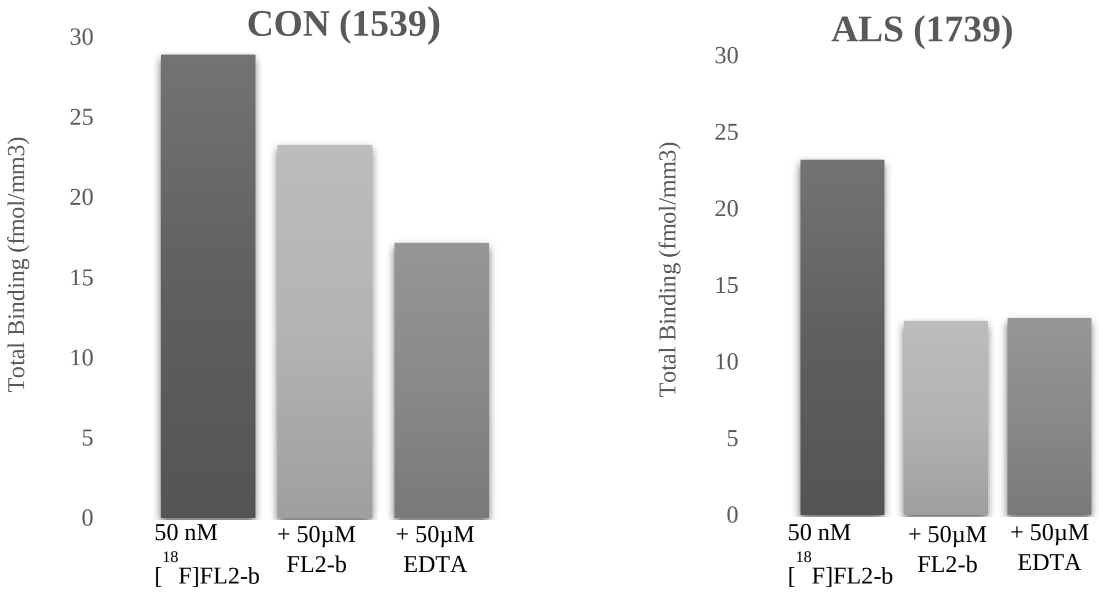

Fig. 3. 5: Total binding of [^{18}F]FL2-b and total binding after blocking with cold standard FL2-b and EDTA in a) Control (CON) and b) ALS motor cortex tissue

To further investigate the possibility of [^{18}F]FL2-b binding to TDP-43 aggregates, overlaying of immunohistochemical data (obtained with TDP-43 antibodies) over autoradiography images was done to identify if specific binding of the radiotracer could be correlated to the regional distribution of TDP-43 aggregates associated with ALS (**Figure 3.6**). Immunohistochemistry using anti-pTDP-43 antibody was performed to visualize the different types of aggregates present in ALS. Although intranuclear inclusions (red, **Figure 3.6**) form as a result of normal aging, cytosolic inclusions and dystrophic neurites (green, **Figure 3.6**) are forms of toxic TDP-43 aggregates that precede motor neuron degeneration.[14] The distribution of toxic TDP-43 aggregates was concentrated in the gray matter, falling off in concentration or almost nonexistent when examining the white matter, as has also been previously reported from other post-mortem immunohistochemical analysis of pTDP-43 in ALS.[15] Autoradiographic saturated binding studies showed that [^{18}F]FL2-b has specific binding in the gray matter where the toxic TDP-43 aggregates are most abundant. Binding of [^{18}F]FL2-b in the white matter was found to be linear with concentration and non-displaceable, meaning only nonspecific binding was occurring in this region. Since metal-TDP-43 aggregates have only been formed *in vitro* and not isolated from tissue samples, the cause of [^{18}F]FL2-b's specific binding cannot be definitively concluded at this time. However, with the affinity of [^{18}F]FL2-b for TDP-43 aggregates, higher B_{max} in ALS tissue and colocalization with cytosolic TDP43 inclusions and dystrophic neurites in the gray matter identified by immunohistochemistry, are encouraging signs that quantifying TDP-43 with [^{18}F]FL2-b offers a potential imaging biomarker for ALS.

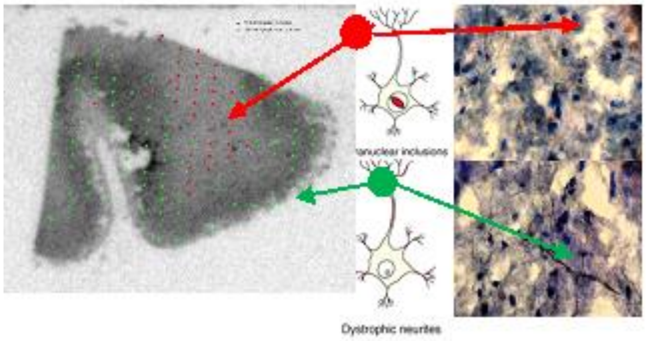

Fig. 3. 6: IHC overlay on autoradiographic motor cortex slide showing specific binding of [^{18}F]FL2-b is colocalized to the toxic TDP43 aggregate type "dystrophic neurite"

3.3. Conclusion

As of yet, no PET tracers specific for ALS biomarkers has been developed. We showed that [^{18}F]FL2-b, colocalizes in areas with TDP-43 aggregates. Given that the compound was designed to target copper/zinc-protein complexes and that TDP-43 can bind Zn^{2+}, we believe we have a tracer that is potentially binding TDP-43 aggregates. Further, autoradiography has shown that the tracer has a higher binding potential in ALS tissue when compared to healthy control. A fluorine-18 analog of HQ415 is still of interest as it has been shown to also save cells burdened with TDP-43 toxicity. An alternate synthesis will need to be constructed that yields high fluorination of the quinoline scaffold.

3.4. Materials and Methods

For Organic Synthesis: All solvents and reagents were commercially available and used without further purification unless otherwise stated. N,N-dimethyl-p-phenylenediamine was purchased from Sigma Aldrich. 6-Fluoropyridinecarboxaldehyde and 6-chloropyridinecarboxaldehyde were purchased from Oakwood Chemical. NMR spectra were recorded with a Varian 400 MHz instrument at room temperature with tetramethylsilane (TMS) as an internal standard. 1H, 13C, and 19F spectra were recorded at 400 MHz, 100 MHz, and 376 MHz, respectively. Mass spectra were performed on an Agilent 6230 TOF HPLC-MS, Agilent Q-TOF HPLC-MS or a VG (Micromass) 70-250-S Magnetic sector mass employing the electrospray ionization (ESI) method. High performance liquid chromatography (HPLC) was performed using a Shimadzu LC-2010A HT system equipped with a Bioscan B-FC-1000 radiation detector. All procedures including anhydrous solvents were performed using Schlenk techniques with rigorously dried glassware.

3.4.1. *Synthesis of HQ415 Precursors and Standards*

Preparation of 2-chloro-7-((3-ethoxy-4-methoxyphenyl)((4-methylpyridin-2-yl)amino)methyl)quinolin-8-ol (**4**):

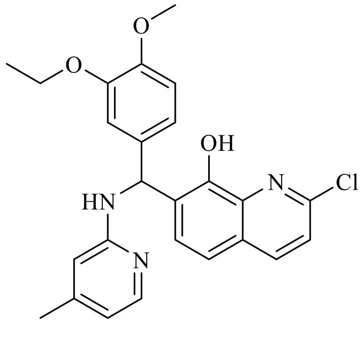

Dissolved 800 mg of 4-methylpyridin-2-amine (**3**) in 25 mL of ethanol (EtOH). Immediately added 1.01 g 3-ethoxy-4-methoxybenzaldehyde (**2**) to this solution. The mixture was stirred for 20 minutes before adding 813 mg of 2-chloroquinolin-8-ol (**1**). This mixture was left to stir at room temperature for 2 weeks before extraction with ethyl acetate (EtAc) 3x in water, then dried over sodium sulfate (Na_2SO_4). The crude product was purified using flash chromatography with a dichloromethane (DCM) and EtAc gradient to yield **4** in 28% yield. ^{1}H NMR (400 MHz, Chloroform-*d*) δ 8.04 (d, *J* = 8.6 Hz, 1H), 7.95 (d, *J* = 5.2 Hz, 1H), 7.55 (d, *J* = 8.5 Hz, 1H), 7.36 (d, *J* = 8.6 Hz, 1H), 7.29 (d, *J* = 8.6 Hz, 1H), 6.99 (d, *J* = 2.0 Hz, 1H), 6.94 – 6.87 (m, 1H), 6.79 (d, *J* = 8.4 Hz, 1H), 6.47 – 6.37 (m, 1H), 6.33 (d, *J* = 6.4 Hz, 1H), 6.25 – 6.17 (m, 1H), 4.06 – 3.96 (m, 2H), 3.83 (s, 3H), 2.15 (s, 3H), 2.04 (s, 2H), 1.40 (t, *J* = 7.0 Hz, 3H). [M + H]+: Expected 450.1579, Found 450.1579

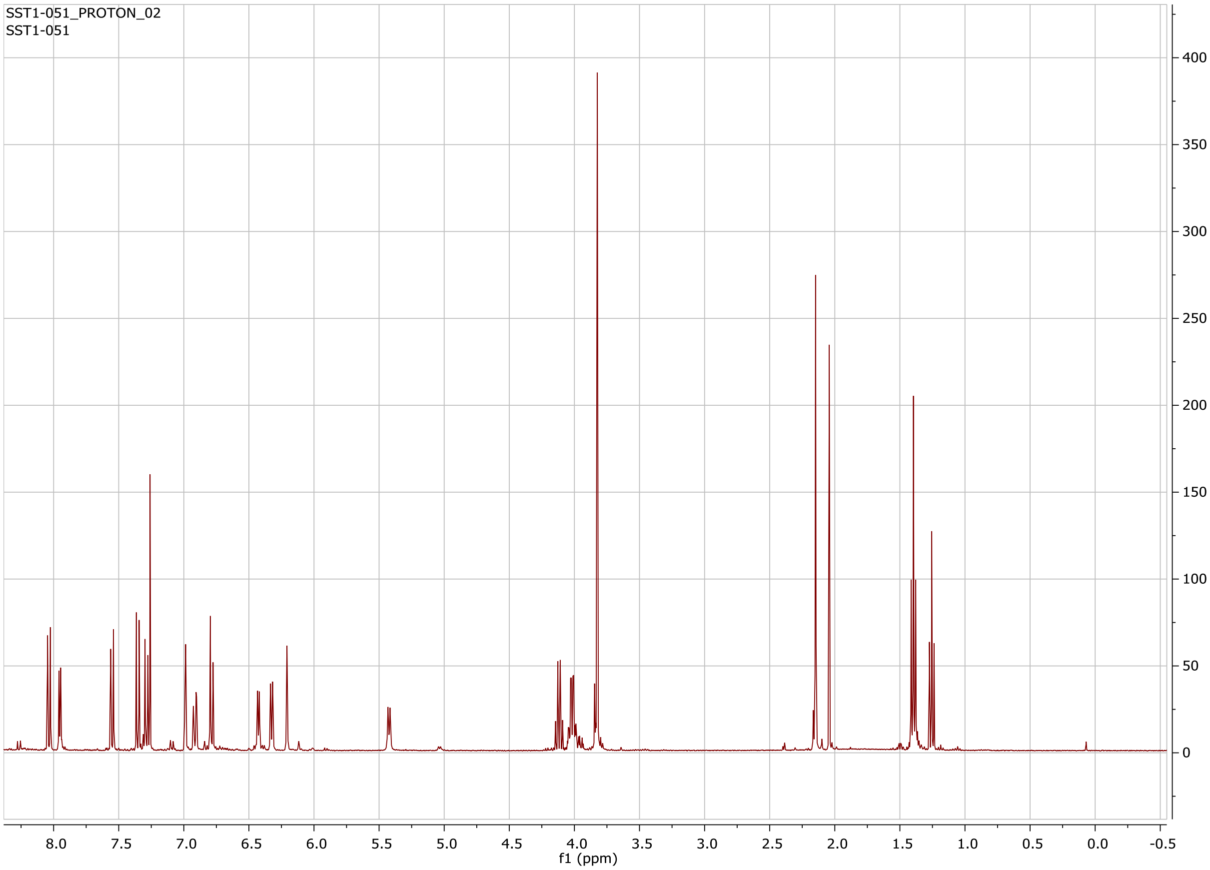

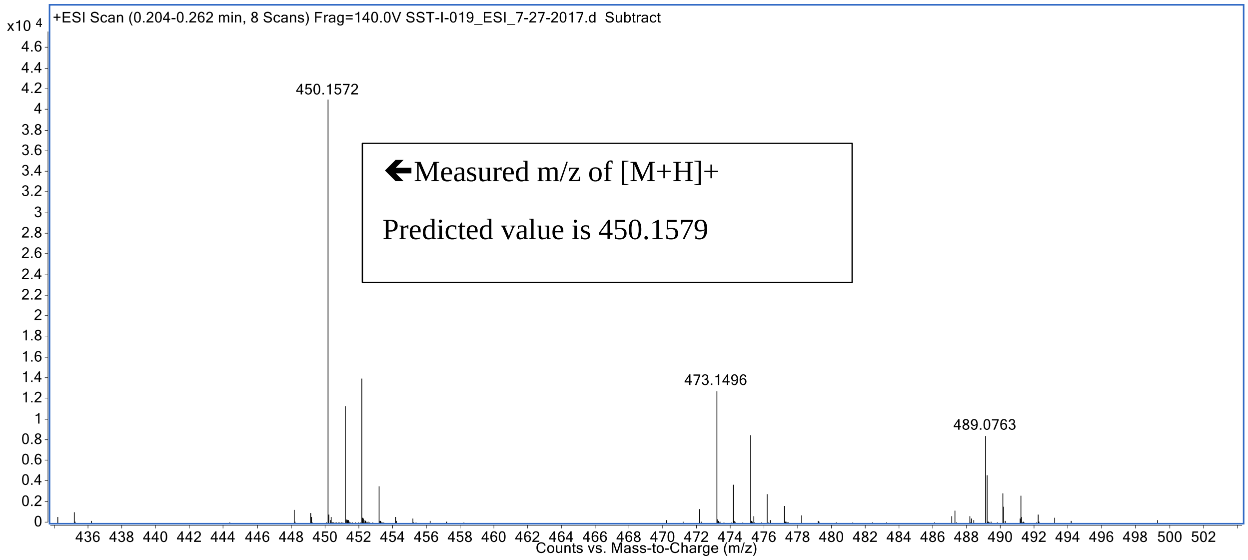

🡐Measured m/z of [M+H]+

Predicted value is 450.1579

Preparation of N-((2-chloro-8-(methoxymethoxy)quinolin-7-yl)(3-ethoxy-4-methoxyphenyl)methyl)-4-methylpyridin-2-amine (**5**):

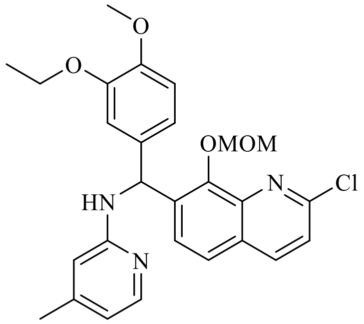

Dissolved 300 mg (0.667 mmol) **4** and 184 mg potassium carbonate (K_2CO_3, 1.33 mmol, 2 eq.) in 5 mL of DCM in a flame dried round bottom flask. Placed flask in an ice bath to chill to 0°C before slowly adding 232 µL N,N-diisopropylethylamine (DIPEA or commonly Hünigs base, 1.33 mmol, 2 eq.) while stirring. After 10 minutes, 200 µL methyl chloromethyl ether (MOMCl, 2.67 mmol, 4 eq.) was slowly added dropwise. The reaction was left to stir overnight and warm to room temperature. The reaction was quenched with water, filtered through celite, extracted with DCM 3x, rinsed with brine, and dried over Na_2SO_4. Purification of the crude product with flash chromatography using a DCM/EtAc gradient yielded **5** in 18% yield. ^{1}H NMR (400 MHz, Chloroform-*d*) δ 8.05 (d, *J* = 8.6 Hz, 1H), 7.92 (d, *J* = 5.2 Hz, 1H), 7.62 (d, *J* = 8.5 Hz, 1H), 7.53 (d, *J* = 8.5 Hz, 1H), 6.96 (d, *J* = 2.0 Hz, 1H), 6.86 (dd, *J* = 8.2, 1.9 Hz, 1H), 6.77 (d, *J* = 8.3 Hz, 1H), 6.64 – 6.58 (m, 0H), 6.48 – 6.39 (m, 2H), 6.27 (s, 1H), 5.61 (d, *J* = 5.9 Hz, 1H), 5.49 (d, *J* = 6.0 Hz, 1H), 5.41 (d, *J* = 6.1 Hz, 1H), 4.12 (q, *J* = 7.2 Hz, 1H), 4.00 (qd, *J* = 7.0, 4.6 Hz, 2H), 3.82 (s, 3H), 3.60 (s, 3H), 3.59 – 3.52 (m, 0H), 2.18 (d, *J* = 8.4 Hz, 0H), 2.15 (s, 3H), 2.09 (d, *J* = 6.9 Hz, 0H), 1.39 (t, *J* = 7.0 Hz, 3H), 1.26 (t, *J* = 7.1 Hz, 1H), 0.85 (s, 0H). [M + H]+: Expected 494.1841, Found 494.1841

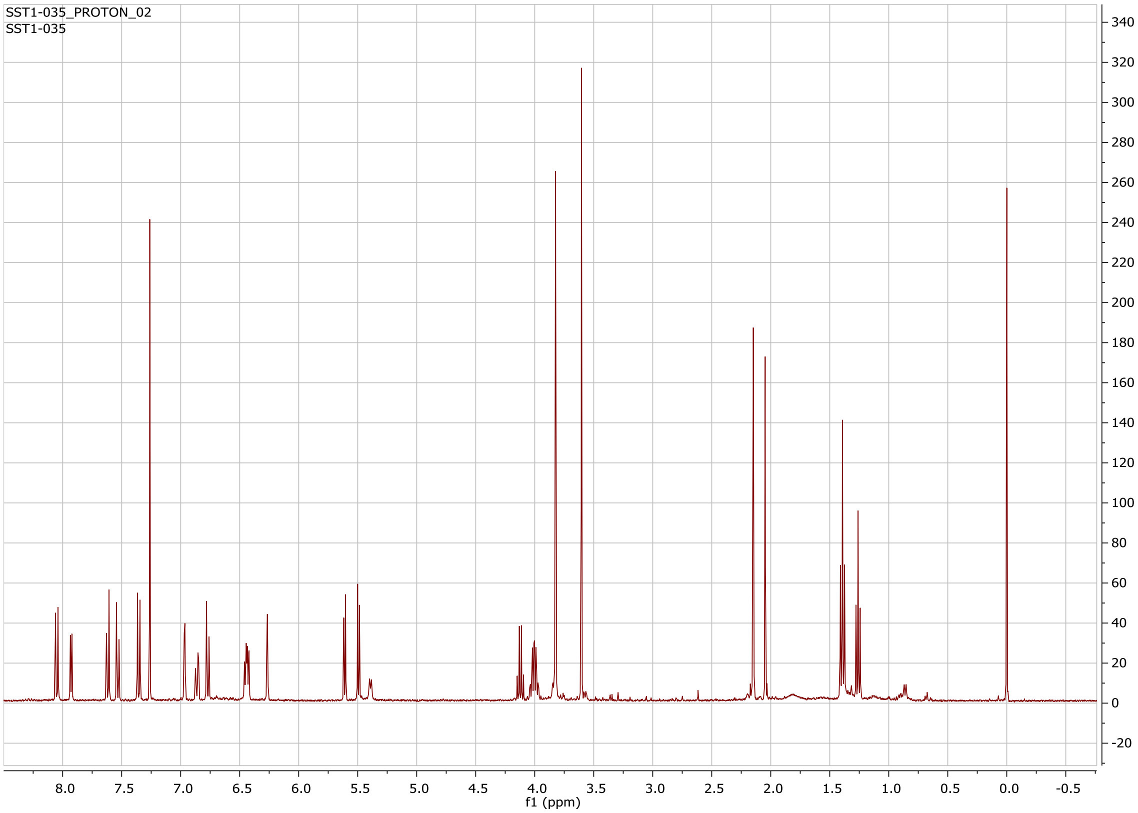

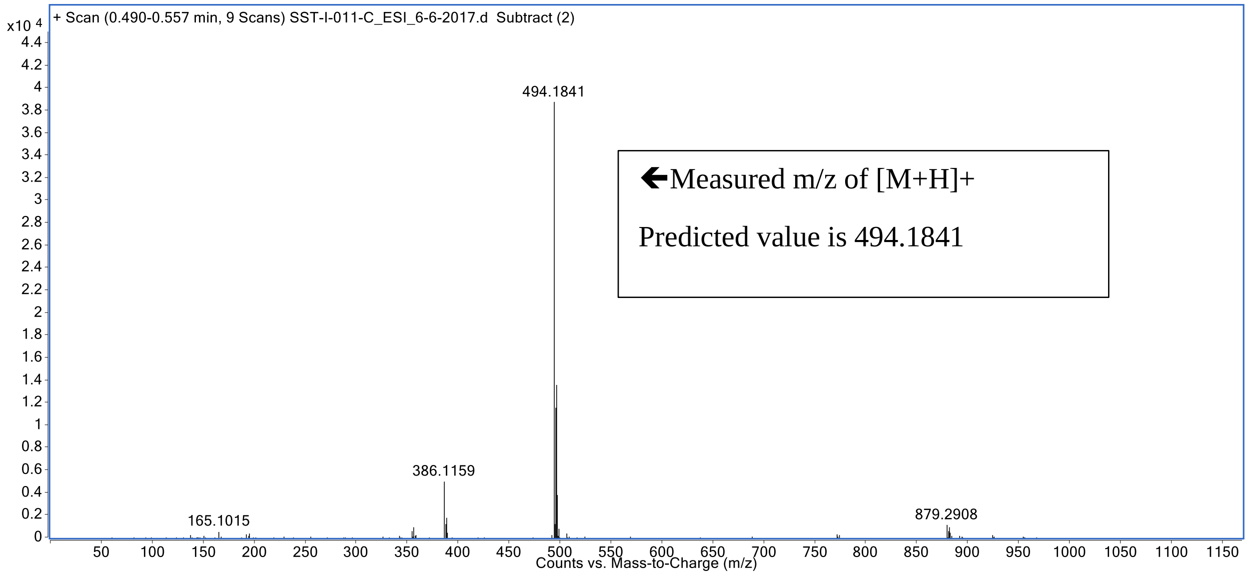

🡐Measured m/z of [M+H]+

Predicted value is 494.1841

Preparation of N-((3-ethoxy-4-methoxyphenyl)(2-fluoro-8-(methoxymethoxy)quinolin-7-yl)methyl)-4-methylpyridin-2-amine (**6**):

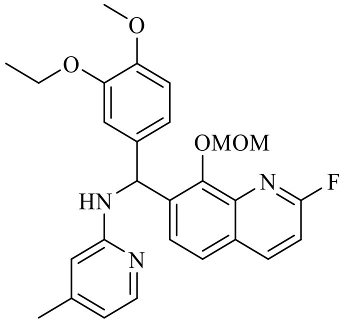

Partitioned 45 mg (0.1 mmol) **5** into a microwave reaction vessel. Aliquoted 16 equivalents 1M TBAF in THF in a 50 mL round bottom flask. Removed tetrahydrofuran (THF) by rotovap. Resuspended TBAF in 10 mL dimethyl sulfoxide (DMSO) and transferred to reaction vessel containing **5**. Bring total volume to 20 mL with DMSO. Placed in microwave for 1.5 hours at 140°C. The reaction was extracted with EtAc 3x, rinsed with brine, and dried over Na_2SO_4. Purification using flash chromatography with a DCM/EtAc gradient gave **6** 30% yield. ^{1}H NMR (400 MHz, Chloroform-*d*) δ 8.23 (s, 1H), 8.12 (d, *J* = 5.1 Hz, 1H), 7.97 – 7.87 (m, 2H), 7.54 – 7.36 (m, 4H), 6.97 (d, *J* = 2.0 Hz, 1H), 6.94 – 6.83 (m, 4H), 6.77 (t, *J* = 6.8 Hz, 2H), 6.42 (q, *J* =

5.6, 4.8 Hz, 2H), 6.28 (s, 1H), 5.72 – 5.62 (m, 1H), 5.62 – 5.50 (m, 2H), 5.46 (dd, *J* = 5.7, 4.3 Hz, 1H), 3.99 (qt, *J* = 6.6, 3.3 Hz, 2H), 3.93 (s, 2H), 3.81 (s, 3H), 3.57 (s, 2H), 2.39 (s, 3H), 2.14 (s, 3H), 0.96 (t, *J* = 7.3 Hz, 6H). ^{19}F NMR (376 MHz, Chloroform-*d*) δ -78.37. [M + H]+: Expected 478.2137, Found 478.2137

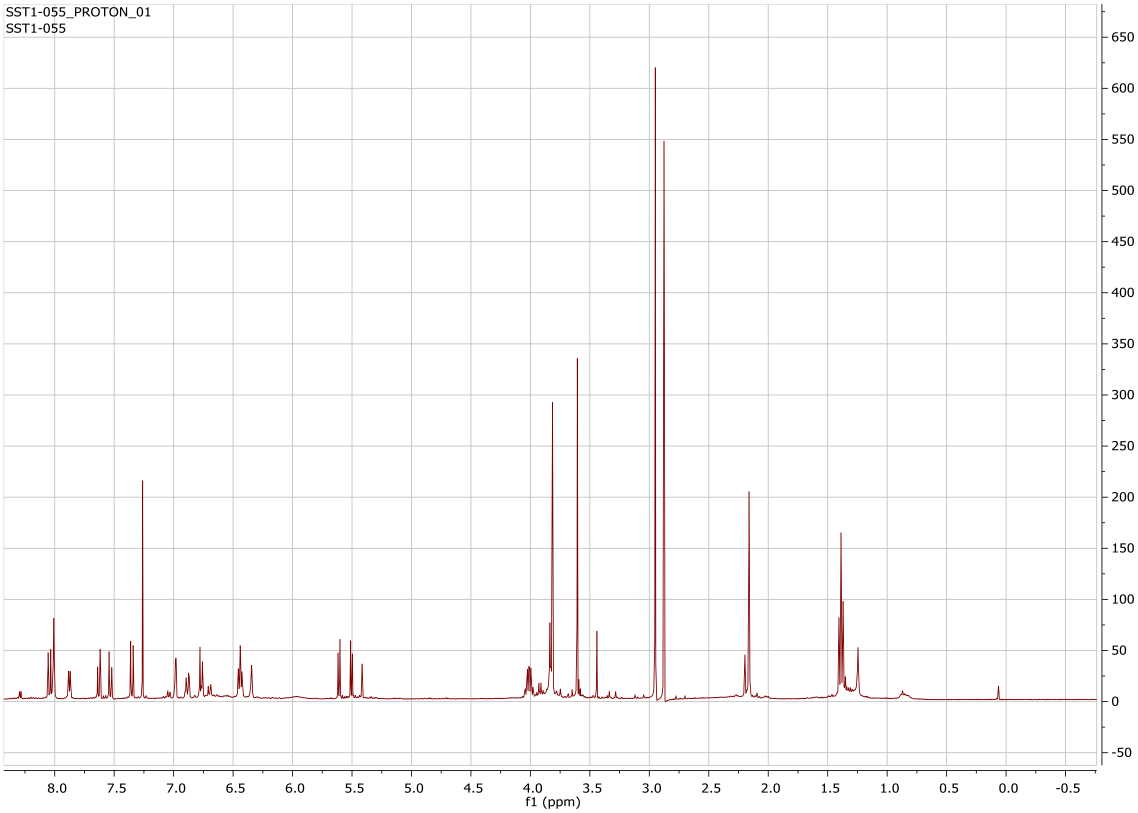

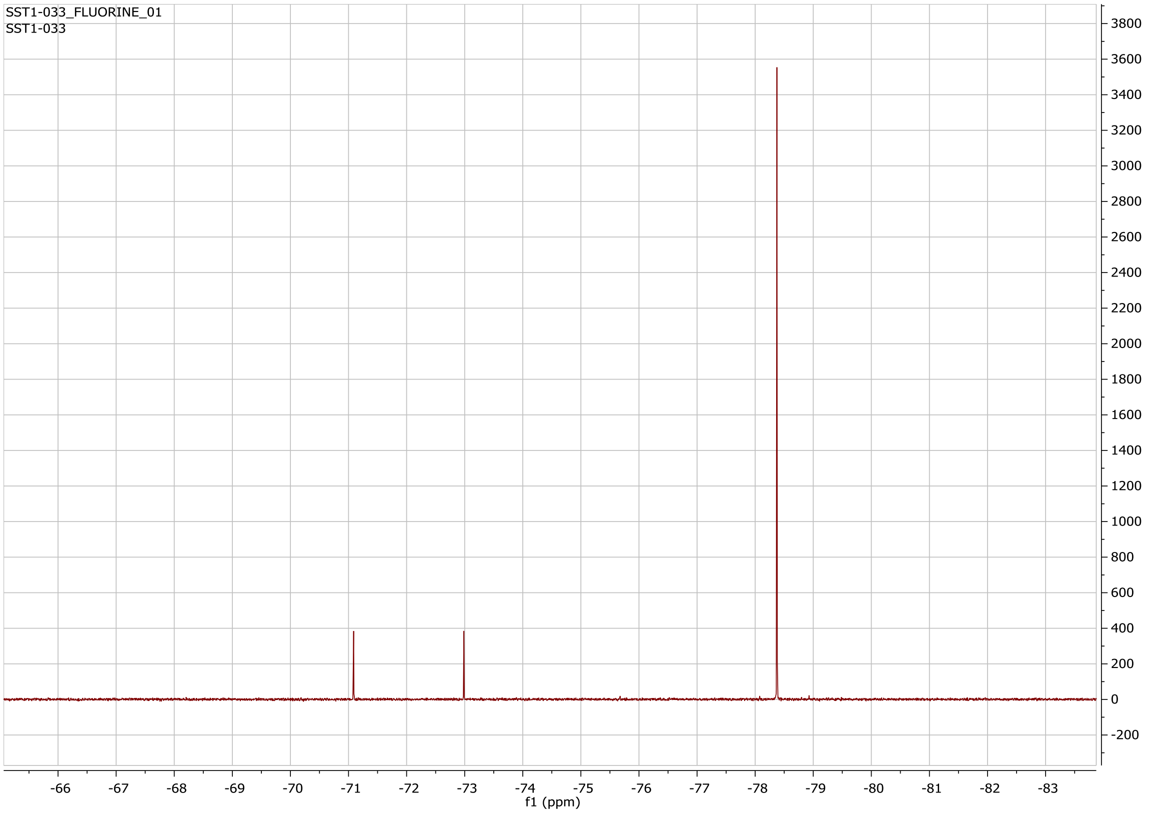

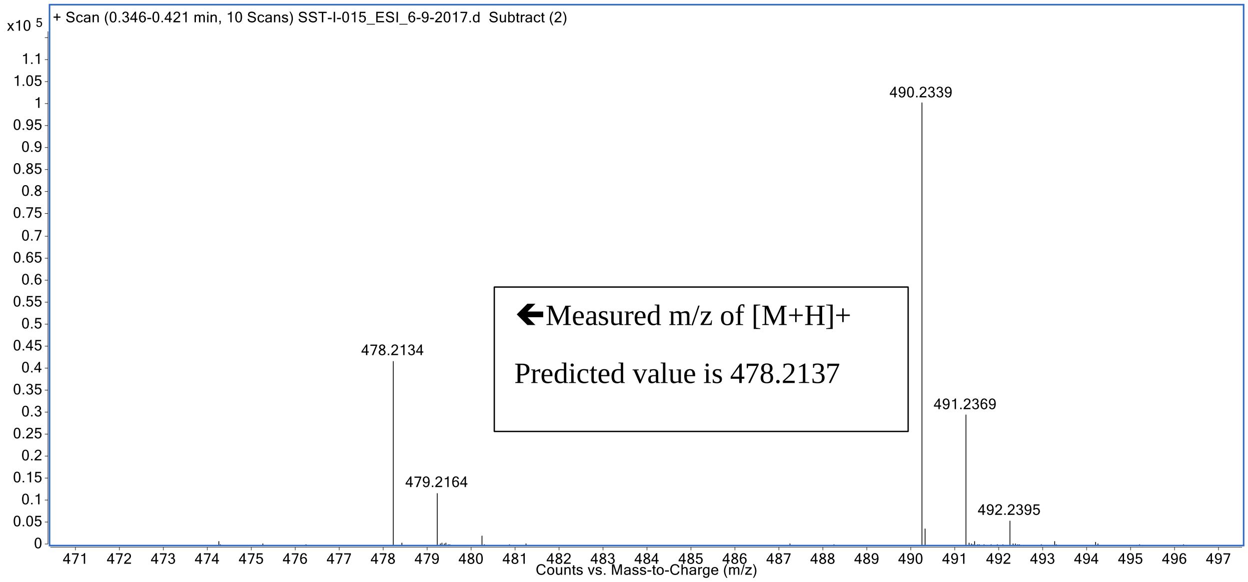

🡐Measured m/z of [M+H]+

Predicted value is 478.2137

Preparation of 7-((3-ethoxy-4-methoxyphenyl)((4-methylpyridin-2-yl)amino)methyl)-2-fluoroquinolin-8-ol (**7**):

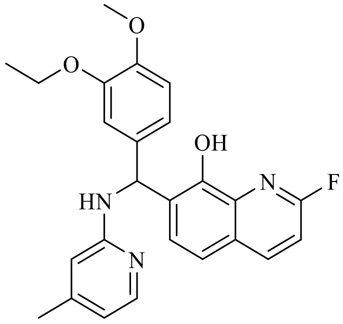

Dissolved 10 mg (0.021 mmol) in 1 mL THF in a round bottom flask. Added 10 drops of 4M HCl in dioxane and stirred at 50°C for 3 hours. Quenched with a couple drops of a saturated sodium bicarbonate solution ($NaHCO_3$), extracted with EtAc 3x, and purified by flash chromatography using a Hexane (Hex)/EtAc gradient to give **7** in 54% yield. ^{1}H NMR (400 MHz, Chloroform-*d*) δ 8.69 (s, 0H), 8.24 (s, 0H), 8.15 (d, *J* = 5.1 Hz, 0H), 7.55 – 7.46 (m, 1H), 7.01 – 6.87 (m, 2H), 6.81 (s, 0H), 5.02 (s, 0H), 4.20 (q, *J* = 7.0 Hz, 1H), 4.06 (s, 1H), 3.95 (s, 1H), 3.92 – 3.73 (m, 5H), 3.74 – 3.55 (m, 5H), 3.02 (t, *J* = 8.6 Hz, 1H), 2.43 (d, *J* = 19.4 Hz, 1H), 2.27 (s, 2H), 2.18 (d, *J* = 7.3 Hz, 0H), 1.50 (d, *J* = 14.0 Hz, 1H), 1.43 (s, 9H), 1.25 (s, 4H), 1.11 (s, 0H), 0.98 (t, *J* = 7.5 Hz, 1H), 0.95 – 0.83 (m, 1H), 0.87 (s, 4H), 0.07 (s, 9H). ^{19}F NMR (376 MHz, Chloroform-*d*) δ -78.37. [M + H]+: Expected 434.1874, Found 434.1874

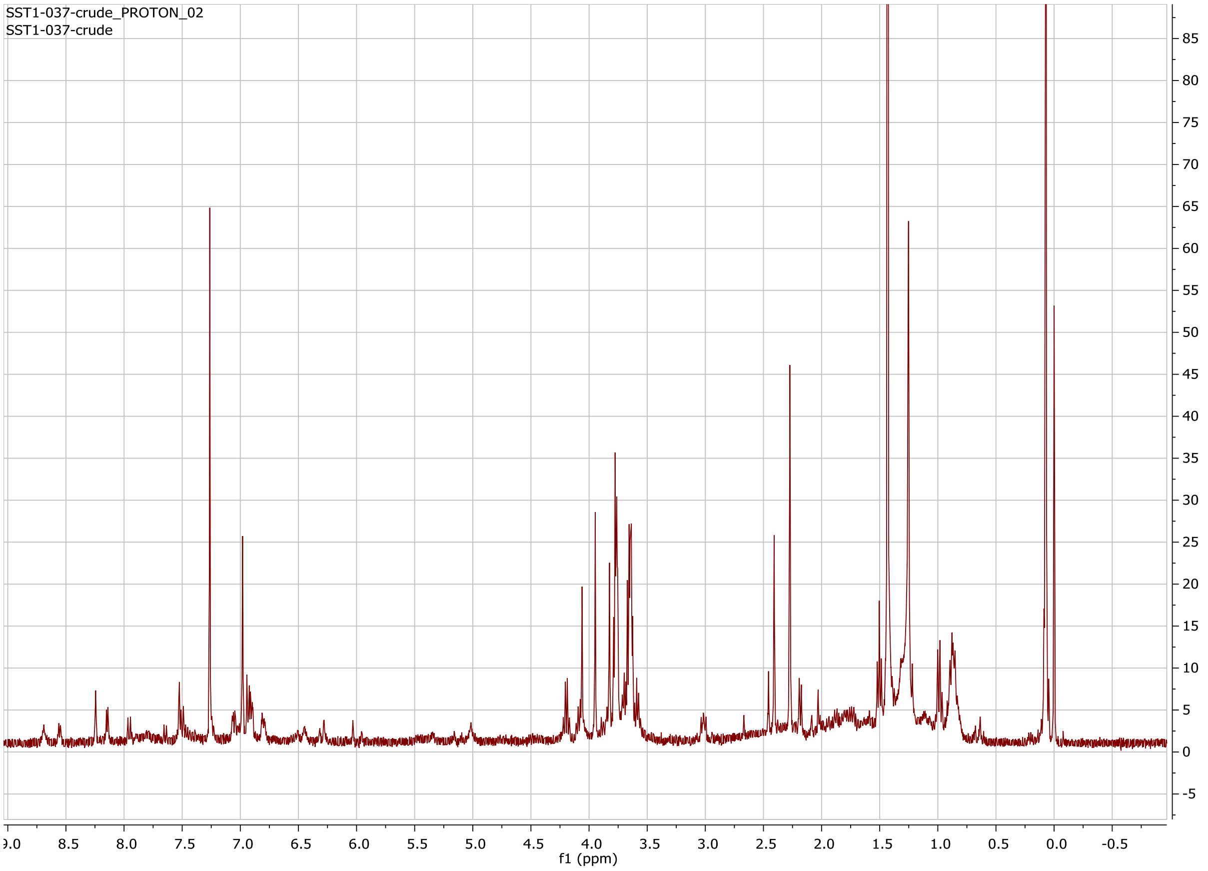

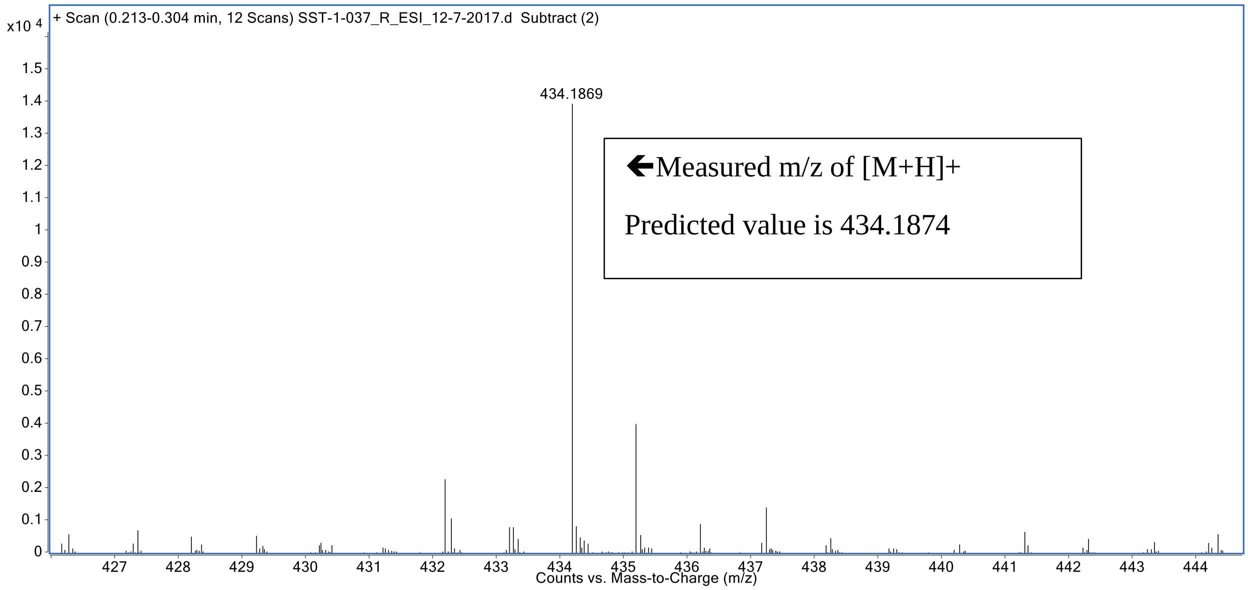

🡐Measured m/z of [M+H]+

Predicted value is 434.1874

Preparation of tert-butyl ((2-chloro-8-(methoxymethoxy)quinolin-7-yl)(3-ethoxy-4-methoxyphenyl)methyl)(4-methylpyridin-2-yl)carbamate (**8**):

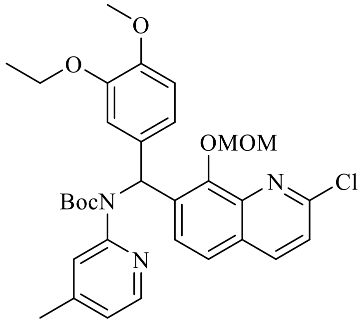

Dissolved 90 mg (0.182 mmol) of starting material **5** was dissolved in 1.5 mL of THF and transferred to a 4 mL scintillation vial. The solution was charged with 84 mg (0.364 mmol) of di-tert-butyl decarbonate and placed in a heating mantle at 40°C for 24 hours. For workup, the THF was removed by evaporation before redissolving in DCM and extracting 3x with water. After rinsing with brine and drying over Na_2SO_4, the crude reaction mixture was purified with flash chromatography using a Hex/EtAc step gradient from 10% EtAc to 24% EtAc. Purification gave a 34% yield (20 mg) of **8**. ^{1}H NMR (499 MHz, Chloroform-*d*) δ 8.16 (d, *J* = 5.1 Hz, 1H), 7.97 (d, *J* = 8.6 Hz, 1H), 7.63 (d, *J* = 8.6 Hz, 1H), 7.36 – 7.25 (m, 3H), 7.17 (d, *J* = 2.1 Hz, 1H), 6.98 – 6.92 (m, 2H), 6.79 – 6.71 (m, 2H), 5.54 (d, *J* = 6.0 Hz, 1H), 5.47 (d, *J* = 6.0 Hz, 1H), 4.07 – 3.94 (m, 2H), 3.83 (s, 3H), 3.62 (s, 3H), 2.11 (s, 3H), 1.39 (t, *J* = 7.0 Hz, 3H), 1.29 (s, 9H), 1.25 (d, *J* = 6.7 Hz, 1H), 0.84 (s, 0H). [M + H]+: Expected 594.2365, Found 594.2377

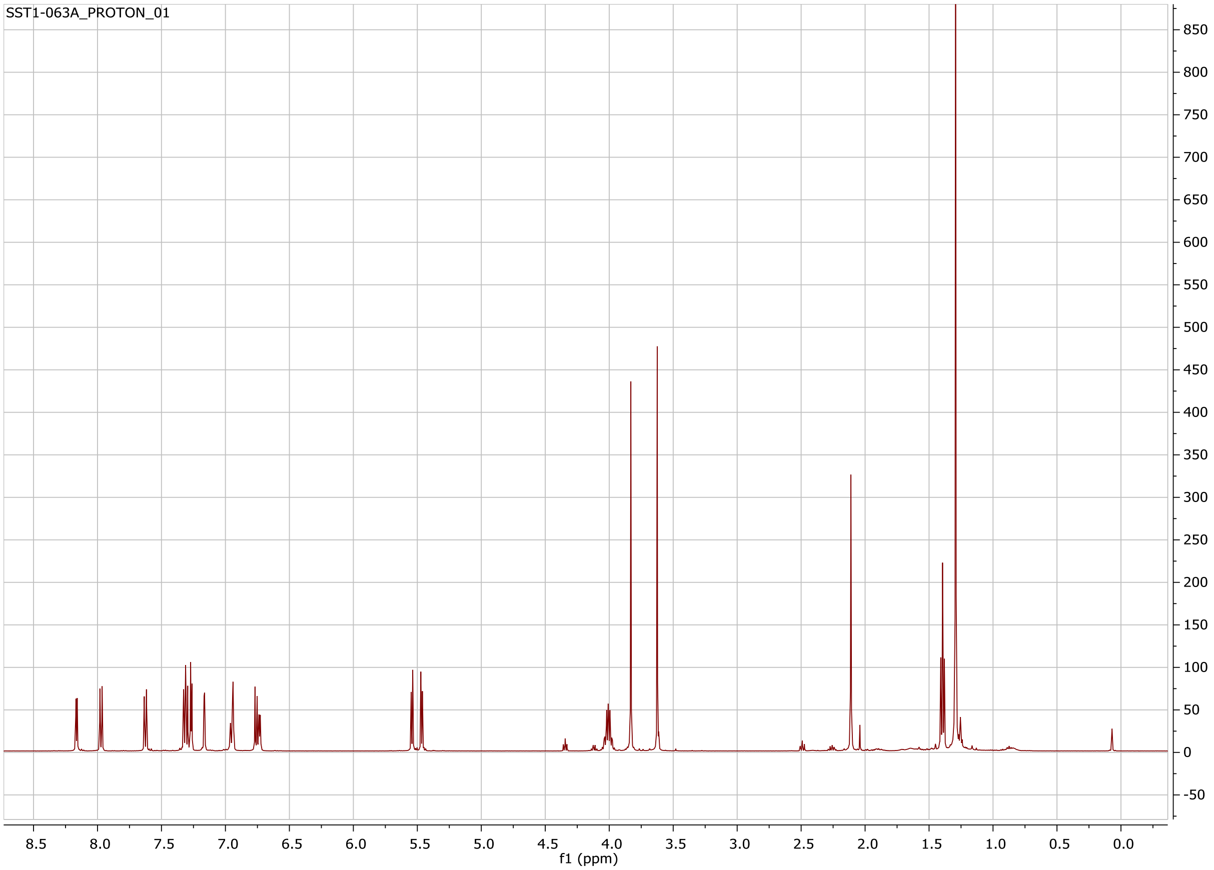

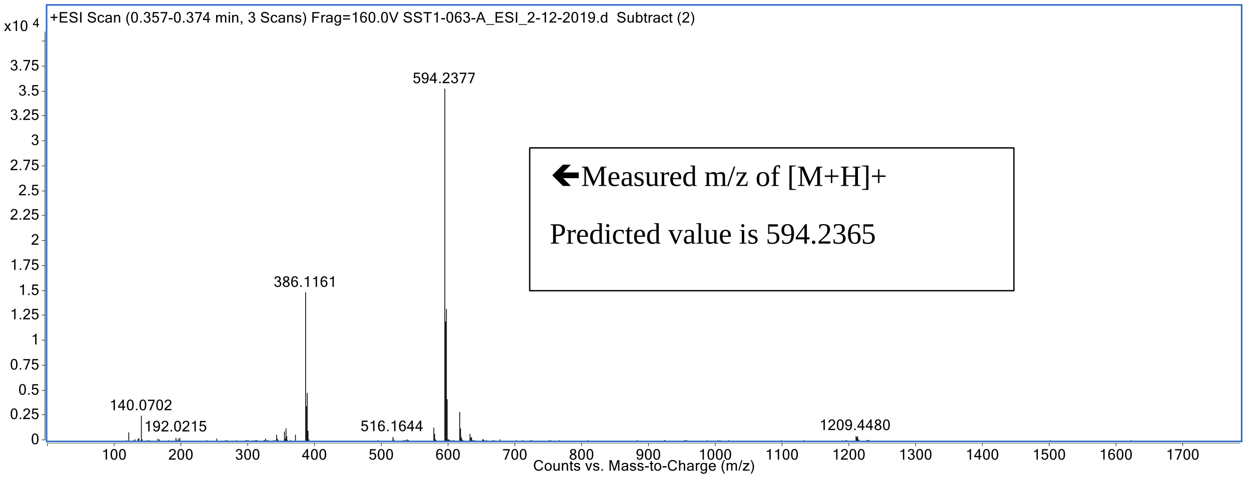

🡐Measured m/z of [M+H]+

Predicted value is 594.2365

Preparation of tert-butyl ((3-ethoxy-4-methoxyphenyl)(2-fluoro-8-(methoxymethoxy)quinolin-7-yl)methyl)(4-methylpyridin-2-yl)carbamate (**11**):

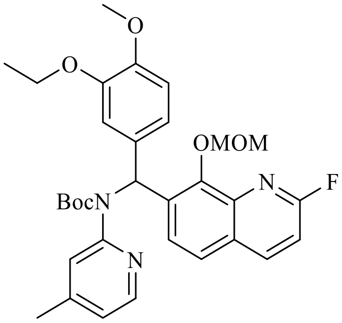

Dissolved 20 mg (0.033 mmol) **10** in 2 mL of dimethylformamide (DMF) and transferred to a 4 mL scintillation vial. The solution was charged with 9.4 mg (0.1 mmol) tetramethylammonium fluoride and stirred at room temperature for 24 hours. The reaction mixture was extracted with 25 mL of EtAc 3x from water, rinsed with brine, and dried over Na_2SO_4. The crude reaction mixture was purified by flash chromatography in 25% EtAc/Hex to give a 21% yield (4 mg) of **11**. ^{1}H NMR (499 MHz, Chloroform-*d*) δ 8.16 (d, *J* = 5.1 Hz, 1H), 7.97 (d, *J* = 8.6 Hz, 1H), 7.63 (d, *J* = 8.6 Hz, 1H), 7.36 – 7.25 (m, 3H), 7.17 (d, *J* = 2.1 Hz, 1H), 6.98 – 6.92 (m, 2H), 6.79 – 6.71 (m, 2H), 5.54 (d, *J* = 6.0 Hz, 1H), 5.47 (d, *J* = 6.0 Hz, 1H), 4.07 – 3.94 (m, 2H), 3.83 (s, 3H), 3.62 (s, 3H), 2.11 (s, 3H), 1.39 (t, *J* = 7.0 Hz, 3H), 1.29 (s, 9H), 1.25 (d, *J* = 6.7 Hz, 1H), 0.84 (s, 0H). ^{19}F NMR (376 MHz, Chloroform-*d*) δ -61.01 – -61.12 (m). [M + H]+: Expected 578.2661, Found 578.2661

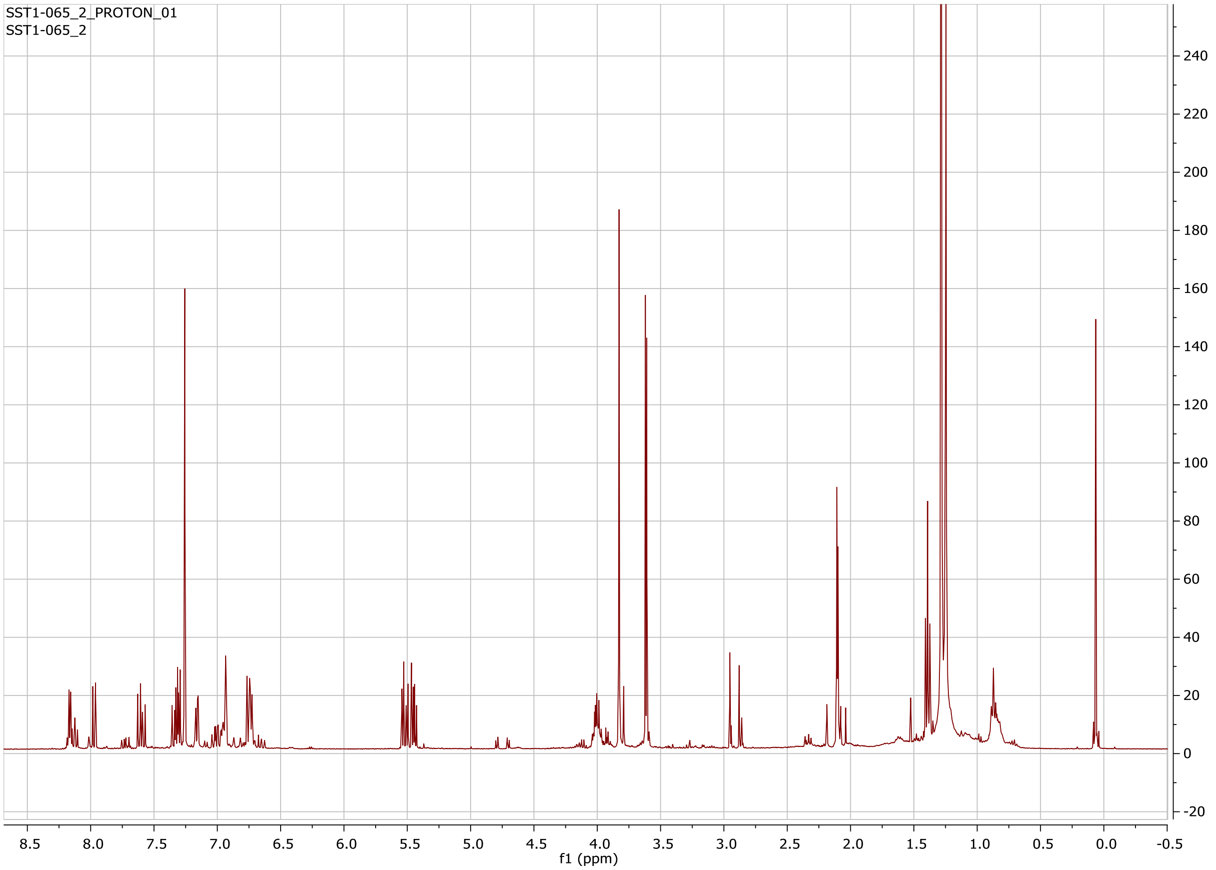
SST1-065_2_PROTON_01
SST1-065_2
240
220
200
180
160
140
120
100
80
60
40
20
0
-20
8.5
8.0
7.5
7.0
6.5
6.0
5.5
5.0
4.5
4.0
3.5
3.0
2.5
2.0
1.5
1.0
0.5
0.0
-0.5
f1 (ppm)

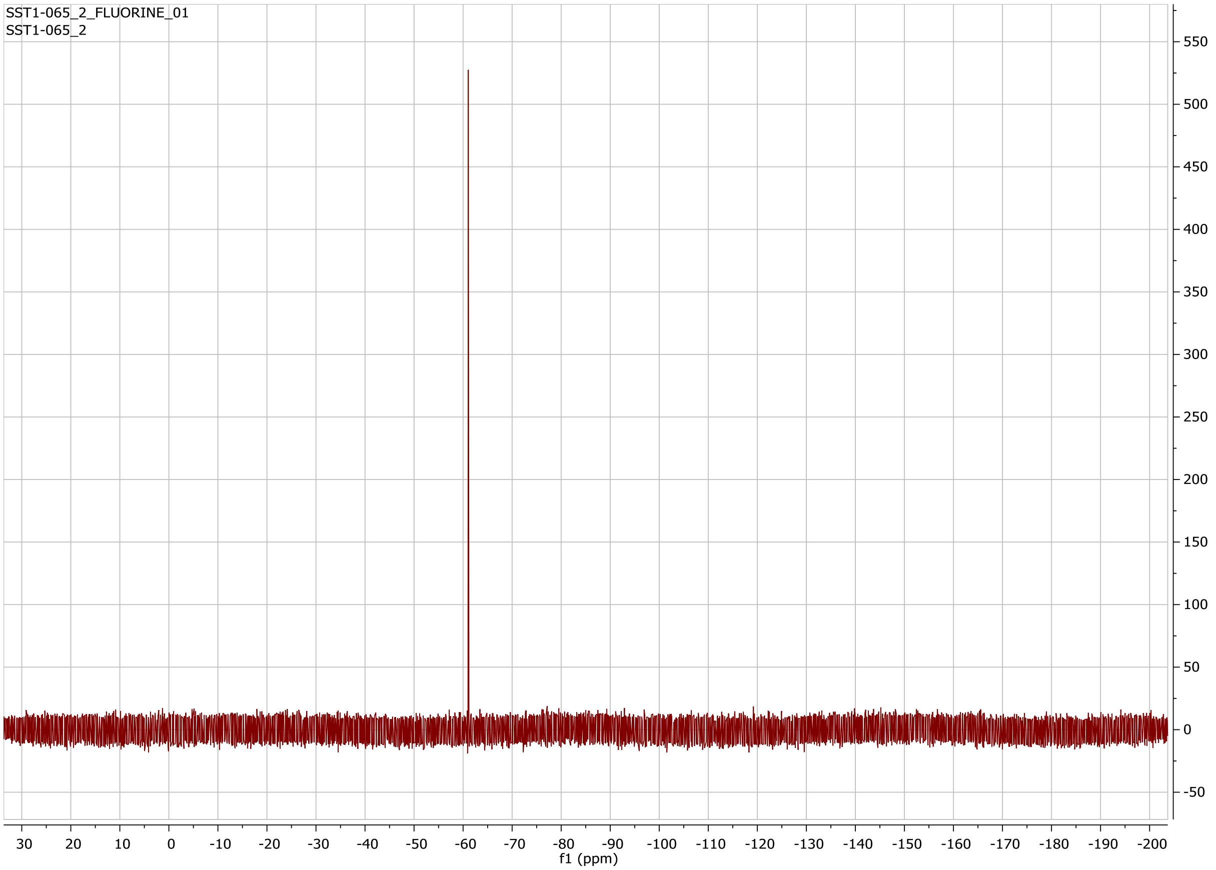

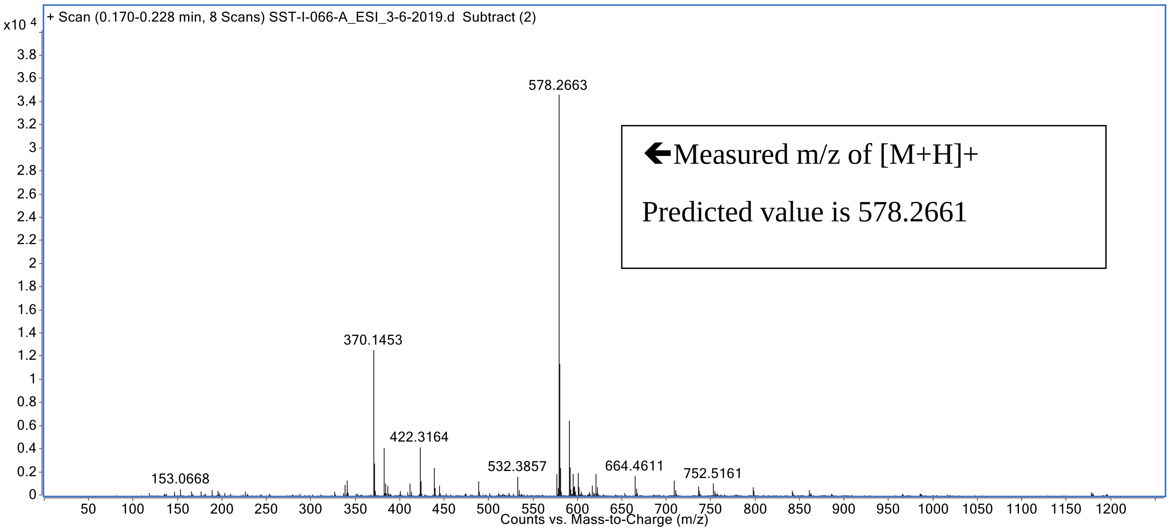

🡐Measured m/z of [M+H]+

Predicted value is 578.2661

Preparation of tert-butyl ((8-((tert-butoxycarbonyl)oxy)-2-chloroquinolin-7-yl)(3-ethoxy-4-methoxyphenyl)methyl)(4-methylpyridin-2-yl)carbamate (**12**):

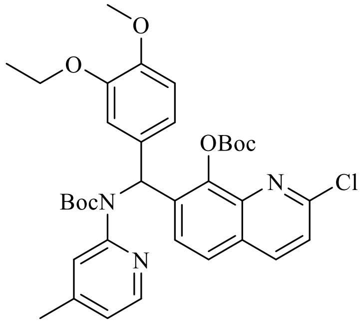

Dissolved 100 mg (0.222 mmol) of **5** and 203.8 mg (1.11 mmol, 5 eq.) of Boc_2O in 0.5 mL THF within a 4 mL scintillation vial. This solution was then charged with 1.36 mg (5-mol-%) 4-dimethylaminopyridine (DMAP) . After stirring for 20 minutes the reaction mixture became coagulated at which point another 0.5 mL of THF was added for a total volume of 1 mL. The reaction was stirred for 24 hours at room temperature. For workup, the THF was removed by evaporation before redissolving in DCM and extracting 3x with water. After rinsing with brine and drying over Na_2SO_4, the crude reaction mixture was purified with flash chromatography using a Hex/EtAc step gradient from 10% EtAc to 24% EtAc. Purification gave a 66% yield (96 mg) of **12**. ^{1}H NMR (499 MHz, Chloroform-*d*) δ 8.18 (d, *J* = 5.0 Hz, 1H), 8.02 (d, *J* = 8.6 Hz, 1H), 7.88 (d, *J* = 8.7 Hz, 1H), 7.55 (d, *J* = 8.7 Hz, 1H), 7.33 (d, *J* = 8.5 Hz, 1H), 7.11 (s, 1H), 7.01 – 6.93 (m, 2H), 6.87 (dd, *J* = 8.6, 2.1 Hz, 1H), 6.79 – 6.69 (m, 2H), 4.12 (q, *J* = 7.1 Hz, 0H), 4.02 – 3.89 (m, 2H), 3.81 (s, 3H), 2.17 (s, 3H), 2.04 (s, 1H), 1.45 (s, 8H), 1.37 (t, *J* = 7.0 Hz, 3H), 1.30 (s, 9H), 1.29 – 1.22 (m, 1H), 0.84 (s, 0H). [M + H]+: Expected 650.2628, Found 650.2625

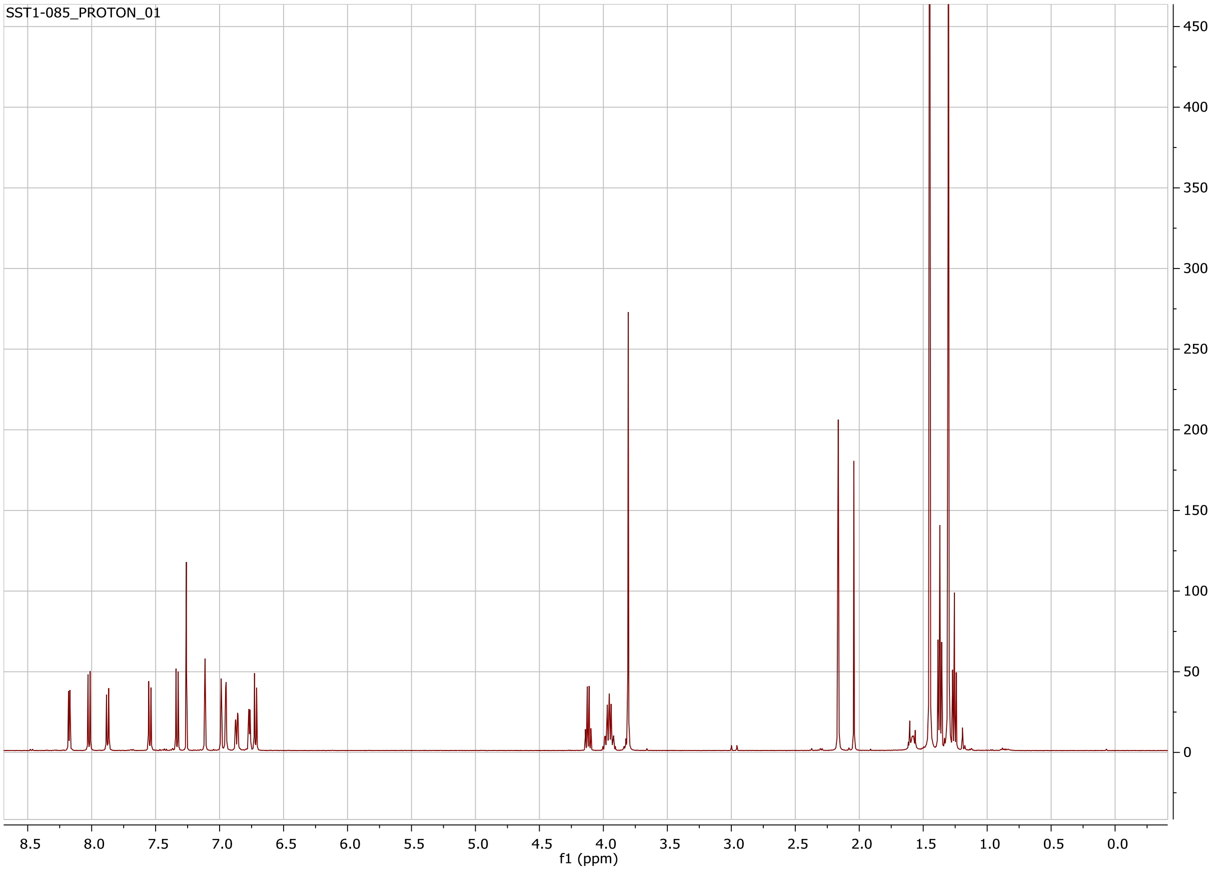

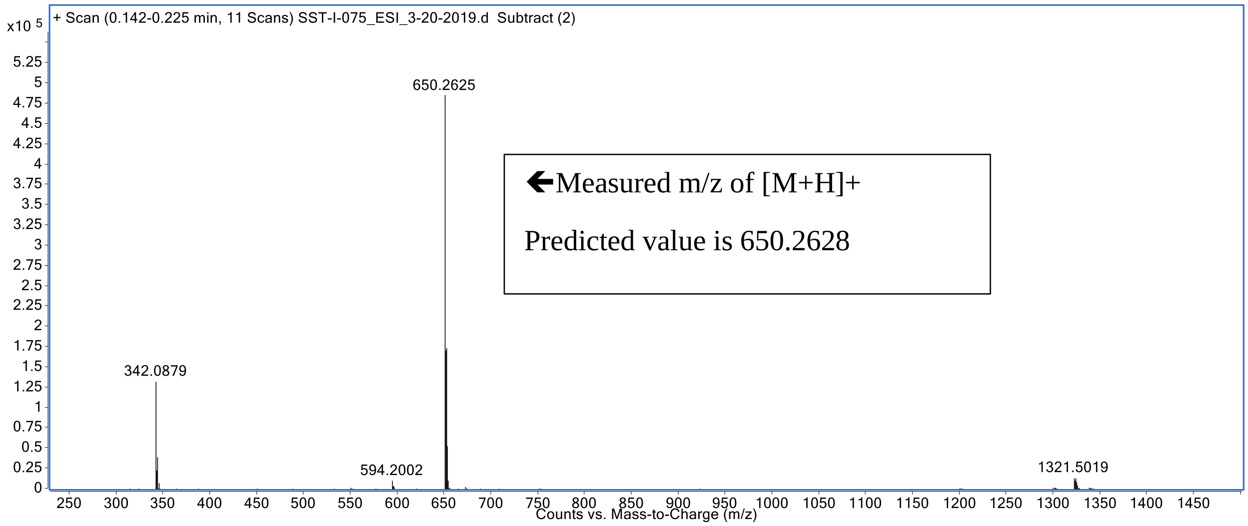

🡐Measured m/z of [M+H]+

Predicted value is 650.2628

Preparation of tert-butyl ((8-((tert-butoxycarbonyl)oxy)-2-fluoroquinolin-7-yl)(3-ethoxy-4-methoxyphenyl)methyl)(4-methylpyridin-2-yl)carbamate (**13**):

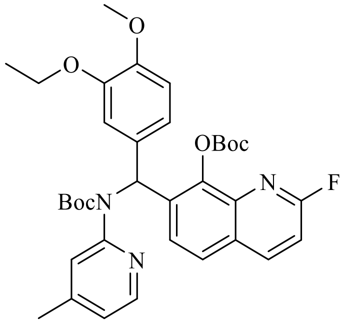

Dissolved 12 mg (0.019 mmol) **12** in 1 mL of dimethylformamide (DMF) and transferred to a 4 mL scintillation vial. The solution was charged with 5.16 mg (0.056 mmol, 3 eq.) tetramethylammonium fluoride and stirred at room temperature for 24 hours. The reaction mixture was extracted with 25 mL of EtAc 3x from water, rinsed with brine, and dried over Na_2SO_4. The crude reaction mixture was purified by flash chromatography in 25% EtAc/Hex to give a 43% yield (5 mg) of **13**. ^{1}H NMR (400 MHz, Chloroform-*d*) δ 8.18 (d, *J* = 5.0 Hz, 1H), 8.02 (d, *J* = 8.6 Hz, 1H), 7.88 (d, *J* = 8.7 Hz, 1H), 7.59 – 7.51 (m, 1H), 7.33 (d, *J* = 8.6 Hz, 1H), 7.11 (s, 1H), 7.00 – 6.92 (m, 2H), 6.86 (dd, *J* = 8.3, 2.1 Hz, 1H), 6.77 (dt, *J* = 4.7, 0.9 Hz, 1H), 6.72 (d, *J* = 8.4 Hz, 1H), 4.02 – 3.88 (m, 2H), 3.80 (s, 3H), 2.16 (s, 3H), 2.04 (s, 1H), 1.45 (s, 7H), 1.37 (t, *J* = 7.0 Hz, 3H), 1.30 (s, 7H). ^{19}F NMR (376 MHz, Chloroform-*d*) δ -60.55 (dd, *J* = 7.7, 2.8 Hz). [M + H]+: Expected 634.2923, Found 634.2923

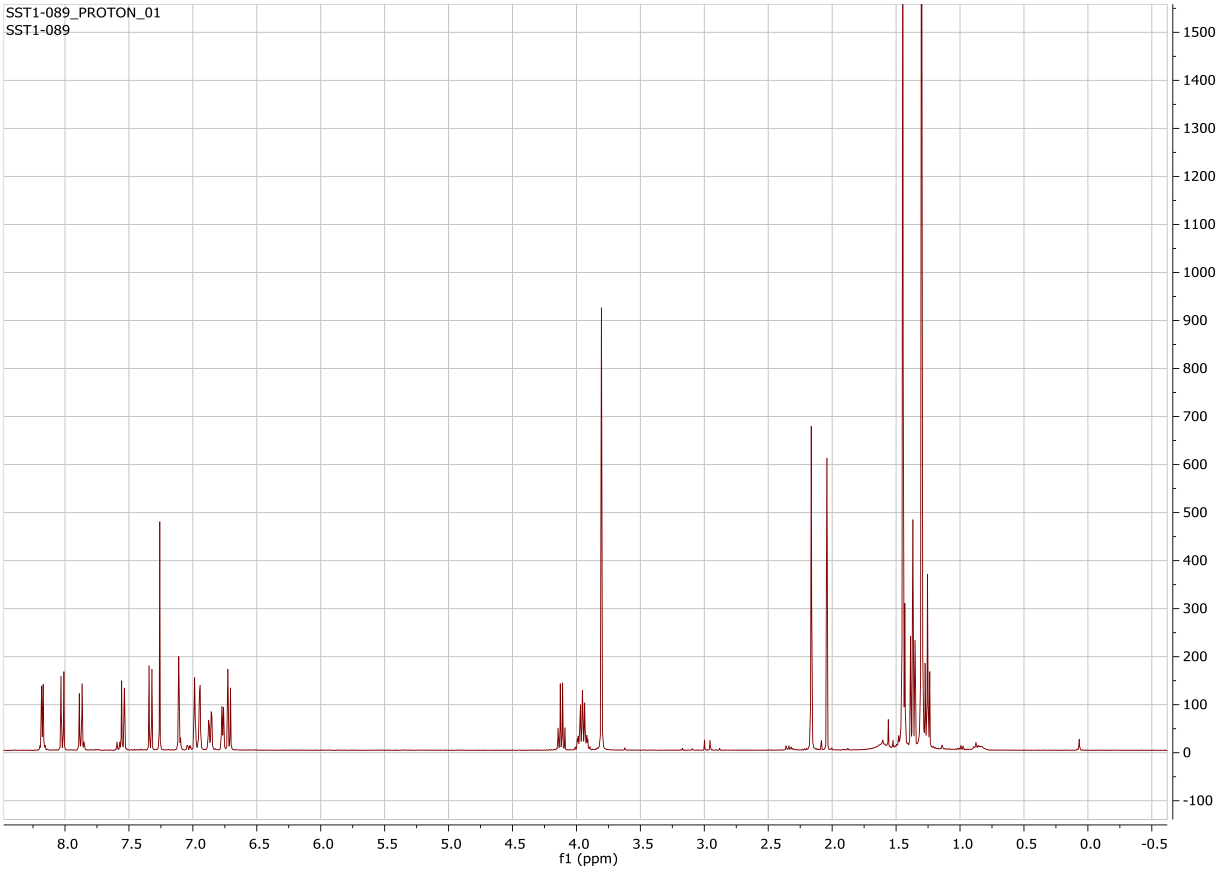
SST1-089_PROTON_01
SST1-089
8.0
7.5
7.0
6.5
6.0
5.5
5.0
4.5
4.0
3.5
3.0
2.5
2.0
1.5
1.0
0.5
0.0
-0.5
f1 (ppm)
1500
1400
1300
1200
1100
1000
900
800
700
600
500
400
300
200
100
0
-100

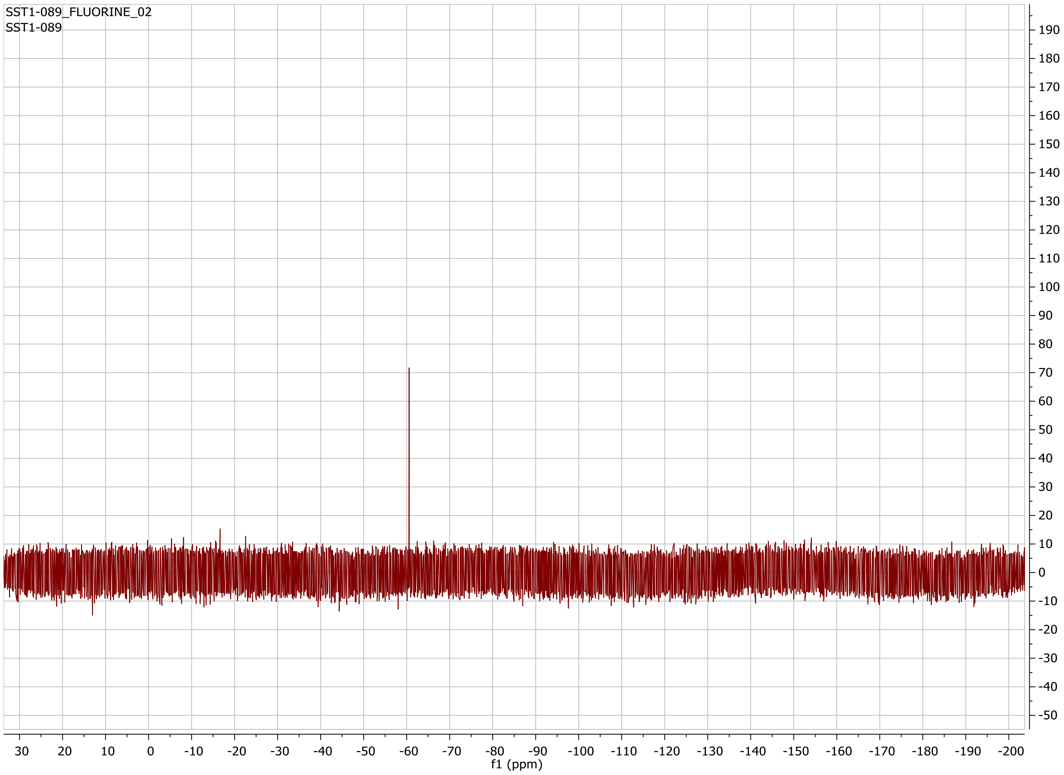
SST1-089_FLUORINE_02
SST1-089
30
20
10
0
-10
-20
-30
-40
-50
-60
-70
-80
-90
-100
-110
-120
-130
-140
-150
-160
-170
-180
-190
-200
f1 (ppm)
190
180
170
160
150
140
130
120
110
100
90
80
70
60
50
40
30
20
10
0
-10
-20
-30
-40
-50

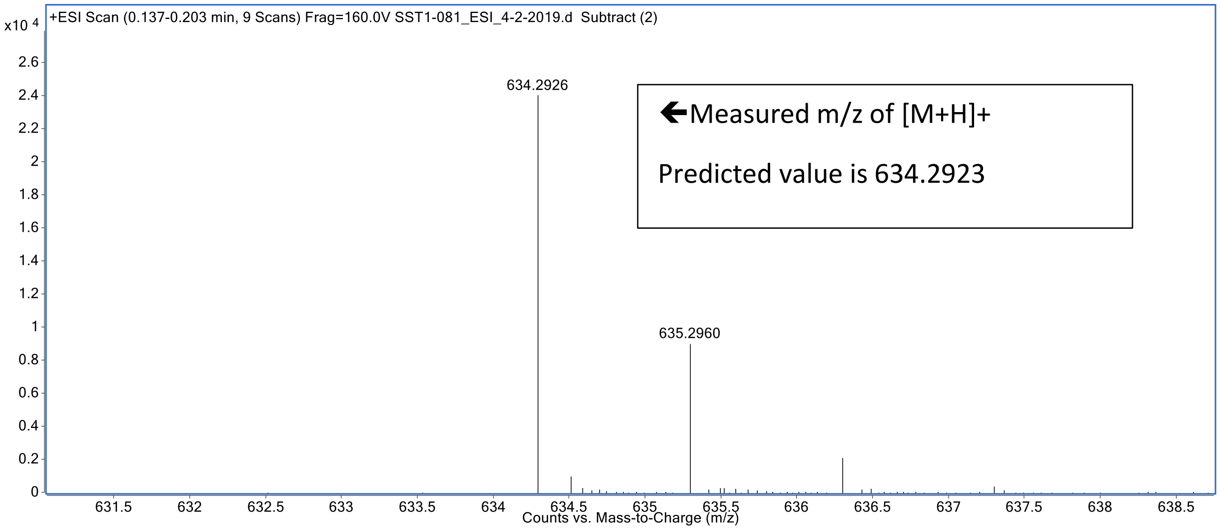

←Measured m/z of [M+H]+

Predicted value is 634.2923

Preparation of FL2-b (**14**) *standard and [^{18}F]FL2-b precursor* (**15**):

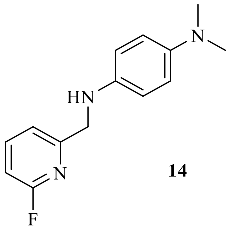

14

6-Fluoropicolinaldehyde (184 mg, 1.47 mmol) was added to N^1,N^1-dimethylbenzene-1,4-diamine (200 mg, 1.47 mmol) in anhydrous MeOH (5 mL). To the solution was added sodium sulfate (Na_2SO_4). After 24h of stirring under argon, the solution was filtered and concentrated under vacuum. The crude product was weighed and then dissolved in anhydrous methanol (4 mL) and cooled to 0° C in a round-bottom flask. Sodium borohydride ($NaBH_4$, 30.3 mg, 0.801 mmol) was slowly added, and the mixture was stirred at 0° C under argon for 2 h. After this time had elapsed, the reaction was quenched with water (10 mL). The product was extracted with diethyl ether, dried over sodium sulfate, and the solvent was removed in vacuo. The crude product was purified via silica gel chromatography (SiO_2, 3:1 = hexanes: ethyl acetate). This process provided FL2-b standard (**14**) as a yellow oil (85.4 mg, 22%). ^{1}H NMR (400 MHz, Chloroform-*d*) δ 7.58 (t, *J* =

7.7 Hz, 1H), 7.29 (d, *J* = 7.6 Hz, 1H), 7.20 (d, *J* = 7.9 Hz, 1H), 6.72 (d, *J* = 8.9 Hz, 2H), 6.61 (d, *J* = 8.9 Hz, 2H), 4.40 (s, 2H), 2.82 (s, 7H).

^{1}H NMR (400 MHz) of (14):

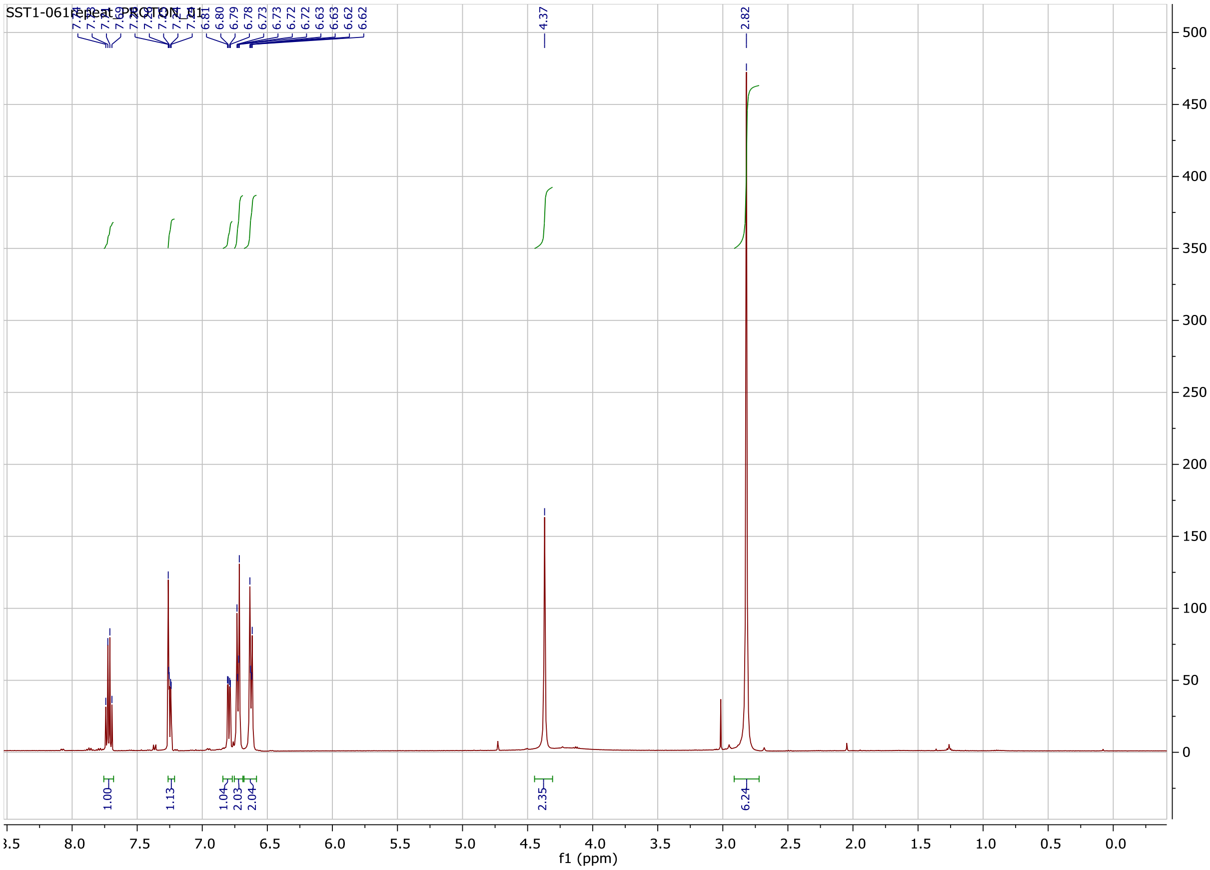

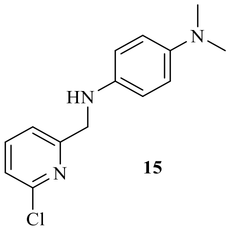

15

To a round bottom flask was added 6-chloropicolinaldehyde (425 mg, 2.94 mmol) and N^1,N^1-dimethylbenzene-1,4-diamine (400 mg, 2.94 mmol) dissolved in methanol (10 mL). Sodium sulfate was added, and the mixture was stirred for 24 h at room temperature. The mixture was filtered, and the filtrate was concentrated under vacuum. The crude product was weighed and then dissolved in anhydrous methanol (4 mL) and cooled to 0° C in a round-bottom flask. Sodium borohydride (($NaBH_4$, 10.2 mg, 0.27 mmol) was slowly added, and the mixture was stirred at 0° C under argon for 2 h. After this time had elapsed, the reaction was quenched with water (10 mL). The product was extracted with diethyl ether, dried over sodium sulfate, and the solvent was removed in vacuo. The crude product was purified via silica gel chromatography (SiO_2, 3:1 = hexanes: ethyl acetate). This process provided [^{18}F]FL2-b precursor (**2**) as a yellow solid (19 mg, 5% yield). ^{1}H NMR (499 MHz, Chloroform-d) δ 7.72 (q, J = 7.9 Hz, 1H), 7.25 (dd, 1H), 6.79 (dd, J = 8.1, 2.8 Hz, 1H), 6.72 (d, 2H), 6.62 (d, 2H), 4.37 (s, 2H), 2.82 (s, 6H).

^{1}H NMR (500Hz) of 15:

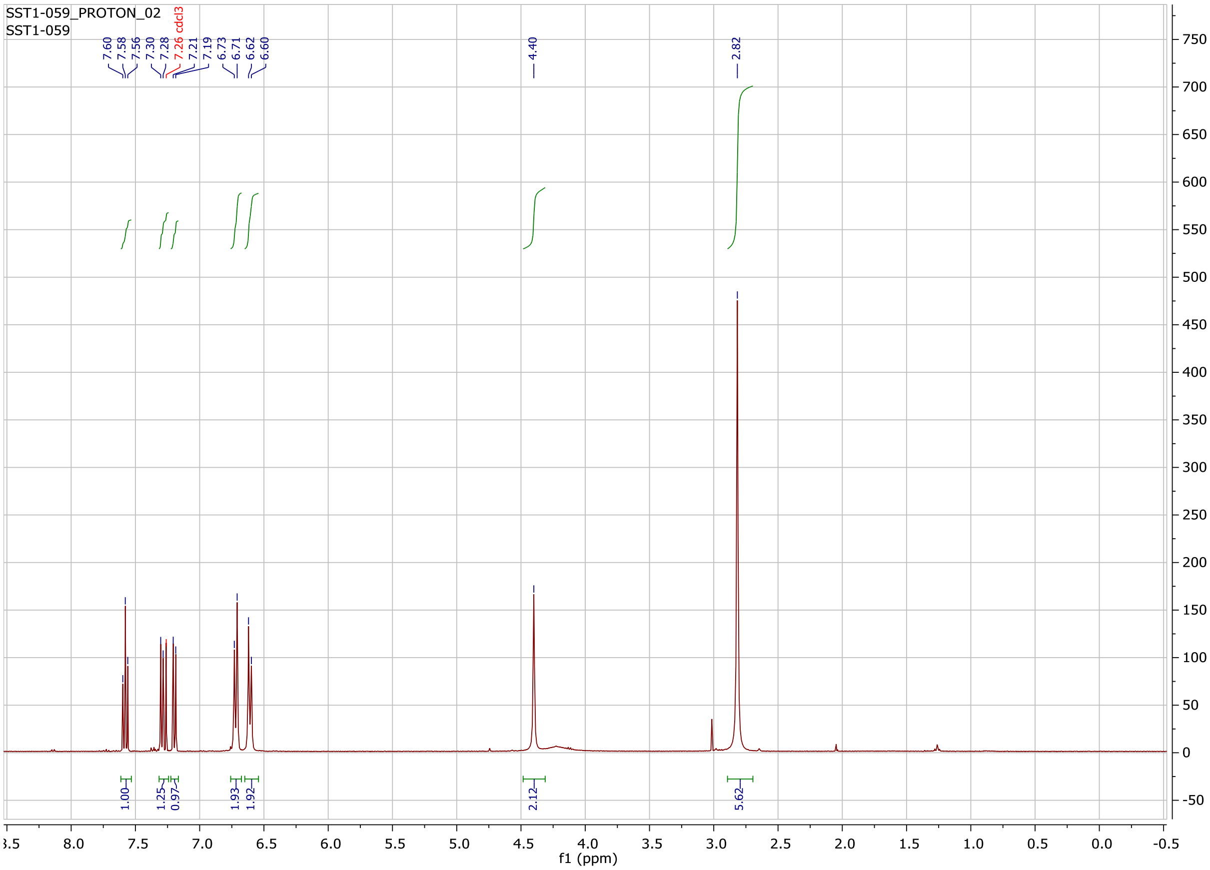

For Radiochemistry: Reagents and solvents were commercially available and used without further purification, unless otherwise noted: sodium chloride, 0.9% USP and sterile water for Injection, USP were purchased from Hospira; Dehydrated Alcohol for Injection, USP was obtained from Akorn Inc.; Ascorbic Acid for Injection, USP was acquired from Bioniche Pharma; Ammonium Bicarbonate was obtained from Fisher Scientific. Shimalite-Nickel was purchased from Shimadzu; iodine was obtained from EMD; phosphorus pentoxide was acquired from Fluka; molecular sieves were purchased from Alltech; and HPLC columns were acquired from Phenomenex. Other synthesis components were obtained as follows: sterile filters were acquired from Millipore; C18-light Sep-Paks and Porapak Q were purchased from Waters Corporation; 10 cc sterile vials were obtained from HollisterStier. Sep-Paks were flushed with 10 mL of ethanol followed by 10 mL of sterile water prior to use.

General Procedures for Fluoride Preparation to be used in Radiochemical Synthesis:

Potassium [^{18}F]fluoride was prepared using a TRACERLab FX_{FN} automated radiochemistry synthesis module (General Electric, GE). [^{18}F]Fluoride was produced via the $^{18}O(p,n)^{18}F$ nuclear reaction using a 16 MeV GE PETTrace cyclotron (40 µA beam for 30 min generated 1500 mCi of [^{18}F]fluoride). The [^{18}F]fluoride was delivered to the synthesis module (in a 1.5 mL bolus of [^{18}O]water) and trapped on a QMA-light Sep-Pak preconditioned with ethanol, water, and a 4M bicarbonate solution to remove [^{18}O]water. [^{18}F]Fluoride was eluted into the reaction vessel using aqueous tetraethylammonium (TEA) bicarbonate (3.5 mg in 0.5 mL of water). Acetonitrile (MeCN, 1 mL) was added to the reaction vessel, and the resulting solution was dried azeotropically to give dry TEA-[^{18}F]fluoride. Evaporation was achieved by heating the reaction vessel to 100 °C and drawing full vacuum for 4 min. After this time, the reaction vessel was subjected to an argon stream and simultaneous vacuum draw for an additional 4 min.

Radiochemical Synthesis of MOM-protected [^{18}F]FHQ415 (**8**):

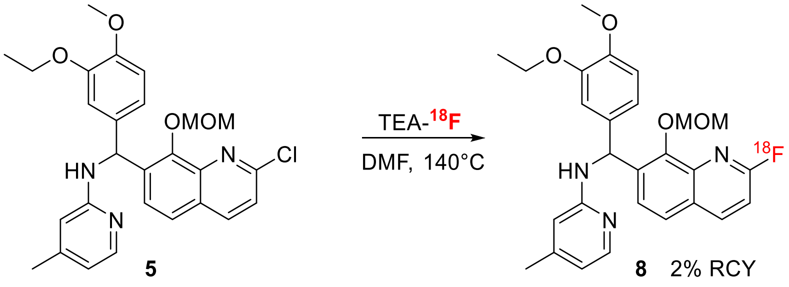

A solution of O-MOM protected chloro-HQ415 precursor (**5**, 5 mg) dissolved in anhydrous DMF (1 mL) was added to the reactor, and the mixture was stirred at 140°C for 20 min. The reactor was cooled to 60°C, and 2 mL of semi-preparative HPLC buffer was added to the crude reaction mixture. The reaction mixture was transferred to the product vial. The reactor was rinsed with 3 mL's of DMF and transferred to the product vial containing the reaction mixture. A sample of this solution was taken for HPLC and rad-TLC analysis to reveal that the protected fluorine-18 analogue had been made in 18% RCY as determined by HPLC.

*Deprotection screen of **8** to produce [^{18}F]FHQ415* (**9**):

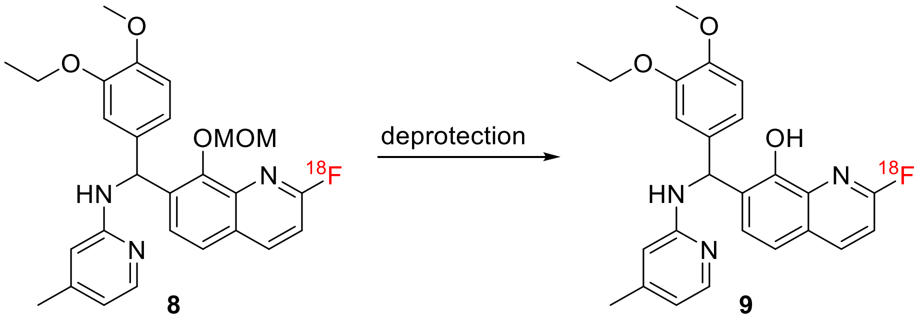

In 4 mL scintillation vials was added 0.5 mLs of the reaction mixture containing **8**. Another 0.5 mL of either concentrated (conc.) HCl (**Table 3.1, entry A and B**), 4 M HCl (**Table 3.1, entry C and D**), or trifluoroacetic acid (TFA, **Table 3.1, entry E and F**). The vials were shaken to mix and either added to a heating mantle set at 100°C or left to sit at room temperature for 10 minutes. After this time, samples were taken for HPLC and rad-TLC analysis.

Chromatograms from HPLC and rad-TLC for [^{18}F]FHQ415 analysis :

A Phenomenex Luna C18 5µ 150x4.6 mm HPLC column was used to analyze both the reaction mixture to produce **8** and the deprotection screen in an attempt to produce **9**. A 40% EtOH 10mM ammonium acetate (NH_4OAc) buffer at pH 4.5 afforded efficient separation of the protected and deprotected chloro-precursors (**4** and **5**) and fluorine standards (**6** and **7**) with r.t.'s at 11.08 (**4**), 14.68 (**5**), 11.96 (**6**) and 7.84 (**7**).

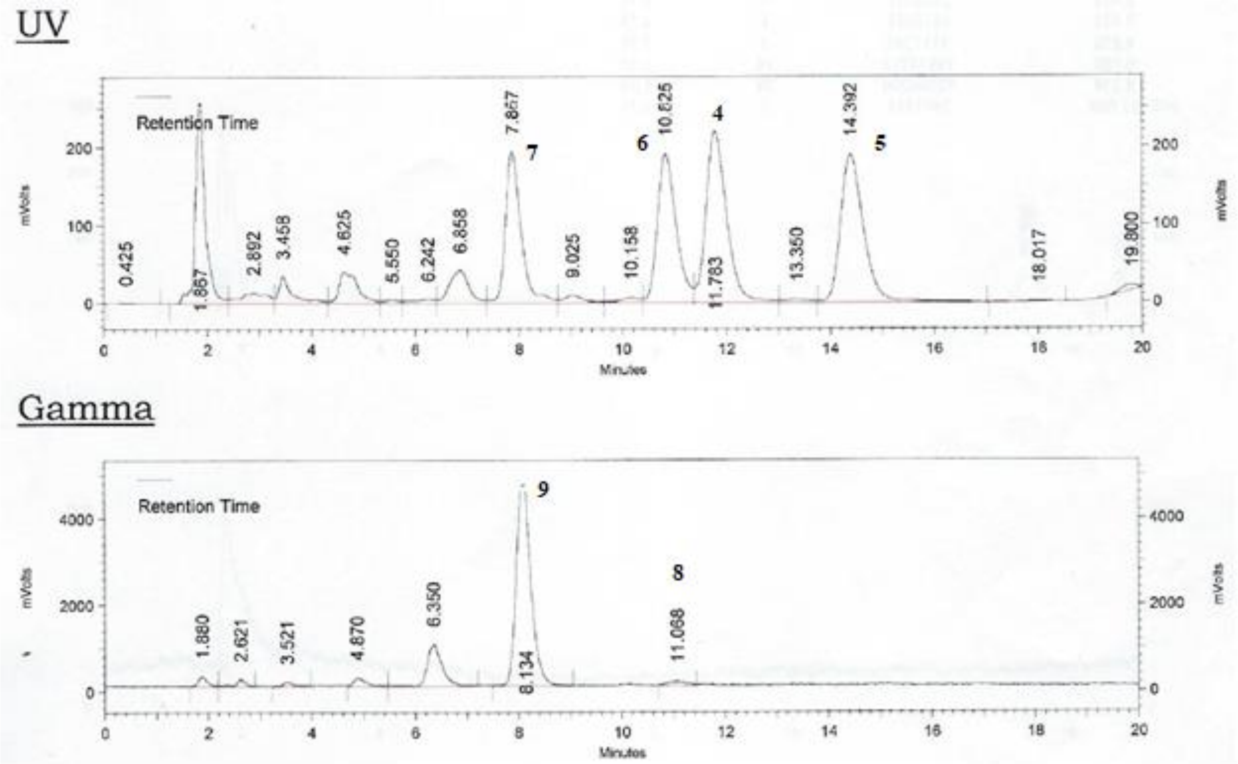

Fig. 3. 7: QC chromatogram for identity check of **9** confirmed by co-injection with standard **7**

3.4.2. *Radiochemical Synthesis of [^{18}F]FL2-b (**16**):*

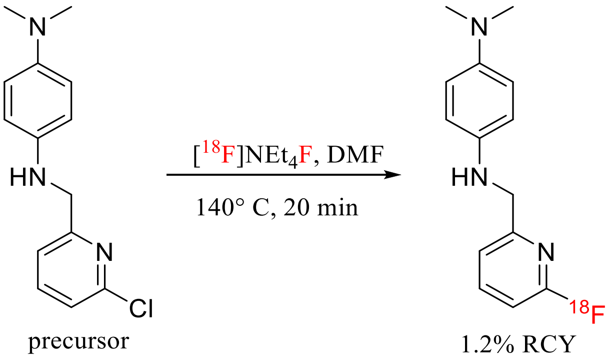

Scheme 3. 7: Synthesis of [^{18}F]FL2-b

A solution of vacuum dried 2-chloropyridine precursor (1.0 mg) dissolved in anhydrous DMF (1 mL) was added to the reactor, and the mixture was stirred at 140°C for 20 min. The reactor was cooled to 60°C, and 2 mL of semi-preparative HPLC buffer was added to the crude reaction mixture. The resulting solution was purified using HPLC (column: Phenomenex Gemini C18, 250x10 mm, mobile phase: 10 mM NH_4HCO_3 in 40% MeCN supplemented with 1 mM L-ascorbic acid, pH ~9.7 adjusted with 3mL/L sat. NH_4OH, flow rate: 2.5 mL/min) The product peak (~27 min retention time) was collected and diluted into a round-bottom flask containing 50 mL water supplemented with 50 µL ascorbic acid solution (500mg/mL Ascorbic Acid in water). The solution was then passed through a C-18 extraction cartridge to remove organic solvent. The disk was washed with 5 mL sterile water supplemented with 10µL ascorbic acid solution (500mg/mL in water). The product was eluted with 0.5 mL of ethanol into the product vial followed by 4.5 mL of sterile water supplemented with 10 µL ascorbic acid solution (500mg/mL in water). The final formulation was passed through a 0.2 µM needle filter into a sterile dose vial [3.2% non-decay corrected radiochemical yield, mean yield at end of synthesis = 58 mCi, >99% radiochemical purity, specific activity = 3100 Ci/mmol, clear and colorless, n = 4].

Quality control of [^{18}F]FL2-b

Radiochemical purity of [^{18}F]FL2-b was assessed using Shimadzu LC-2010A HT system equipped with the UV and Rad detectors (column: Phenomenex Gemini C18, 250x4.6 mm; mobile phase: 10 mM NH_4HCO_3 in 30% MeCN, pH 10 adjusted with 3mL/L sat. NH_4OH solution; flow rate: 2.0 mL/min; wavelength: 254 nm; room temperature; product peak: ~18 min)

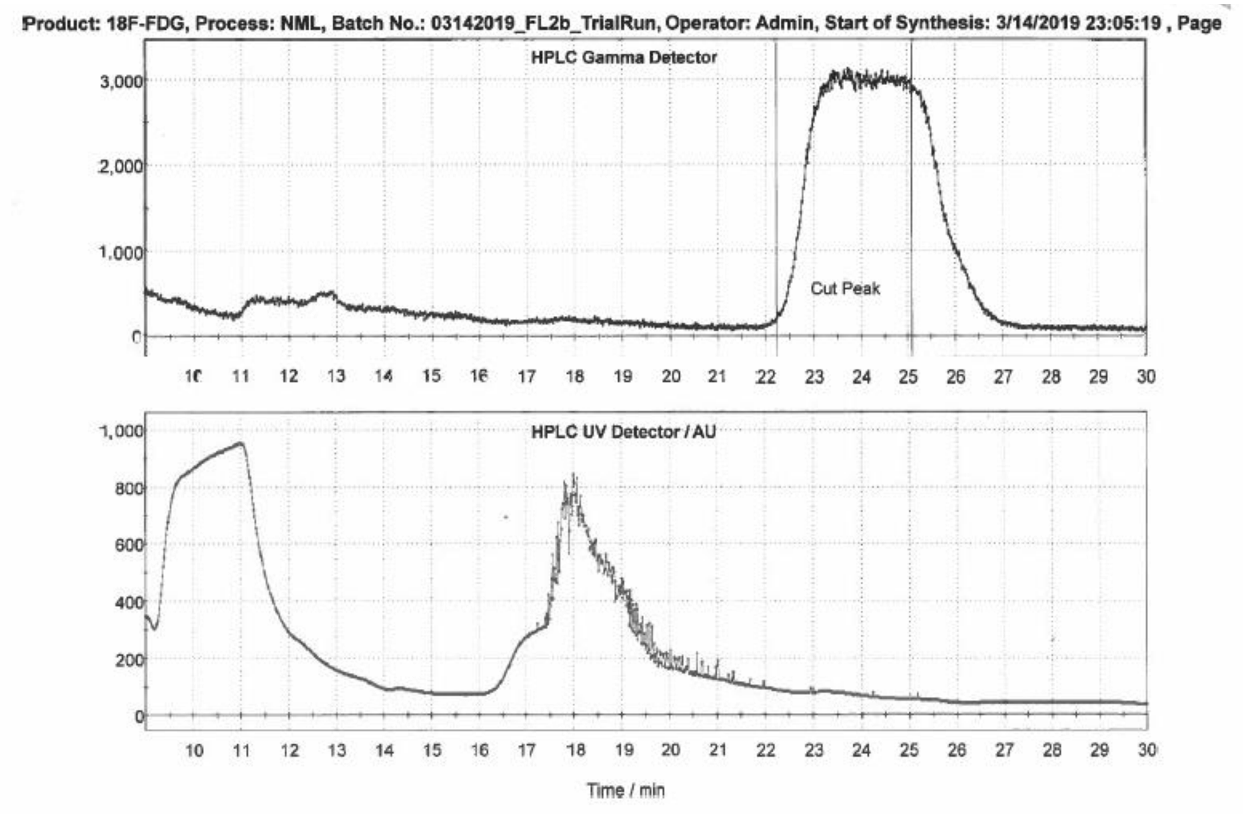

Fig. 3. 8: Semipreparative HPLC chromatogram of [^{18}F]FL2-b reaction

3.4.3. *[^{18}F]FL2-b In Vitro studies:*

Frozen blocks (1x1 inch) of motor cortex from the postmortem brain of ALS patient and age-matched control were used for the autoradiography binding studies. Frozen blocks were sliced into 20 µm sections using a Hacker Instruments cryostat set to -15ºC. Tissue was thaw-mounted on the 1x3 inch polylysine-subbed glass slides. Sections used for autoradiography experiments were incubated for 5 min with phosphate buffer saline (PBS) buffer pH 7.4. To determine total binding, brain sections were transferred to a solution of various [^{18}F]FL2-b concentrations (**Figure**

3.7, 3.8, and 3.9) in PBS (pH 7.4) and incubated for 30 min. Similarly, the non- specific binding and displacement experiments were conducted by incubating adjacent tissue sections in the same concentration of [^{18}F]FL2-b, but supplementing them with 1 μM of "cold" FL2-b in PBS (pH 7.4) for 30 min at room temperature. Subsequently, all tissue sections were washed with PBS (pH 7.4) for 2 min (x2) and rinsed with water for 5 sec to remove unbound radioactivity. Finally, all slides were dried under continuous airflow for 5 min before being exposed to a high-resolution phosphor imaging plate for 15 min. The exposed plate was then scanned using Typhoon 7000 phosphoimager. Image analysis was performed using software ImageQuant (Molecular Dynamics).

Binding Study: To quantify the amount of bound radiotracer to the brain sections, calibration curves were made for each autoradiography experiment. The various [^{18}F]FL2-b concentration solutions were prepared by first calculating the concentration of [^{18}F]FL2-b in the final dose (radioactivity concentration(Ci/mL) divided by molar activity(mmol/Ci)), creating 100 nM and 10 nM [^{18}F]FL2-b stock solutions, then subsequently diluting with milliQ water to the desired concentrations (1, 2, 5, 20, 30, 40, 50, 60, 70 nM) in cytomailers. By pipetting a series of 2 µL drops of the known [^{18}F]FL2-b concentrations onto a TLC plate and exposing them simultaneously with the brain sections to the phosphor imaging plate, a standard curve could be generated by drawing regions around the pipetted spots using ImageQuant software and plotting the intensities against their corresponding concentrations. The standard curve (fmol of substance vs total counts) could then be used to calculate fmol of radiotracer bound in the area of interest on the brain tissue. The phosphoimager presents the signal for the region of interest as counts per pixel. Therefore, we used a known pixel size (25 µm) to calculate counts per square millimeter. The final calculation involved conversion of counts per square millimeter to femtomoles per square millimeter in the regions of interest. Data analysis including determination of Kd and Bmax values was performed with GraphPad Prism (Version 8.0) using nonlinear regression.

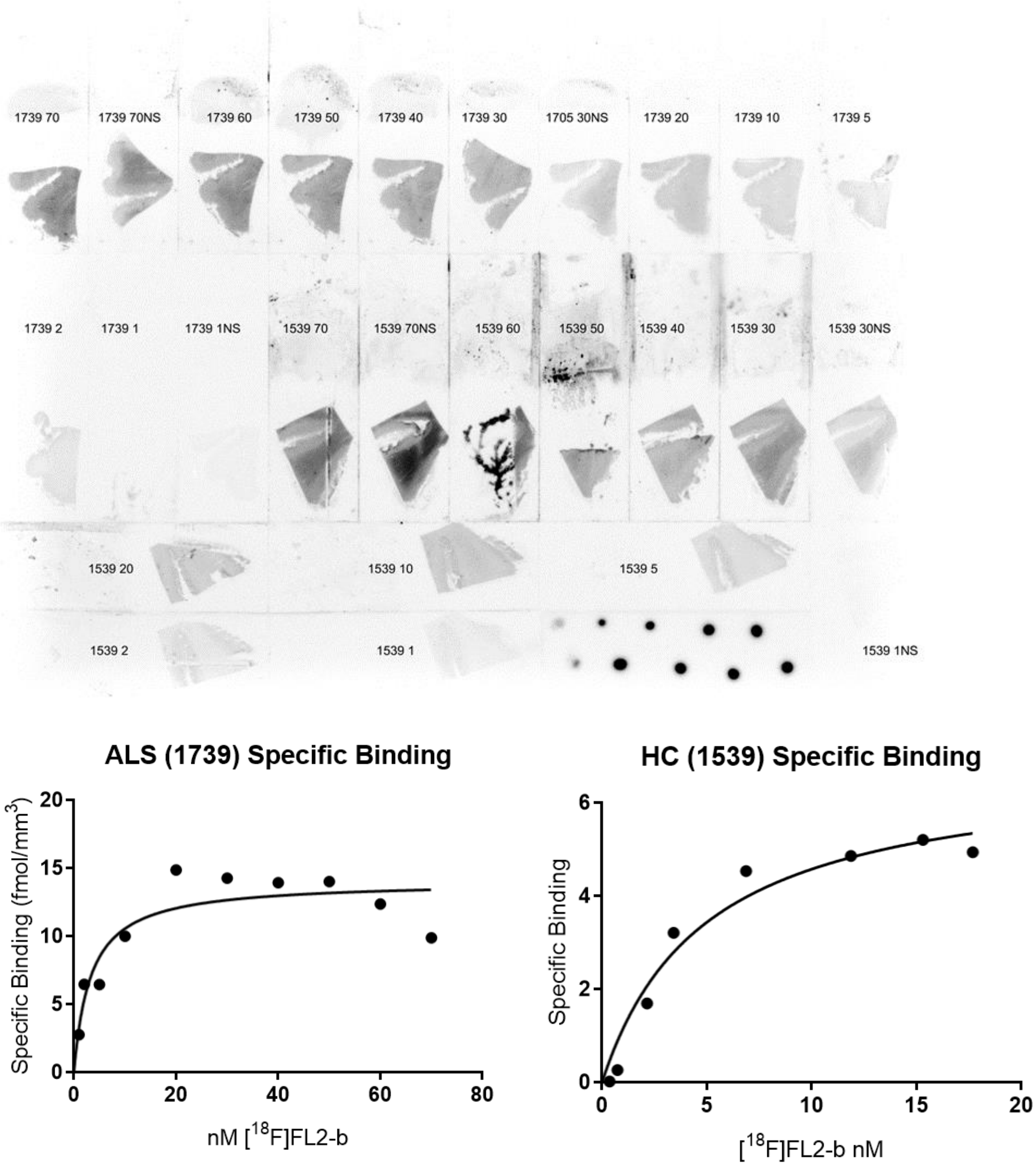

Fig. 3. 9: Autoradiographic phosphor imaging plate and saturated binding curves of [^{18}F]FL2-b on motor cortex tissue (Patient ID: 1739 and 1539)

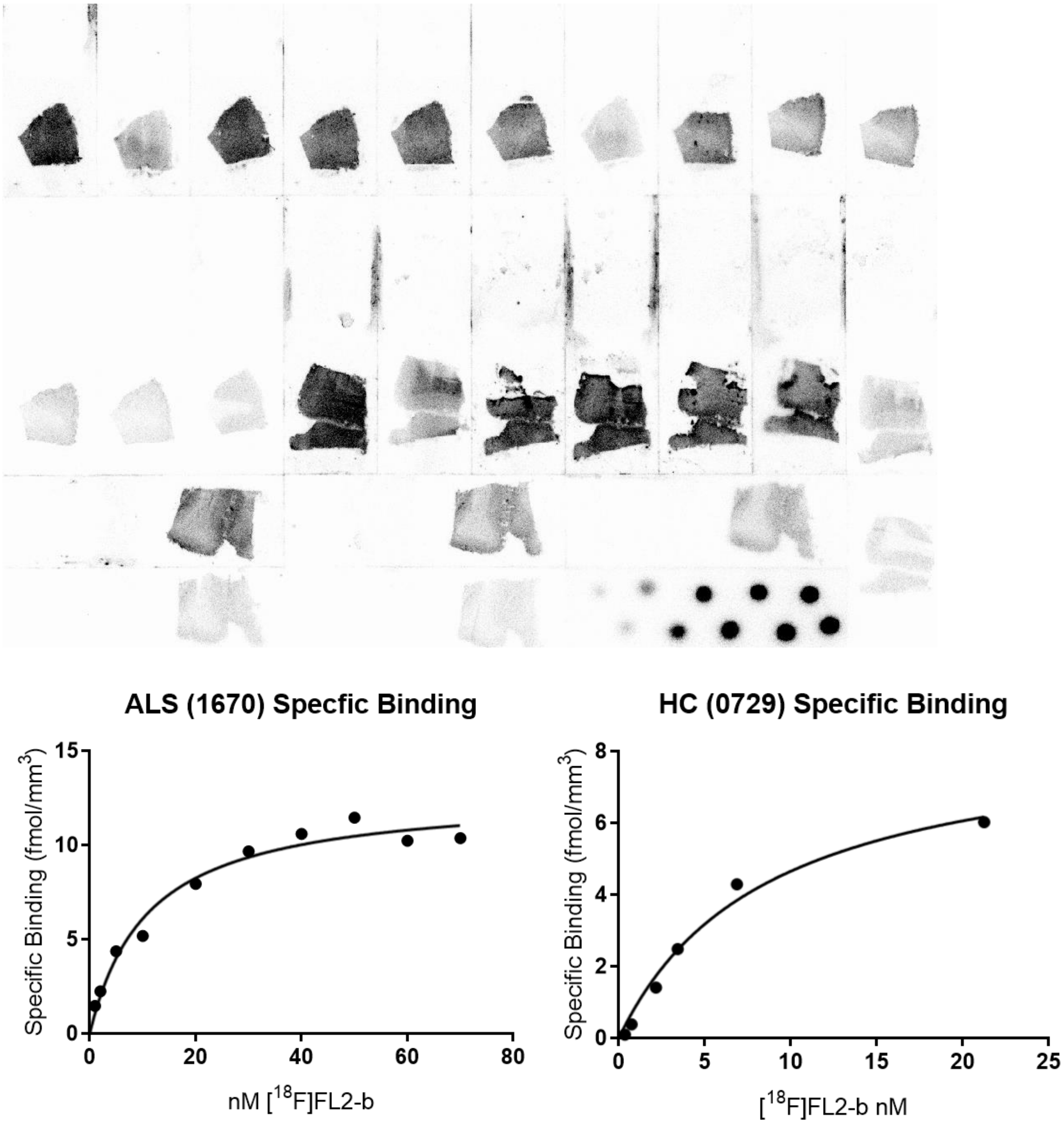

Fig. 3. 10: Autoradiographic phosphor imaging plate and saturated binding curves of [^{18}F]FL2-b on motor cortex tissue (Patient ID: 1670 and 0729)

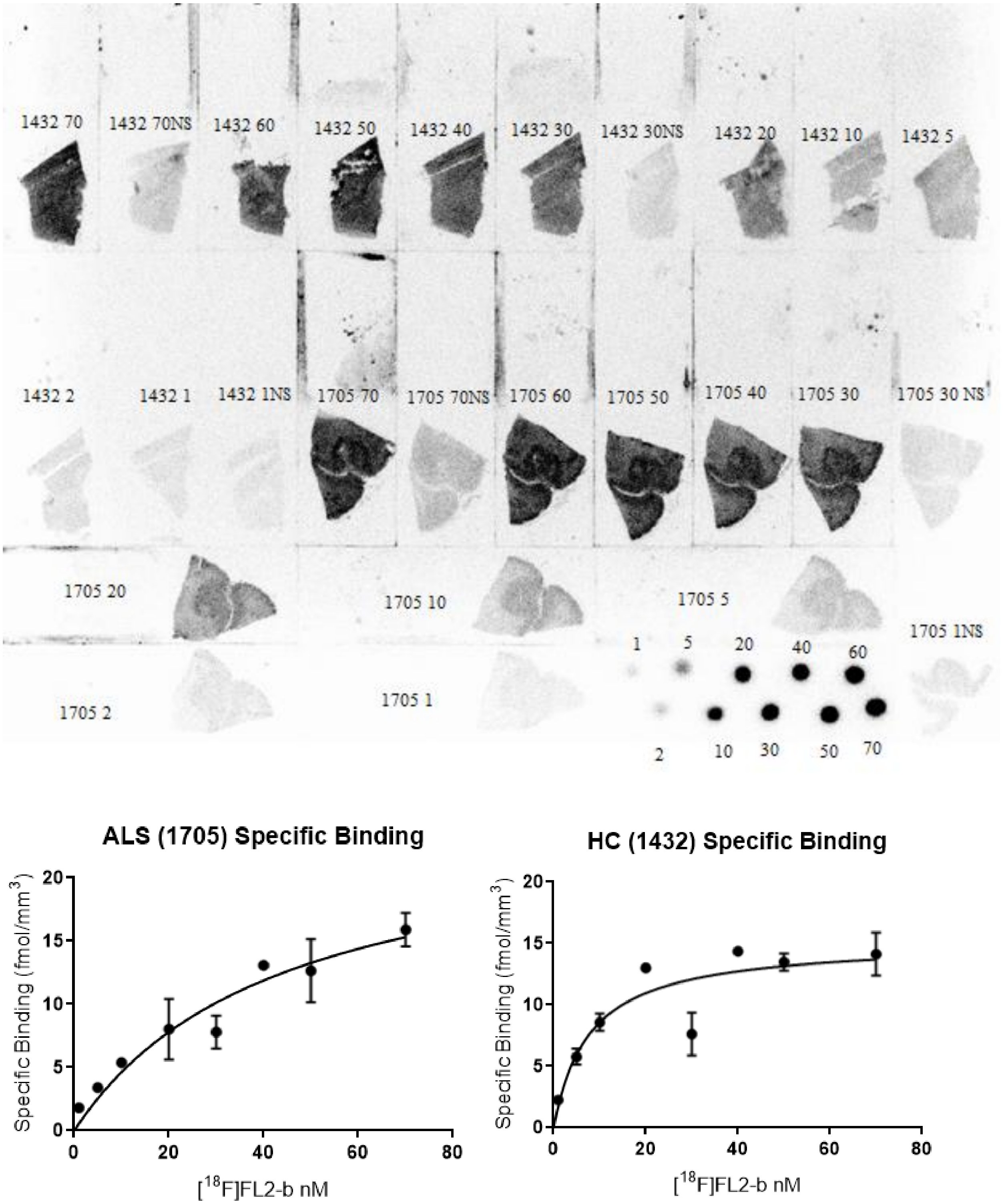

Fig. 3. 11: Autoradiographic phosphor imaging plate and saturated binding curves of [^{18}F]FL2-b on motor cortex tissue (Patient ID: 1705 and 1432)

Immunohistochemistry:

TDP-43 aggregate burden was established in ALS brain tissue using Anti-pTDP-43 antibody (**Figure 3.10**). Anti-pTDP-43 Antibody: Immunohistochemistry was performed according to Vectastain Elite ABC Kit instructions. Briefly, 20 µm tissue sections used for autoradiography were fixed with Davidson's Fixative overnight and used directly for immunohistochemistry. Fixed sections were washed in 70% ethanol for 30 min followed by incubation with 1% sodium dodecyl sulfate (SDS) for 15 min at rt. Next, tissue sections were briefly washed with PBS pH 7.4 and then endogenous peroxidase activity was quenched with 0.3% H_2O_2 in 70% methanol for 15 min at room temperature. These sections were washed with PBS-T solution for 1 min (x3) and blocked with PBS-TBA for 30 min at room temperature. Then, the tissue slides were incubated for 24 hours at 4°C with primary antibody (Millipore anti-pTDP-43) diluted 1:1000 in PBS-TBA. After 24 hours, these sections were washed with PBS-T for 5 min (x3) followed by the biotinylated secondary antibody application for 30 min at room temperature (diluted in PBS-T per Vectastain instructions). Once secondary antibody incubation was complete, all sections were washed in PBS-T for 5 min (x3). The ABC solution (diluted in PBS-T per Vectastain instructions) was applied for 30 min at room temperature. Then, a 5 min rinse (x3) was performed before transferring sections to the DAB solution (tablet by Sigma) for 10 min at room temperature. Finally, the tissue sections were rinsed in water pH 4.0 and counterstained with Giemsa before cover slipping them with Permount. Histological slides were visualized under a light microscope so that markers could be placed at nuclei containing TDP-43 aggregation.

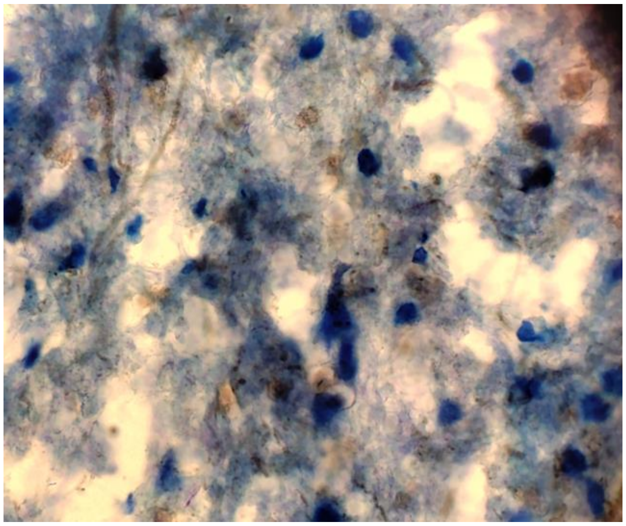

Fig. 3. 12: TDP-43 aggregate IHC showing cytoplasmic inclusions (brown circles) and dystrophic neurites (brown rods)

3.5. REFERENCES

1 R. Giampietro, F. Spinelli, M. Contino and N. A. Colabufo, *Mol. Pharm.*, 2018, **15**, 808–820.

2 X. Huang, C. S. Atwood, R. D. Moir, M. A. Hartshorn, R. E. Tanzi and A. I. Bush, *J. Biol. Inorg. Chem.*, 2004, **9**, 954–960.

3 C. Garnier, F. Devred, D. Byrne, R. Puppo, A. Y. Roman, S. Malesinski, A. V. Golovin, R. Lebrun, N. N. Ninkina and P. O. Tsvetkov, *Sci. Rep.*, 2017, **7**, 1–10.

4 C. Opazo, S. Luza, V. L. Villemagne, I. Volitakis, C. Rowe, K. J. Barnham, D. Strozyk, C. L. Masters, R. A. Cherny and A. I. Bush, *Aging Cell*, 2006, **5**, 69–79.

5 C. W. Ritchie, A. I. Bush, A. Mackinnon, S. Macfarlane, M. Mastwyk, L. MacGregor, L. Kiers, R. Cherny, Q.-X. Li, A. Tammer, D. Carrington, C. Mavros, I. Volitakis, M. Xilinas, D. Ames, S. Davis, K. Beyreuther, R. E. Tanzi and C. L. Masters, *Arch. Neurol.*, 2003, **60**, 1685–1691.

6 N. Vasdev, P. Cao, E. M. van Oosten, A. A. Wilson, S. Houle, G. Hao, X. Sun, N. Slavine, M. Alhasan, P. P. Antich, F. J. Bonte and P. Kulkarni, *Med. Chem. Comm.*, 2012, **3**, 1228–1230.

7 S. H. Liang, J. P. Holland, N. A. Stephenson, A. Kassenbrock, B. H. Rotstein, C. P. Daignault, R. Lewis, L. Collier, J. M. Hooker and N. Vasdev, *ACS Chem. Neurosci.*, 2015, **6**, 535–541.

8 H. S. Krishnan, V. Bernard-Gauthier, M. S. Placzek, K. Dahl, V. Narayanaswami, E. Livni, Z. Chen, J. Yang, T. L. Collier, C. Ran, J. M. Hooker, S. H. Liang and N. Vasdev, *Mol. Pharm.*, 2018, **15**, 695–702.

9 S. Tanzey, S. Thompson, X. Shao, A. Brooks and P. Scott, *J. Nucl. Med.*, 2018, **59**, 1019–1019.

10 J. S. Choi, J. J. Braymer, R. P. R. Nanga, A. Ramamoorthy and M. H. Lim, *Proc. Natl. Acad. Sci. U. S. A.*, 2010, **107**, 21990–21995.

11 M. W. Beck, S. B. Oh, R. A. Kerr, H. J. Lee, S. H. Kim, S. Kim, M. Jang, B. T. Ruotolo, J. Y. Lee and M. H. Lim, *Chem. Sci.*, 2015, **6**, 1879–1886.

12 B. P. Cary, A. F. Brooks, M. V Fawaz, X. Shao, T. J. Desmond, G. M. Carpenter, P. Sherman, C. A. Quesada, R. L. Albin and P. J. H. Scott, *ACS Med. Chem. Lett.*, 2015, **6**, 112–116.

13 A. Brooks, S. Tanzey, X. Shao and P. Scott, *J. Nucl. Med.*, 2018, **59**, 613–613.

14 M. S. Forman, J. Q. Trojanowski and V. M. Y. Lee, *Curr. Opin. Neurobiol.*, 2007, **17**, 548–555.

15 M. Fatima, R. Tan, G. M. Halliday and J. J. Kril, *Acta Neuropathol. Commun.*, 2015, **3**, 47.

CHAPTER 4

Synthesis and Initial In Vivo Evaluation of [^{11}C]AZ683—A Novel PET Radiotracer for Colony Stimulating Factor 1 Receptor (CSF1R)[1]

4.1. Introduction

Development of novel Positron Emission Tomography (PET) tracers is driven by the need to understand the mechanisms underlying human diseases. To understand neurodegenerative diseases (NDs), knowledge of potential biomarkers must be elucidated. Once a novel radiotracer has been synthesized, it can be used to determine if a biomarker of interest is altered in a human and at what time point during the disease. Since NDs are still poorly understood, PET imaging can be used to assess what biomarkers play a true role in the causation and progression of these debilitating diseases.

Efforts to synthesize novel radiotracers described in this work thus far have been driven by the metal hypothesis of neurodegeneration. Chapter 2 saw the development of an iron chelator PET tracer to probe iron accumulation in NDs and Chapter 3 focused on developing a PET probe for the accumulation of metal-protein aggregates induced by copper or zinc. Though it is suspected that transition metals play one of the earliest roles in neurodegeneration, it does not tell the whole story. After uncontrolled, toxic reactivity of the transition metals iron and copper, reactive oxygen-species are formed. This oxidative stress promotes inflammatory signaling, recruiting immune cells such as microglia leading to neuroinflammation (**Figure 4.1**). Neuroinflammation being a hallmark of most NDs, has been shown to play an early role as well.

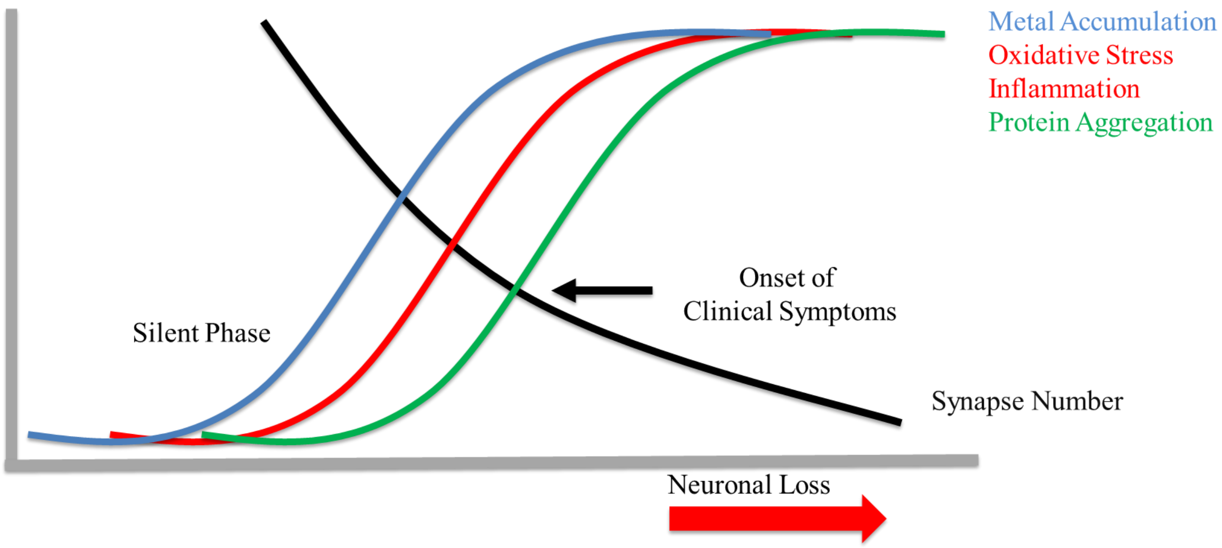

Fig. 4. 1: Progression of Neurodegenerative Diseases (NDs) is indicated by a decrease in synaptic density and accompanied by the accumulation of certain biomarkers (metal accumulation, oxidative stress, inflammation, and protein aggregation) at various stages of the disease. Initially NDs have a silent phase where no clinical symptoms are apparent until a sufficient loss in the number of synapses has occurred.

Neuroinflammation propagates an oxidatively stressed environment by producing more ROS to clean up factors that caused it initially. A vicious circle ensues, leading to DNA damage, protein aggregation, and finally apoptosis of neurons. The death of neuronal cells leads to a decrease in the number of synapses formed by these cell types. After a certain point neuron cell death, clinical symptoms start to manifest in the patient as a decrease in neurotransmitters are being produced and not functioning to initiate signals from the brain. Eventually, so many cells have died that structural abnormalities can be seen in the brain by imaging techniques like magnetic resonance imaging (MRI), termed neuronal loss, and ultimately leading to death.

Just as the development of metal chelating PET tracers were developed to investigate metals in NDs, so to can other small molecule PET tracers be developed for biomarkers of neuroinflammation. One biomarker of interest specific to neuroinflammation is colony stimulating factor-1 receptor (CSF1R, M-CSF, or cFMS).CSF1R is a class III receptor tyrosine kinase[2] that regulates immune response by controlling the survival and activity of macrophages and macrophage-like cells.[3] Abnormal expression of CSF1R, or over activity of its endogenous ligands

(CSF1 and IL-34), plays a role in many disorders that have an immune/inflammatory component.[4] Specifically, chronic inflammation caused by increased activity of macrophages is present in many autoimmune disorders such as rheumatoid arthritis (RA), inflammatory bowel disease, and autoimmune nephritis, among others.[5,6] The overactivity of the macrophages in these processes is thought to be due to increased CSF1R activation. The contribution of CSF1R to symptomatic Alzheimer's Disease (AD) is also well known, due in part to its proliferative effects on microglia, which are associated with neuroinflammation, a hallmark clinical symptom of AD.[7,8] A mechanism for CSF1R involvement in inter-neuronal transmission of pathogenic tau protein by microglia was also recently elucidated.[9] Involvement of CSF1R in certain types of cancers, such as gliomas, also correlates with poor disease prognosis, as proliferation of CSF1R-controlled tumor-associated macrophages (TAMs) correlates with tumor angiogenesis and metastasis.[5,10–12] Thus, CSF1R PET imaging would be useful for more than just ND analysis.

CSF1R inhibitors (both small molecules and biologics) have been proposed as a means of controlling inflammation in this multitude of diseases and disorders via macrophage depletion/regulation.[13] Many CSF1R inhibitors can be found in both academic and patent literature,[5,6,14] and several have proceeded to clinical trials for the treatment of RA[15] and various types of cancer.[12] However, not all macrophage populations are CSF1R-sensitive, necessitating that CSF1R involvement must be positively identified prior to the start of treatment, which can be achieved by a CSF1R specific PET imaging agent.CSF1R upregulation is only present at the site of inflammation. Although blood biomarkers can be used to directly measure CSF1R involvement in certain diseases, such as lymphoma,[12] methods of determining CSF1R involvement and quantifying CSF1R levels at locations not directly connected to the central circulatory system is difficult, particularly in the CNS, and employs either indirect means (i.e., measurement of CSF1 levels as a proxy for CSF1R)[15] or invasive procedures (i.e., immunohistochemistry using a biopsy sample or surgically excised tissue).[16,17] In fact, despite the implication of irregular CSF1R levels in numerous diseases,[5] quantitative information on expression levels in disease is generally lacking from the literature. In part this is currently no non-invasive method that can positively identify and quantify CSF1R involvement in disease. This unmet need can be readily achieved with PET imaging, wherein a CSF1R-selective radiolabeled ligand (radiopharmaceutical) would be used to detect changes in activity, expression levels, and localization of CSF1R in a minimally invasive manner. Furthermore, a brain-penetrant CSF1R-selective PET imaging agent could be used to selectively image microglia, as they are the only cells in the brain that express CSF1R under normal conditions.[18] Microglial cells tend to surround sites with amyloid beta (Aß) plaques in order to remove them from the extracellular environment.[19] Current imaging of macrophages/microglia is achieved by using PET tracers that target the translocator protein 18 kDa (TSPO). However, TSPO is not an ideal imaging target since it is expressed in various tissue types (in addition to immune cells). Moreover, a single nucleotide polymorphism (SNP) in the TSPO gene has been identified that leads to considerable variability in its expression levels between patients and, consequently, variability in PET data between patients.[20] These SNPs are known to cause low to no binding affinity with the clinically available PET tracers for this target and thus reduced signaling is observed. Therefore, an imaging agent selective for microglia is of considerable interest for using PET by quantifying CSF1R. Radiopharmaceuticals used in PET imaging are often structural analogs of existing pharmaceutical agents that have been labeled with a positron-emitting radionuclide such as carbon-11 (^{11}C) or fluorine-18 (^{18}F). As such, the radiopharmaceutical can be expected to possess the same pharmacokinetic properties as its nonradioactive counterpart and behave accordingly in vivo. Fortunately, lead identification for

CSF1R PET radiopharmaceutical development is relatively straightforward because recent interest in developing CSF1R inhibitors has led to hundreds of active compounds, several of which have also been translated into clinical trials (see **Figure 4.2** for several leads).[5,6,14] PET imaging agents for CSF1R have been reported previously,[21,22] but none have seen widespread use to date. One is a mixed inhibitor of both CSF1R and tropomyosin receptor kinases B and C (Trk B/C),[21] while the second ([^{11}C]JHU11744) has shown promise in preliminary evaluation in rodent models of AD and neuroinflammation.[22] PET imaging of CSF1R therefore remains underdeveloped and an attempt to address this issue through development of [^{11}C]AZ683 is reported herein,.

AZ683 (**Figure 4.2**) was selected because it has >250-fold selectivity for CSF1R over 95 other kinases, low plasma protein binding, a good pharmacokinetic (PK) profile, and both fluorine and N-methyl moieties which are potential sites for radiolabeling with ^{18}F or ^{11}C, respectively.[23–25] Moreover, AZ683 has low nanomolar affinity for CSF1R (K_i = 8 nM; IC_{50} = 6 nM), making it ideal for PET studies which typically utilize nanomoles-picomoles of radiotracer, and the cLogP of the neutral (uncharged) compound is 3.1 which suggests that it should cross the BBB. Since N-methylation of the desmethyl precursor with [^{11}C]MeI (or [^{11}C]MeOTf) was envisioned to be simpler than ^{18}F-labeling of this scaffold, the synthesis and carbon-11 radiolabeling of [^{11}C]AZ683 was undertaken for initial evaluation and is described herein. We also report preliminary evaluation of the radiotracer as a CSF1R imaging agent in rodent and non-human primate PET imaging studies.

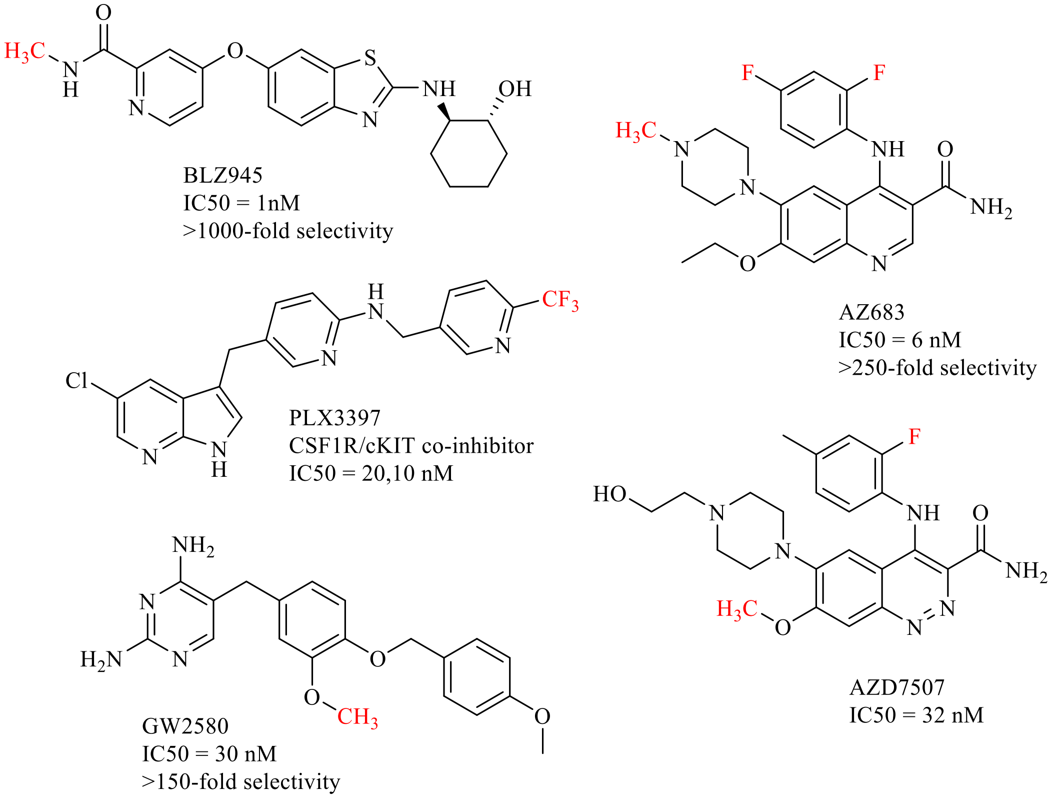

Fig. 4. 2: Potential lead compounds for CSF1R radiopharmaceuticals. Adapted from ref. 2 with permission from MDPI

4.2. Results and Discussion

4.2.1. *Synthesis of Carbon-11 Reference Standard and Precursor*

The AZ683 reference standard **6a** and N-desmethyl precursor **7** were synthesized via modified literature procedures in five and six steps, respectively (**Scheme 4.1**).[24] Both syntheses diverged from a common intermediate **4**. This common intermediate was synthesized via condensation of 4-bromo-3-ethoxyaniline (**1**) with diethylethoxymethylenemalonate to yield **2**. This was followed by cyclization/chlorination with $POCl_3$ and tetrabutylammonium chloride to form chloroquinoline **3**. A subsequent SN_{Ar} reaction with 2,4-difluoroaniline yielded intermediate **4**. Buchwald–Hartwig cross-coupling was then used to couple either N-Boc piperazine or N-methylpiperazine with **4**, yielding intermediates **5a** and **5b** for the reference standard and precursor, respectively. Amidation of the ethyl ester of **5** was performed using formamide/NaOEt to generate reference standard **6a** and N-Boc protected precursor **6b**. Final deprotection of the Boc group of **6b** with trimethylsilyl chloride in methanol furnished precursor **7**. Precursor **7** and reference standard **6a** were readily separable on analytical and semipreparative Phenomenex Luna C18 columns using a 30% ethanolic eluent buffered with sodium phosphate at a pH of 6.6 (see Materials and Methods for details, Section 4.5).

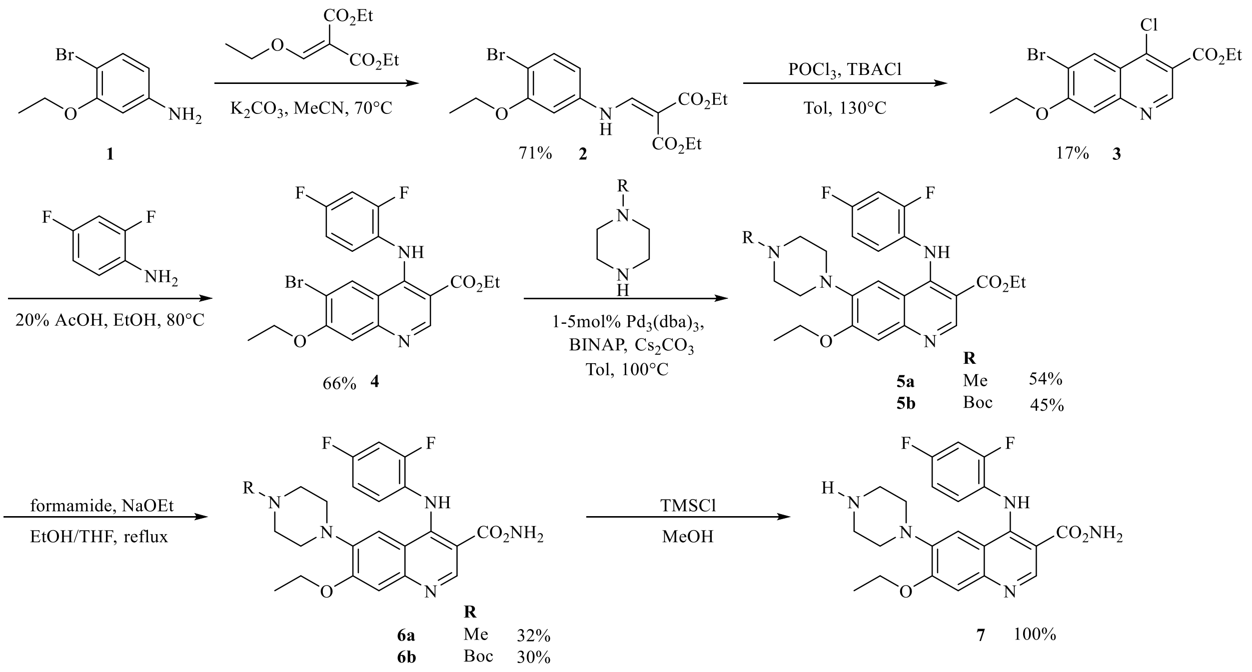

Scheme 4. 1: Synthesis of precursor 6a and reference standard 7 for [^{11}C]AZ683.

4.2.2. *Radiosynthesis of [^{11}C]AZ683*

Radiolabeling of [^{11}C]AZ683 was accomplished by treating precursor **7** with [^{11}C]MeOTf (**Scheme 4.2**). The labeling reaction was automated using a TRACERLab FX$_{\text{C-pro}}$ synthesis module and our standard carbon-11 procedures.[26] Following radiolabeling, [^{11}C]AZ683 was purified within the synthesis module via semipreparative HPLC and formulated for injection (0.9% saline solution containing 10% ethanol) using a Waters C18 1cc vac cartridge to trap/release the product. This resulted in an overall non-decay corrected activity yield of 1125 ± 229 MBq (3.0% based upon 37 GBq of [^{11}C]MeOTf), radiochemical purity >99%, and molar activity of 153 ± 38 GBq/µmol (n = 4), confirming doses were suitable for preclinical evaluation.

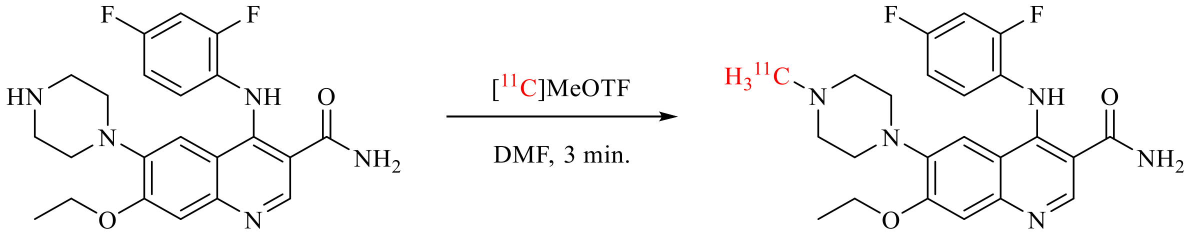

7

[^{11}C]AZ683

Scheme 4. 2: Radiosynthesis of [^{11}C]AZ683 in 3.2% activity yield

4.2.3. *Approaches towards a Precursor for [^{18}F]AZ683*

Concurrent with our efforts to prepare [^{11}C]AZ683, a fluorine-18 analogue of AZ683 was desired by our group due to its longer half-life and as an option to showcase recently developed copper-mediated radiofluorination chemistry used in our lab[27,28] on a drug molecule (**Scheme 4.3**).To this end we began by attempting to synthesize the requisite BPin precursor for radiolabeling, and first postulated that a Bpin-flouro aniline could be used in step 3 of **Scheme 4.1** to yield the desired precursor, preventing major deviation from the already established synthesis route of the carbon-11 precursor and AZ683 reference standard (**Scheme 4.4**).

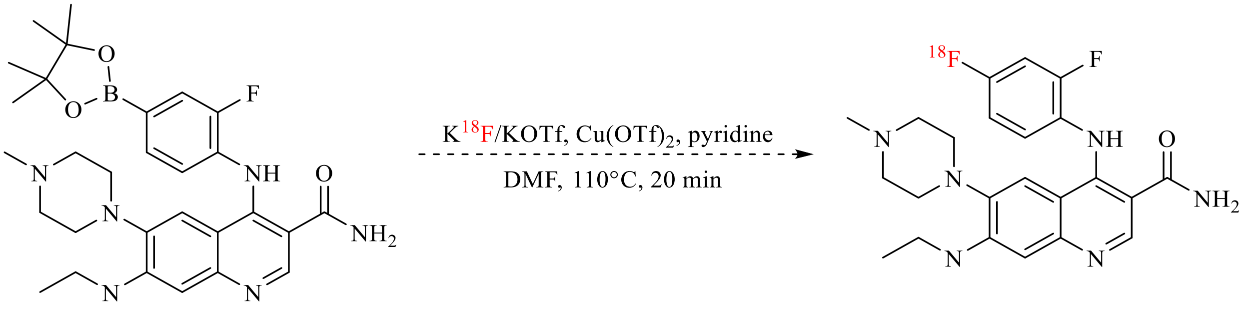

8

[^{18}F]AZ683

Scheme 4. 3: Potential radiosynthesis of [^{18}F]AZ683 using CMRF conditions

To this end, to synthesize the requisite precursor, we initially coupled the BPin aniline with **2** to generate intermediate **9** in 53% yield (**Scheme 4.4**). However**,** synthesis of the requisite ^{18}F precursor **8** has proven more complicated than initially anticipated because an analogous Buchwald-Hartwig coupling reaction failed to generate intermediate **10**. As confirmed by mass spectrometry, the boronic acid ester provided a site for palladium complexation that could result in inter-Suzuki coupling (**Figure 4.4**). Efforts to develop a synthesis of [^{18}F]AZ683 continue, but once the challenges with the proposed synthetic pathway were discovered, we chose to pursue preclinical evaluation of [^{11}C]AZ683.

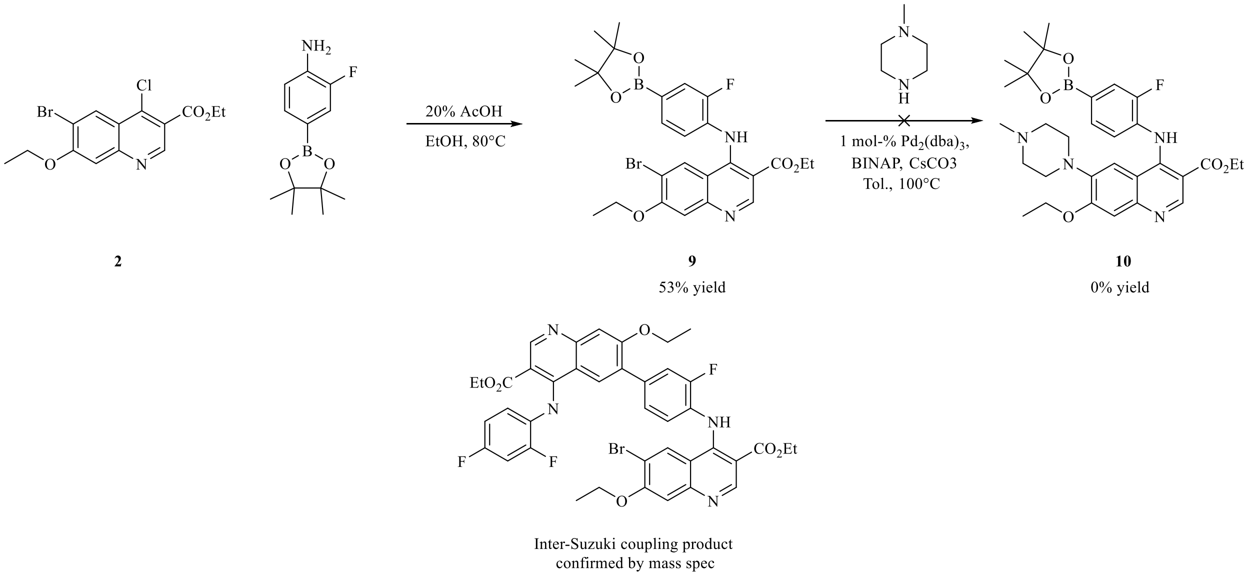

Scheme 4. 4: Attempted Synthesis of an [^{18}F]AZ683 bpin precursor.10

4.2.4. *Preclinical PET Imaging*

Initial evaluation of the imaging properties of [^{11}C]AZ683 was undertaken in female Sprague–Dawley rat (**Figure 4.2**, top). [^{11}C]AZ683 was administered intravenously through the tail vein and rodent brain imaging was conducted for 60 min. Surprisingly, [^{11}C]AZ683 showed little brain uptake. However, high uptake and retention in what looks like the pituitary and thyroid glands (**Figure 4.2**, left) was observed. Although both glands are known for expression of CSF1R protein (thyroid) and CSF1R RNA (thyroid and pituitary),[29] the very high uptake is more likely indicative of non-specific binding associated with the lipophilic nature of the compound (**Table 4.1**). This could be tested by self-blocking studies, which has yet to be done.

It is known that inter-species differences exist between rodents and non-human primates due to the higher metabolic rate in rodents and differing BBB efflux systems. Therefore, imaging in rhesus macaque brain was also performed. The primate imaging results largely mirrored the rat data, with fairly poor brain influx during the early frames, followed by almost complete washout and little brain retention in a normal brain (**Figure 4.2**, right). The signal observed in the central region of the brain could possibly be ventricular uptake. As before, the pituitary gland could be observed in frame which showed a much greater degree of uptake than brain. Overall, brain uptake in monkey was higher than in rat along with some focal uptake in the monkey cerebellum (standardized uptake value (SUV) ~0.3–0.4 at late time points). Given that the cerebellum is an area of known CSF1R expression in humans,[29] and CSF1R function is thought to be conserved between vertebrates,[30] this signal could correspond to CSF1R, presumably associated with microglia found in the monkey cerebellum.[31] However, this will need to be confirmed in future in vitro experiments with primate brain sections. Target receptor density of CSF1R could ostensibly be low in a non-diseased control animal and would explain poor brain retention, but again normal CSF1R levels are challenging to quantify in vivo as they are transient and expected to fluctuate with the turnover of macrophages and microglia. However, low receptor density would not limit first pass brain influx and efflux which was also quite low. Overall, these PET imaging data suggest imaging CSF1R associated with neuroinflammation using [^{11}C]AZ683 may be challenging. That being said, the uptake observed in monkey could be sufficient to observe accumulation in a brain inflammation model. There is literature precedent for TSPO radiotracers with low brain uptake being used to successfully image inflammation in rat models.[32,33] Moreover, the present studies do not rule out labeling the scaffold with a longer-lived PET radionuclide (e.g., ^{18}F or ^{124}I) and using a prolonged infusion protocol so that sufficient radiotracer accumulates at sites of inflammation. [^{11}C]AZ683 could also possibly be used for imaging of peripheral CSF1R to evaluate its role in inflammation outside of the brain.

Given that [^{11}C]AZ683 possesses properties mostly consistent with BBB permeability (**Table 4.1**),[24,34,35] the lack of brain uptake was unexpected and the reasons for it are unclear. It is possible that [^{11}C]AZ683 is a substrate for an efflux transporter on the BBB being that compounds containing a lot of nitrogens tend to be substrates for p-glycoprotein (P-gp).P-gp expression is higher in rodents than monkeys and humans.[36] This could explain the 2–3-fold higher uptake of the radiotracer observed in monkey brain. Given the differences in type and expression levels of efflux transporters between species, monkeys are better for predicting the role of P-gp in limiting brain penetration of drugs in humans.[36] However, as we take a conservative view towards primate safety, methods to determine whether efflux activity is responsible for the low brain uptake of [^{11}C]AZ683 (e.g., cyclosporin A blockade of the P-gp transporter)[37] have not been pursued at this time. Alternatively, in this case, cLogP estimates (**Table 4.1**) may not be a good indicator of BBB permeability. [^{11}C]AZ683 has multiple groups containing nitrogen and oxygen atoms which are ionizable, corresponding to multiple pKa values (**Figure 4.3**).[35] We do not expect the primary amide to limit BBB permeability since we conduct brain imaging with other primary amide-containing radiopharmaceuticals such as [^{11}C]LY2795050.[38] Understanding the relationship between cLogP of charged species as a function of pH is complicated,[34] but it is likely that AZ683 is charged at physiological pH and this could be the reason for poor brain uptake. The oxygen and nitrogen atoms in question also participate in hydrogen bonding, and cLogP—the total number of oxygen and nitrogen atoms in a drug molecule (N + O) offers information about logBBB. If cLogP—(N + O) > 0, logBBB is likely to be positive and the drug has a good probability of entering the CNS.[34] In the case of AZ863, cLogP—(N + O) = −4, suggesting the number of oxygen and nitrogen atoms may be too high for good CNS penetration. All these issues should be considered in the design of next generation CSF1R radiopharmaceuticals going forward.

Property	**Preferred value for successful CNS drugs**[23]	**[^{11}C]AZ683**[21, 24]
Activity	Low nM	K_i = 8 nM; IC_{50} = 6 nM
cLogP	<5	3.0
tPSA	60-70 Å^2	83 Å^2
molecular weight	≤450 g/mol	441 g/mol
H-bond donors	≤3	2
H-bond acceptors	≤7	6
Metabolic stability	$T_{1/2}$ > 3.1 h	2.1 h
Solubility	>60 µg/mL	128 µg/mL
pKa	7.5-10.5	6.5-7.5

Table 4. 1: Properties of [^{11}C]AZ683 compared to a typical CNS drug. Adapted from ref. 2 with permission from MDPI

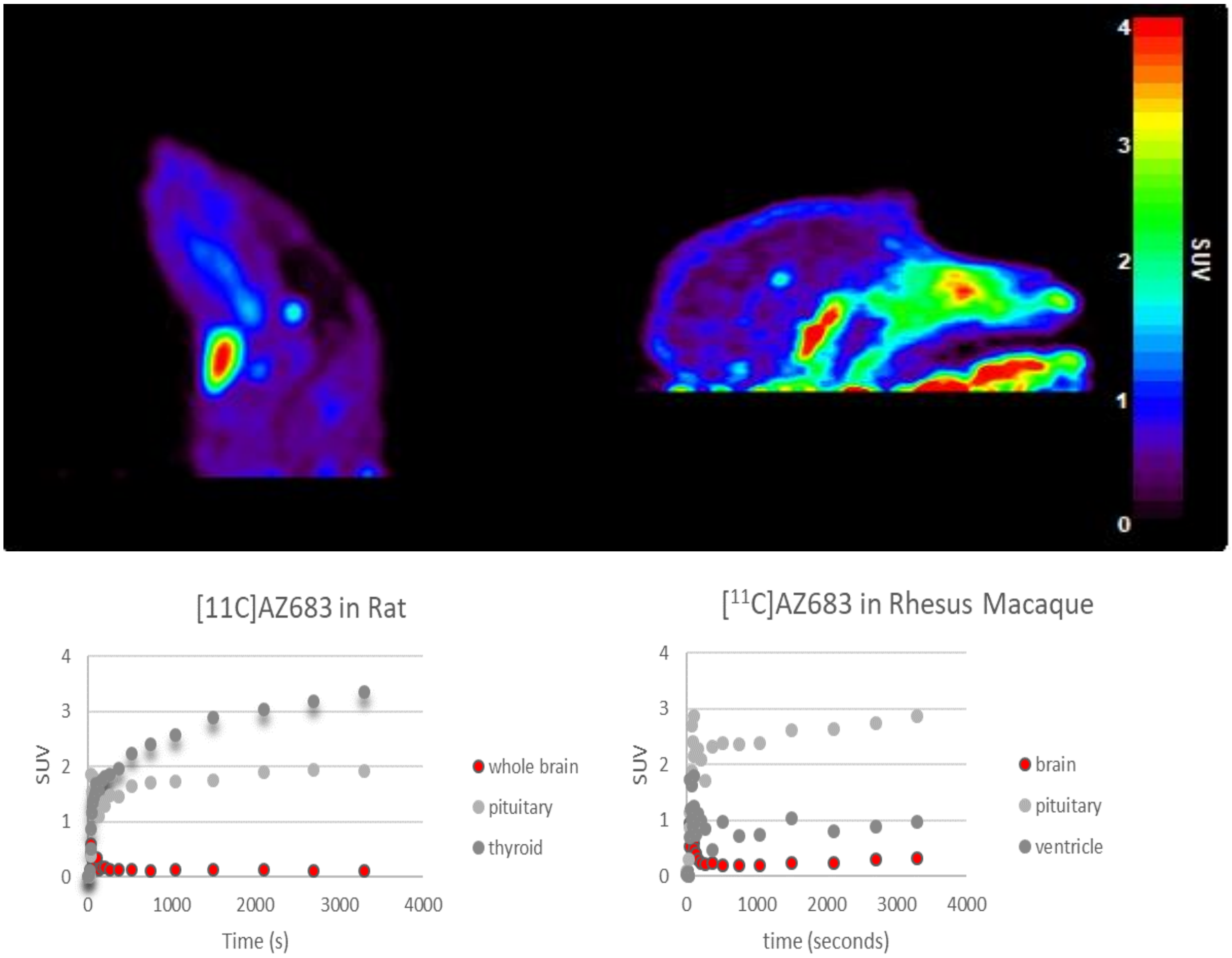

Fig. 4. 3: Summed rodent (left) and primate (right) PET images of [^{11}C]AZ683 (0–60 min after injection of the radiotracer) and associated time–radioactivity curves (SUV = standardized uptake value). Adapted from ref. 2 with permission from MDPI

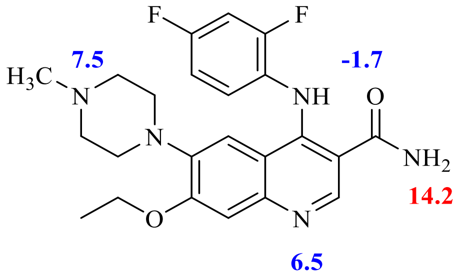

Fig. 4. 4: Multiple pKa values for AZ683.[35] Adapted from ref. 2 with permission from MDPI

4.3. Conclusions

In conclusion, we have developed a radiosynthesis of [^{11}C]AZ683 for PET imaging of CSF1R and neuroinflammation that provides doses suitable for preclinical use. However, preliminary preclinical PET imaging in rodents and nonhuman primates revealed low brain uptake of [^{11}C]AZ683. Overall, these PET imaging data suggest imaging CSF1R associated with neuroinflammation using [^{11}C]AZ683 could be challenging and emphasize that high affinity, good selectivity, and appropriate drug-like properties do not guarantee that a compound will make a good radiopharmaceutical for in vivo brain PET. Nevertheless, uptake in monkey could be sufficient to observe accumulation in a brain inflammation model. These studies also do not rule out labeling the scaffold with a longer-lived PET radionuclide (e.g., ^{18}F or ^{124}I) and using a prolonged infusion protocol to ensure that sufficient radiotracer accumulates at sites of inflammation for imaging and quantitation of CSF1R. [^{11}C]AZ683 could potentially also be used for imaging of peripheral CSF1R to evaluate its role in inflammation outside the brain. Future evaluation in animal models of inflammation appears warranted.

4.4. Materials and Methods

General Considerations

All the chemicals were purchased from commercially available suppliers and used without purification. Automated flash chromatography was performed with Biotage Isolera Prime system. High-performance liquid chromatography (HPLC) was performed using a Shimadzu LC-2010A HT system. ^{1}HNMR spectra were acquired using a Varian 400 apparatus (400 MHz) in $CDCl_3$ or CD_3OD. δ are reported in ppm relative to tetramethylsilane ($\delta = 0$), J are given in Hz. Mass spectra were measured on an Agilent Technologies (Santa Clara CA, USA) Q-TOF HPLC-MS or Micromass (Manchester, UK) VG 70-250-S Magnetic sector mass spectrometer employing the electrospray ionization (ESI) method.

4.5.1. *Compounds Synthesized*

Preparation of Diethyl 2-(((4-bromo-3-ethoxyphenyl)amino)methylene)malonate (**2**).

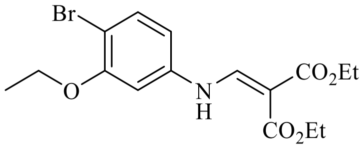

To a solution mixture of 4-bromo-3-ethoxyaniline hydrochloride (**1**) (0.66 g, 3 mmol) and K_2CO_3 (1.68 g, 12.2 mmol) in MeCN (30 mL) was added diethyl-ethoxymethylene malonate (620 µL, 3 mmol). The reaction was heated to reflux and allowed to stir for 36 h, at which time it was cooled, and vacuum filtrated through celite to remove potassium carbonate. The filtrate was purified by flash chromatography using a hexane-EtOAc gradient to yield **2** (0.84 g, 71%). ^{1}H-NMR (400 MHz, $CDCl_3$) δ 11.00 (d, J = 13.5 Hz, 1H), 8.45 (d, J = 13.5 Hz, 1H), 7.49 (d, J = 8.5 Hz, 1H), 6.63 (d, J = 8.5 Hz, 1H), 6.59 (d, J = 2.4 Hz, 1H), 4.33–4.22 (m, 4H), 4.09 (q, J = 7.0 Hz, 2H), 1.49 (t, J = 7.0 Hz, 3H), 1.38–1.31 (m, 6H). [M + H]+: Expected 386.0598, Found 386.0604.

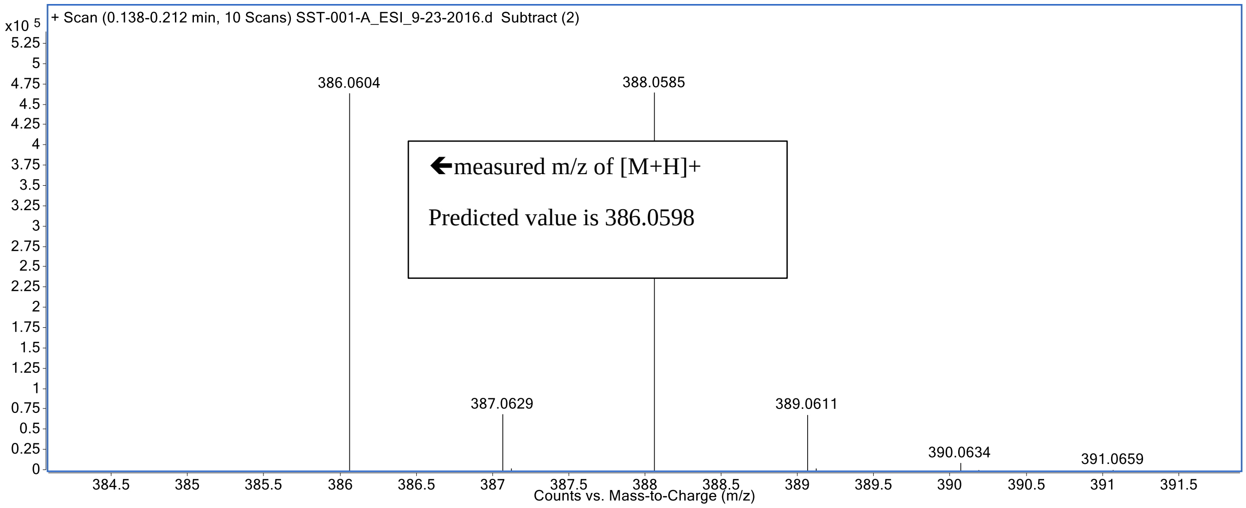

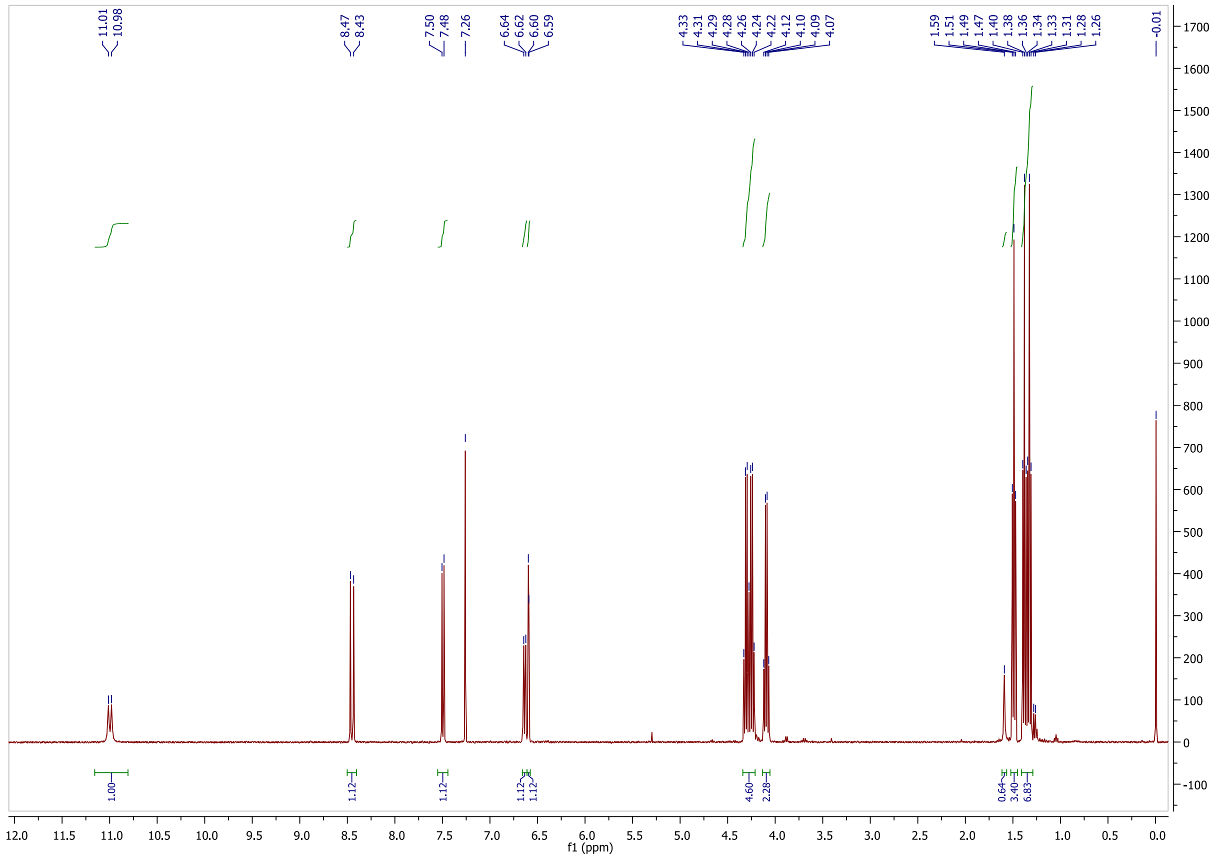

Preparation of Ethyl 6-bromo-4-chloro-7-ethoxyquinoline-3-carboxylate (**3**).

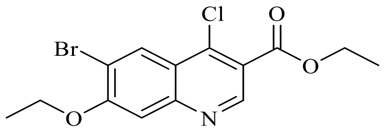

Compound **2** (0.84 g, 2.2 mmol) was dissolved in dry Toluene (2.5 mL). Tert-Butyl ammonium chloride (TBACl: 1.94 g, 7 mmol) was added, followed by $POCl_3$ (2 mL, 22 mmol) while stirring at room temperature for 5 min. The reaction mixture was then heated to reflux and stirred for 68 h. After this time, the reaction was cooled, diluted with DCM (30 mL), and quenched with water (30 mL). The aq. layer was extracted with further DCM (30 mL) and the combined organic fractions were washed with brine (60 mL), dried (Na_2SO_4) and concentrated. The crude material was purified by flash chromatography using a hexane/EtOAc gradient to yield 3 (0.15 g, 17%). ^{1}H-NMR (400 MHz, $CDCl_3$) δ 9.16 (s, 1H), 8.61 (s, 1H), 7.42 (s, 1H), 4.48 (q, J = 7.2 Hz, 2H), 4.28 (dd, J = 14.1, 7.0 Hz, 2H), 1.58 (t, J = 7.0 Hz, 3H), 1.45 (t, J = 7.2 Hz, 3H). [M + H]+: Expected 357.9840, Found 359.9820. Cl-37 accounts for difference in expected value.

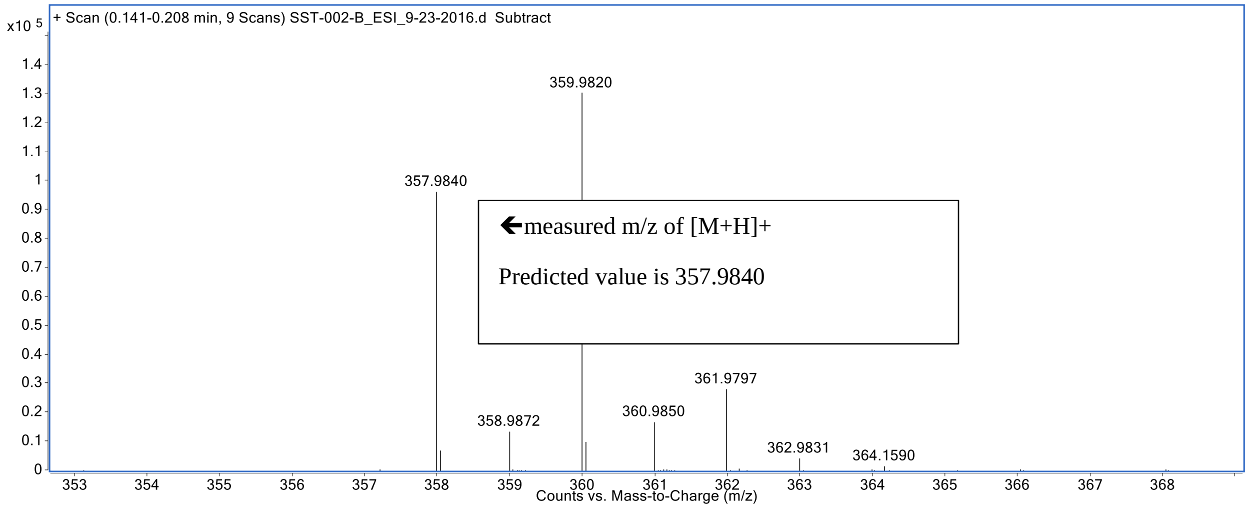

←measured m/z of [M+H]+

Predicted value is 357.9840

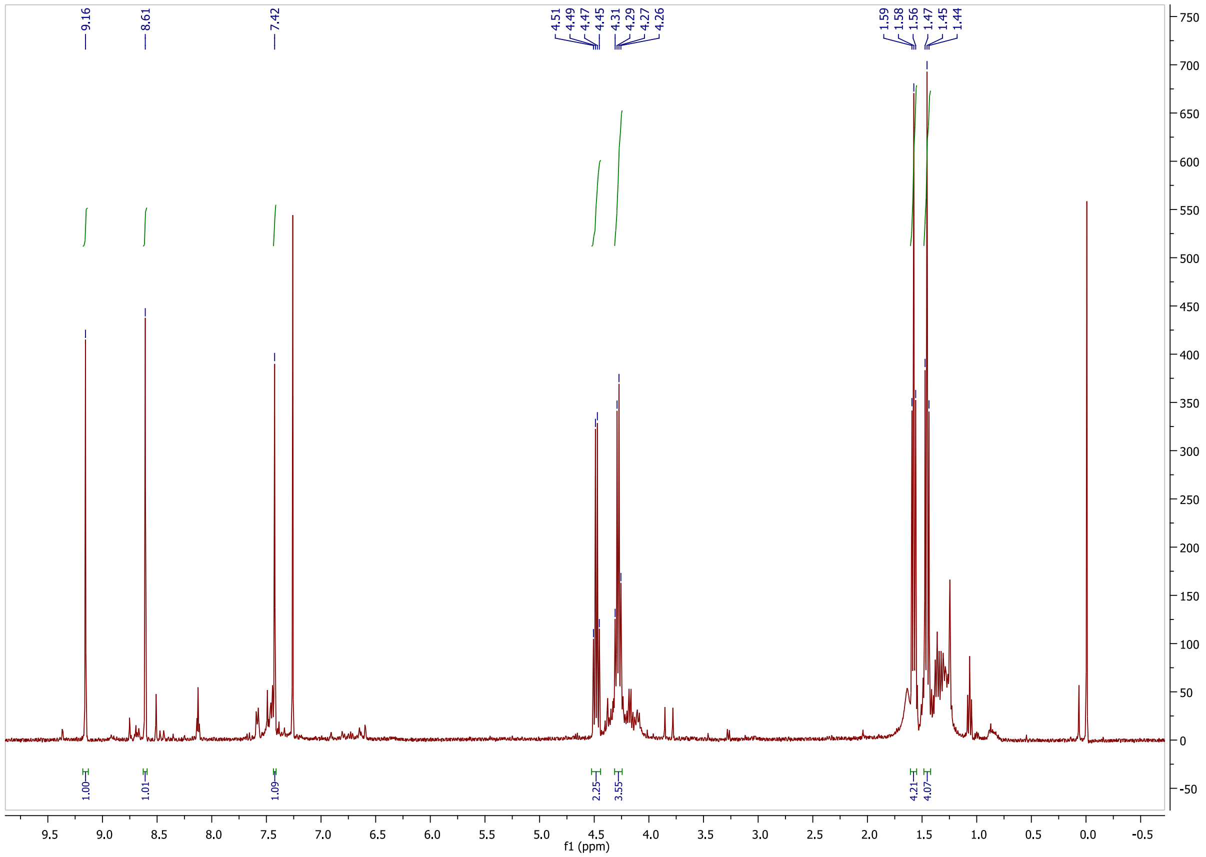

Preparation of Ethyl 6-bromo-4-((2,4-difluorophenyl)amino)-7-ethoxyquinoline-3-carboxylate (**4**).

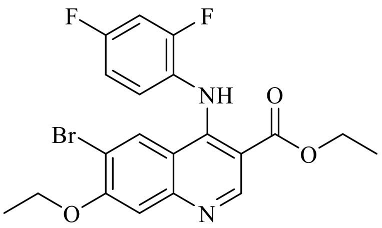

Compound **3** (0.15 g, 0.41 mmol) was dissolved in ethanol (10 mL). 20 mol % acetic acid (4.7 µL, 0.082 mmol) was added followed by 2,4-difluoroaniline (46 µL, 0.45 mmol, 1.1 eq.). The reaction was heated to reflux and stirred for 24 h. After this time, the reaction was cooled and Et_3N (100 µL) was added to neutralize acetic acid. The crude reaction mixture was purified by flash chromatography to yield title compound **4** (0.11 g, 66%). ^{1}H-NMR (400 MHz, $CDCl_3$) δ 10.30 (s, 1H), 9.19 (s, 1H), 7.73 (s, 1H), 7.03 (s, 1H), 6.97–6.94 (m, 1H), 6.94–6.92 (m, 1H), 6.84 (t, J = 8.3 Hz, 1H), 4.43 (q, J = 7.1 Hz, 2H), 4.23 (q, J = 7.0 Hz, 2H), 1.53 (t, J = 7.0 Hz, 3H), 1.45 (t, J = 7.1 Hz, 3H). [M + H]+: Expected 451.0463, Found 451.0463.

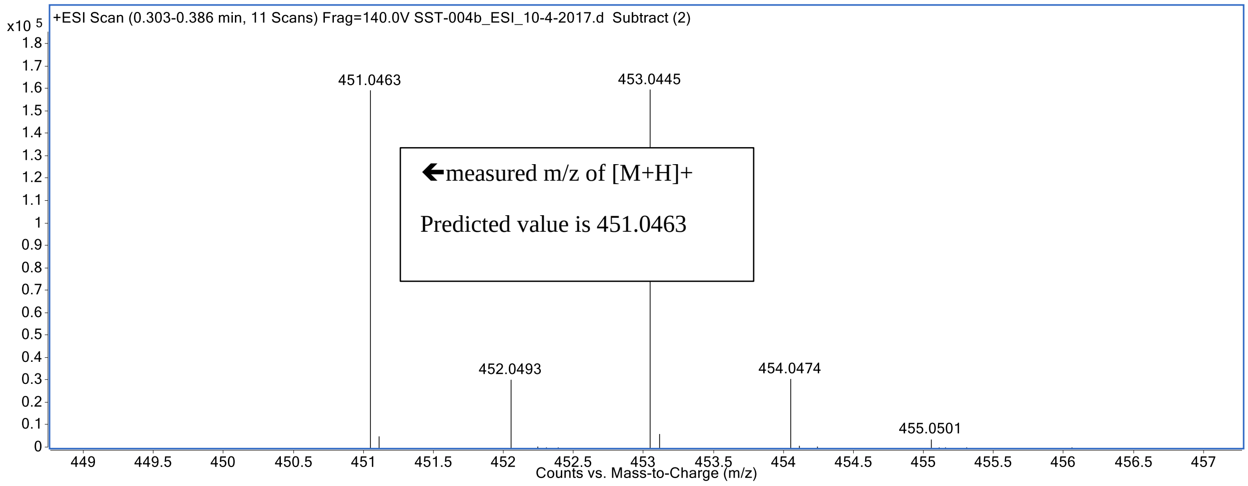

🡐measured m/z of [M+H]+

Predicted value is 451.0463

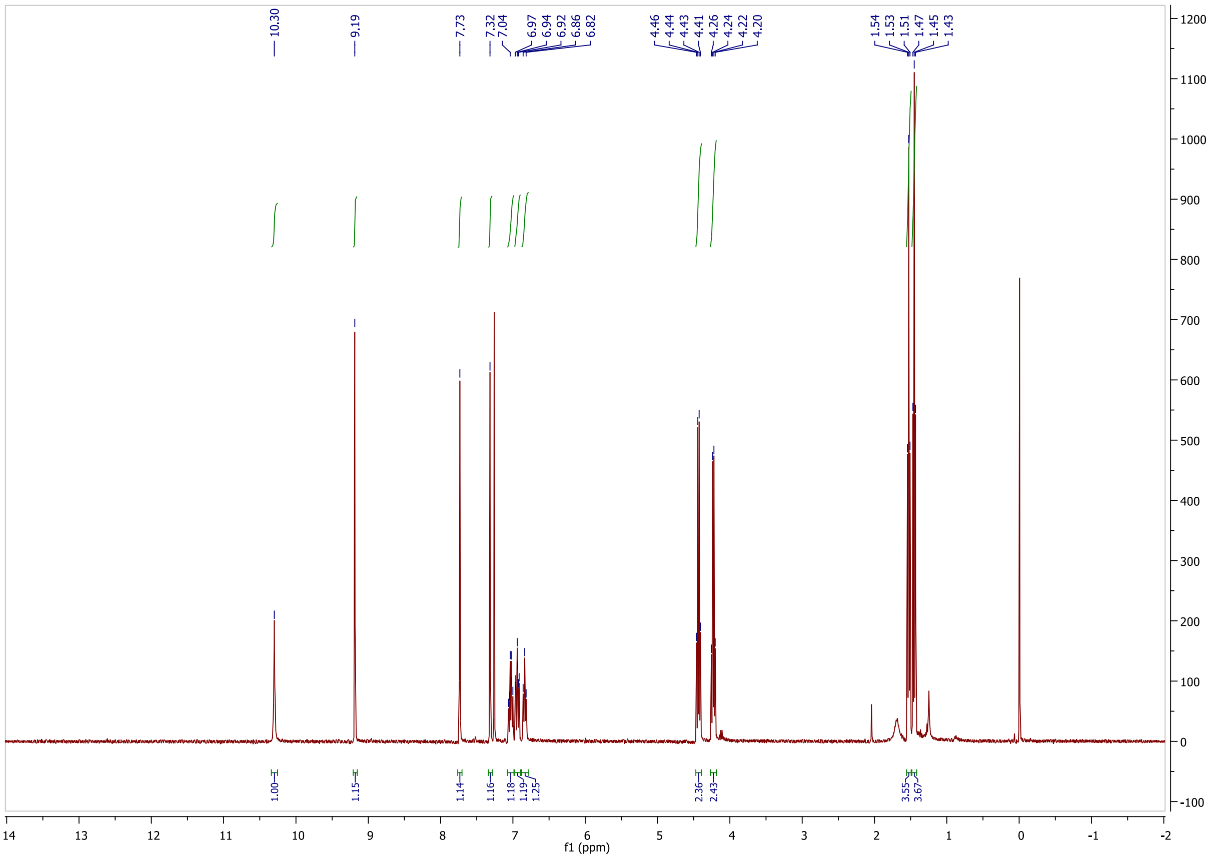

Preparation of Ethyl 4-((2,4-difluorophenyl)amino)-7-ethoxy-6-(4-methylpiperazin-1-yl)quinoline-3-carboxylate (**5a**).

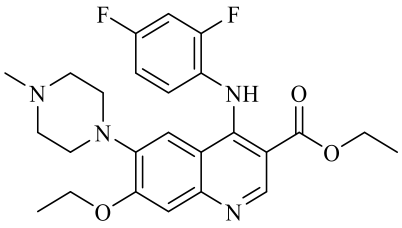

Compound **4** (113 mg, 0.251 mmol) was dissolved in dry toluene (10 mL). To this solution, 1-methylpiperizine (33.4 µL, 0.301 mmol, 1.2 eq.) was added. This solution was aspirated with a syringe and added to a mixture of 2.5 mol % $Pd_2(dba)_3$ (5.75 mg, 0.007 mmol), 2.5 mol % BINAP (3.9 mg, 0.007 mmol) and 1.6 eq. of Cs_2CO_3 (0.13 g, 0.402 mmol) under Ar. The reaction was heated to 100°C and stirred for 60 h. After this time, the reaction was cooled and quenched with satd. $KHCO_3$ (20 mL). The organic layer was washed with water (50 mL) and the water was extracted twice with EtOAc. The organic layers were combined, washed with brine (60 mL), concentrated and dried (Na_2SO_4). The residue was purified by flash chromatography using an EtOAc/MeOH gradient to yield compound **5a** (64 mg, 54%). ^{1}H-NMR (400 MHz, $CDCl_3$) δ 10.14 (s, 1H), 9.11 (s, 1H), 7.32 (s, 1H), 7.26 (s, 1H), 7.00–6.90 (m, 1H), 6.89 (s, 1H), 6.75 (t, J = 8.4 Hz, 1H), 4.42 (q, J = 7.1 Hz, 2H), 4.21 (q, J = 6.9 Hz, 2H), 2.83 (m, 4H), 2.55 (m, 4H), 2.30 (s, 3H), 1.51 (t, J = 6.9 Hz, 3H), 1.48–1.44 (m, 3H). [M + H]+: Expected 471.2202, Found 471.2202.

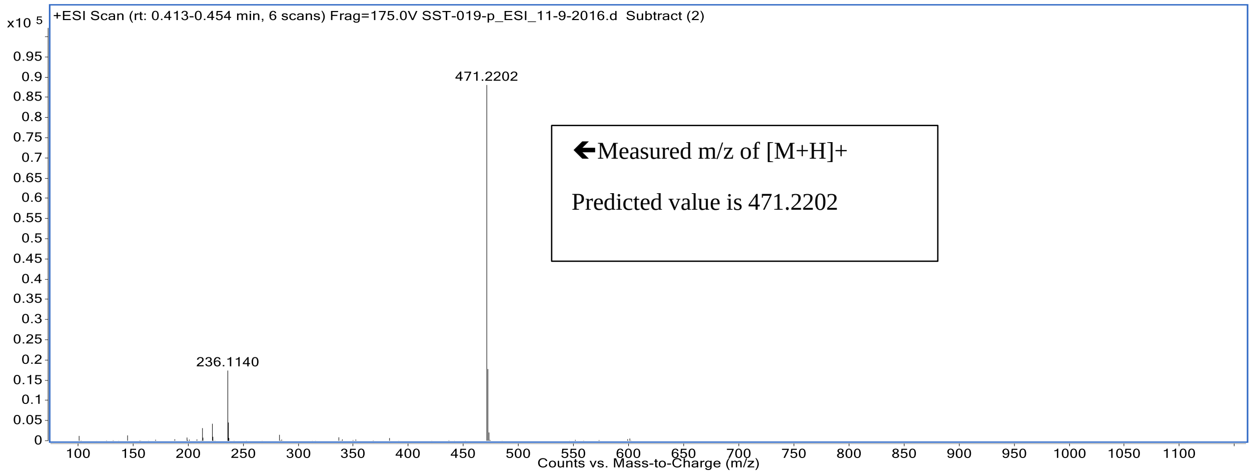
+ESI Scan (rt: 0.413-0.454 min, 6 scans) Frag=175.0V SST-019-p_ESI_11-9-2016.d Subtract (2)

🡐Measured m/z of [M+H]+

Predicted value is 471.2202

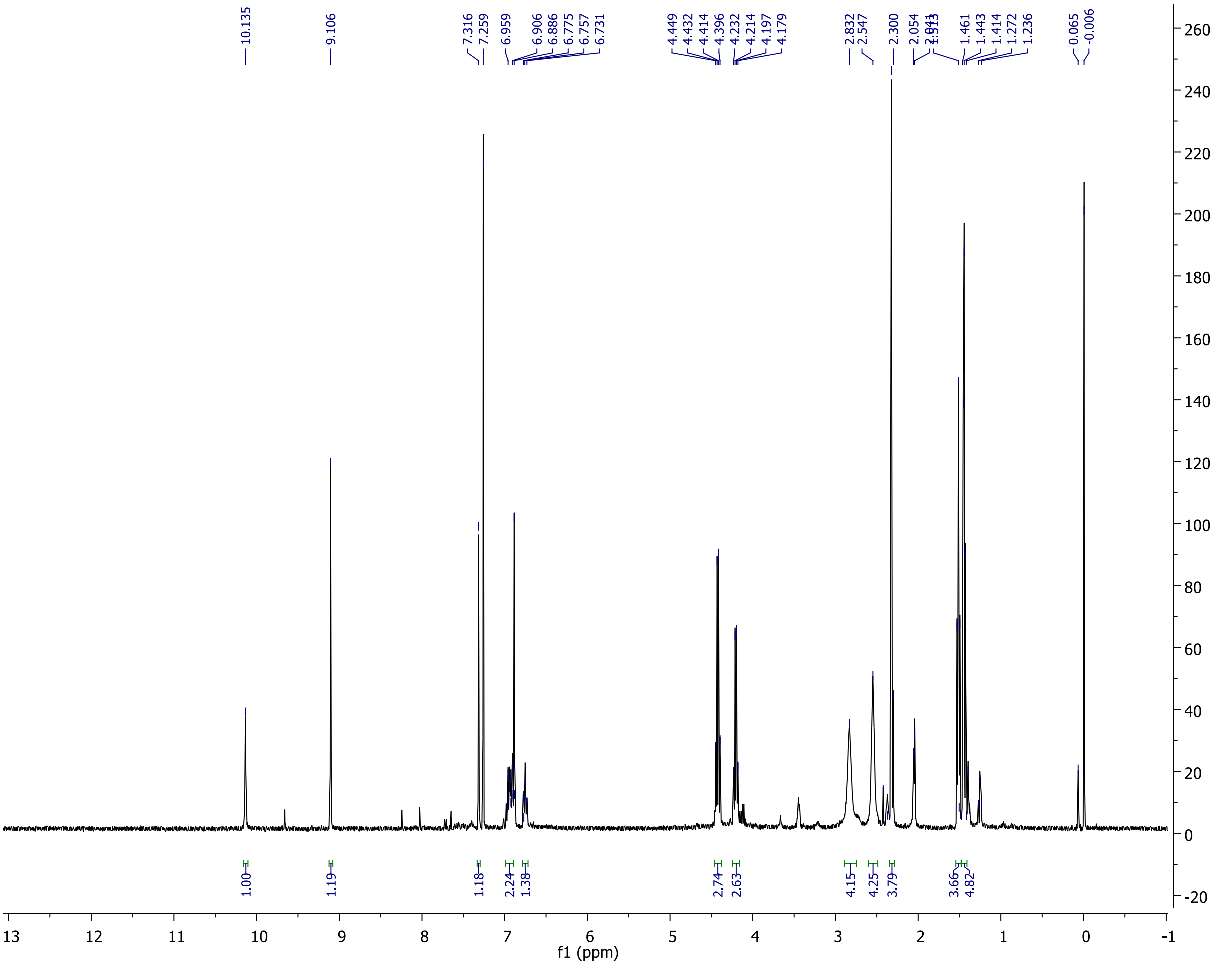

Preparation of Ethyl 6-(4-(tert-butoxycarbonyl)piperazin-1-yl)-4-((2,4-difluorophenyl)amino)-7-ethoxyquinoline -3-carboxylate (**5b**).

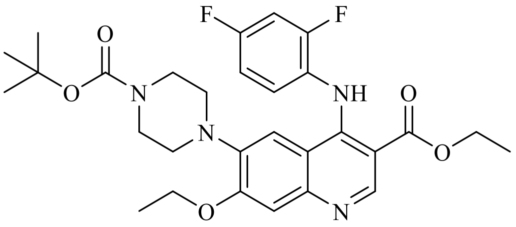

The same procedure described for the synthesis of **5a** was also used to prepare **5b** (61 mg, 44.5%). ^{1}H-NMR (400 MHz, CDCl$_3$) δ 10.08 (s, 1H), 9.12 (s, 1H), 7.30 (s, 1H), 6.96–6.88 (m, 2H), 6.86 (s, 1H), 6.75 (t, J = 8.2 Hz, 1H), 4.43 (q, J = 7.1 Hz, 3H), 4.21 (q, J = 7.0 Hz, 2H), 3.53–

3.45 (m, 4H), 2.75–2.67 (m, 4H), 1.52 (t, J = 7.0 Hz, 3H), 1.47 (s, 9H), 1.44 (d, J = 7.1 Hz, 3H). [M + H]+: Expected 557.2571, Found 557.2571.

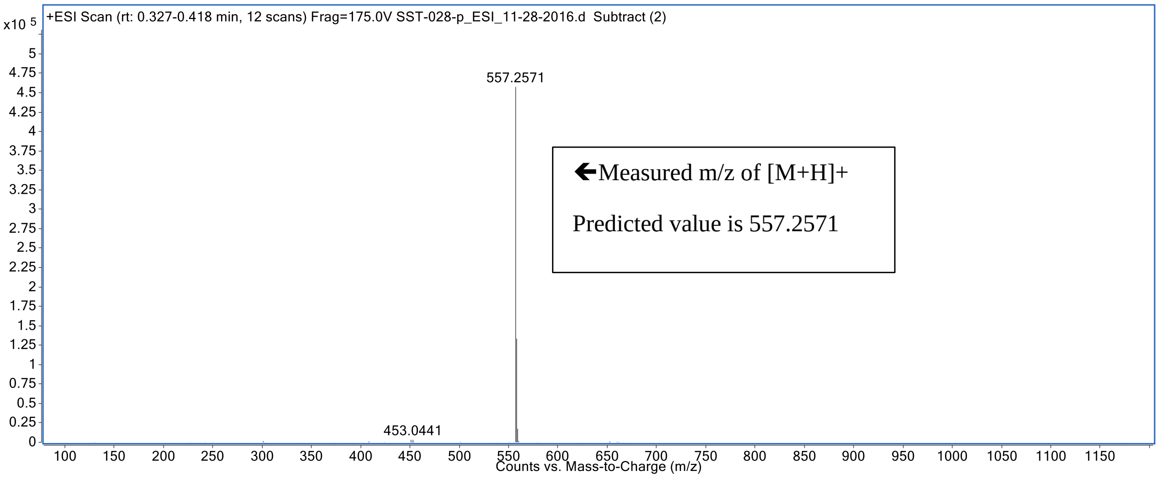

←Measured m/z of [M+H]+

Predicted value is 557.2571

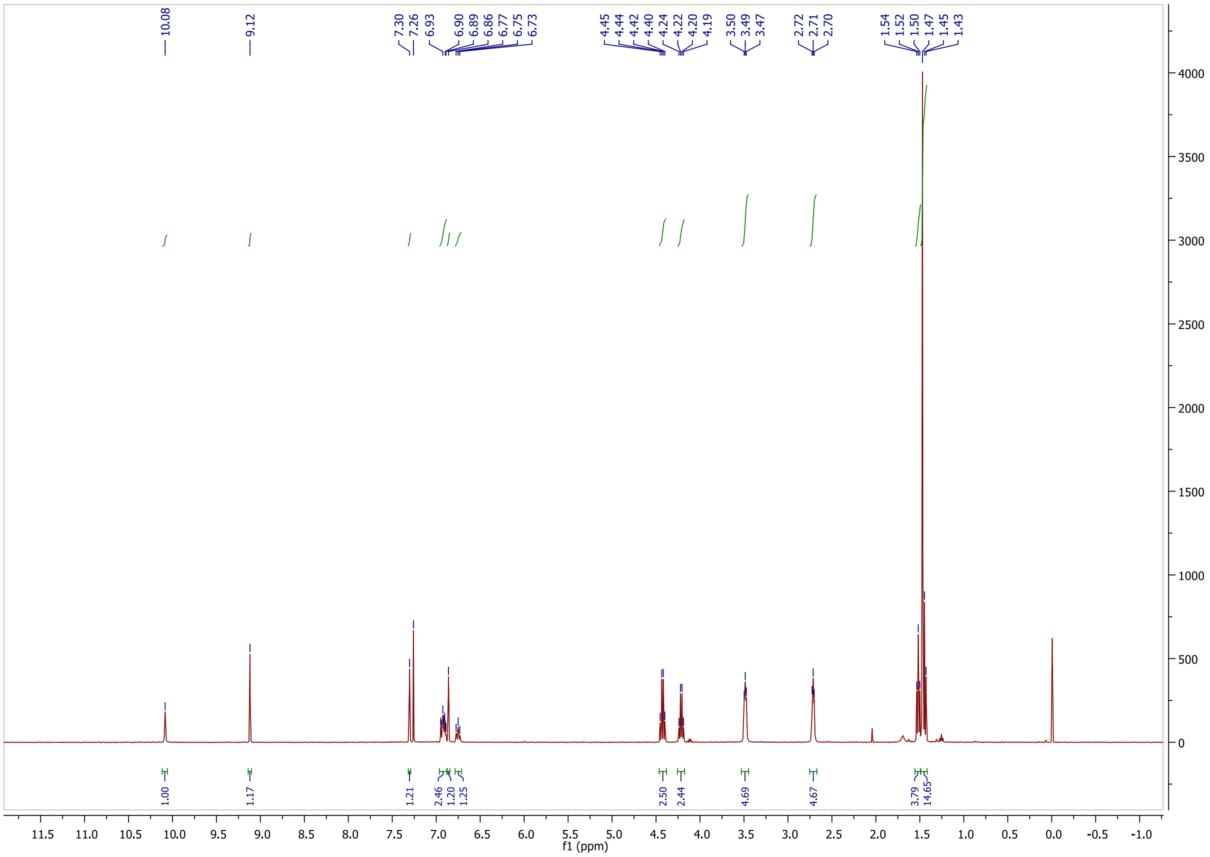

Preparation of 4-((2.,4-Difluorophenyl)amino)-7-ethoxy-6-(4-methylpiperazin-1-yl)quinoline-3-carboxamide (AZ683 Reference Standard **6a**).

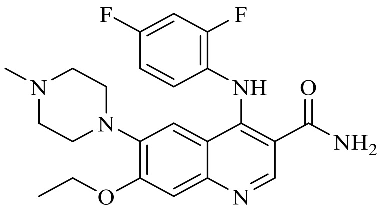

Compound **5a** (53 mg, 0.113 mmol) was dissolved in THF (0.1 mL) and formamide (22.4 µL, 0.563 mmol, 5 eq.) was added. To this solution, a 21% wt solution of NaOEt in EtOH (231 µL, 0.563 mmol, 5 eq.) was added. The reaction was heated to reflux and stirred for 16 h, after which time it was cooled and quenched with NH_4Cl (53 mg, 1 mmol). The reaction mixture was concentrated onto silica and purified by flash chromatography using an EtOAc/MeOH gradient to yield compound **6a** (16 mg, 32%). ^{1}H-NMR (400 MHz, CD_3OD) δ 8.78 (s, 1H), 7.27 (s, 1H), 7.16–7.06 (m, 3H), 6.95 (t, J = 8.6 Hz, 1H), 4.25 (q, J = 6.9 Hz, 3H), 3.10 (m, 4H), 2.73 (m, 4H), 1.96 (s, 3H), 1.51 (t, J = 6.9 Hz, 3H). [M + H]+: Expected 442.2049, Found 442.2048.

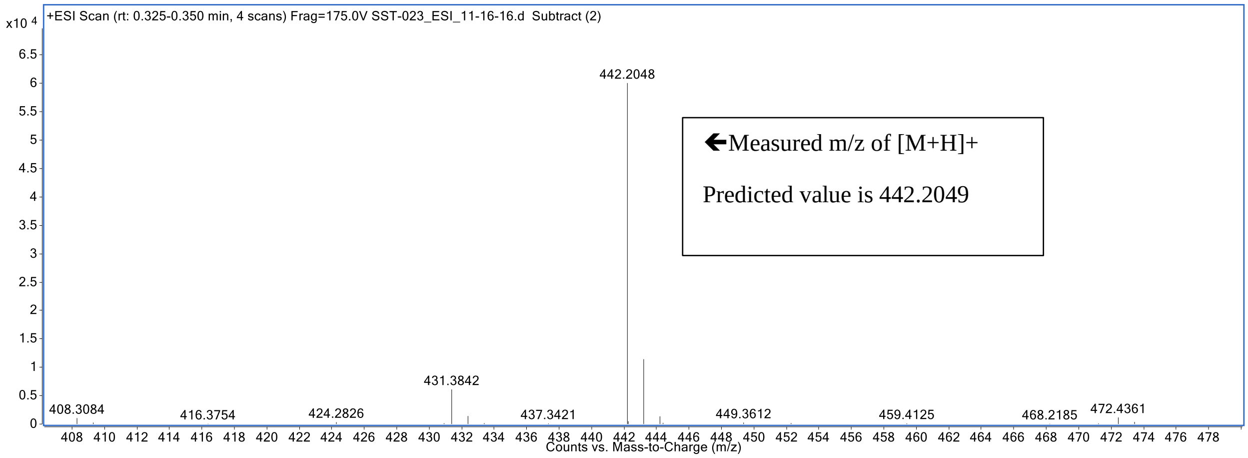

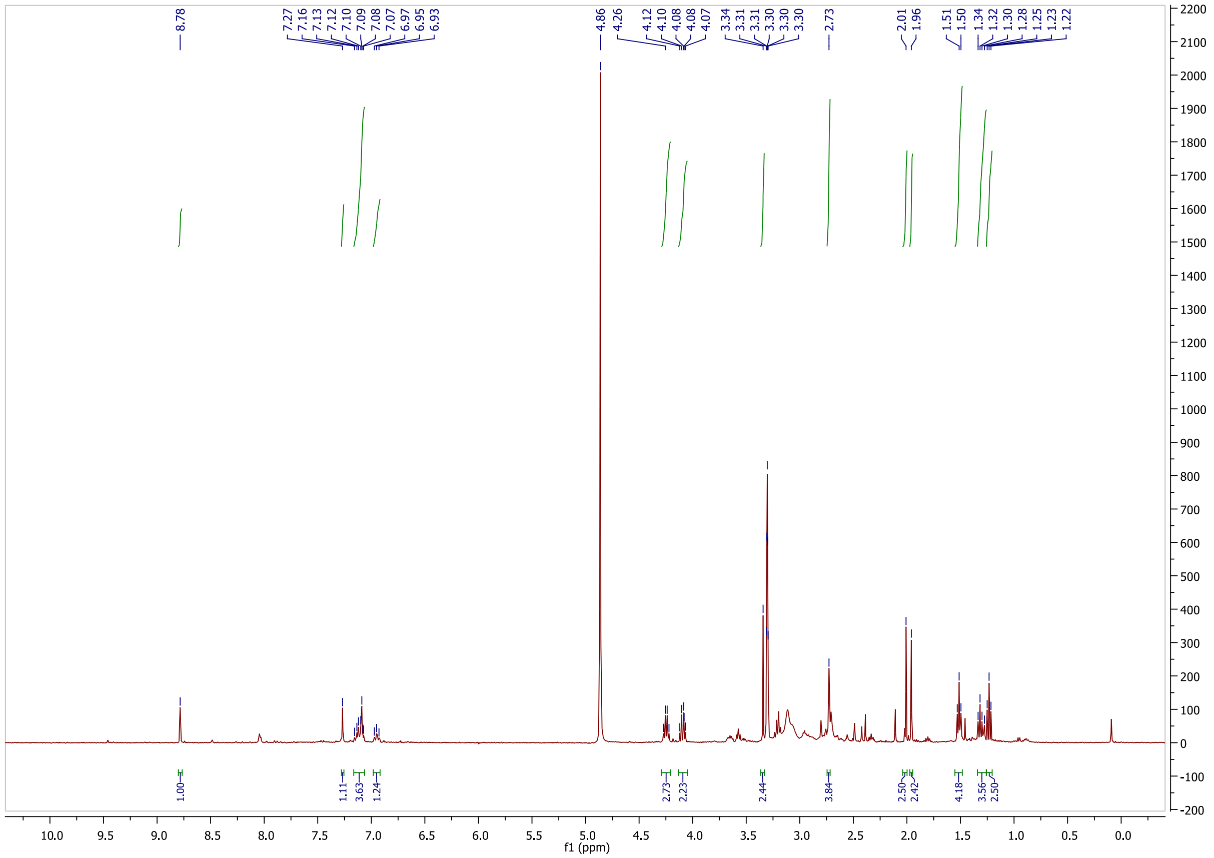

Preparation of tert-Butyl 4-(3-carbamoyl-4-((2,4-difluorophenyl)amino)-7-ethoxyquinolin-6-yl) piperazine-1-carboxylate (**6b**).

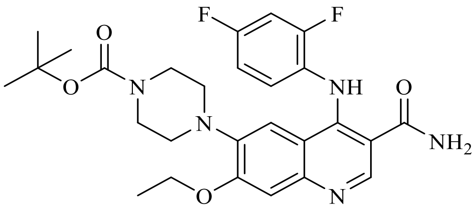

The same procedure described for the synthesis of **6a** was used to prepare **6b** (18 mg, 30%). ^{1}H-NMR (400 MHz, $CDCl_3$) δ 10.44 (s, 1H), 8.76 (s, 1H), 7.27 (s, 1H), 6.94–6.88 (m, 2H), 6.87 (s, 1H), 6.74 (t, J = 8.3 Hz, 1H), 6.21 (br. s, 1H), 4.20 (q, J = 6.9 Hz, 2H), 3.48–3.47 (m, 4H), 2.73–2.71 (m, 4H), 1.51 (t, J = 6.9 Hz, 3H), 1.47 (s, 9H). [M + H]+: Expected 528.2417, Found 528.2419.

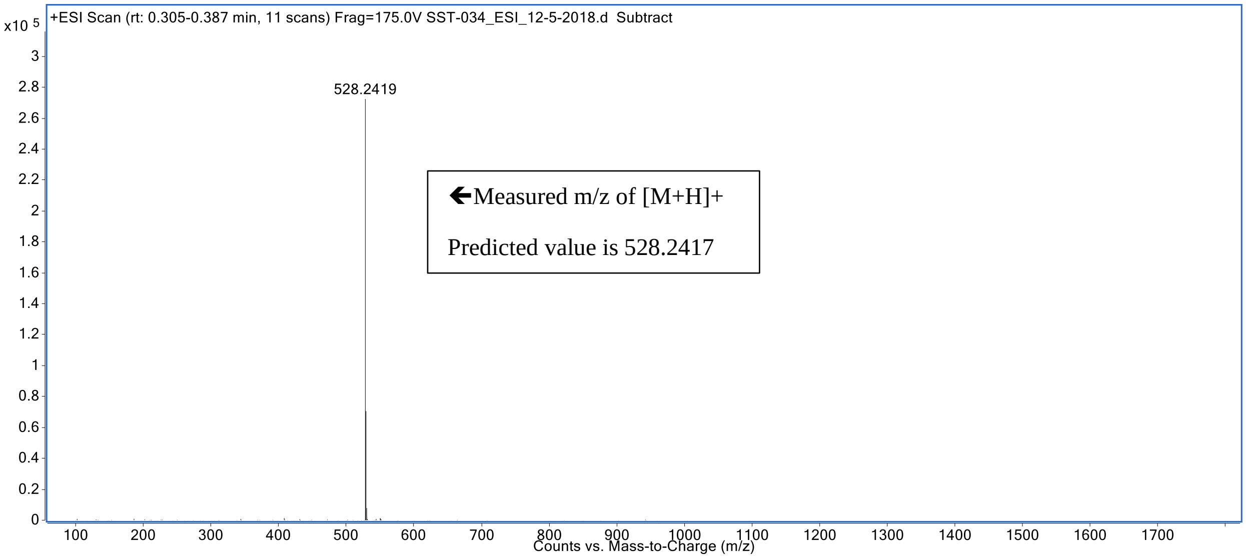

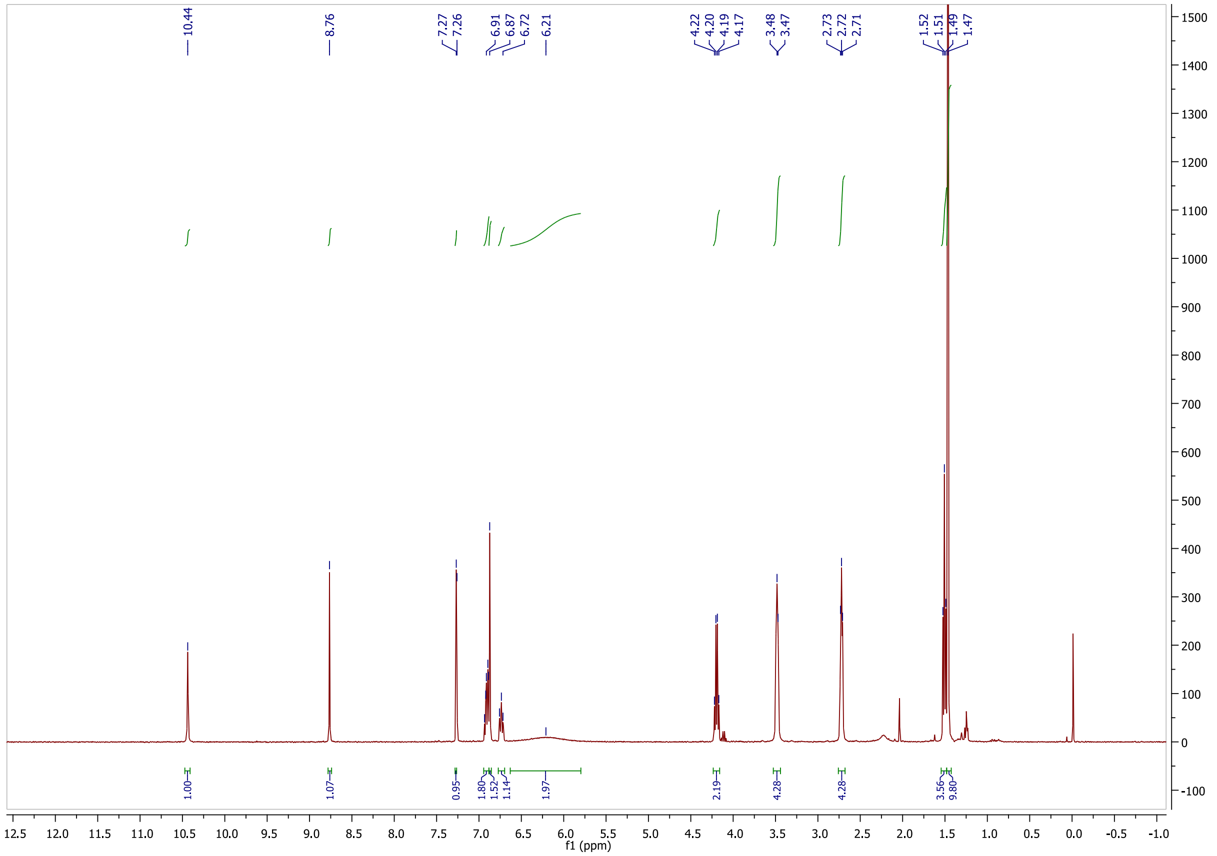

Preparation of 4-((2,4-Difluorophenyl)amino)-7-ethoxy-6-(piperazin-1-yl)quinoline-3-carboxamide (**7**).

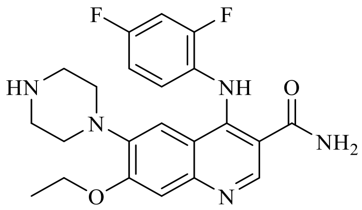

Compound **6b** (18 mg, 0.034 mmol) was dissolved in dry MeOH (5 mL) and cooled to 78°C for 5 min. Trimethylsilyl chloride (TMS-Cl, 43.3 µL, 0.341 mmol, 10 eq.) was added and the reaction was allowed to warm up to room temperature and was stirred until deprotection was complete as determined by TLC (~25 h). The reaction was quenched with water and concentrated to remove solvent and excess TMS-Cl. The concentrate was re-dissolved in MeOH and re-concentrated two more times to ensure complete removal of TMS-Cl. The product was further dried in a vacuum desiccator to yield compound **7** (15 mg, 100%). **1**H-NMR (400 MHz, CD_3OD) δ 8.80 (s, 1H), 7.56–7.50 (m, 1H), 7.38 (s, 1H), 7.34 (s, 1H), 7.26–7.18 (m, 1H), 7.14 (t, J = 8.4 Hz, 1H), 4.33 (q, J = 7.0 Hz, 2H), 3.39–3.33 (m, 4H). 3.22–3.20 (m, 4H), 1.55 (t, J = 7.0 Hz, 3H). [M + H]+: Expected 428.1893, Found 428.1892.

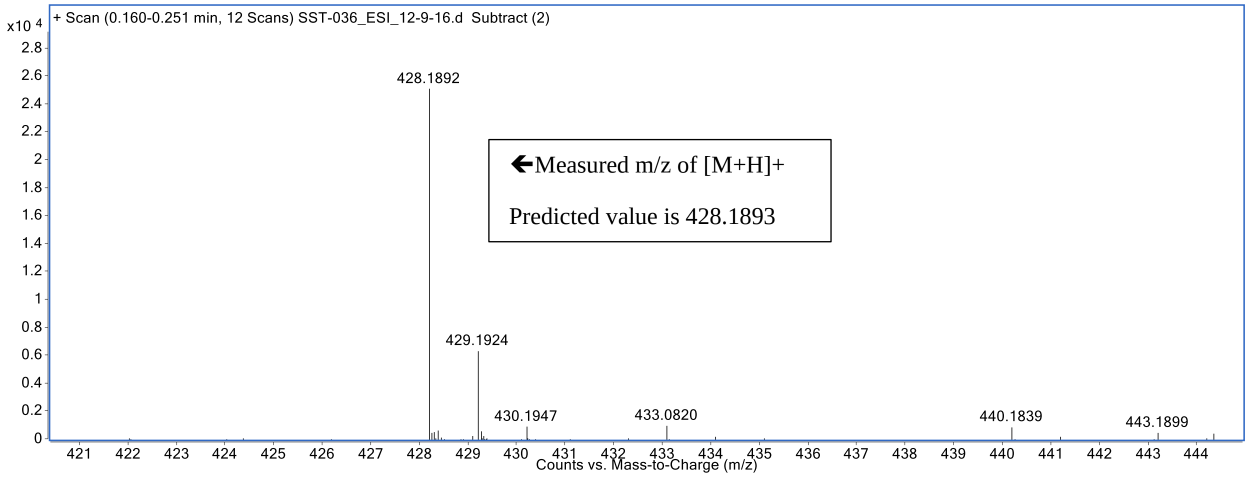

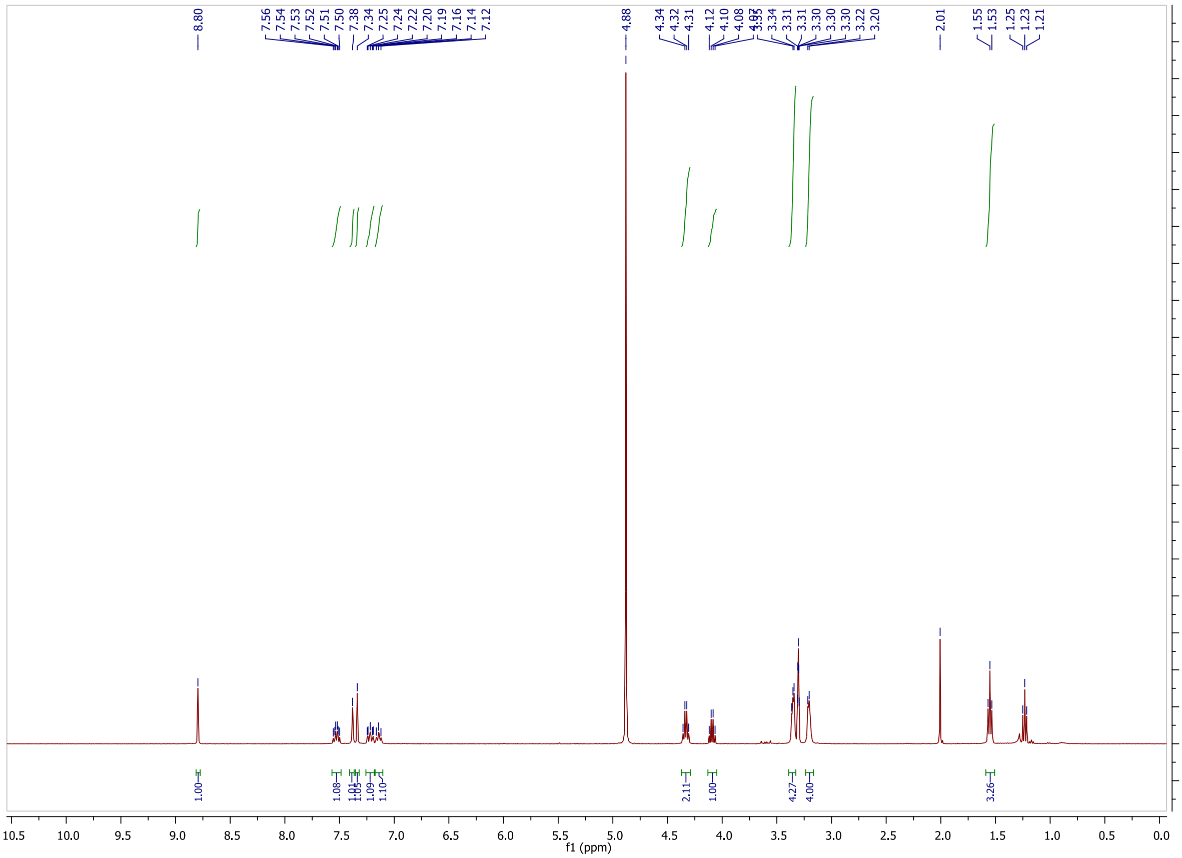

Preparation of Ethyl 6-bromo-7-ethoxy-4-((2-fluoro-4-(4,4,5,5-tetramethyl-1,3,2-dioxaborolan-2-yl)phenyl)amino)quinoline-3-carboxylate (**9**)

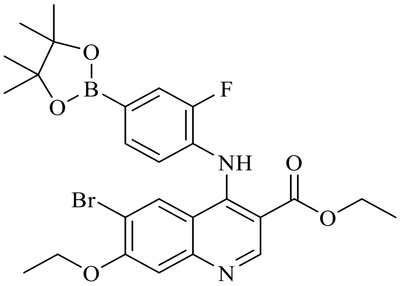

Compound **9** was prepared exactly as compound **3** was prepared, with the exception of using 4-amino-3fluorobenzenboronic acid pinacol ester in place of 2,4,-difluoroaniline. Compound **2** (0.122g, 0.342mmol) was dissolved in a scintillation vial with ethanol (3 mL) and transferred to 100 mL round bottom flask. The vial was rinsed with ethanol and added to flask for a total volume of 10 mL. 20 mol-% acetic acid (3.9 μL, 0.068 mmol) was added to flask via pipette. Finally, 4-amino-3fluorobenzenboronic acid pinacol ester (89mg, 0.375mmol) was added to the solution and immediately placed in oil bath at 80°C to be stirred while under reflux and argon flow. The reaction was stirred for twenty-four hours until stopped and cooled. Tetraethylammonium (TEA: 100 μL) was added to neutralize acetic acid. The reaction mixture was put directly onto silica and purified with flash chromatography to yield (0.101 g, 53%) compound **9.** ^{1}H NMR (400 MHz, $CDCl_3$) δ 10.18 (s, 1H), 9.22 (s, 1H), 7.91 (s, 1H), 7.57 (d, *J* = 10.8 Hz, 1H), 7.40 (d, *J* = 8.0 Hz, 1H), 7.35 (s, 1H), 6.85 (t, *J* = 7.9 Hz, 1H), 4.43 (q, *J* = 7.1 Hz, 2H), 4.25 (q, *J* = 7.0 Hz, 2H), 1.54 (t, *J* = 7.0 Hz, 3H), 1.44 (t, *J* = 7.1 Hz, 3H), 1.34 (s, 17H). [M + H], Expected 559.141, Found 559.1412

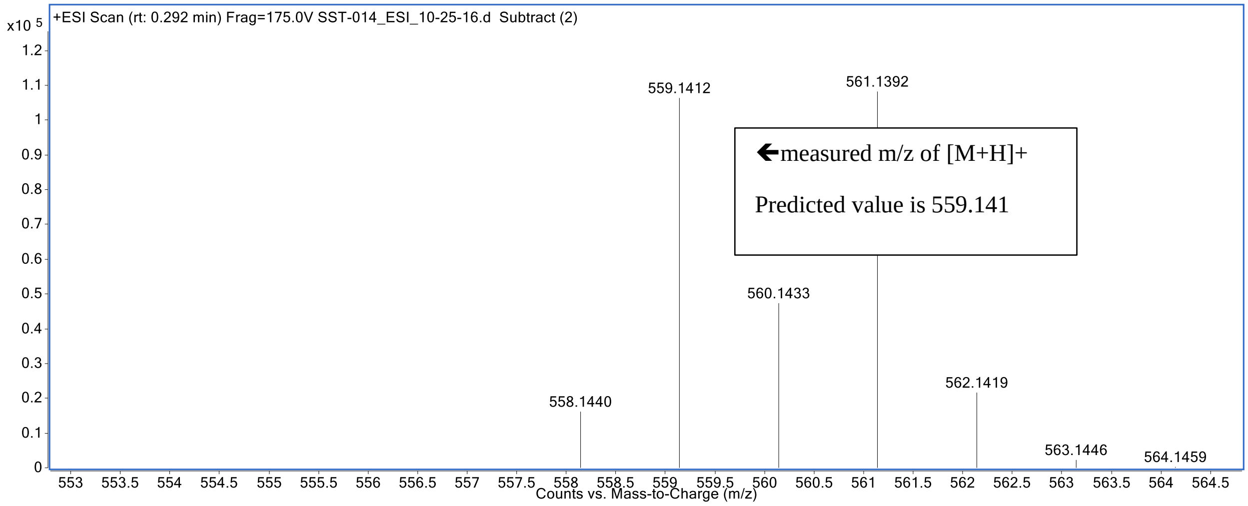

🡐measured m/z of [M+H]+

Predicted value is 559.141

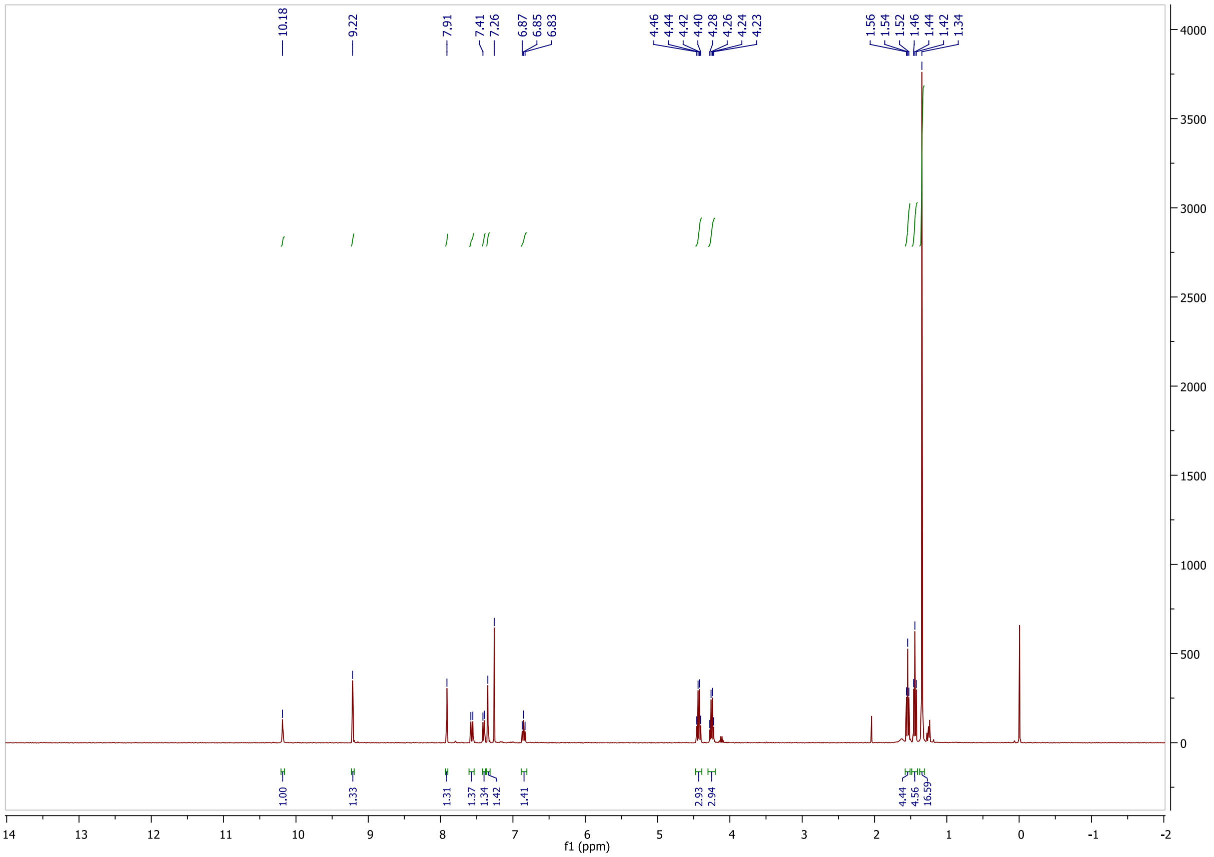

4.5.2. *Radiochemistry*

General Considerations

All the chemicals (except for reference standard **6a** and precursor **7** noted above) were purchased from commercially available suppliers and used without purification: sodium chloride, 0.9% USP and Sterile Water for Injection, USP were purchased from Hospira; Dehydrated Alcohol for Injection, USP was obtained from Akorn Inc. (Lake Forest IL, USA) HPLC was performed using a Shimadzu (Kyoto, Japan) LC-2010A HT system equipped with a Bioscan B-FC-1000 radiation detector, and HPLC columns were acquired from Phenomenex (Torrance CA, USA). Other synthesis components were obtained as follows: sterile filters were acquired from MilliporeSigma (Burlington MA, USA); C18 Vac 1cc Sep-Paks were purchased from Waters

Corporation (Milford MA, USA); Sep-Paks were flushed with 5 mL of ethanol followed by 10 mL of sterile water prior to use.

Radiosynthesis of [^{11}C]AZ683

[^{11}C]CO_2 was produced with a General Electric Healthcare (GE, Uppsala, Sweden) PETTrace cyclotron via the ^{14}N(p,α)^{11}C reaction. High purity N_2 (g) containing 0.5% O_2 was irradiated at 40 µA for 30 min to generate [^{11}C]CO_2 (~111 GBq), which was delivered to a GE TRACERLab FXC-Pro synthesis module and converted to [^{11}C]MeOTf (~37 GBq) as previously described.[26] [^{11}C]MeOTf was bubbled at 15 mL/min through a solution of precursor **7** (1 mg) in DMF (100 µL) at room temperature for 3 min. Following radiolabeling, the reaction mixture was diluted with HPLC mobile phase and purified by semipreparative HPLC (column: Phenomenex Luna C18, 10µ, 10 × 250 mm; mobile phase: 27% ethanol, 10 mM Na_2HPO_4, pH = 5.75; flow rate: 5 mL/min; see **Figure 4.5** for a representative semipreparative HPLC trace). The peak corresponding to [^{11}C]AZ683 (t_R ~12–14 min) was collected, diluted in water (50 mL), and the resulting solution was passed through a Waters C18 1cc vac cartridge to trap the product. [^{11}C]AZ683 was eluted from the cartridge with ethanol (1 mL) and diluted with 0.9% saline solution (9 mL) to provide the formulated product in 10% EtOH. The dose was passed through a 0.22 µm sterile filter into a sterile dose vial. The overall non-decay corrected activity yield of [^{11}C]AZ683 was 1125 ± 229 MBq (3.0% based upon 37 GBq of [^{11}C]MeOTf) and quality control testing (see below) confirmed radiochemical purity >99%, and molar activity of 153 ± 38 GBq/µmol (n = 4), confirming doses were suitable for preclinical evaluation.

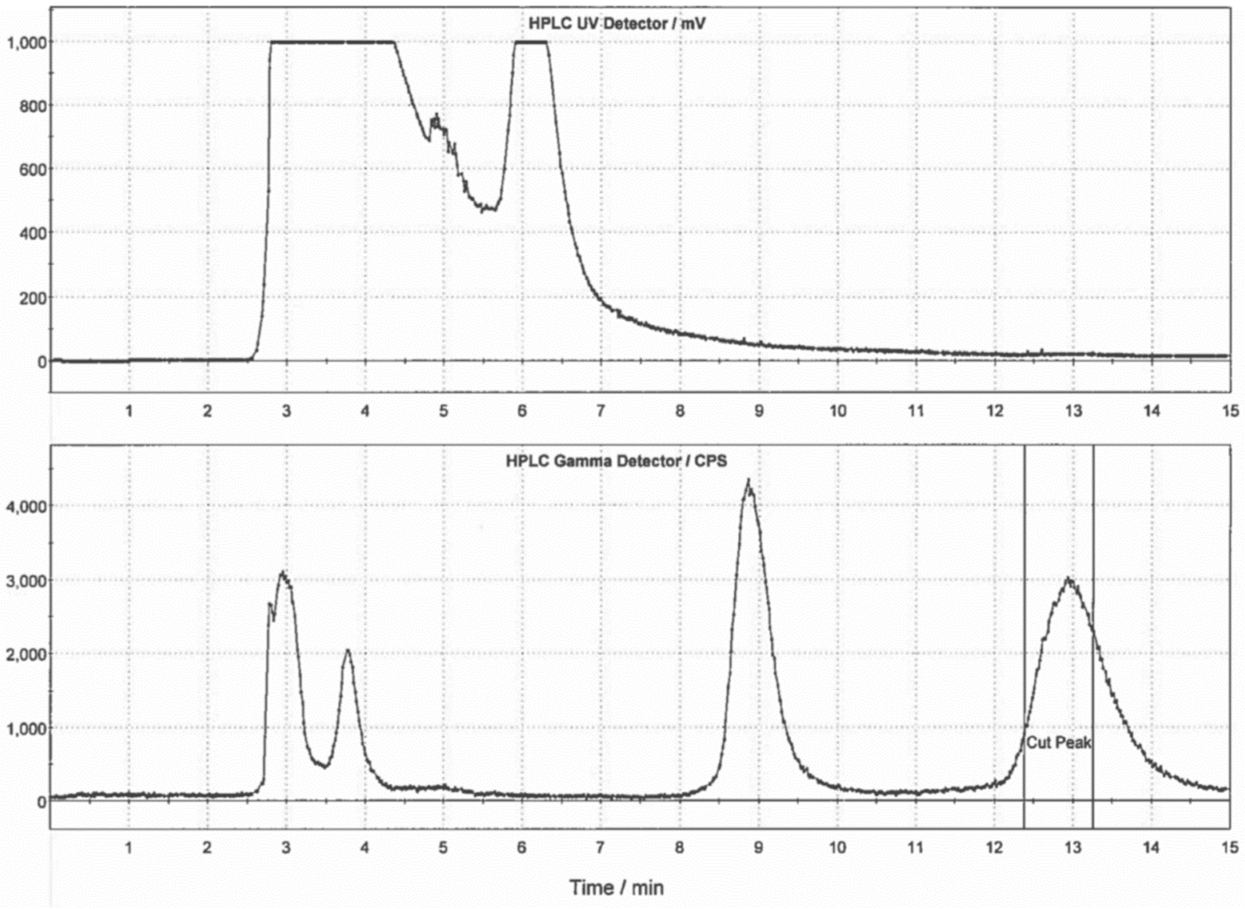

Fig. 4. 5: Typical semi-preparative HPLC trace for [^{11}C]AZ683. Adapted from ref. 2 with permission from MDPI.

Quality Control Testing of [^{11}C]AZ683

Visual inspection Doses were visually examined and required to be clear, colorless, and free of particulate matter. The pH of the doses was determined by applying a small amount of the dose to pH-indicator strips and determined by visual comparison to the scale provided. pH needs to be between 4.5 and 7.5, and the pH of each [^{11}C]AZ683 dose synthesized in this study was 5.0.

Analytical HPLC Analytical HPLC was performed using a Shimadzu LC-2010A HT system equipped with a Bioscan B-FC-1000 radiation detector (column: Phenomenex Luna C18, 5µ, 4.6 × 150 mm; mobile phase: 27% ethanol, 10 mM Na_2HPO_4, pH: 5.75; flow rate: 0.75 mL/min). Analysis confirmed radiochemical purity >99% (t_R of [^{11}C]AZ683 ~6 min; see **Figure**

4.5 for a typical analytical HPLC trace) and coinjection with unlabeled reference standard **6a** confirmed radiochemical identity (see **Figure 4.6** for a coinjection HPLC trace).

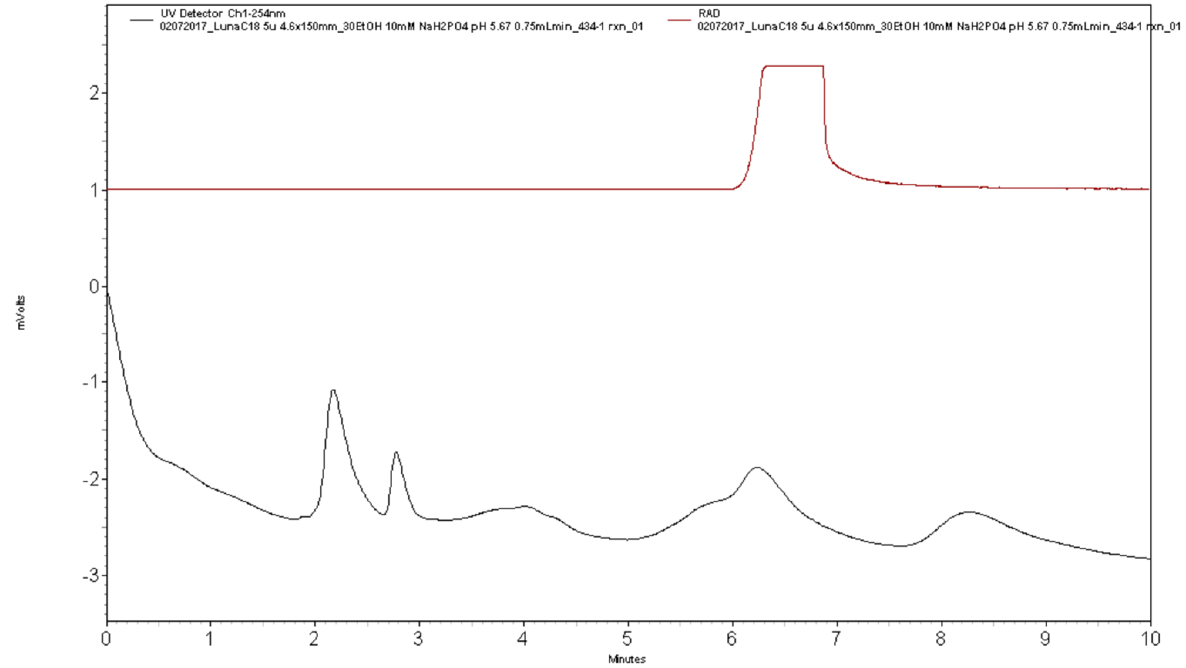

Fig. 4. 6:Analytical HPLC trace for formulated [^{11}C]AZ683 dose. Adapted from ref. 2 with permission from MDPI

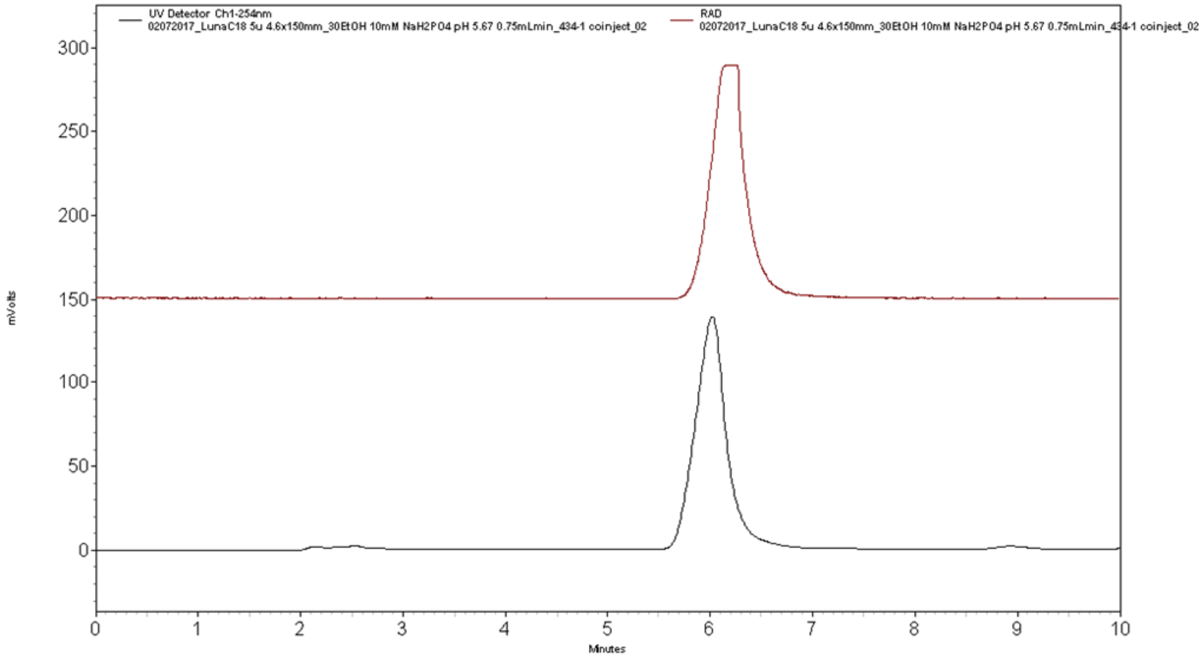

Fig. 4. 7: Analytical HPLC trace for formulated [^{11}C]AZ683 dose co-injected with AZ683 reference standard **6a**. Adapted from ref. 2 with permission from MDPI

4.5.3. *Preclinical PET Imaging*

General Considerations

Rodent and primate imaging studies were performed at the University of Michigan (UM) using a Concorde (CTI-Concorde, Knoxville TN, USA) MicroPET P4 scanner. The University of Michigan is accredited by the Council on Accreditation of the Association for Assessment and Accreditation of Laboratory Animal Care (AAALAC International, Frederick MD, USA) and imaging studies were conducted in accordance with the standards set by the Institutional Animal Care and Use Committee (IACUC) at the University of Michigan (PRO00008103: Biodistribution and Pharmacokinetics of Radiolabeled Compounds; Approval date: 1/16/2018).

Animal Husbandry and Housing

Husbandry and housing for rodents and primates is provided by the University Laboratory for Animal Medicine (ULAM) at UM, and animal facilities are in compliance with the regulations defined by the US Department of Agriculture (USDA).

Monkeys: The University of Michigan PET Center has maintained 2 rhesus macaques for ~15 years and the monkeys are individually housed in adjacent steel cages (83.3 cm high × 152.4 cm wide × 78.8 cm deep) equipped with foraging boxes. They are currently housed in adjacent cages as repeated attempts to socially house them in the same cage have been unsuccessful due to aggressive incompatibility. Cages are metal and do contain gridded floors for radiation safety reasons (radioactive waste is contained to the gridded floor and is easier to clean). Temperature and humidity are carefully controlled, and the monkeys are kept on a 12 h light/12 h dark schedule. Monkeys are fed Lab Fiber Plus Monkey Diet (PMI Nutrition Intl. LLC, Shoreview MN, USA) that is supplemented with fresh fruit and vegetables daily. Water and enrichment toys (manipulanda and food-based treats) are available continuously in the home cage.

Rodents: Rats are housed in Allentown #3 micro ventilated cages (27 cm wide × 49 cm deep × 27 cm high, floor area 923 Sq cm) with animal housing densities set by ULAM and the Guide for the Care and Use of Laboratory Animals. Housing is located on ventilated racks with continuous water and air supply exchange. All animals are provided with LabDiet 5LOD as well as enrichment materials and are on a light schedule of 12 h light/12 h dark.

Rodent Imaging Protocol

Rodent imaging studies were done using a female Sprague–Dawley rat (weight = 237 g, n = 1). The rat was anesthetized (isoflurane), intubated, and positioned in the PET scanner. Following a transmission scan, the animal was injected (via intravenous (i.v.) tail vein injection) with [^{11}C]AZ683 (14.8 MBq) as a bolus over 1 min, and the brain imaged for 60 min (5 × 1 min frames-2 × 2.5 min frames-2 × 5 min frames-4 × 10 min frames).

Primate Imaging Protocol

Primate imaging studies were done using a mature female rhesus monkey (weight = 9.4 kg, n = 1).The animal was anesthetized in the home cage with ketamine and transported to the PET imaging suite. The monkey was intubated for mechanical ventilation, and anesthesia was continued with isoflurane. Anesthesia was maintained throughout the duration of the PET scan. A venous catheter was inserted into one hind limb and the monkey was placed on the PET gantry with its head secured to prevent motion artifacts. Following a transmission scan, the animal was injected i.v. with [^{11}C]AZ683 (145.0 MBq) as a bolus over 1 min, and the brain imaged for 60 min (5 × 2 min frames-4 × 5 min frames-3 × 10 min frames).

PET Image Analysis

Emission data were corrected for attenuation and scatter, and reconstructed using the 3D maximum a priori (3D MAP) method. By using a summed image, regions of interest (ROI) were drawn on multiple planes, and the volumetric ROIs were then applied to the full dynamic data set to generate time-radioactivity curves.

4.5. References

1 S. Tanzey, X. Shao, J. Stauff, J. Arteaga, P. Sherman, P. Scott and A. Mossine, *Pharmaceuticals*, 2018, **11**, 136.

2 K. Verstraete and S. N. Savvides, *Nat. Rev. Cancer*, 2012, **12**, 753–766.

3 M. A. Michell-Robinson, H. Touil, L. M. Healy, D. R. Owen, B. A. Durafourt, A. Bar-Or, J. P. Antel and C. S. Moore, *Brain*, 2015, **138**, 1138–1159.

4 Y. Nakamichi, N. Udagawa and N. Takahashi, *J. Bone Miner. Metab.*, 2013, **31**, 486–495.

5 M. I. El-Gamal, S. K. Al-Ameen, D. M. Al-Koumi, M. G. Hamad, N. A. Jalal and C. H. Oh, *J. Med. Chem.*, 2018, **61**, 5450–5466.

6 C. J. Burns and A. F. Wilks, *Expert Opin. Ther. Pat.*, 2011, **21**, 147–165.

7 E. E. Spangenberg, R. J. Lee, A. R. Najafi, R. A. Rice, M. R. P. Elmore, M. Blurton-Jones, B. L. West and K. N. Green, *Brain*, 2016, **139**, 1265–1281.

8 A. Olmos-Alonso, S. T. T. Schetters, S. Sri, K. Askew, R. Mancuso, M. Vargas-Caballero, C. Holscher, V. H. Perry and D. Gomez-Nicola, *Brain*, 2016, **139**, 891–907.

9 H. Asai, S. Ikezu, S. Tsunoda, M. Medalla, J. Luebke, T. Haydar, B. Wolozin, O. Butovsky, S. Kügler and T. Ikezu, *Nat. Neurosci.*, 2015, **18**, 1584–1593.

10 S. M. Pyonteck, L. Akkari, A. J. Schuhmacher, R. L. Bowman, L. Sevenich, D. F. Quail, O. C. Olson, M. L. Quick, J. T. Huse, V. Teijeiro, M. Setty, C. S. Leslie, Y. Oei, A. Pedraza, J. Zhang, C. W. Brennan, J. C. Sutton, E. C. Holland, D. Daniel and J. A. Joyce, *Nat Med*, 2013, **19**, 1264–1272.

11 S. J. Coniglio, E. Eugenin, K. Dobrenis, E. R. Stanley, B. L. West, M. H. Symons and J. E. Segall, *Mol. Med.*, 2012, **18**, 519–527.

12 B. Von Tresckow, F. Morschhauser, V. Ribrag, M. S. Topp, C. Chien, S. Seetharam, R. Aquino, S. Kotoulek, C. J. De Boer and A. Engert, *Clin. Cancer Res.*, 2015, **21**, 1843–1850.

13 M. R. P. Elmore, R. J. Lee, B. L. West and K. N. Green, *PLoS One*, 2015, **10**, 1–18.

14 S. Patel and M. R. Player, *Curr. Top. Med. Chem.*, 2009, **9**, 599–610.

15 M. C. Genovese, E. Hsia, S. M. Belkowski, C. Chien, T. Masterson, R. L. Thurmond, C. L. Manthey, X. Yan, T. Ge, C. Franks and A. Greenspan, *J. Rheumatol.*, 2015, **42**, 1752–1760.

16 C. H. Ries, M. A. Cannarile, S. Hoves, J. Benz, K. Wartha, V. Runza, F. Rey-Giraud, L. P. Pradel, F. Feuerhake, I. Klaman, T. Jones, U. Jucknischke, S. Scheiblich, K. Kaluza, I. H.

Gorr, A. Walz, K. Abiraj, P. A. Cassier, A. Sica, C. Gomez-Roca, K. E. deVisser, A. Italiano, C. LeTourneau, J. P. Delord, H. Levitsky, J. Y. Blay and D. Rüttinger, *Cancer Cell*, 2014, **25**, 846–859.

17 T. Ota, H. Urakawa, E. Kozawa, K. Ikuta, S. Hamada, S. Tsukushi, Y. Shimoyama, N. Ishiguro and Y. Nishida, *Tumor Biol.*, 2015, **36**, 5361–5367.

18 M. R. P. Elmore, A. R. Najafi, M. A. Koike, N. N. Dagher, E. E. Spangenberg, R. A. Rice, M. Kitazawa, B. Matusow, H. Nguyen, B. L. West and K. N. Green, *Neuron*, 2014, **82**, 380–397.

19 N. N. Dagher, A. R. Najafi, K. M. N. Kayala, M. R. P. Elmore, T. E. White, R. Medeiros, B. L. West and K. N. Green, *J. Neuroinflammation*, 2015, **12**, 1–14.

20 F. E. Turkheimer, G. Rizzo, P. S. Bloomfield, O. Howes, P. Zanotti-Fregonara, A. Bertoldo and M. Veronese, *Biochem. Soc. Trans.*, 2015, **43**, 586–592.

21 V. Bernard-Gauthier and R. Schirrmacher, *Bioorganic Med. Chem. Lett.*, 2014, **24**, 4784–4790.

22 R. Naik, V. Misheneva, I. Minn, T. Melnikova, W. Mathews, R. Dannals, M. Pomper, A. Savonenko, M. Pletnikov and A. Horti, *J. Nucl. Med.*, 2018, **59**, 547–547.

23 D. A. Scott, C. L. Balliet, D. J. Cook, A. M. Davies, T. W. Gero, C. A. Omer, S. Poondru, M. E. Theoclitou, B. Tyurin and M. J. Zinda, *Bioorganic Med. Chem. Lett.*, 2009, **19**, 697–700.

24 D. A. Scott, K. J. Bell, C. T. Campbell, D. J. Cook, L. A. Dakin, D. J. Del Valle, L. Drew, T. W. Gero, M. M. Hattersley, C. A. Omer, B. Tyurin and X. Zheng, *Bioorganic Med. Chem. Lett.*, 2009, **19**, 701–705.

25 D. A. Scott, L. A. Dakin, D. J. Del Valle, R. Bruce Diebold, L. Drew, T. W. Gero, C. A. Ogoe, C. A. Omer, G. Repik, K. Thakur, Q. Ye and X. Zheng, *Bioorganic Med. Chem. Lett.*, 2011, **21**, 1382–1384.

26 X. Shao, R. Hoareau, A. C. Runkle, L. J. M. Tluczek, B. G. Hockley, B. D. Henderson and P. J. H. Scott, *J. Label. Compd. Radiopharm.*, 2011, **54**, 819–838.

27 A. V Mossine, A. F. Brooks, K. J. Makaravage, J. M. Miller, N. Ichiishi, M. S. Sanford and P. J. H. Scott, *Org. Lett.*, 2015, **17**, 5780–5783.

28 A. V Mossine, A. F. Brooks, V. Bernard-Gauthier, J. J. Bailey, N. Ichiishi, R. Schirrmacher, M. S. Sanford and P. J. H. Scott, *J. Label. Compd. Radiopharm.*, 2018, **61**, 228–236.

29 CSF1R, https://www.proteinatlas.org/ENSG00000182578-CSF1R/tissue, (accessed 26 November 2018).

30 N. Droin and E. Solary, *J. Leukoc. Biol.*, 2010, **87**, 745–747.

31 J. Cammermeyer, *Neurosci. Res. (N. Y).*, 1970, **3**, 43–129.

32 A. K. Tiwari, B. Ji, J. Yui, M. Fujinaga, T. Yamasaki, L. Xie, R. Luo, Y. Shimoda, K. Kumata, Y. Zhang, A. Hatori, J. Maeda, M. Higuchi, F. Wang and M. R. Zhang,

Theranostics, 2015, **5**, 961–969.

33 S. Sridharan, F. X. Lepelletier, W. Trigg, S. Banister, T. Reekie, M. Kassiou, A. Gerhard, R. Hinz and H. Boutin, *Mol. Imaging Biol.*, 2017, **19**, 77–89.

34 H. Pajouhesh and G. R. Lenz, *NeuroRx*, 2005, **2**, 541–553.

35 cLogP and tSPA values were estimated using ChemDraw Professional 16.0 (PerkinElmer, Waltham, MA, USA) and pKa values were estimated using MarvinSketch (ChemAxon, Budapest, Hungary)

36 X. Chu, K. Bleasby and R. Evers, *Expert Opin. Drug Metab. Toxicol.*, 2013, **9**, 237–252.

37 M. V. Fawaz, A. F. Brooks, M. E. Rodnick, G. M. Carpenter, X. Shao, T. J. Desmond, P. Sherman, C. A. Quesada, B. G. Hockley, M. R. Kilbourn, R. L. Albin, K. A. Frey and P. J. H. Scott, *ACS Chem. Neurosci.*, 2014, **5**, 718–730.

38 L. Yang, A. F. Brooks, K. J. Makaravage, H. Zhang, M. S. Sanford, P. J. H. Scott and X. Shao, *ACS Med. Chem. Lett.*, 2018, **9**, 1274–1279.

CHAPTER 5

Synthesis of High-molar-activity [^{18}F]6-fluoro-L- DOPA Suitable for Human Use via Cu-mediated Fluorodeborylation of a BPin Precursor

5.1. Introduction

Creation of novel Positron Emission Tomography (PET) tracers with the hope of achieving a clinical tracer has been the focus of this work so far. PET tracers that have already achieved clinical approval are not always routinely synthesized in PET production facilities. This is normally due to low demand of the tracers by clinicians. Sometimes the reported syntheses of these tracers are tedious to perform on a daily basis within a current good manufacturing process (cGMP) facility where extensive regulation of synthesis schemes ensures normality between productions. During the development of novel PET tracers, the limitations enforced by agencies such as the Food and Drug Administration (FDA) and United States Pharmacopeia (USP), are kept in mind. This prevents the use of certain chemicals and high-performance liquid chromatography (HPLC) buffers. Examples of this line of thinking have been explored in the previous chapters. Ethanol buffers are often preferred for purification over other solvents such as methanol or acetonitrile because it has low toxic potential according to the USP being a class 3 solvent (acetonitrile and methanol being a class 2 solvent and having very limited injectability). To overcome elution buffers that utilize class-2 solvents, reformulation is performed to achieve an injectable dose in either 0.9% saline, sterile water, or a 10% ethanol solution. This has been demonstrated in the synthesis of [^{11}C]AZ683 and [^{18}F]FL2-b for pre-clinical studies in chapters 3 and 4. Finally, Fluorine-18 (^{18}F) labeling of molecules is not always easily achieved. Typically, [^{18}F]fluoride is used in a salt form (i.e. potassium fluoride, KF) with the help of a phase transfer catalyst. Much effort has been taken to optimize conditions to achieve high yielding synthesis of fluorine-18 PET tracers. In the primary organic literature, multiple transition metal catalysts have been used to achieve this result such as palladium. However, copper has been used extensively in PET radiochemistry methodology because of its high injectability and low toxicity. The process of validating a new reaction process is demonstrated here in the synthesis of 6-[^{18}F]Fluoro-L-DOPA ([^{18}F]FDOPA). This requires three successful validation runs with multiple quality control (QC) tests to ensure the final dose meets production regulations dictated by the FDA and USP.

5.1.1. *[^{18}F]FDOPA Overview*

[^{18}F]FDOPA is a diagnostic radiopharmaceutical that has been used for PET imaging for a number of years after it was first synthesized.[1] The first use of [^{18}F]FDOPA[2,3] for imaging of the human brain[4] was for imaging of the large amino acid transport and dopaminergic neurons in the early 1980s. Reflecting this, [^{18}F]FDOPA PET finds application in Parkinson's disease,[5] neuro-oncology,[6,7] and focal hyperinsulinism of infancy.[8]

Even though [^{18}F]FDOPA is extensively used for a wide range of indications, the radiopharmaceutical remains underutilized because of challenges associated with synthesizing the radiotracer for clinical use.[3] These issues arise from difficulties in radio-fluorinating a highly electron-rich aromatic ring and the need to protect (and deprotect) both catechol and amino acid functionalities. Historically, [^{18}F]FDOPA was synthesized via electrophilic aromatic substitution (S_EAr) using electrophilic fluorinating agents (e.g., [^{18}F]F_2 or [^{18}F]acetyl hypofluorite) and an appropriate precursor such as an organostannane (**Figure 5.2.a**).[9,10] New variants of such methods continue to be reported,[11] but S_EAr reactions are challenging because of the need for specialized equipment, modest site- and chemoselectivities, and low-molar-activity products.[3]

Electrophilic radiofluorination reactions have inherent limitations including fluorine-19 being present in the carrier gas or electrophilic fluorination reagents (i.e. diethlaminosulfur trifluoride, DAST) leading to low molecular activity (MA) of the tracer being produced. Therefore, a synthesis of [^{18}F]FDOPA that uses nucleophilic [^{18}F]fluoride has long been in demand. In contrast to electrophilic reagents such as [^{18}F]F_2, [^{18}F]fluoride is readily available in multi-Curie amounts and high molar activity from small, on-site medical cyclotrons and is used daily in radiochemistry production facilities all over the world. As such, substantial research has been aimed at developing a synthesis of [^{18}F]FDOPA using nucleophilic [^{18}F]fluoride. However, the electronic mismatch between the nucleophilic [^{18}F]fluoride and the electron rich catechol ring has mitigated efforts to develop an operationally simple nucleophilic synthesis of high molar activity [^{18}F]FDOPA. The typical approach involves nucleophilic radiofluorination of a benzaldehyde precursor with an appropriate leaving group (e.g. –Cl, $–NO_2$, $–N^+Me_3$).[3] Depending on the choice of precursor, the synthesis then either involves coupling of the amino acid side chain[12–15] or a Dakin Oxidation that consists of an oxidation of the ^{18}F-labeled aldehyde intermediate (usually with *meta*-chloroperoxybenzoic acid (mCPBA)) and hydrolysis of the resulting ester to yield the required catechol.[16–18] In either case, final deprotection with concentrated HI or HBr generates [^{18}F]FDOPA (**Figure 5.2.b**). This strategy has been used to synthesize [^{18}F]FDOPA in good yields and molar activity, and commercial cassette solutions using this synthesis scheme are available.[14,19,20] However, operational complexity, stemming from the need to conduct multiple steps after labeling with fluorine-18 and the use of corrosive acids for deprotection has limited such methods to certain synthesis modules or manual radiochemistry setups. The complexity of this process results in multiple potential fail points (both chemical and mechanical) during automated radiosynthesis, and results in complicated quality control analysis where multiple side products need to be tested for to ensure chemical and radiochemical purity. As such, there remains a need for a simple one-pot, two-step (fluorination + deprotection) synthesis of [^{18}F]FDOPA using nucleophilic [^{18}F]fluoride that is high yielding, uses milder reagents, and can be easily automated using standard, commercial radiochemistry synthesis modules. While such a method has eluded radiochemists to date, fluorine-18 radiochemistry has undergone a tremendous amount of growth in recent years.

5.1.2. *Copper-mediated radiofluorination technique overview*

Within the past few years, development of new fluorine-18 radiochemistry (for recent reviews, see refs: 21–24) methods enabling radiofluorination of hypervalent iodine reagents,[25–28] organoborons,[29,30] organostannanes,[31] Pd-complexes,[32] and Ni-complexes,[33] and phenols[34] with nucleophilic [^{18}F]fluoride have led to facile radiolabeling of electron-rich arenes. Of these new approaches, Cu-mediated fluorination has emerged as a powerful labeling technique that has been widely adopted by the PET radiochemistry community. Originally introduced by the Sanford lab in 2013 for fluorination of iodonium salts and organoborons,[35,36] the first report adapting the method for radiofluorination by Ichiishi et al. discussed a method for the Cu-mediated ^{18}F-fluorination of (mesityl)(aryl)iodonium salts.[28] Subsequently, the Gouverneur lab reported a method for the Cu-mediated ^{18}F-fluorination of pinacol boronate (BPin) esters.[29] Since [^{18}F]FDOPA was not the main focus of that paper, extensive development work was not done and the method gives doses of [^{18}F]FDOPA contaminated with a chemical impurity that disqualify it from clinical use. Moreover, the requirement to introduce air into the radiofluorination reaction is difficult to automate given that radiochemistry synthesis modules are typically kept under an inert atmosphere and closed to the environment. The use of 57% HI in the deprotection step is also problematic as it is highly corrosive to the valves and lines employed in automated synthesis modules. The Scott and Sanford labs reported ^{18}F-fluorination of organoborons,[30] organostannanes,[31] and aromatic C–H bonds.[37] These methods enable direct introduction of nucleophilic [^{18}F]fluoride into electron-rich arenes and are ideally suited to the synthesis of [^{18}F]FDOPA. A number of these approaches have been used to synthesize [^{18}F]FDOPA in preliminary proof-of-concept studies (**Figure 5.2.c**)[28,31,33,38–42] and a recently developed method that is compliant with cGMP is the subject of our published protocol (**Figure 5.2.d**).[43] This method has been validated for production of human doses and can be used as a starting point for creating regulatory filings (e.g., a Chemistry, Manufacturing and Controls (CMC) section for an Investigational New Drug (IND) application or an Abbreviated New Drug Application (ANDA)). A comparison of these new methods for preparing [^{18}F]FDOPA with the historical approaches is provided in **Figure 5.2**, along with a summary of the advantages and limitations of each strategy. To address the outstanding need in the PET radiochemistry community for ready access to [^{18}F]FDOPA, a new one-pot, two-step synthesis of the radiotracer from a BPin precursor, and validate it for pro- duction of clinical doses (**Figure 5.1**) is described. Precursor **1** was selected because it is commercially available (ABX Advanced Biochemicals).The MOM and Boc protecting groups ensure that mild global deprotection conditions with HCl can be utilized. In addition, our radiofluorination methodology does not require the introduction of air, simplifying automation. Lastly, we have also developed a new approach for purification and reformulation of [^{18}F]FDOPA that utilizes hydrophilic interaction liquid chromatography (HILIC). HILIC is an alternative technique to reverse phase HPLC for separating particularly polar compounds (for an overview of the method, see: 44). HILIC employs traditional polar stationary phases or polar end capping of the bead (e.g. silica, amino or cyano), but mobile phases used are similar to reversed-phase HPLC and, in this case, it provided [^{18}F]FDOPA in high chemical, and radiochemical yield;

with enantiomeric purity of the radiochemistry production method confirmed by chiral chromatography during quality control (QC) testing.

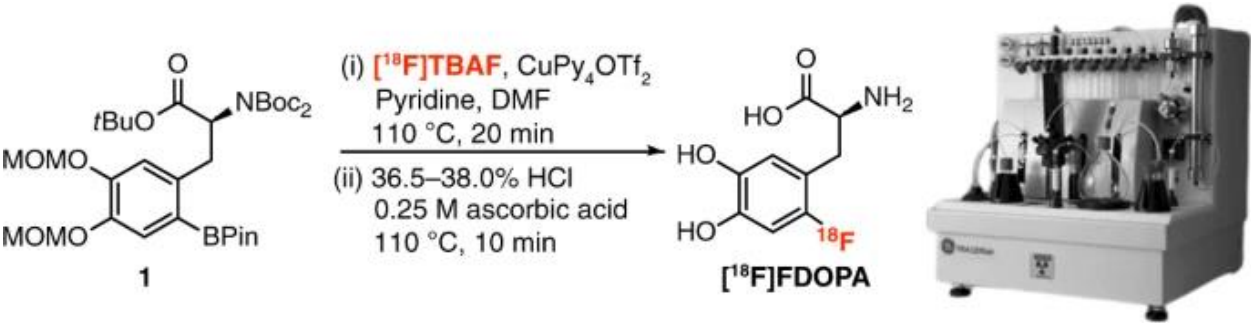

Fig. 5. 1: Radiosynthesis of [^{18}F]FDOPA and the TRACERLab automated synthesis module. Left, diagram of precursor 1, reaction, and product ([^{18}F]FDOPA). Right, TRACERLab automated synthesis module. Synthesis(module schematics (**Fig. 5.8**) are provided in the Materials and Methods section 5.4. Adapted from ref. 58 with permission from The Royal Society of Chemistry.

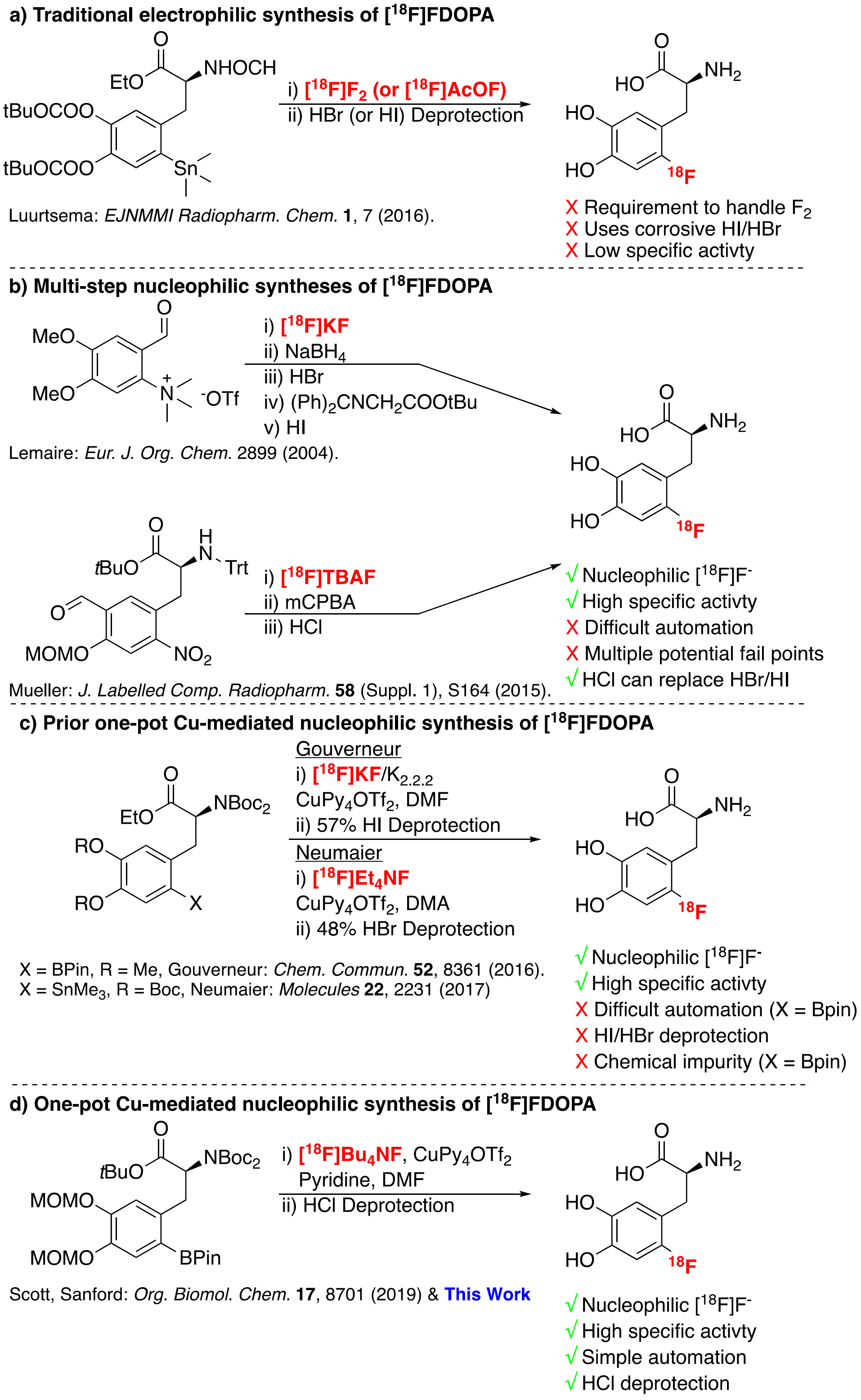

Fig. 5. 2: Radiosyntheses of [^{18}F]FDOPA and motivation for this work. a, Traditional electronic synthesis of [^{18}F] FDOPA. b, Multistep nucleophilic synthesis of [^{18}F]FDOPA. c, Prior one-pot Cu-mediated nucleophilic synthesis of [^{18}F]FDOPA. d, One-pot Cu-mediated nucleophilic synthesis of [^{18}F]FDOPA shown in this protocol. Adapted from ref. 43 with permission from The Royal Society of Chemistry.

5.2. Results

5.2.1. *Optimization of the Copper Mediated Fluoro-Deborylation Radiosynthesis for [^{18}F]FDOPA*

Synthesis of [^{18}F]FDOPA, was achieved by the use of recently reported copper-mediated radiofluorination conditions of organoboron precursors,[30] which was expected to simplify automation as, unlike the methods described above, it does not require air. Radiofluorination of BPin **1** using a TRACERLab FX_{FN} synthesis module under different conditions **Table 5.1**. [^{18}F]Fluoride from the cyclotron was trapped on a bicarbonate-pre-conditioned quaternary ammonium (QMA) cartridge, eluted into the reactor with an aqueous solution of 10 mg/mL KOTf/ 0.1 mg/mL K_2CO_3 (0.5 mL) and azeotropically dried with MeCN (1 mL). For initial proof-of-concept, manual radiofluorination was conducted using our standard labelling protocol (**1** (4 µmol), $Cu(OTf)_2$ (20 µmol) and pyridine (500 µmol) in 1 mL DMF for 20 min at 110 °C). This provided protected [^{18}F]FDOPA in 49 ± 7% radiochemical yield (RCY) (**Table 5.1**, entry 1). This process was readily translated to an automated process on the synthesis module to provide **2** in 38 ± 4% RCY (**Table 5.1**, entry 2).

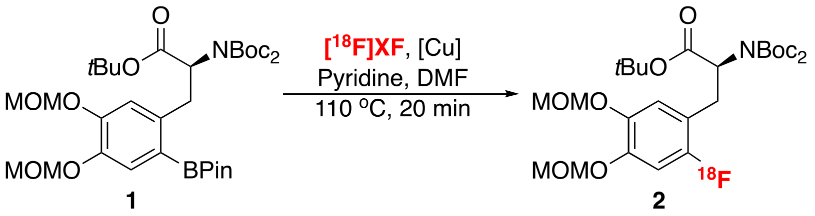

Entry[a]	[^{18}F]XF	RCY¶
1[b]	[^{18}F]KF	49 ± 7%
2[c]	[^{18}F]KF	38 ± 4%
3[c]	[^{18}F]TBAF	55 ± 13%

[a] Conditions: **1BPin** (4 µmol), $Cu(OTf)_2$ (20 µmol), and pyridine (500 µmol) in DMF at 4 mM concentration of the BPin precursor in DMF, [^{18}F]XF, 110 °C, 20 min. **b** Manual syntheses. **c** Automated syntheses

Table 5. 1: Optimization of the Labelling of **1**. Adapted from ref. 43 with permission from Royal Society of Chemistry

The next step was to focus on optimizing the radiofluorination reaction. Prior work has shown that both the [^{18}F]fluoride processing technique and the order/temperature of reagent addition were both key to reaction outcome in related systems.[45,46]. Previous work showed that the dissolution of [^{18}F]fluoride before heating the fluorination reaction proved critical to avoid competing reactions (e.g. protodeborylation and/or hydroxydeborylation) that competitively consume **1**.[45,46] To address this issue, an alternate eluent in order to facilitate rapid dissolution of [^{18}F]fluoride was developed. Given the greater solubility of tetrabutylammonium (TBA$^+$) and Cs$^+$ cations relative to K$^+$ in DMF, without loss of anion exchange properties, an aqueous eluent consisting of 15 mg/mL tetrabutylammonium triflate (TBAOTf) and 0.2 mg/mL Cs_2CO_3 (0.5 mL), as a replacement for KOTf and K_2CO_3, respectively was used. This eluent gave good recovery of [^{18}F]fluoride from the QMA and improved the RCY of **2** to 55 ± 13% (**Table 5.1**, **entry 3**).

With an optimized fluorination in hand, the deprotection step was optimized next. As previously mentioned, deprotection steps to generate [^{18}F]FDOPA have commonly utilized concentrated HI or HBr to remove methoxy protecting groups.[2] These chemical reagents are highly corrosive and greatly reduce the lifetime of lines and valves in the synthesis module. This would be detrimental for to routine production of the radiopharmaceutical because of maintenance costs and time to keep replacing these parts on the synthesis module. Therefore, a milder acid for deprotection was used and reasoned that HCl, albeit at maximum concentration, should be both compatible with our synthesis module and adequate to deprotect the methoxymethyl ether (MOM) and tert-butyl ester groups of **2** (**Table 5.2**). Initial attempts to treat **2** in the fluorination reaction mixture with 12N HCl resulted in significant decomposition and minimal (<1%) [^{18}F]FDOPA (**Table 5.2**, **entry 1**). It was hypothesized that the decomposition could be due to the presence of Cu(II) salts,[47,48] which could promote numerous potential side reactions. As such, the addition of ascorbic acid during the deprotection, as this is known to reduce the Cu(II) to Cu(I) was examined. Gratifyingly, this resulted in a dramatic enhancement in the yield of the deprotection step, providing [^{18}F]FDOPA in 84 ± 8% RCY (**Table 5.2**, **entry 2**). Intermediate **2** could also be purified by SPE prior to deprotection using a modified synthesis module. This resulted in an even cleaner deprotection that proceeded in >99% RCY (**Table 5.2**, **entry 3**).

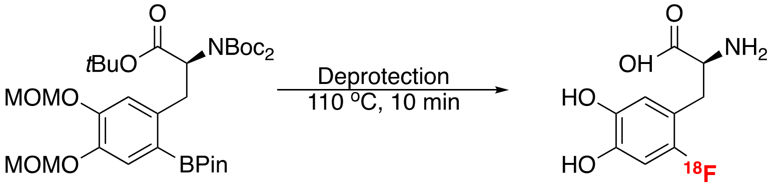

2 **3**

Entry^{a}	**Deprotection**	**RCY**^{b}
1	12 M HCl	Decomp.
2	12 M HCl + 0.25 M Ascorbic Acid	84 ± 8%
3^{c}	12 M HCl + 0.25 M Ascorbic Acid	>99%

[a]Conditions: HCl ± ascorbic acid, 110 °C, 10 min. [b]RCY represents transformation of **2** → **3**. [c]**2** purified by SPE prior to deprotection.

Table 5. 2: Optimization of the Deprotection of [^{18}F]**2**. Adapted from ref. 43 with permission from Royal Society of Chemistry.

After deprotection, purification of [^{18}F]FDOPA from reactants and potential by-products (e.g. OH-DOPA and H-DOPA) can be achieved by semi-preparative chromatography, followed by subsequent reformulation in a suitable, injectable solvent. Prior reports utilized reverse-phase HPLC with C18 columns, but these were found to be unsatisfactory due to the close retention times of [^{18}F]FDOPA and both OH-DOPA (a neurotoxic agent) and H-DOPA by-products which result from competing hydroxy- and protodeborylation, respectively. Therefore, HILIC purification was used and evaluated with several different stationary phase column types. The best results were achieved using a Phenomenex Luna NH_2 5µ column and an eluent with a high organic content: 75% MeCN including 10 mM KOAc buffered with acetic acid to pH: 5.0–5.5 (near the theoretical isoelectric point of FDOPA). This system enables adequate separation of FDOPA, OH-DOPA and H-DOPA using both semi-preparative and analytical columns. PET radiotracers purified using MeCN-based HILIC eluents require reformulation into an injectable matrix such as ethanolic saline. Reverse phase SPE is typically used for reformulation of small molecule radiopharmaceuticals using, for example, C18 or Oasis HLB cartridges, but this is not possible with [^{18}F]FDOPA due to its hydrophilicity. Thus, a HILIC Strata NH_2 cartridge for reformulation was utilized. We found trapping/release efficiency for [^{18}F]FDOPA of 70% and 75% for the 100 mg and 200 mg cartridges, respectively, and selected the 200 mg cartridges for routine use.

Finally, we automated the one-pot, two-step synthesis of [^{18}F]FDOPA using a TRACERLab FX_{FN} synthesis module and validated the synthesis for cGMP production of doses for clinical use. To simplify routine automation, we changed the copper source from $Cu(OTf)_2$ to the less hygroscopic Cu $(pyridine)_4(OTf)_2$. This coper source has been used for the radiofluorination of BPin esters by Gouverneur but, as stated above, that method requires the introduction of air into the radiofluorination reaction which is difficult to automate.[29,38] To negate this issue, we adapted $Cu(Py)_4(OTf)_2$ for use in our chemistry, which is compatible with the inert atmosphere of the TRACERLab synthesis module,[30] by maintaining the same relative ratio of substrate: copper: pyridine (1BPin (4 μmol), Cu (20 μmol), and pyridine (420 μmol)). Radiofluorination and de- protection then proceeded as described above. The reaction mixture was diluted with MeCN (3 mL) and purified by semi- preparative HILIC. The peak corresponding to [^{18}F]FDOPA (t_R ~22–23 min) was collected in 100 mL MeCN and this solution was passed through the HILIC Strata NH_2 cartridge to trap the radiotracer. Following trapping and rinsing with USP grade ethanol (2–3 mL) to remove residual MeCN, [^{18}F]FDOPA was eluted from the cartridge with 0.9% saline, USP (10 mL) to produce doses formulated for injection. The final drug product was dispensed into a septum-sealed, sterile, pyrogen- free glass vial through a 0.22 μm sterile filter (Millex GV) to afford formulated doses of [^{18}F]FDOPA (104 ± 16 mCi, n = 3). The total synthesis time was approximately 110 min from end- of-bombardment, and the activity yield

(AY) was 6 ± 1%, based upon 1.8 Ci of [^{18}F]fluoride. Radiochemical purity (RCP) was >99% and molar activity was 3799 ± 2087 Ci/mmol. Doses were submitted for full QC testing to validate the method, and all doses met or exceeded release criteria for clinical application at the University of Michigan, including purity, sterility, residual TBA levels, and residual solvent analysis. Notably, enantiomeric purity was found to be >99% using chiral HPLC, confirming that the stereochemistry of the precursor was retained throughout the entire manufacturing process. Doses produced using copper-mediated reactions also need to be free of residual copper if they are to be applied in the clinic, since the permitted daily exposure limit for copper is ≤ 340 µg/day for parenteral administration.[49] Samples from each of the qualification runs were submitted for inductively coupled plasma mass spectrometry (ICP-MS) analysis and were found to contain residual Cu below the limit of quantification (0.11 ± 0.02 ppm), well under the established limit for copper.

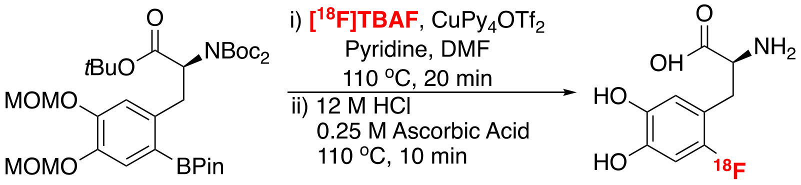

1 **3**

QC Test	Specifications	Result (n = 3)
Radioactivity Conc.	≥10mCi/batch	104 ± 16 mCi
FDOPA Conc.	≤5µg/mL	0.69 ± 0.47 µg/mL
Molar activity	≥ 500 Ci/mmol	3799 ± 2087 Ci/mmol
Radiochemical Purity	>90%	99.7 ± 0.3
Radiochemical Identity	RRT[a] = 0.9-1.1	1.02 ± 0.002
Enantiomeric Purity	≥ 95% L-FDOPA	100 ± 0%
Visual Inspection	Clear, colorless, no ppt	Pass
pH	4.5-7.5	5.5 ± 0
Radionuclidic Identity	$T_{1/2}$ = 105-115 min	112 ± 2 min
Residual TBA$^+$	≤260 µg/mL by Dragendorff reagent	< 260 µg/mL
Residual DMF	≤880 ppm	106 ± 56 ppm
Residual MeCN	≤410 ppm	179 ± 78 ppm
Residual Cu	≤34 ppm	0.11 ± 0.02 ppm
Filter membrane integrity	≥50 psi	56 ± 1 psi
Bacterial endotoxins	≤ 2.00 EU[b]/mL	<2.00 EU[b]/mL
Sterility	No microbial growth	Pass

[a] Relative retention time (RRT) = [HPLC retention time of [^{18}F]FDOPA / HPLC retention time of FDOPA reference standard]; [b] EU = endotoxin units.

Table 5. 3: Validated cGMP Synthesis of [^{18}F]FDOPA **3**. Adapted from ref. 43 with permission from Royal Society of Chemistry

5.2.2. *Development of a Fast TLC Spot Test for the Analysis of Residual TBA Levels*

Many of the developments in synthesis, QC testing and regulatory oversight pertaining to fluorine-18 radiochemistry have been steered by the need to manufacture [^{18}F]FDG for widespread clinical use. For example, synthesis of [^{18}F]FDG (and many historical radiotracers) involves use of kryptofix-2.2.2 ($K_{2.2.2}$) as a phase transfer catalyst to enhance the reactivity of nucleophilic [^{18}F]KF, and over ten years ago the Michigan Cyclotron and Radiochemistry Facility reported a method for analyzing residual $K_{2.2.2}$ levels in formulated radiotracer doses.[50] However, increases in utilization of PET are, in part, being driven by demand for new radiotracers. The last 10 years has seen FDA approval of several new ^{18}F-labeled radiotracers for PET imaging of amyloid plagues (Amyvid, Vizamyl, Neuraceq), tau (Tauvid), prostate cancer (auxumin), and breast cancer (Cerianna),[51] as well as an increase in the use of labeled drug assets to support pharmaceutical R and D.[52] This expansion in the utilization of PET has created a need to radiolabel more diverse and complex molecules which, in turn, has spurred development of new methods for incorporating fluorine-18 into bioactive molecules.[22] In particular, transition metal-mediated reactions using high molar activity [^{18}F]fluoride have changed the way radiochemists form C–^{18}F bonds[53] and, as described above, copper-mediated radiofluorination (CMRF) has proven one of the most versatile of approaches to date (for a review of radiotracers synthesized by CMRF, see ref. 54). Key to the development and optimization of new radiofluorination reactions in our laboratory has been venturing beyond the traditional [^{18}F]KF•$K_{2.2.2}$ paradigm to explore new elution strategies[45] and alternate sources of [^{18}F]fluoride such as [^{18}F]AgF, [^{18}F]HF and [^{18}F]tetrabutylammonium fluoride ([^{18}F]TBAF).[55–58]

The tetrabutylammonium (TBA, **4**) cation is a reliable [^{18}F]fluoride counterion for the efficient elution and solubilization of [^{18}F]fluoride in aprotic solvents and is applicable to a range of fluorination conditions (i.e. in the presence or absence of a metal catalyst).[59–61] As described above (**Table 2.1**), our new synthesis of [^{18}F]F-l-DOPA ([^{18}F]FDOPA, **2**), requires TBA elution to generate [^{18}F]TBAF in order to give optimal RCYs.[62] In order to elute [^{18}F]fluoride completely from a SPE cartridge, however, a quantity of TBA exceeding the dose limit (2.6 mg/*V* (per patient dose)), set by the European Pharmacopeia (*Ph. Eur.*), is typically used. TBA is also used in the preparation of carbon-11 PET imaging agents. TBA phenolate or carboxylate salts of the desmethyl precursors (such as [^{11}C]carfentanil ([^{11}C]CFN, **5**)), furnish a very reactive site for carbon-11 methylation (when using, for example [^{11}C]CH_3I or [^{11}C]CH_3OTf).[63–65]

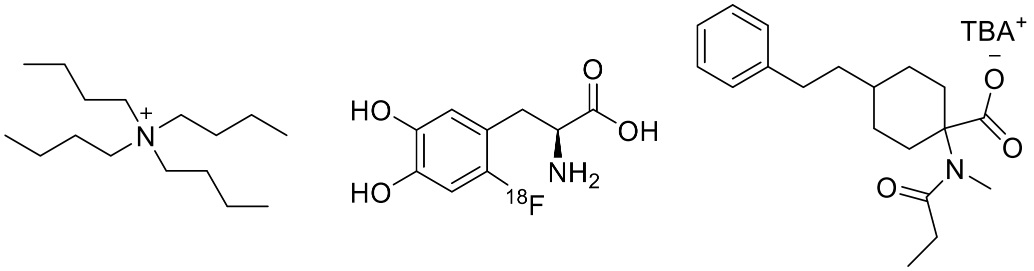

4 TBA^{+} **2** [^{18}F]FDOPA **5** [^{11}C]CFN precursor

Fig. 5. 3: Structures of TBA and radiopharmaceuticals that use TBA during synthesis.

The *Ph. Eur.* Suggests performing HPLC when analyzing residual TBA. However, the considerable amount of time and the expense of equipment required, especially as this requires multiple HPLC systems since this test and the test for radiochemical identity needs to be completed within 30 minutes from the end of synthesis, makes this a less than ideal approach. For the widespread implementation of TBA in the preparation of fluorine-18 and carbon-11 radiopharmaceuticals a simple straightforward QC test is required. A spot test analogous to the one currently in use for detection of $K_{2.2.2}$ is ideal for speed, consistency and ease of use for staff scientists and technicians.[50] A fast TLC spot test utilizing iodine vapor has been developed for analyzing the presence of TBA in radiopharmaceutical doses, but unfortunately it does not quantitatively assess TBA concentration for release.[66] The iodine test stains TBA well below the dose limit with a detection limit of 0.04 mg/mL, making it difficult to assess a clear pass or fail result. In addition, routine use of iodine vapors by the staff requires a containment hood for safe use.

More recently, Halvorsen and Kvernenes adapted the classical iodoplatinate reagent used in $K_{2.2.2}$ analysis for detecting TBA.[67] Although this method is useful for testing standard volumes of 10 mL doses, corresponding to a concentration of TBA at 0.26 mg/mL, the method's limit of detection (LoD) cannot be altered, and therefore it is challenging to use for other desired injection volumes (V), which have different TBA concentrations. Since we were in need of a TLC method to determine residual TBA levels in doses of [^{18}F]FDOPA,[57,58] independent of these other efforts we have developed a fast and quantitative spot test that employs the classical Dragendorff stain.[68,69] This new method has high specificity for TBA (compared to the radiotracer and other formulation components), and is applicable to a wide range of radiotracer doses. The TLC spot test requires very limited equipment and can be completed quickly within the constraints of PET radiotracer quality control which usually needs to be completed ≤20 min. At TBA levels ≥2.6 mg/V the spot test results in an easily detectable spot, while at concentrations ≤2.6 mg/V it does not, allowing for easy go/no-go decisions on dose release to be made during quality control testing.

Therefore, a fast and quantitative spot test that is applicable to a wide range of radiopharmaceutical doses where the stain used has high specificity for TBA compared to the imaging agent and other formulation components was developed. In addition, our goal was to develop a spot test where an amount of TBA above Ph. Eur.'s dose limit gave an easily detected spot while a dose below that limit did not. A fast spot test that requires a very limited amount of equipment and can be completed quickly within the constraints of PET radiopharmaceutical manufacturing for the detection of TBA will be a benefit for the PET imaging community by allowing for widespread utilization of TBA in PET radiochemistry.

In our recently developed synthesis of [^{18}F]FDOPA using CMRF, 7.5 mg of TBAOTf is used to generate [^{18}F]TBAF,[57,58] while the commercially cassettes available for production of [^{18}F]FDOPA utilize 24 mg TBAHCO$_3$.[70] In the event of a purification problem, it is possible that levels of TBA in the final product prepared using either method exceed the established concentration limit defined by *Ph Eur* (2.6 mg/V, where V = 10 mL[57,58] or 28 mL,[70] respectively). It should be noted that for the different formulation volumes the limit, and thus the sensitivity of the test, will vary (e.g. limit in 28 and 10 mL doses are of 0.09 and 0.26 mg/mL, respectively, assuming the entire dose is administered to a single patient).

Initial studies of known TLC stains for quaternaryalkyl ammonium cations like TBA were performed. Three of the most promising, iodoplatinate that is used for K$_{2.2.2}$, Dragendorff stain (potassium bismuth iodide), and iodine vapor were tested for their ability to visualize TBA at different concentrations between 0.001 and 10 mg/mL (**Table 5.4** and **Figure 5.4**). Standards were prepared by serial dilution of TBAOTf in water, and the LoD was determined for each TLC stain was determined.

Visualization of TBA using pre-developed iodoplatinate plates proved challenging in our hands and results were difficult to interpret (**Figure 5.4.a**). The staining pattern of TBA was difficult to distinguish from a control spot (water) with the same colored concentric circles surrounding the spot of interest. Iodine staining showed a robust spot at the 10 mg/mL TBA concentration, but quickly lost intensity with further dilution (**Figure 5.4.c**). Although iodine and iodoplatinate staining of TBA indicated positive staining at ≥0.25 mg/mL TBA, they did not provide a positive stain at 0.1 mg/mL, meaning they are not suitable tests for larger more dilute formulations that are common in multidose preparation of fluorine-18 radiotracers.[70] Iodine staining has been published as a viable method for TBA assessment, but requires the addition of 10 μL of MeOH/NH_4OH (90:10 v/v) to the TBA spot in order to enhance the signal and reduce the LoD.[66] The goal was to establish a quick TLC method that did not require more than just spotting the solution of interest and applying a stain in order to reduce complexity and minimize potential for test error, and thus focus was shifted to investigating the Dragendorff stain for analysis of TBA.

TBA (mg/ml)	**Iodine**	**Iodoplatinate**	Manually prepared **Dragendorf**f
10	Rust orange spot	Solid redwood spot	Solid orange spot
1	faint orange spot	Solid redwood spot with gray halo	Faint orange spot
0.5	faint orange halo	Solid redwood spot with gray halo	Orange halo
0.26 (standard 10 mL dose limit)			
0.25	faint orange halo	Solid redwood spot with gray halo	Orange halo
0.1 (26 mL dose limit)	ND	ND	Faint orange halo
0.9 (28 mL dose limit)			
0.01	ND	ND	Faint orange halo
0.001	ND	ND	ND

Table 5. 4: Various TLC Stains for the detection of TBA (ND = not detectable). Adapted from ref. 83 with permission from Royal Society of Chemistry

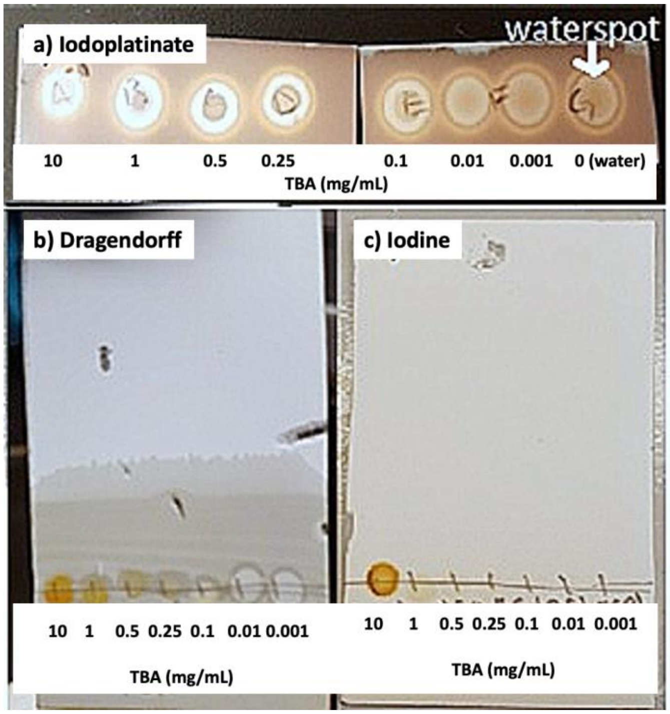

Fig. 5. 4: TLC Staining of TBA standards using a) pre-developed iodoplatinate plates, b) manual Dragendorff stain, and c) iodine chamber. Adapted from ref. 83 with permission from Royal Society of Chemistry

Dragendorff reagent, which is commercially available as a spray solution or as an even more concentrated dipping solution (see Materials and Methods, Section 5.4), and has known specificity for alkaloids and quaternaryalkyl ammonium bases.[71] The specificity of Dragendorff reagent for TBA proceeds through a single displacement reaction, with TBA thought to exchange with potassium in the active ingredient ($KBiI_4$) to generate an easily visualized orange precipitate (**Equation 5.1**).[72]

$$[Bu_4NH]^{18}F + K[BiI_4] \longrightarrow [^{18}F]KF + \underset{\text{Insoluble Orange Salt}}{[Bu_4NH][BiI_4]}$$

Eq. 5. 1: Reaction of Dragendorff reagent with TBA to form orange precipitate

Use of either commercially available Dragendorff spray or dipping solution resulted in a pale orange background on which to interpret a positive stain, with an LoD of 0.14 mg/mL TBA (**Figure 5.5**). It was concluded that the orange background would make it difficult to quantify the presence of residual TBA accurately and rapidly in radiotracer doses, particularly at low concentrations. The preparation of a custom Dragendorff stock solution was undertaken in order to tune its sensitivity and eliminate the background color for higher spot contrast. After optimization, our prepared Dragendorff reagent (see Materials and Methods section 5.4 for preparation of Dragendorff's staining solution), provided positive orange spots with a white background and an LoD of 0.01 mg/mL (**Figure 5.4.b**). The TLC stain provided a clear background for confident identification of a positive spot at (or above) the allowable limit for injection (LoI). A semiquantitative TLC method for TBA using prepared Dragendorff solution was further developed. Although the active ingredient (BiI_4^-) remains the same in both the commercial products and our custom solution, the use of acetic acid and ethyl acetate as solvents in the commercial products (versus nitric acid and water used to prepare our version) may contribute to the orange background seen with the commercial stains (**Figure 5.5**). The exact contents of commercially available Dragendorff reagent are proprietary, limiting further speculation.

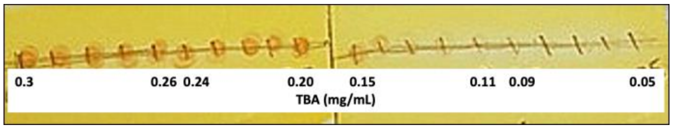

Fig. 5. 5: Representative commercial Dragendorff stain of TBA standards. Adapted from ref. 83 with permission from Royal Society of Chemistry

In order to develop a quick pass or fail spot test for TBA in different radiotracer formulations, it was hypothesized that the LoD of Dragendorff stain could be varied by dilution to match the appropriate LoI for TBA in a given formulation volume. A test where any TBA concentration above the LoI would give a positive response and any concentration below would not yield a spot by staining was the goal of our development. As proof of concept, it was hoped that a stain could be developed for analyzing residual TBA levels in the two formulations of [^{18}F]FDOPA utilized in our laboratory (10 mL of saline[57,58] and 28 mL of PBS[70]). Standards were prepared spanning the TBA LoD (≤ 0.26 mg/mL) for a 10 mL dose formulated in normal saline (**Table 5.5** and **Figure 5.6.a**, A-K) as well as standards spanning the LoD (≤0.1 mg/mL) for a 28 mL dose formulated in PBS (**Table 5.5** and **Fig. 5.6.b**, L-V), and explored development of custom Dragendorff stains for both.

Identifier	A	B	C	D	E	F	G	H	I	J	K
TBA (mg/mL)	0.3	0.29	0.28	0.27	0.26	0.25	0.24	0.23	0.22	0.21	0.2
Identifier	L	M	N	O	P	Q	R	S	T	U	V
TBA (mg/mL)	0.15	0.14	0.13	0.12	0.11	0.1	0.09	0.08	0.07	0.06	0.05

Table 5. 5: TBA concentration identifiers A-V. Adapted from ref. 83 with permission from Royal Society of Chemistry

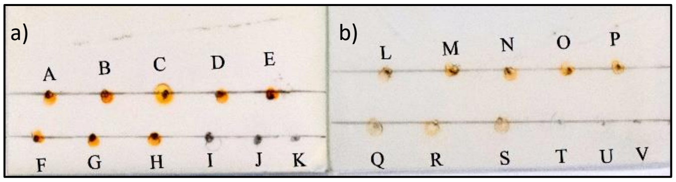

Fig. 5. 6: Dragendorff stain of a) saline prepared TBA standards and b) PBS prepared TBA standards. Adapted from ref. 83 with permission from Royal Society of Chemistry

Diluting our custom Dragendorff solution with water (1:15 when staining TBA standards representative of [^{18}F]FDOPA formulated in 10 mL saline, and 1:9 when staining standards representative of FDOPA dissolved in 28 mL of PBS) proved optimal and solid orange spots were observed down to the LoI for both formulations (0.23 mg/mL (**Figure 5.6.a**) and 0.08 mg/mL (**Figure 5.6.b**), respectively). Gratifyingly, no matrix interference was observed from saline or PBS. This demonstrated the robustness of the prepared Dragendorff reagent spot test and also the ability to customize it for a given radiotracer formulation.

With a pass or fail TLC spot test for TBA in hand, analysis of residual TBA levels in [^{18}F]FDOPA batches prepared for clinical use using either a GE TRACERlab FX$_{FN}$ [57,58] or a GE FASTlab2[70] and formulated in 10 mL saline (n = 3, **Figure 5.7**) or 28 mL of PBS (n = 4), respectively (**Table 5.6**) were performed. To test for the possibility of false negative results, an aliquot of the final dose was also spiked with an internal TBA standard corresponding to the LoI.

By spotting the final dose, the final dose with an internal standard, a TBA standard equal to that of the LoI and a negative control (water) on the same plate, it was possible to determine with confidence that doses of [^{18}F]FDOPA prepared via either method did not contain TBA above the LoI, and were thus suitable for human use.

[^{18}F]FDOPA Formulation	LoI (mg/mL)	Dose	Standard	Dose spiked with Std	Water	n
10 mL Saline	≤0.26	○	●	●	○	3
28 mL PBS	≤0.09	○	●	●	○	4
10 mL Saline	≤0.26	○	●	●	○	1[a]

Table 5. 6: QC Analysis of [^{18}F]FDOPA for TBA. Adapted with permission from Royal Society of Chemistry. [a] using 14 d old Dragendorff

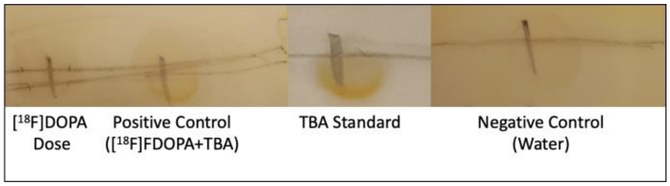

Fig. 5. 7: Dragendorff testing of [^{18}F]FDOPA doses. Adapted from ref. 83 with permission from Royal Society of Chemistry

Finally, the longevity of the stain was tested by performing residual TBA analysis every other day for two weeks. The stain was kept in a fume hood at room temperature during this time. The same results were obtained over the two week duration (**Table 2.6**), indicating that our custom Dragendorff stain is shelf stable and can be used for routine radiotracer QC testing.

5.3. Discussion and Conclusions

Radiofluorination of organoborons, reported independently by Tredwell *et al.*[29] and Mossine *et al.*,[30] has proven one of the most versatile approaches for the late-stage fluorination of bioactive molecules to date. We have further optimized the approach for use with automated radiochemistry synthesis modules,[45,46] and additional variants of the original methods have subsequently been reported by Zischler *et al.*[42] and Zlatopolskiy *et al.*[73] The methodology has been rapidly adopted by the PET radiochemistry community, and a number of independent groups have used the technique to synthesize new PET radiopharmaceuticals for preclinical and clinical use.[74–81] Given the historical challenges associated with synthesizing [^{18}F]FDOPA from nucleophilic [^{18}F]fluoride, we were motivated to overcome these issues through development of a one-pot, two-step synthesis of high-molar-activity [^{18}F]FDOPA by copper-mediated fluorination of a BPin precursor. Here, a method that primarily uses off-the-shelf reagents and a commonly available synthesis module was validated for production of [^{18}F]FDOPA for clinical use by preparing process-verification batches.[43] The one-pot production method provides [^{18}F]FDOPA in reasonable radiochemical yield (3.85 ± 0.59 GBq, 104 ± 16 mCi, 6 ± 1% based upon ~66.6 GBq (1,800 mCi) of starting [^{18}F]fluoride), excellent radiochemical (>99%, **Figure 5.10**) and enantiomeric (>99%, **Figure 5.11**) purity, and high molar activity (141 ± 77 TBq/mmol, 3,799 ± 2,087 Ci/mmol), n = 3. All other QC testing confirmed that each dose met or exceeded QC criteria established for human use of PET radiopharmaceuticals (**Table 5.3**). The one-pot method with HLB purification between fluorination and deprotection also provides [^{18}F]FDOPA in moderate radiochemical yield (2.26 ± 0.48 GBq, 61 ± 13 mCi, 5 ± 1% based upon 45.6 ± 11.0 GBq (1,232 ± 298 mCi) of starting [^{18}F]fluoride), excellent radiochemical purity (>98%) and high molar activity (71 ± 17 TBq/mmol, 1,909 ± 459 Ci/mmol), n = 23. The method has been validated to work well at two separate sites, an academic facility with a cyclotron on site (University of Michigan (UM)) and an industry lab purchasing [^{18}F]fluoride from an outside vendor (AbbVie). We were gratified that the yield of [^{18}F]FDOPA was comparable at the two sites (UM: 6 ± 1%; AbbVie: 5 ± 1%). Given the operational simplicity of the method, which uses a standard radiochemistry synthesis module, and the demonstrated robustness of this protocol, we anticipate that the reliability of synthesizing [^{18}F]FDOPA with this method will be high. As such, we expect that this method (or a modification thereof) will be useful to research facilities that own a TRACERLab FX_{FN} or similar system and that want access to a straightforward procedure for producing [^{18}F]FDOPA.

Also, a quick reliable TLC spot test for determining residual TBA levels in radiotracer formulations has been developed using the Dragendorff reagent. The test is straightforward, does not require expensive equipment to implement, can easily be tuned for different radiotracer formulations, and is analogous to existing QC TLC spot tests for $K_{2.2.2}$ allowing easy implementation at PET Centers using [^{18}F]TBAF to produce clinical radiotracers. This spot test is also expected to facilitate use of [^{18}F]TBAF at more facilities in the future as it allows easy QC testing without causing workflow issues or mandating costly equipment acquisitions. Our facility has implemented this TLC spot test for analysis of residual TBA^+ in radiotracers prepared for clinical use with [^{18}F]TBAF.

Radiofluorination can be accomplished using $Cu(Py)_4(OTf)_2$ (Step 13A) or $Cu(OTf)_2$ (Step 13B). To simplify automation, we prefer to use the less hygroscopic $Cu(Py)_4(OTf)_2$. Two variations that have also been used for removal of the methoxymethyl acetal (MOM) and tert-butyloxycarbonyl (Boc) groups from protected [^{18}F]FDOPA perform similarly and can be selected on the basis of available equipment and site radiochemistry preferences. The first is a standard one-pot synthesis that uses a standard TRACERLab FX_{FN} synthesis module setup; the deprotection cocktail (HCl/ascorbic acid) is added to the crude reaction mixture following fluorination (Step 16A). Following deprotection, the entire reaction mixture is then injected onto the column for purification of [^{18}F]FDOPA by semi-preparative HPLC. The second variation is a pseudo-one-pot synthesis involving pre-purification of the protected-[^{18}F]FDOPA intermediate before deprotection (Step 16B). Briefly, the radiofluorination reaction mixture is diluted in an aqueous solution containing ascorbic acid and/or ethylenediaminetetraacetic acid (EDTA) to reduce and coordinate copper, respectively, and is then passed through a reversed-phase C18 plus or Oasis hydrophilic–lipophilic–balanced (HLB) SPE cartridge to trap the lipophilic protected [^{18}F]FDOPA intermediate. Protected [^{18}F]FDOPA is then eluted from the SPE cartridge with ethanol back into the reactor, resulting in a partially purified solution of protected [^{18}F]FDOPA. Deprotection then proceeds as for Step 16A. This pre-purification requires a modified TRACERLab FX_{FN} synthesis module (see Method 1 for time list), and has two benefits: (i) it removes most of the copper, potentially reducing the extent of oxidative [^{18}F]FDOPA degradation during deprotection and (ii) it removes N-N-dimethylformamide (DMF), which simplifies semi-preparative HPLC. The net result is a more consistent radiochemical yield (RCY) run to run. It is also possible to synthesize [^{18}F]FDOPA using a manual procedure. This method uses lower amounts of starting [^{18}F]fluoride than automated clinical-scale production and can be used in facilities without access to automated synthesis modules. It is also appropriate when only a small amount of [^{18}F]FDOPA is required for a chemistry or animal imaging experiment. Last, we showcase Cu-mediated radiofluorination for the synthesis of [^{18}F]FDOPA in this protocol. However, the method is readily adaptable to the synthesis of other PET radiotracers after appropriate development of radiolabelling and deprotection conditions.

5.4. Materials and Methods

General Considerations

Unless otherwise stated, reagents and solvents were commercially available and used without further purification: O-MOM-N-Boc-protected Bpin precursor (Part No. 1312) and authentic reference standards of 6-F-l-DOPA (Part No. 1310), 6-F-d,l-DOPA (Part No. 1311), and 6-OH-d,l-DOPA (Part No. 1332) were purchased from ABX. 6-H-l-DOPA (Part No. D9628), anhydrous pyridine (Part No. 270970), Tetrakispyridine copper(II) trifluoromethanesulfonate (Part No. 34527), ascorbic acid (Part No. 255564), hydrochloric acid (Part No. h1758), Tetrabutylammonium trifluoromethanesulfonate (Part No. 86888), and cesium carbonate (Part No. 41902) were purchased from Sigma Aldrich. Anhydrous N,N-dimethylformamide was purchased from Acros (Part No. 448381000). HPLC-grade Acetonitrile (Part No. A998-4), potassium acetate Part No. P171-500), acetic acid (Part No. A38S-500), and sodium bicarbonate (Part No. S233-500) were purchased from Fisher Scientific. Ethanol (200 proof, USP) was purchased from Decon Laboratories, Inc. Sodium chloride 0.9%, USP and sterile water for injection, USP were sourced from Hospira. Other synthesis components were obtained as follows: Sterile vials were obtained from Hollister-Stier, Millex filters were from Millipore (Part No. SLFG025LS and SLGV013SL or GV and FG, respectively), and QMA-light cartridges were purchased from Waters. Luna NH_2 micron 10x250 mm and 4.6x150 mm HPLC columns (Part No. 00g-4378-n0 and 00f-4378-e0), Luna NH_2 guard cartridge discs (Part No. 00G-4454-N0PRP-214513), and Strata® 200 mg SPE cartridges Part No. 8B-5009-FBJ) were purchased from Phenomenex. Astec® CHIROBIOTIC® T Chiral HPLC column (Part No. 12024AST) was purchased from Sigma Aldrich. QMA cartridges were conditioned with ethanol, 0.5M $NaHCO_3$, and sterile water (10 mL of each, in that order) prior to use. Strata cartridges were conditioned with ethanol, sterile water, and acetonitrile (10 mL of each, in that order) prior to use

Safety and hazards

All hazardous laboratory chemicals were used under the supervision of University of Michigan (UM) Environmental Health and Safety. Radioactivity was used by trained personnel under the approval of the UM Radiation Policy Committee (Protocol 12-029) and supervision of the UM Radiation Safety Service and according to ALARA (as low as reasonably achievable) principles.

All reactions involving radioactivity were conducted in a lead-shielded fume hood or hot-cell, and followed appropriate institutional, state and/or federal radiation safety guidelines.

Preparation of TBA Standards

A 1mg/mL TBA solution was created by dissolving 16.15 mg of TBAOTf in 10 mL of either water, saline, or PBS. A series of 1 mL standard concentrations were made by serial diluting the 1 mg/mL solution in its appropriate buffer to create a range from 0.3 mg/mL – 0.05 mg/mL.

TLC Procedure

2 μL spots of TBA standards or formulated dose were applied to silica plates or pre-developed plates containing iodoplatinate solution via an auto-pipette. In the case of Dragendorff or iodine staining, the spots were then dried with a cool air stream for 30 seconds. For Dragendorff staining, the TLC plates were dipped into the Dragendorff solution to fully immerse the spots for 10-20 seconds to allow for the formation of orange precipitate. Once removed, plates were photographed immediately and visually analyzed. Air drying after the Dragendorff staining can enhance the intensity of the spots, however using warm air resulted in a whiting out of the plate.

5.4.1. *Synthesis and Purification of [^{18}F]FDOPA*

Reagent Setup

- **TBAOTf/Cs_2CO_3 eluent solution (Step 11):** Weigh out 150 mg TBAOTf and 2 mg Cs_2CO_3 in a 20 mL scintillation vial. Add 10 mL water and a stirrer bar and cover (but do not seal) the scintillation vial. Heat while stirring until solution is near-boiling and all solids have dissolved. Remove stirrer bar, cap vial and allow to cool to room temperature. A small amount of crystalline material may form on cooling around lip of container, but this will re-dissolve in the solution over time. Store this eluent at room temperature for up to 3 months.

- **FDOPA BPin precursor (1) stock solution (4 µmol/200 µL):** Using a syringe, transfer 1.5 mL of anhydrous DMF into the sealed vial containing 20 mg dry BPin precursor (**1**). Vortex for at least 1 min to dissolve all precursor. Precursor stock solution can be stored for up to 3 months in the -20 °C freezer, vial placed in a sealed jar containing Drierite®.
- **FDOPA reactant solution (Step 13A):** Weigh out 13.5 ± 0.5 mg of $Cu(py)_4(OTf)_2$ into a 4 mL glass vial. Add 0.8 mL of anhydrous DMF then cap vial and fully dissolve the solid by vortexing for 30 sec. Add 33.2 µL anhydrous pyridine followed by 0.2 mL of precursor stock solution. Agitate briefly, then use immediately after preparation. Do not heat this solution at any stage of preparation.
- **Alternative FDOPA reactant solution (Step 13B):** Weigh out 7.5 ± 0.5 mg of $Cu(OTf)_2$ into a 4 mL glass vial. Add 1.0 mL of anhydrous DMF then cap vial and fully dissolve the solid by vortexing for 30 sec. Add 80 µL anhydrous pyridine followed by 0.2 mL of precursor stock solution. Agitate briefly, then use immediately after preparation. Do not heat this solution at any stage of preparation.
- **0.25M ascorbic acid solution:** Weigh out 440 mg ascorbic acid in a 20 mL scintillation vial and dissolve in 10 mL water. Cap vial and store in refrigerator for up to 1 month.
- **0.10M ascorbic acid solution:** Weigh out 176 mg ascorbic acid in a 20 mL scintillation vial and dissolve in 10 mL water. Cap vial and store in refrigerator for up to 1 month.
- **0.10M ascorbic acid/0.01M EDTA solution (Step 14B, i):** Weigh out 176 mg ascorbic acid and 42 mg EDTA in a 20 mL scintillation vial and dissolve in 10 mL HPLC grade water. Cap vial and store in refrigerator for up to 1 month.
- **Deprotecting solution (Step 14A):** Mix 0.2 mL 0.25M ascorbic acid solution with 0.6 mL 36.5 – 38.0% HCl. Use immediately after preparation.

- **Alternative Deprotecting solution (Step 14B, iii):** Mix 0.25 mL of 0.10M ascorbic acid solution with 0.25 mL of 36.5 – 38.0% HCl. Use immediately after preparation.
- **Semi-preparative HPLC eluent #1 (90% MeCN) (Steps 3, 4 and 16):** Dissolve approximately 1 g KOAc in 100 mL water, add 1 mL AcOH followed by 900 mL MeCN. Ensure the pH of this solution lies between 7.0 and 8.0 using a pH sensor. Adjust accordingly with KOAc/AcOH if outside of range. Sonicate before using. Store for up to 1 week.
- **Semi-preparative HPLC eluent #2 (75% MeCN) (Steps 3 and 16):** Dissolve approximately 1 g KOAc in 250 mL water, add 10 mL AcOH followed by 750 mL MeCN. Ensure that pH of this solution lies between 5.0 and 5.5 using a pH sensor. Adjust accordingly with KOH/AcOH if outside of range. Sonicate before using. Store for up to 1 week.
- **Analytical HPLC eluent (70% MeCN) (Step 25):** Dissolve approximately 1 g KOAc in 300 mL water, add 1 mL AcOH followed by 700 mL MeCN. Ensure the pH of this solution lies between 5.0 and 5.5 using a pH sensor. Adjust accordingly with KOAc/AcOH if outside of range. Sonicate before using. Store for up to 1 week.
- **Chiral Analytical HPLC eluent (30% EtOH) (Step 27):** Dissolve approximately 1 g KOAc in 700 mL water, add 1 mL AcOH followed by 300 mL EtOH. Ensure the pH of this solution lies between 5.0 and 5.5 using a pH sensor. Adjust accordingly with KOAc/AcOH if outside of range. Sonicate before using. Store for up to 1 week.
- **0.5 M $NaHCO_3$ solution:** Dissolve 8.4 g $NaHCO_3$ in 200 mL water. Can be stored sealed at room temperature for up to 1 month.

- **Preparation of Dragendorff solution**: Stock Dragendorff solution was prepared according to a literature procedure[82]:

  Solution A:

  (a) 8.0 g bismuth(III) nitrate was dissolved in 25 mL 25% Nitric Acid (bismuth solution)

  (b) 20 g potassium iodide was used to make a slurry in 1 mL 6 N HCl and 5 mL water (slurry)

  (c) The bismuth solution was added to the slurry slowly while stirring

  (d) The resulting solution was diluted with 100 mL water and any solid present was removed by filtration

  Dragendorff stock solution:

  (a) In a solution containing 20 mL water and 5 mL 6 N HCl was added 2 mL of Solution A followed by 6 mL 6N NaOH. Due to the presence of bismuth hydroxide not fully dissolving by shaking, several drops of 6 N HCl were added for a yellow-orange translucent solution.

***Dragendorff dilution*: Dragendorff stock solution was diluted 1:15 or 1:9 in H_2O and a cloudy solution was formed. 6N HCl was then added dropwise to the diluted stain solution until a transparent yellow solution was formed.**

Equipment Setup

- Waters Light QMA cartridge: Flush sequentially with 10 mL absolute ethanol, 10 mL 0.5M sodium bicarbonate solution, and 10 mL water (Milli-Q or ACS Reagent for ultratrace). Attach it to the synthesis module.
- Waters HLB Short Plus cartridge (for alternate method with HLB purification between fluorination and deprotection, **Step 8B**): Flush sequentially with 10 mL absolute ethanol,

10 mL HPLC grade water. Attach to the synthesis module in the “intermediate cartridge” position.

- Strata® NH_2 200mg SPE cartridge: Flush sequentially with 10 mL absolute ethanol, 10 mL water, and 10 mL acetonitrile. Attach it to the reformulation module of the synthesis module.
- Preparation of semi-preparative (Luna NH_2 5µ 10 x 250 mm) HPLC column: Assemble guard column as per manufacturer instructions and attach to semi-preparative HPLC column. Flush column for 15 – 3 min at 5 mL/min with 90% MeCN (Semi-preparative HPLC eluent #1) prior to installation in the synthesis module. Replace guard column cartridges as needed (every 1-3 months depending on frequency of use). We also recommend flushing the column with water containing 0.1% trifluoroacetic acid for 15 min at 5mL/min once every 5 runs.

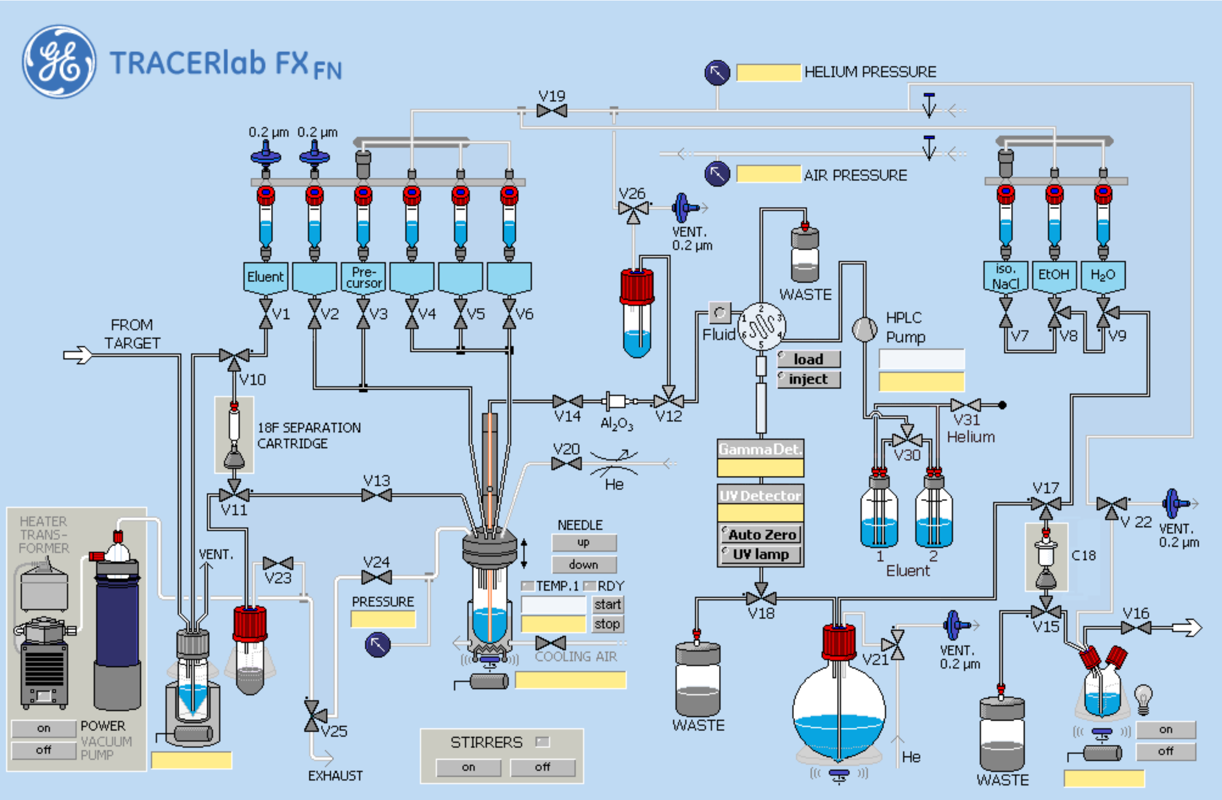

Fig. 5. 8: GE TRACERLab FXFN configuration

Hot Cell and TRACERLab FX_{FN} Preparation

Preparation for the synthesis of [^{18}F]FDOPA should begin at least 15-30 min before start of cyclotron production of [^{18}F]fluoride.

1| Turn on the TRACERLab FX_{FN} module and computer. Start the Tracerlab FX_{FN} software program and fill the module's dewar with liquid nitrogen. Verify the machine has been cleaned, disinfected and dried using approved methods (clean if necessary) and that all components are in working order.

2| Remove and clean the synthesis module reactor with 1) 0.5M $NaHCO_3$ solution, 2) water, 3) ethanol and 4) acetone, then rinse with acetone and thoroughly dry. After drying, equip the reactor with a stirrer bar and reinstall on the TRACERLab.

Cleaning of TRACERLab FX_{FN} synthesis module: Follow manufacturer instructions/facility standard operating procedures in cleaning, disinfecting, and drying the synthesis module. We recommend using 70% ethanol as disinfectant. Both the glass and glassy carbon reactors can be used in the synthesis of [^{18}F]FDOPA.

3| Install HPLC eluents on the TRACERLab system (Reservoir 1: 90% MeCN; Reservoir 2: 75% MeCN).

4| Attach a guard column to the semi-preparative HPLC column and install on the TRACERLab module. Flush the column with 90% acetonitrile (Reservoir 1) for 15-30 min at 5 mL/min.

5| Start the FDOPA production method in the synthesis module software

6| Attach the QMA, optional HLB, and Strata® NH_2 cartridges to the synthesis module. See Equipment Setup for preconditioning protocols.

7| Fill vials accordingly if using a TRACERLab FXFN synthesis module, the vials should be filled as follows: vial 1: TBAOTf/Cs_2CO_3 eluent solution (0.5 mL, Step 11); vial 2: acetonitrile (1 mL, Step 12); vial 3: FDOPA reactant solution (0.5 mL, Step 13A) or alternative FDOPA reactant solution (1.25 mL, Step 13B); vial 4: deprotecting solution (0.8 mL, Step 16A) or alternative deprotecting solution (0.5 mL, Step 16B(iii)); vial 5: ascorbic acid/EDTA solution (10 mL, Step 16B(i), only if using the alternative method with HLB purification between fluorination and deprotection); vial 6: acetonitrile (3 mL for one-pot procedure; 2 mL for alternative method with HLB purification); vial 7: 10 mL of USP saline; vial 8: 3 mL of dehydrated ethanol, USP; intermediate vial: absolute ethanol (2 mL, Step 16B(ii), only if using the alternative method with HLB purification); dilution flask: acetonitrile (100 mL). Fill dilution flask with 100 mL acetonitrile. If using the alternate procedure involving purification with an HLB cartridge between fluorination and deprotection, also add 2 mL of absolute ethanol to the intermediate vial.

8| Aseptically assemble the final dose vial by inserting an inlet needle and 13 mm Millex GV filter and a vent needle with FG filter according to local procedures. Attach the TRACERLab product delivery line to the final dose vial via the 13 mm GV filter.

Final dose vials should be assembled using aseptic technique in a Class 5 laminar airflow hood (or equivalent) and in compliance with local drug manufacturing and/or pharmacy regulations.

Preparation of [^{18}F]fluoride

9| Produce fluorine-18 in the cyclotron via the ^{18}O(p,n)^{18}F nuclear reaction (55 µA for 30 min or as needed) and transfer it to the target vial of the TRACERLab FX_{FN} synthesis module.

Synthesis of [^{18}F]FDOPA

10| Slowly transfer the solution of [^{18}F]fluoride in [^{18}O]H_2O through the QMA cartridge, trapping the [^{18}F]fluoride and recovering the [^{18}O]H_2O for proper disposal or recycling.

11| Elute [^{18}F]fluoride from the QMA cartridge into the TRACERLab reactor with 0.5 mL Eluent Solution (see Reagent Setup).

12| Add 1 mL of MeCN to the reactor and then heat to 100 °C while applying vacuum and/or argon flow to azeotropically dry the [^{18}F]fluoride.

13| After drying is complete, cool the reactor to 50 °C and add either $Cu(Py)_4(OTf)_2$ or $Cu(OTf)_2$.

	Reagent Setup Name	Volume (ml)
A) $Cu(Py)_4(OTf)_2$	FDOPA reactant solution	0.5
B) $Cu(OTf)_2$	Alternative FDOPA Reactant Solution	1.25

14| Stir at 50 °C for 5 min.

15| Increase the reactor temperature to 110 °C and continue heating for 20 min (**Note:** 20 mins is the optimal reaction time for this chemistry).[46]

16| Do the deprotection reaction either without pre-purification (one-pot method, option A) or with pre-purification of the protected-[^{18}F]FDOPA intermediate prior to deprotection (alternate one-pot method with HLB purification, option B).

(A) One-pot Method

i. Cool the reactor to 50 °C, add the Deprotecting Solution to the reactor (see Reagent Preparation) and heat at 100 °C for 10 min.

(B) Alternate One-pot Method with HLB purification between Fluorination and Deprotection

i. Cool the reactor to 50 °C and add ascorbic acid/EDTA solution (see Reagent Preparation) into the reactor. Stir for 30 s, and then load the reaction mixture onto the HLB cartridge, trapping protected [^{18}F]FDOPA on the cartridge.

ii. Elute protected [^{18}F]FDOPA from the HLB cartridge back into the reactor using ethanol (2 mL) from the intermediate vial.

iii. Add the Alternative Deprotecting Solution to the reactor (see Reagent preparation), and heat at 100 °C for 10 min.

17| Cool reactor to 50 °C and add 2 mL acetonitrile.

Purification and Reformulation of [^{18}F]FDOPA

18| Load reactor contents onto a 5 mL HPLC loop, then inject onto the HPLC column. Purify by semi-preparative HPLC. Flow rate should be set to 5 mL/min, reservoir 1 (90% MeCN). Elute column for 10 minutes at 5 mL/min. Switch eluent to reservoir 2 (75% acetonitrile) and continue to elute column at 5 mL/min.

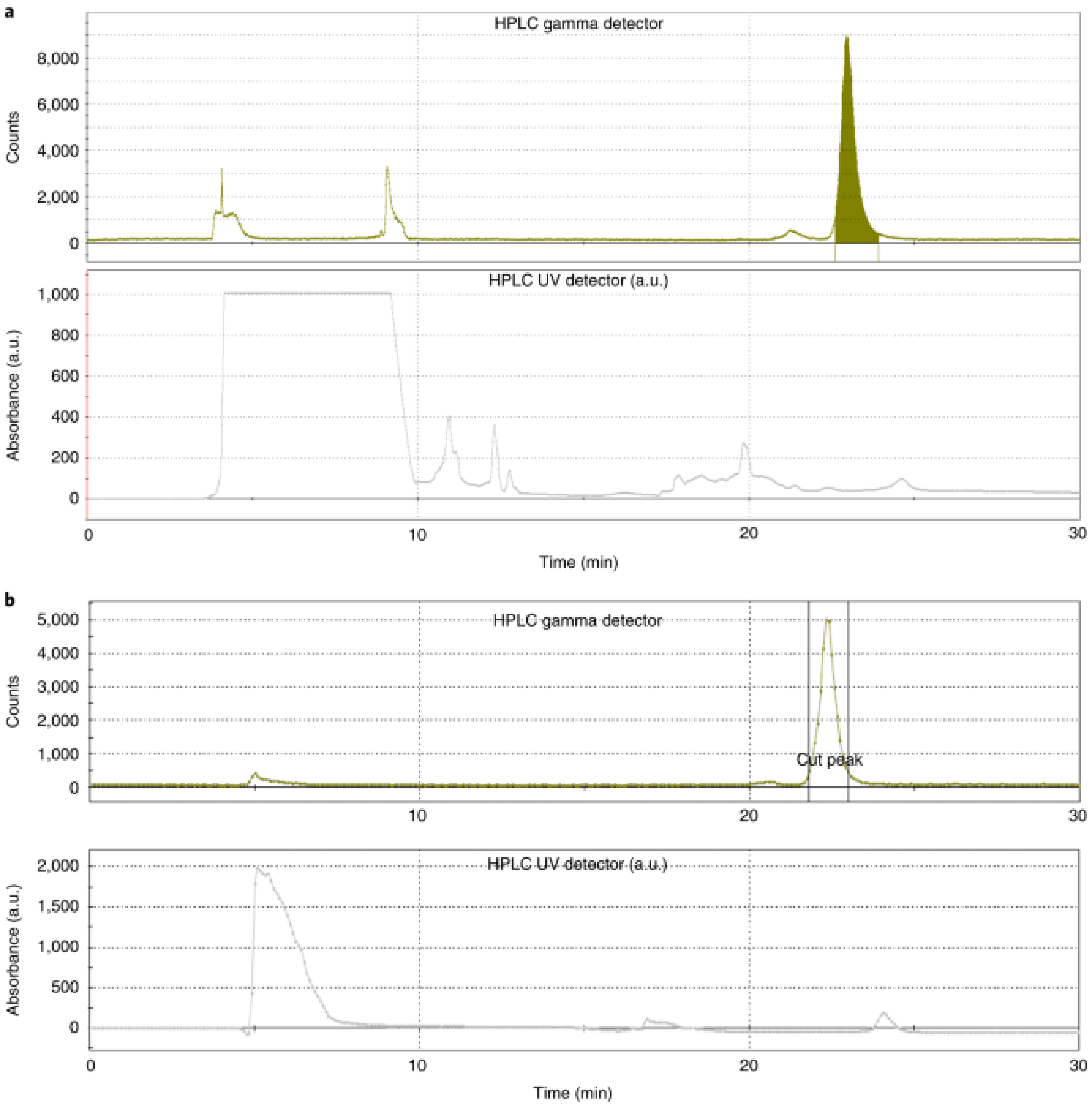

Fig. 5. 9: Semi-preparative HPLC traces for [^{18}F]FDOPA prepared using two different methods. a,[^{18}F]FDOPA prepared using the one-pot method. b,[^{18}F]FDOPA prepared using the alternative one-pot method with HLB purification between fluorination and deprotection. a.u., absorbance units. Adapted from ref. 43 with permission from Royal Society of Chemistry.

19| Collect the HPLC product fraction corresponding to [^{18}F]FDOPA into a dilution flask containing MeCN (100 mL). Collect the peak corresponding to [^{18}F]FDOPA at the appropriate retention time (~22 – 23 min, see **Figure 5.9**). Collect for approximately 2 min from the time liquid begins dripping into collection vial (fraction should elute in ≤ 1.5 min).

20| Briefly stir the dilution flask contents, then transfer the solution through the Strata® NH_2 SPE cartridge, trapping [^{18}F]FDOPA. Dry with argon flow for at least 2 min. Drying step is important to remove residual MeCN.

21| Wash the Strata® NH_2 cartridge with 3 mL absolute ethanol, then dry with argon flow for at least 3 min. Washing and drying steps are important to ensure there is no residual MeCN in final dose.

22| Elute Strata® NH_2 SPE cartridge with 10 mL 0.9% saline into a product collection vial.

23| Transfer the formulated [^{18}F]FDOPA through the 13 mm GV sterile filter into the sterile product vial. Aseptically remove 0.5 mL of the batch and place it in a 2cc sterile dose vial for quality control (QC) testing.

2.4.6. *Manual synthesis of [^{18}F]FDOPA using low levels of [^{18}F]fluoride*

1. Slowly transfer a solution of [^{18}F]fluoride (e.g., 100 mCi) in [^{18}O]H_2O through a QMA cartridge, trapping the [^{18}F]fluoride
2. Elute [^{18}F]fluoride from the QMA cartridge into a synthesis module reactor or manual radiochemistry setup with 0.5 mL TBAOTf/Cs_2CO_3 eluent solution (Reagent setup) and azeotropically dry it. Resolubilize in DMF (4 mL); depending on time and elution efficiency, strength will be ~10-20 mCi/mL
3. Add 0.4 M of the [^{18}F]fluoride stock solution to a glass vial containing BPin precursor **1** (4 µmol), $Cu(OTf)_2$ (20 µmol), and pyridine (500 µmol) in DMF (1 mL). Heat at 110°C for 20 min.
4. Cool the reaction to 50°C and dilute it with 0.10M ascorbic acid/0.01 M EDTA solution (Reagent setup). Stir for 30 s, and then load the reaction mixture onto an HLB cartridge,

trapping protected [^{18}F]FDOPA on the cartridge. Elute protected [^{18}F]FDOPA from the HLB cartridge back into a clean vial using absolute ethanol (2 mL)

5. Add alternative deprotecting solution (Reagent setup) and heat at 110°C for 20 min.
6. Allow mixture to cool to 50°C before purifying and reformulating [^{18}F]FDOPA according to Steps 18-23 of the main Procedure.
7. Complete QC testing as required for chemistry or animal studies according to the methods described in Steps 24-36 of the main Procedure.
8. Typical radiochemical yields of [^{18}F]FDOPA are 35-55% over two steps using this manual method.

5.4.2. *Quality Control of [^{18}F]FDOPA*

Pre-release QC Testing

24| Conduct a visual inspection of the QC sample to ensure the dose is clear, colourless and free of particulate matter.

25| Analyze the pH of the [^{18}F]FDOPA dose by applying a small amount of the dose to a pH-indicator strip and compare it to the scale provided. Dose pH is required to be between 4.5 and 7.5.

26| Determine residual TBA$^+$ levels in [^{18}F]FDOPA doses using Dragendorff stain and confirm that they are less than the *Ph. Eur.* requirement of <0.26 mg/mL TBA$^+$ (no USP limits currently exist for TBA$^+$).[83]

27| Analyze [^{18}F]FDOPA by analytical HPLC (**Figure 5.10** to determine identity, radiochemical and chemical purity (column: Luna NH$_2$ 5µ 4.6 x 150 mm column; mobile phase: 70% MeCN 10 mM KOAc, pH 5.2; flow rate: 1.5 mL/min). Radiochemical purity should be >90% and there should be <50 µg/mL of OH-DOPA and H-DOPA by-products which result from competing hydroxy- and proto-deborylation, respectively (see ref **Error! Bookmark not defined.** for more details). I dentity is confirmed by comparing the retention time of the radiolabelled product with that of the corresponding unlabelled FDOPA reference standard.

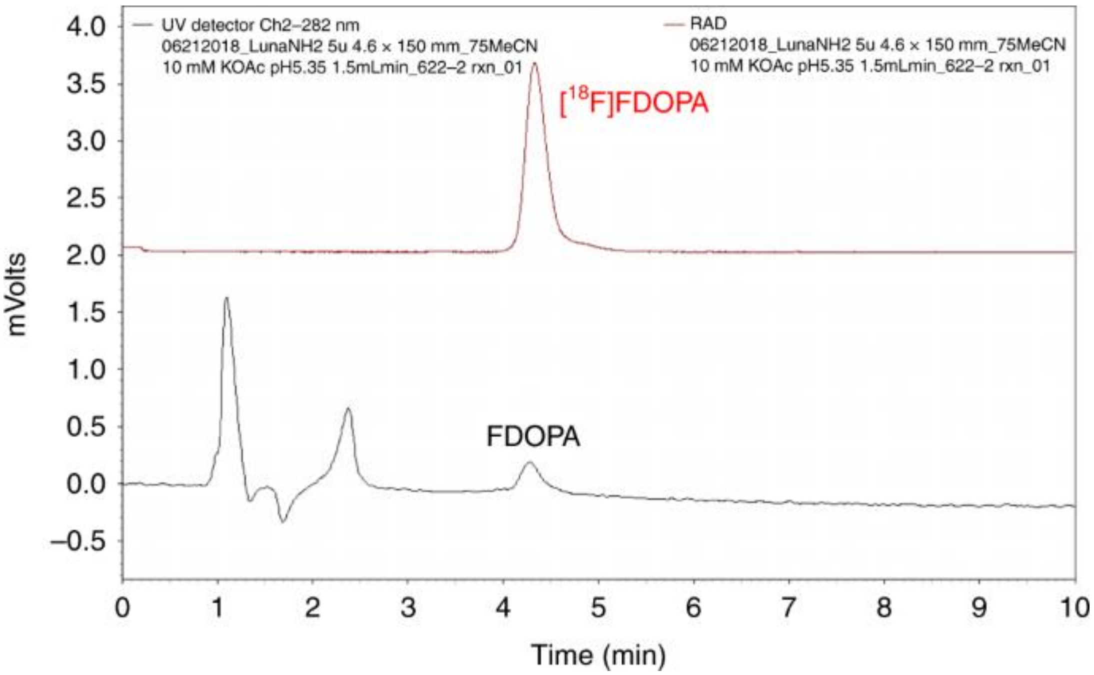

Fig. 5. 10: Analytical HPLC traces of [^{18}F]FDOPA using a Luna NH$_2$ analytical column. Top, RAD; bottom, 282-nm UV. Reproduced from ref. 43 with permission from The Royal Society of Chemistry

28| Use analytical HPLC data to calculate molar activity. Molar activity needs to be ≥18.5 TBq/mmol (>500 Ci/mmol).

27| Analyze [^{18}F]FDOPA by chiral HPLC to determine enantiomeric purity detector (column: Astec Chirobiotic T 5 µ250 x 4.6 mm analytical column; mobile phase: 30% ethanol 10mM KOAc pH 5.13, flow rate: 1.5mL/min). Enantiomeric purity is determined by comparison to 6-F-D,L-DOPA and/or 6-F-L-DOPA reference standards (**Figure5.11**. Enantiomeric purity of [^{18}F]FDOPA needs to be >95% of the L enantiomer.

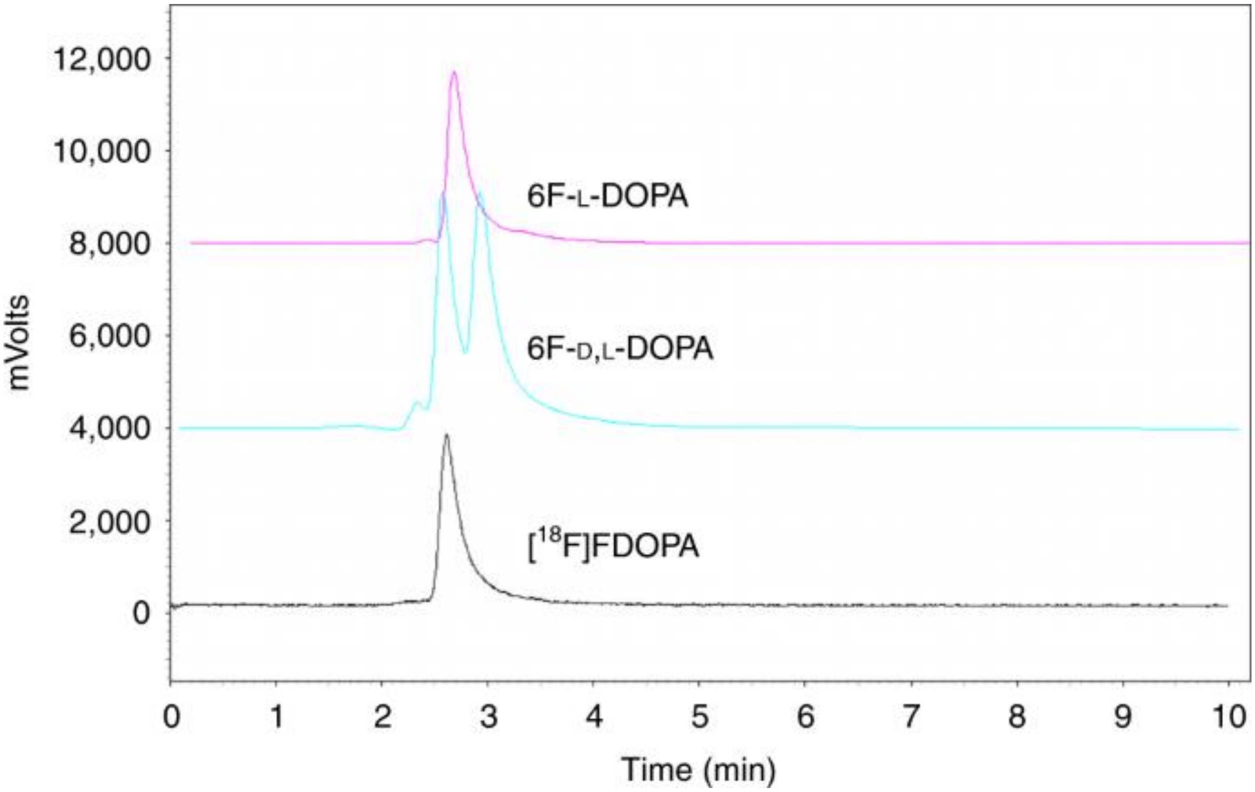

Fig. 5. 11: Chiral HPLC trace of production of [^{18}F]FDOPA, 6-F-D,L-DOPA reference standard, and 6F-L-DOPA reference standard using a Chirobiotic T analytical column. Top, 6F-L-DOPA reference standard (282 nm, magenta); middle, 6F-D,L-DOPA reference standard (282 nm, teal); and bottom, [^{18}F]FDOPA (RAD, black). Adapted from ref. 43 with permission from The Royal Society of Chemistry.

28| Analyze levels of residual solvents in [^{18}F]FDOPA doses using a Shimadzu GC-2010 with an AOC-20 autoinjector, split/splitless inlet, a flame ionization detector (or equivalent), and a Restek column (Stabilwax 30 m 0.25 mm, 0.25 m G16 stationary phase). Limits of residual solvents are based upon the International Conference on Harmonisation of Technical Requirements for Registration of Pharmaceuticals for Human Use guidelines (MeCN: ≤410 ppm; DMF: ≤880 ppm).[84]

29| Confirm radionuclide identity by determining the half-life of the [^{18}F]FDOPA dose and compare it to the known half-life of fluorine-18 (109.77 min). Measure radioactivity at 2 time points using a Capintec dose calibrator (or equivalent) and determine half-life ($T_{1/2}$ = -ln2(Time Difference / (ln(ending activity/starting activity)))). Calculated half-life must be 105–115 min.

30| Determine integrity of the 13 mm GV sterile filter using the bubble point test. The filter from the dose (with needle still attached) is connected to a nitrogen supply via a regulator. The needle is then submerged in water and the nitrogen pressure is gradually increased. If the pressure can be raised above the filter acceptance pressure (50 psi for 0.9% saline) without seeing a stream of bubbles, the filter is considered intact.

31| Determine endotoxin content in [^{18}F]FDOPA doses according to the US Pharmacopeia using a Charles River Laboratories EndoSafe® Portable Testing System (or equivalent). Doses must contain ≤175 Endotoxin Units (EU), or ≤17.5 EU/mL.

Sterility Testing

32| Sterility testing is a post-release test for short-lived radiopharmaceuticals. Within 24 h of end-of-synthesis, inoculate culture tubes of fluid thioglycolate media (FTM) and tryptic soy broth (TSB) with samples of [^{18}F]FDOPA and incubate (along with positive and negative controls) for 14 days. FTM is used to test for anaerobes, aerobes and microaerophiles while TSB is used to test for non-fastidious and fastidious microorganisms.

33| Visually inspect the culture tubes on the 3rd, 7th and 14th days of the test period and compare these to the positive and negative standards. Positive standards need to show growth (turbidity) in the tubes, and [^{18}F]FDOPA doses/negative controls need to show no culture growth after 14 days to be indicative of sterility.

Step	Problem	Possible Reason	Solution
11	[18F]Fluoride does not elute off QMA cartridge	Connections to QMA cartridge are either leaking, wrong cartridge used, or not properly conditioned	Check connections, replace as needed
15	Low incorporation of 18F- to precursor	Equipment malfunction, decomposition of reactants	Ensure syntheis module is clean and functional, check and replace reactants as needed
16A(i), 16B (iii)	Low radiochemical purity	Ascorbic acid has gone bad	Ehck and replace expired ascorbic acid if needed
18	Reaction mixture is slow to load onto HPLC loop or does not load at all	HPLC loop is blocked or screw cap to vial is not properly tightened	Clean out HPLC loop or tighten intermediate vial
	More radioactive impurities in HPLC trace than usual	Not enough acid in deprotection solution	Increase the amount of conc. HCl in deprotecting solution in 0.1 mL increments, or use frech conc. HCl
20,21,30	Too much MeCN in [18F]FDOPA product	MeCN was not adequately removed during washing of reformulaion cartridge	Optimize rinsig and drying in Steps 20 and 21, possibly by rinsing with more water

Table 5. 7: Troubleshooting Table. Adapted from ref 58 with permission from Nature

5.5. REFERENCES

1 S. M. Ametamey, M. Honer and P. A. Schubiger, *Chem. Rev.*, 2008, **108**, 1501–1516.

2 M. Pretze, C. Wängler and B. Wängler, *Biomed Res. Int.*, 2014, **2014**, 1–12.

3 D. Taïeb, A. Imperiale and K. Pacak, *Eur. J. Nucl. Med. Mol. Imaging*, 2016, **43**, 1187–1189.

4 E. S. Garnett, G. Firnau and C. Nahmias, *Nature*, 1983, **305**, 137–138.

5 J. Darcourt, A. Schiazza, N. Sapin, M. Dufour, M. J. Ouvrier, D. Benisvy, X. Fontana and P. M. Koulibaly, *Q. J. Nucl. Med. Mol. Imaging*, 2014, **58**, 355–65.

6 F. Calabria and G. L. Cascini, *Hell. J. Nucl. Med.*, 2015, **18**, 152–6.

7 H. Nandu, P. Y. Wen and R. Y. Huang, *Ther. Adv. Neurol. Disord.*, 2018, **11**, 1–19.

8 P. Shah, H. Demirbilek and K. Hussain, *Semin. Pediatr. Surg.*, 2014, **23**, 76–82.

9 A. Luxen, M. Perlmutter, G. T. Bida, G. Van Moffaert, J. S. Cook, N. Satyamurthy, M. E. Phelps and J. R. Barrio, *Int. J. Radiat. Appl. Instrumentation. Part A. Appl. Radiat. Isot.*, 1990, **41**, 275–281.

10 F. Füchtner, J. Zessin, P. Mäding and F. Wüst, *Nuklearmedizin.*, 2008, **47**, 62–64.

11 G. Luurtsema, H. H. Boersma, M. Schepers, A. M. T. de Vries, B. Maas, R. Zijlma, E. F. J. de Vries and P. H. Elsinga, *EJNMMI Radiopharm. Chem.*, 2017, **1**, 1–10.

12 C. Lemaire, S. Gillet, S. Guillouet, A. Plenevaux, J. Aerts and A. Luxen, *European J. Org. Chem.*, 2004, 2899–2904.

13 L. C. Libert, X. Franci, A. R. Plenevaux, T. Ooi, K. Maruoka, A. J. Luxen and C. F. Lemaire, *J. Nucl. Med.*, 2013, **54**, 1154–1161.

14 C. Lemaire, L. Libert, X. Franci, J. L. Genon, S. Kuci, F. Giacomelli and A. Luxen, *J. Label. Compd. Radiopharm.*, 2015, **58**, 281–290.

15 B. Shen, W. Ehrlichmann, M. Uebele, H. J. Machulla and G. Reischl, *Appl. Radiat. Isot.*, 2009, **67**, 1650–1653.

16 T. Tierling, K. Hamacher and H. H. Coenen, *J. Label. Compd. Radiopharm.*, 2001, **44**, S146–S147.

17 F. M. Wagner, J. Ermert and H. H. Coenen, *J. Nucl. Med.*, 2009, **50**, 1724–1729.

18 M. M. and D. G. C. Sauvage , N. Lazarova, *J. Label. Compd. Radiopharm.*, 2015, **58**, S164.

19 Trasis. [18F]FDOPA nucleophlic process., http://www.trasis.com/tracers/18ffdopa.

20 ABX. Reagents kits, http://www.abx.de/Information/Index?viewId=Synthesizer.

21 M. G. Campbell and T. Ritter, *Chem. Rev.*, 2015, **115**, 612–633.

22 A. F. Brooks, J. J. Topczewski, N. Ichiishi, M. S. Sanford and P. J. H. Scott, *Chem. Sci.*, 2014, **5**, 4545–4553.

23 X. Deng, J. Rong, L. Wang, N. Vasdev, L. Zhang, L. Josephson and S. H. Liang, *Angew. Chemie - Int. Ed.*, 2019, **58**, 2580–2605.

24 S. Preshlock, M. Tredwell and V. Gouverneur, *Chem. Rev.*, 2016, 116.

25 V. W. Pike, *J. Label. Compd. Radiopharm.*, 2018, **61**, 196–227.

26 B. H. Rotstein, N. A. Stephenson, N. Vasdev and S. H. Liang, *Nat. Commun.*, 2014, **5**, 1–7.

27 S. H. Liang, L. Wang, N. A. Stephenson, B. H. Rotstein and N. Vasdev, *Nat. Protoc.*, 2019, **14**, 1530–1545.

28 N. Ichiishi, A. F. Brooks, J. J. Topczewski, M. E. Rodnick, M. S. Sanford and P. J. H. Scott, *Org. Lett.*, 2014, **16**, 3224–3227.

29 M. Tredwell, S. M. Preshlock, N. J. Taylor, S. Gruber, M. Huiban, J. Passchier, J. Mercier, C. Génicot and V. Gouverneur, *Angew. Chemie - Int. Ed.*, 2014, **53**, 7751–7755.

30 A. V Mossine, A. F. Brooks, K. J. Makaravage, J. M. Miller, N. Ichiishi, M. S. Sanford and P. J. H. Scott, *Org. Lett.*, 2015, **17**, 5780–5783.

31 K. J. Makaravage, A. F. Brooks, A. V. Mossine, M. S. Sanford and P. J. H. Scott, *Org. Lett.*, 2016, **18**, 5440–5443.

32 E. Lee, A. S. Kamlet, D. C. Powers, C. N. Neumann, G. B. Boursalian, T. Furuya, D. C. Choi, J. M. Hooker and T. Ritter, *Science (80-.).*, 2011, **334**, 639–642.

33 E. Lee, J. M. Hooker and T. Ritter, *J. Am. Chem. Soc.*, 2012, **134**, 17456–17458.

34 C. N. Neumann, J. M. Hooker and T. Ritter, *Nature*, 2016, **534**, 369–373.

35 N. Ichiishi, A. J. Canty, B. F. Yates and M. S. Sanford, *Org. Lett.*, 2013, **15**, 5134–5137.

36 Y. Ye, S. D. Schimler, P. S. Hanley and M. S. Sanford, *J. Am. Chem. Soc.*, 2013, **135**, 16292–16295.

37 S. J. Lee, K. J. Makaravage, A. F. Brooks, P. J. H. Scott and M. S. Sanford, *Angew. Chemie Int. Ed.*, , DOI:10.1002/anie.201812701.

38 S. Preshlock, S. Calderwood, S. Verhoog, M. Tredwell, M. Huiban, A. Hienzsch, S. Gruber, T. C. Wilson, N. J. Taylor, T. Cailly, M. Schedler, T. L. Collier, J. Passchier, R. Smits, J. Mollitor, A. Hoepping, M. Mueller, C. Genicot, J. Mercier and V. Gouverneur, *Chem. Commun.*, 2016, **52**, 8361–8364.

39 A. Maisonial-Besset, A. Serre, A. Ouadi, S. Schmitt, D. Canitrot, F. Léal, E. Miot-Noirault, D. Brasse, P. Marchand and J. M. Chezal, *European J. Org. Chem.*, 2018, **2018**, 7058–7065.

40 W. J. Kuik, I. P. Kema, A. H. Brouwers, R. Zijlma, K. D. Neumann, R. A. J. O. Dierckx, S. G. DiMagno and P. H. Elsinga, *J. Nucl. Med.*, 2015, **56**, 106–112.

41 F. Zarrad, B. D. Zlatopolskiy, P. Krapf, J. Zischler and B. Neumaier, *Molecules*, , DOI:10.3390/molecules22122231.

42 J. Zischler, N. Kolks, D. Modemann, B. Neumaier and B. D. Zlatopolskiy, *Chem. - A Eur. J.*, 2017, **23**, 3251–3256.

43 A. V. Mossine, S. S. Tanzey, A. F. Brooks, K. J. Makaravage, N. Ichiishi, J. M. Miller, B. D. Henderson, M. B. Skaddan, M. S. Sanford and P. J. H. Scott, *Org. Biomol. Chem.*, 2019, **17**, 8701–8705.

44 B. Buszewski and S. Noga, *Anal. Bioanal. Chem.*, 2012, **402**, 231–247.

45 A. V Mossine, A. F. Brooks, N. Ichiishi, K. J. Makaravage, M. S. Sanford and P. J. H. Scott, *Sci. Rep.*, 2017, **7**, 233.

46 A. V Mossine, A. F. Brooks, V. Bernard-Gauthier, J. J. Bailey, N. Ichiishi, R. Schirrmacher, M. S. Sanford and P. J. H. Scott, *J. Label. Compd. Radiopharm.*, 2018, **61**, 228–236.

47 S. E. Allen, R. R. Walvoord, R. Padilla-Salinas and M. C. Kozlowski, *Chem. Rev.*, 2013, **113**, 6234–6458.

48 S. D. McCann and S. S. Stahl, *Acc. Chem. Res.*, 2015, **48**, 1756–1766.

49 Guidelines for Elemental Impurities, https://www.ich.org/page/quality-guidelines.

50 P. J. H. Scott and M. R. Kilbourn, *Appl. Radiat. Isot.*, 2007, **65**, 1359–1362.

51 A. L. Vavere and P. J. H. Scott, *Semin. Nucl. Med.*, 2017, **47**, 429–453.

52 D. J. Donnelly, *Semin. Nucl. Med.*, 2017, **47**, 454–460.

53 S. Preshlock, M. Tredwell and V. Gouverneur, *Chem. Rev.*, 2016, **116**, 719–766.

54 J. S. Wright, T. Kaur, S. Preshlock, S. S. Tanzey, W. P. Winton, L. S. Sharninghausen, A. F. Brooks, M. S. Sanford and P. J. H. Scott, *Copper-Mediated Late-stage Radiofluorination: Five Years of Impact on Pre-clinical and Clinical PET Imaging*, Springer International Publishing, 2020.

55 S. J. Lee, A. F. Brooks, N. Ichiishi, K. J. Makaravage, A. V. Mossine, M. S. Sanford and P. J. H. Scott, *Chem. Commun.*, 2019, **55**, 2976–2979.

56 S. Verhoog, A. F. Brooks, W. P. Winton, B. Viglianti, M. S. Sanford and P. J. H. Scott, *Chem. Commun.*, 2019, 2–6.

57 A. V. Mossine, S. S. Tanzey, A. F. Brooks, K. J. Makaravage, N. Ichiishi, J. M. Miller, B. D. Henderson, M. B. Skaddan, M. S. Sanford and P. J. H. Scott, *Org. Biomol. Chem.*, 2019, **17**, 8701–8705.

58 A. V. Mossine, S. S. Tanzey, A. F. Brooks, K. J. Makaravage, N. Ichiishi, J. M. Miller, B. D. Henderson, T. Erhard, C. Bruetting, M. B. Skaddan, M. S. Sanford and P. J. H. Scott, *Nat. Protoc.*, 2020, **15**, 1742–1759.

59 C. Perrio, S. Schmitt, D. Pla, F. P. Gabbaï, K. Chansaenpak, B. Mestre-Voegtle and E. Gras, *Chem. Commun.*, 2017, **53**, 340–343.

60 T. Hara, N. Kosaka and H. Kishi, *J Nucl Med*, 2002, **43**, 187–199.

61 C. Sauvage, N. Lazarova and M. Mueller, *J. Nucl. Med.*, 2015, **56**, 1011-.

62 A. Mossine, S. Tanzey, A. Brooks, M. Sanford and P. Scott, *J. Nucl. Med.*, 2018, **59**, 184–184.

63 X. Shao, P. L. Schnau, M. V. Fawaz and P. J. H. Scott, *Nucl. Med. Biol.*, 2013, **40**, 109–116.

64 X. Shao, M. V Fawaz, K. Jang and P. J. H. Scott, *Appl. Radiat. Isot.*, 2014, **89**, 125–129.

65 J. E. Blecha, B. D. Henderson, B. G. Hockley, H. F. VanBrocklin, J.-K. Zubieta, A. F. DaSilva, M. R. Kilbourn, R. A. Koeppe, P. J. H. Scott and X. Shao, *J. Label. Compd. Radiopharm.*, 2017, **60**, 375–380.

66 M. Kuntzsch, D. Lamparter, N. Brüggener, M. Müller, G. J. Kienzle and G. Reischl, *Pharmaceuticals*, 2014, **7**, 621–633.

67 N. E. Halvorsen and O. H. Kvernenes, *Pharmaceuticals*, 2020, **13**, 27.

68 D. G, *Pharm Zschr Russl*, 1866, **5**, 82–85.

69 H. T. N. A. Raal, A. Meos, T. Hinrikus, J. Heinamaki, E. Romane, V. Gudiene, V. Jakstas, O. Koshovyi, A. Kovaleva, C. Fursenco, T. Chiru, *Pharmazie*, 2020, **75**, 299–306.

70 S. P. Jackson IM, Lee SJ, Sowa AR, Rodnick ME, Bruton L, Clark M, Preshlock S, Rothley J, Rogers VE, Botti LE, Henderson BD, Hockley BG, Torres J, Raffel DM, Brooks AF, Frey KA, Kilbourn MR, Koeppe RA, Shao X, *EJNMMI Radiopharm. Chem*.

71 *Stahl E. Thin-Layer Chromatography. A Laboratory Handbook*, Springer, Berlin, Heidelberg, 1978.

72 M. Eisman, M. Gallego and M. Valcárcel, *J. Anal. At. Spectrom.*, 1993, **8**, 1117–1120.

73 B. D. Zlatopolskiy, J. Zischler, P. Krapf, F. Zarrad, E. A. Urusova, E. Kordys, H. Endepols and B. Neumaier, *Chem. - A Eur. J.*, , DOI:10.1002/chem.201405586.

74 Z. Zhang, C. Zhang, J. Lau, N. Colpo, F. Bénard and K. S. Lin, *J. Label. Compd. Radiopharm.*, 2016, 467–471.

75 I. F. Antunes, A. Van Waarde, R. A. J. O. Dierckx, E. G. E. De Vries, G. A. P. Hospers and E. F. J. De Vries, *J. Nucl. Med.*, 2017, **58**, 554–559.

76 T. Tang, H. S. Gill, A. Ogasawara, J. N. Tinianow, A. N. Vanderbilt, S. P. Williams, G. Hatzivassiliou, S. White, W. Sandoval, K. DeMent, M. Wong and J. Marik, *Nucl. Med. Biol.*, 2017, **51**, 10–17.

77 V. Bernard-Gauthier, A. V. Mossine, A. Mahringer, A. Aliaga, J. J. Bailey, X. Shao, J. Stauff, J. Arteaga, P. Sherman, M. Grand'Maison, P. L. Rochon, B. Wängler, C. Wängler, P. Bartenstein, A. Kostikov, D. R. Kaplan, G. Fricker, P. Rosa-Neto, P. J. H. Scott and R. Schirrmacher, *J. Med. Chem.*, 2018, **61**, 1737–1743.

78 C. C. Constantinescu, C. Tresse, M. Q. Zheng, A. Gouasmat, V. M. Carroll, L. Mistico, D. Alagille, C. M. Sandiego, C. Papin, K. Marek, J. P. Seibyl, G. D. Tamagnan and O. Barret, *Mol. Imaging Biol.*, 2019, **21**, 509–518.

79 J. Elie, J. Vercouillie, N. Arlicot, L. Lemaire, R. Bidault, S. Bodard, C. Hosselet, J. B. Deloye, S. Chalon, P. Emond, D. Guilloteau, F. Buron and S. Routier, *J. Enzyme Inhib. Med. Chem.*, 2019, **34**, 1–7.

80 S. Kaide, M. Ono, H. Watanabe, Y. Shimizu, Y. Nakamoto, K. Togashi, A. Yamaguchi, H. Hanaoka and H. Saji, *Bioorganic Med. Chem.*, 2018, **26**, 3352–3358.

81 Z. Zhang, J. Lau, C. Zhang, N. Colpo, A. Nocentini, C. T. Supuran, F. Bénard and K. S. Lin, *J. Enzyme Inhib. Med. Chem.*, 2017, **32**, 722–730.

82 and C. C. D. Herta M. Bregoff, Eugene Robters, *J. Biol. Chem.*, 1953, **205**, 565–574.

83 S. S. Tanzey, A. Mossine, A. R. Sowa, J. Torres, A. F. Brooks, M. S. Sanford and P. J. H. Scott, *Anal. Methods*, 2020, 323–350.

84 J. Connelly, *Wiley*, 2018, 199–232.

CHAPTER 6

Overall Conclusions and Future Outlook

Neurodegenerative imaging by Positron Emission Tomography (PET) has and will continue to be a considerable challenge while the biological basis for it remains unclear. Although biomarkers that indicate early progression of the disease have been validated, and PET provides a useful tool to assist in the validation of key biological targets, these efforts remain complicated because the cause of neurodegenerative diseases (NDs) has yet to be fully elucidated. For example, PET has been used to determine the depletion of Aß plaques after treatment of Alzheimer's Disease (AD) with anti-Aß antibodies (ab's).[1] Though the amyloid hypothesis of AD remains to be proven,[2] PET imaging allowed pharmaceutical companies to show that ab treatment was working by clearing out plaques from the brain.[3] After long term treatment with these antibodies however, improvements in cognition compared to control were not observed, and this left many questions. Fortunately, with using PET as a pharmacological biomarker confirmed that Aß was cleared from diseased brains, providing motivation for pharmaceutical companies to continue, and after reanalysis of a phase 3 clinical trial for aducanumab, improvement in cognition scores of a large number of patients was reported leading to review by the Food and Drug Administration (FDA).[4] PET will no doubt play an integral role in such trials as the quest to cure AD continues.

Following this, PET imaging of biological targets for Parkinson's Disease (PD) also provide a tool to monitor disease treatments by determining the functioning of the dopaminergic neurons with tracers such as [^{18}F]FDOPA.[5] Unfortunately, routine production of this tracer has been a challenge for many radiosynthetic chemists, thus, limiting research with the radiotracer. To address this ongoing challenge in the radiochemistry community, we developed an efficient, validated synthesis of [^{18}F]FDOPA that is compliant with current good manufacturing processes (cGMP).[6,7] In chapter 5, it was shown that high yields could be obtained using tetrabutylammonium fluoride ([^{18}F]TBAF) with a tetrakispyridine(copper) triflate catalyst to fluorinate a commercial boronic ester precursor. Due to guidelines recommended by the European Pharmacopeia, a quality control test for TBA needed to be developed for our synthesis.[8] We successfully implemented a TLC test in our lab, and future work will concentrate on method validation to enable widespread implementation and acceptance by federal agencies. Validation tests require the test to be reproducible for the quantities measured and the reagents used for the test to be approved under cGMP guidelines.

Even though protein aggregates and neurological function remain a diagnostic and therapeutic target for AD, a preventative approach to AD and related dementias is highly sought. Alternative targets that occur earlier on in the disease progression before clinical symptoms start to manifest in patients are hypothesized to exist, and expected to be druggable targets to prevent neurodegeneration as well as useful biomarkers. PET can be used to image and validate biomarkers thought to play an early role in NDs by developing tracers for these targets and imaging at risk patients such as elderly patients and those diagnosed with mild cognitive impairment (MCI).

Neuroinflammation is a hallmark of many ND processes, and is believed to play an early role in progression. Our effort to synthesize a radiotracer targeting a protein that is overexpressed in microglial cells (colony stimulating factor 1 receptor, CSF1R) during neuroinflammation is described in Chapter 4.[9] We chose the compound AZ683 to radiolabel because of its favorable pharmacokinetic (PK) properties such as high selectivity over other tyrosine kinase receptors, its physiochemical properties that predicted good blood brain barrier (BBB) permeability, and its structure was suitable for either carbon-11 and fluorine-18 labeling. After our successful attempt at synthesizing [^{11}C]AZ683, however, low brain uptake was observed in both rodent and nonhuman primate studies. We hypothesize that this could either be due to the high number of nitrogen atoms contained in the compound, possibly making it a p-glycoprotein (p-gp) efflux substrate or there is not a lot of baseline expression of the target, CSF1R, in healthy animals that is adequate for initial binding and uptake of the tracer. This could be investigated by imaging neuroinflammation animal models to see if the standard uptake value (SUV) is increased for [^{11}C]AZ683. Given that a new PET tracer has been developed by Horti *et al.*[10] for CSF1R that has a higher SUV of 3 compared to our compound peaking at 1 for the whole brain, the BBB permeability of our tracer is likely due to its structure. The SUV of this new tracer was dramatically increased to 8 when imaging LPS-injected baboons, a known method for induction of neuroinflammation modeling. Thus, our tracer though has low initial uptake in normal NHP may be beneficial when comparing to inflammation models and detecting minor changes in CSF1R expression. If our tracer is not adequate for neuroinflammation imaging, it can still be used to detect inflammation in the periphery associated with infections or tumor growth.

Another early biomarker of neurodegeneration that is being considered is the role of physiological transition metals and their dyshomeostasis, specifically iron, copper, and zinc. Evidence for their role comes from *ex vivo* and *in vivo* data showing increased metal concentrations near protein aggregate deposits. It is hypothesized that the regulation preventing too many free metal ions malfunctions and these metals can then induce oxidative stress through redox reactions with multiple molecules and induce aggregation by binding small peptides and causing misfolding. However, validation of this theory requires evidence indicating an increase in the free toxic redox active metals such as iron and copper at earlier time points before clinical symptoms start to manifest. The power of PET allows noninvasive imaging of patients of a test population. However, to get to that point metal chelating PET tracers need to be preclinically validated. Our attempt at this has yielded three new tracers, $[^{18}F]$FL2-b,[11] $[^{11}C]$deferiprone ($[^{11}C]$DFP),[12] and $[^{11}C]$HQ415.[13] The first thing to note about these tracers, that will be the most important factor in developing a PET tracer for the purpose of validating transition metals in the early stages of NDs, is that they have high brain uptake. The specific binding has only been tested for $[^{18}F]$FL2-b, which has high specific binding in the gray matter and low nonspecific binding in the white matter. Even more interesting is the evidence indicating that $[^{18}F]$FL2-b colocalizes with TDP-43 aggregates, making it one of the first tracers that can potentially be used for ALS imaging being that it has higher specific binding in ALS post-mortem motor cortex than age-matched control. Specific binding is used to assess how well a tracer will give a signal when bound to a target versus the background which will affect interpreting images. This has only been measured for $[^{18}F]$FL2-b using autoradiography because it is labelled with a longer-lived isotope. It is much more difficult to get reproducible data with the shorter-lived isotope, carbon-11, when performing self-blocking studies on autoradiography tissue. However, since deferiprone is already FDA approved and has a high dose limit, self-blocking studies with animal imaging can be done to assess the specific binding. Given that the molar activity (MA) of $[^{11}C]$DFP is low, a self-blocking study is warranted to assess if in fact we are seeing mostly nonspecific binding. This also creates a need to synthesize fluorine-18 labeled iron chelators to perform further studies such as autoradiography and perform longer scans. One defining factor of working with metal chelating PET radiotracers has been their stability. Both $[^{18}F]$FL2-b and $[^{11}C]$DFP are prone to radiolysis. This may be because it is their nature to participate in single electron chemistry given that they are metal chelators and are known to participate in redox reactions with them. [^{11}C]HQ415 has not had this problem and may indicate that larger metal chelating molecules are perhaps more stable. However, attempts to synthesize cold fluorinated-HQ415 proved difficult to isolate pure product after deprotection, suggesting the compound easily decomposes. For [^{11}C]DFP to reach the clinic, dosimetry studies need to be done and showing that the tracer has a higher binding potential in post-mortem diseased brain tissue than normal tissue. To enhance the molar activity, either a minimum amount of cold standard should be optimized in the deprotection conditions or an alternate method should be attempted. Nonetheless, this work shows that it is possible to develop metal chelating PET radiotracers that have good brain uptake for the assessment of NDs. Further work is needed to optimize these tracers for the clinic.

REFERENCES

1 H. Fillit, ADDF-Funded PET Imaging Makes Clinical Trial Success Possible, https://www.alzdiscovery.org/news-room/blog/addf-funded-pet-imaging-makes-clinical-trial-success-possible.

2 J. Hardy and D. J. Selkoe, *Science (80-.).*, 2002, **297**, 353 LP – 356.

3 K. Chen, A. Roontiva, P. Thiyyagura, W. Lee, X. Liu, N. Ayutyanont, H. Protas, J. L. Luo, R. Bauer, C. Reschke, D. Bandy, R. A. Koeppe, A. S. Fleisher, R. J. Caselli, S. Landau, W. J. Jagust, M. W. Weiner and E. M. Reiman, *J. Nucl. Med.*, 2015, **56**, 560–566.

4 A. Bigica, FDA Accepts Aducanumab for Review as Alzheimer Disease Treatment, https://www.neurologylive.com/view/fda-accepts-aducanumab-for-review-as-alzheimer-disease-treatment.

5 J. Darcourt, A. Schiazza, N. Sapin, M. Dufour, M. J. Ouvrier, D. Benisvy, X. Fontana and P. M. Koulibaly, *Q. J. Nucl. Med. Mol. Imaging*, 2014, **58**, 355–65.

6 A. V. Mossine, S. S. Tanzey, A. F. Brooks, K. J. Makaravage, N. Ichiishi, J. M. Miller, B. D. Henderson, M. B. Skaddan, M. S. Sanford and P. J. H. Scott, *Org. Biomol. Chem.*, 2019, **17**, 8701–8705.

7 S. S. Tanzey, A. V. Mossine, A. R. Sowa, J. Torres, A. F. Brooks, M. S. Sanford and P. J. H. Scott, *Anal. Methods*, , DOI:10.1039/d0ay01565b.

8 S. S. Tanzey, A. Mossine, A. R. Sowa, J. Torres, A. F. Brooks, M. S. Sanford and P. J. H. Scott, *Anal. Methods*, 2020, 323–350.

9 S. S. Tanzey, X. Shao, J. Stauff, J. Arteaga, P. Sherman, P. J. H. Scott and A. V. Mossine, *Pharmaceuticals*, , DOI:10.3390/PH11040136.

10 A. G. Horti, R. Naik, C. A. Foss, I. Minn, V. Misheneva, Y. Du, Y. Wang, W. B. Mathews, Y. Wu, A. Hall, C. LaCourse, H. H. Ahn, H. Nam, W. G. Lesniak, H. Valentine, O. Pletnikova, J. C. Troncoso, M. D. Smith, P. A. Calabresi, A. V. Savonenko, R. F. Dannals, M. V. Pletnikov and M. G. Pomper, *Proc. Natl. Acad. Sci. U. S. A.*, 2019, **116**, 1686–1691.

11 S. S. Tanzey, A. F. Brooks, X. Shao, T. Desmond and P. J. H. Scott, *J. Cereb. Blood Flow Metab.*, 2019, **39**, 524–608.

12 S. Tanzey, A. Brooks, X. Shao and P. Scott, *J. Nucl. Med.*, 2020, **61**, 1119.

13 S. Tanzey, S. Thompson, X. Shao, A. Brooks and P. Scott, *J. Nucl. Med.*, 2018, **59**, 1019–1019.